NASA/CR-97- 206066

IN-90-CR

11CIT

083436

# FINAL REPORT CONTRACT NAGW-3646
**Performance Period 1/11/93 - 2/28/97, not 2/28/96**

**Rationale** This project "Petrological analysis of astrophysical dust analog evolution' was initiated to try to understand the vapor phase condensation, and the nature of the reaction products, in circumstellar environments, such as the solar nebula 4,500 Myrs ago, and in the interstellar medium. Telescope-based infrared [IR] spectroscopy offers a broad-scale inventory of the various types of dust in these environments but no details on small-scale variations in terms of chemistry and morphology and petrological phase relationships. Vapor phase condensation in these environments is almost certainly a non-equilibrium process. The main challenge to this research was to document the nature of this process that, based on astrophysical observations, seems to yield compositionally consistent materials. This observation may suggest a predictable character during non-equilibrium condensation. These astrophysical environments include two chemically distinct, that is, oxygen-rich and carbon-rich environments. The former is characterized by silicates the latter by carbon-bearing solids. According to cosmological models of stellar evolution circumstellar dust accreted into protoplanets wherein thermal and/or aqueous processes will alter the dust under initially, non-equilibrium conditions.

**Experimental Procedure** This project used the Analytical and Transmission Electron Microscope [ATEM] to obtained the pertinent data on analog materials with compositions that were defined by the observations of interstellar and circumstellar dust, and interplanetary dust particles [IDPs]. Representative portions of condensed samples were embedded in Epoxy (Spurrs) and ultrathin (80-110 nm) sections were obtained for each sample. We analyzed several hundred ultrathin sections of 45 samples provided by Dr. J.A. Nuth III at NASA/GSFC. The condensed samples typically consisted of nanometer (10-20 nm) sized entities. In this project we analyzed these units and determined the chemical composition, size, shape, texture, and morphology for each recognizable unit in the samples in a statistically relevant manner. The changes in these properties as a function of isothermal annealing and/or aqueous alteration were determined in selected samples.

We studied condensation in the binary systems $MgO-SiO_2$, $Fe_2O_3-SiO_2$, $Al_2O_3-SiO_2$, the ternary system $MgO-Fe_2O_3-SiO_2$ and the $C-H_2$ system. Aqueous alteration was studied in the binary system $MgO-SiO_2$ and the effects due to thermal annealing were documented in the binary systems $Al_2O_3-SiO_2$ and $Fe_2O_3-SiO_2$ and in the ternary system $MgO-Fe_2O_3-SiO_2$. During this research we appreciated that the ultrahigh cooling rates during condensation also occur under other natural conditions, such as atmospheric entry flash heating of extraterrestrial IDPs and in materials hit by a lightning strike. Thus, we capitalized on an opportunity to study one sample that was produced by a triggered lightning strike.

**Results** The ATEM study that was conducted under this contract was unprecedented in its detailed mineralogical and chemical characterization of the samples at the level of the individual condensed units. As a result, this project was on a steep learning curve. In particular, it has proven challenging to distinguish experimental artifacts from true condensation effects. We were ultimately successful but, as in all observational studies, we had to accumulate a large database to be able to recognize composition-independent features that included post-condensation thermal equilibration (i.e. autoannealing)

The ATEM analyses showed that the condensed units were chemically homogeneous (zoned grains were rare) and had distinct compositional groupings. The laboratory-produced condensed samples typically had a fluffy morphology that isolated individual grains from 'communication' with each other during subsequent alteration. This intuitively obvious phenomenon was documented in $Al_2O_3-SiO_2$ sample wherein surface tension contracted low-$Al_2O_3$ aluminosilica

grains that changed their composition during thermal annealing compared to the composition of these grains in the condensed sample. The isolated high-$Al_2O_3$ aluminosilica grains didn't change. In the ternary system $MgO$-$Fe_2O_3$-$SiO_2$ the individual units were in physical contact during annealing. As a result, mixed Mg,Fe-olivines and -pyroxenes, iron oxides and periclase ($MgO$) formed as a function of increased annealing time. The resulting mineralogy and textures of the annealed products were indistinguishable from those observed in ultrafine-grained principal components of chondritic IDPs. The principal components that survived in IDPs are remnants of the (at least) 4,500 Myrs-old solar nebula dust.

The results of aqueous alteration of $MgO$-$SiO_2$ condensates showed that (1) $SiO_2$ was purged from the samples during the initial phase and (2) (proto-) layer silicates (smectite) only formed in compacted domains with the appropriate $MgO/SiO_2$ ratio with co-precipitation of rare periclase and/or $Mg(OH)_2$. These results confirmed phase relationships observed in the hydrated subgroup of chondritic IDPs and those predicted to occur in comet P/Halley.

The significant result of this project was that compositions of units produced by vapor phase condensation, and during aqueous alteration, showed identical behavior. That is, the compositions formed distinct clusters with preferred metal oxide/ $SiO_2$ ratios. These cluster compositions in each binary and ternary system that we analyzed matched the metastable eutectic compositions (binary systems), or ternary minimum compositions (ternary systems). This systematic behavior under extreme kinetic conditions was consistent with the phase relationships of the equilibrium phase diagram of these chemical systems (metastable eutectics and cotectic crystallization).

**Implications of this ATEM study** The finding that vapor phase condensation in circumstellar and interstellar environments was constrained by compositions of the metastable eutectic points that are allowed in the equilibrium phase diagrams of the particular chemical systems was a major step towards constraining the nature of naturally occurring dusts. Even more relevant is that (1) the eutectic compositions in the system $MgO$-$SiO_2$ have the $MgO/SiO_2$ ratios of serpentine and smectite, and (2) principal components in chondritic IDPs have serpentine and smectite bulk compositions. The results of this project offer the first experimental evidence that these relics of solar nebula dust formed as non-equilibrium condensates with so-called "non-stoichiometric compositions". Also, astronomical observations of the IR properties of dust should look for serpentine and smectite phases instead of the traditional olivine and pyroxene IR features. When the pyroxene and olivine IR signatures are confirmed, the results of this ATEM study of analog samples confirm aging of dust in the astrophysical environments.

This ATEM project had an unanticipated by-product relevant to ceramics production. Our results on the $MgO$-$SiO_2$ system suggest that the equilibrium phase diagram available in the textbooks is probably incorrect. We predict a stable eutectic point between periclase and olivine, probably at ~85 wt. % MgO. It is noted that this part of this equilibrium phase diagram was never explored experimentally. In general, vapor phase condensation experiments in combination of ATEM analyses of the type supported by this contract offer highly kinetic conditions to explore metastable phase equilibria. This work may offer support for a particular phase diagram topology in favor of other suggested topologies of a chemical system, e.g. $Al_2O_3$-$SiO_2$.

## Publications resulting from this project

### Thesis

1. Karner J.M. (1997) Mineralogy, Morphology and Chemistry of Vapor Condensed Silicate Dust Analogs. M.Sc.Thesis, University of New Mexico, Albuquerque, New Mexico, 148p. Thesis Supervisor: Prof. F.J.M. Rietmeijer

## Peer Reviewed Publications

2. Fu G. and Rietmeijer F.J.M. (1994) Ferrosilite, fayalite and magnesioferrite formation by isothermal annealing of an iron-contaminated Mg-SiO smoke. Lunar Planet. Sci. XXV, 493-494. Lunar and Planetary Institute, Houston
3. Rietmeijer F.J.M. (1995) An analytical electron microscope (AEM) study of hydrous alteration of amorphous magnesiosilica smokes. Lunar Planet. Sci. XXVI, 1163-1164. Lunar and Planetary Institute, Houston
4. Rietmeijer F.J.M. (1996) An analytical electron microscope (AEM) study of hydrous alteration in a smoke of modal forsterite composition. Lunar Planet. Sci. XXVII, 1069-1070. Lunar and Planetary Institute, Houston
5. Karner J.M. and Rietmeijer F.J.M. (1996) A first result of isothermal annealing of an Fe-SiO smoke. Lunar Planet. Sci. XXVII, 647-648. Lunar and Planetary Institute, Houston
6. Karner J.M., Wasilewski P.J., Rietmeijer F.J.M. and Nuth J.A. (1996) Preliminary electron microbeam analyses of lightning induced evaporation and gas phase mixing. Lunar Planet. Sci. XXVII, 649-650. Lunar and Planetary Institute, Houston
7. Rietmeijer F.J.M., Rotundi A., Colangeli L., Mennella V., Palumbo P. and Bussoletti E. (1997) Buckycarbons and fullerenes in interplanetary dust particles based on evidence from a transmission electron microscope (TEM) study of vapor condensed carbons with variable C/H ratio. Lunar Planet. Sci. XXVIII 1175-1176. Lunar and Planetary Institute, Houston
8. Rietmeijer F.J.M., Fu G. and Karner J.M. (1997) Alteration of presolar dust based on transmission electron microscope/analytical electron microscope studies of chondritic interplanetary dust particles and nonequilibrium simulation experiments. In Workshop on Parent-body and Nebular Modification of Chondritic Materials (M.E. Zolensky, A.N. Krot and E.R.D. Scott, eds.), LPI Tech. Rpt. 97-02, Part 1, 51-53
9. Rietmeijer F.J.M., Karner J.M., Nuth J.A., and Wasilewski P.J. (1997) Phase equilibrium in a triggered lightning experiment. European Journal of Mineralogy, *submitted*.
10. Rotundi A., Rietmeijer F.J.M., Colangeli L., Mennella V., Palumbo P. and Bussoletti E. (1997) Identification of carbon forms in soot materials of astrophysical interest. Astron. Astrophys., in press.
11. Rietmeijer F.J.M. and Karner J.M. (1997) Metastable phase equilibria in the system $Al_2O_3$-$SiO_2$, in preparation.

## Abstract

1. Karner J.M., Rietmeijer F.J.M., and Janeczek J. (1996) AEM, XRD, and IR analyses of an AlSiO condensate annealed for 2 hours at room temperature up to 1100°C. Meteoritics Planet. Sci. 31, A69

Frans J.M. Rietmeijer

Albuquerque, October 31, 1997

# FERROSILITE, FAYALITE AND MAGNESIOFERRITE FORMATION BY ISOTHERMAL ANNEALING OF AN IRON-CONTAMINATED Mg-SiO SMOKE.

Fu Guofei and Frans J.M. Rietmeijer, Department of Earth and Planetary Sciences, University of New Mexico, Albuquerque, NM 87131, USA.

Laboratory studies of thermally-annealed vapor condensates will advance the understanding of dust evolution in oxygen-rich protostellar environments. A previous analytical electron microscope (AEM) study of an annealed Mg-SiO smoke showed coarsening of forsterite and enstatite nanocrystals accompanied by equilibration of bulk Mg/Si (at%) ratios as a function of annealing time (2, 4, 8, & 39 hours) *in vacuo* at 1000°K [1]. This AEM study used dispersed, 3-dimensional "bulk" samples [1] in which it was difficult to obtain grain size distributions, and to perform electron diffraction and quantitative chemical analyses of individual nanocrystals. The introduction of serially-sectioned, ultrathin (80-100 nm) sections for AEM analyses of interplanetary dust [2] was the incentive to re-analyse the thermal-annealing history of the Mg-SiO smoke because the individual grains in ultrathin sections are accessible to quantitative chemical, electron diffraction and textural analyses. Traces of an unidentified Fe-bearing contaminant in the "bulk" samples did not react with the Mg-SiO smoke [1]. We exploit the greatly improved sample preparation to look for Fe-silicates that might have formed during annealing. Ultrathin sections of smoke samples annealed for 8, 30 and 167 hours were prepared for AEM analyses using a Jeol 2000FX AEM equipped with a TN-5000 energy dispersive spectrometer [cf. 3]. The samples appear dull-grey to black in white light, but ~40% of the 167h-sample has a yellow tinge that is probably due to ferric iron-bearing phases. We prepared ultrathin sections of the differently-coloured materials.

RESULTS. The annealed samples have an open cluster morphology. Relics of the crude network of interconnected ribbons of the original condensate [1] are still present in the 167h-sample (black fraction). All samples are dominated by equigranular (*i.e.* a narrow size distribution), poorly-crystalline Mg-SiO material with randomly oriented nanocrystals. Distinctly fine-grained (< 20 nm in diameter) polycrystalline materials are in variable proportions associated with coarse-grained material with nanocrystals of ~40-60 nm (8 hours) and ~60-80 nm in diameter (167 hours). The quantity of nanocrystals, and porosity of the Mg-SiO material, gradually increase with annealing time. The fine-grained domains are slightly Mg-richer than coarse-grained polycrystalline materials. The electron diffraction data are consistent with forsterite, enstatite and tridymite. Small amounts of amorphous silica-rich (>95 wt% $SiO_2$) areas and tridymite crystals (both up to ~200 nm in size) occur throughout the Mg-SiO material in all samples. The coarse-grained Mg-SiO material in each sample contains round to irregularly-shaped, platey single-crystal grains of ~100 nm up to ~500 nm in diameter. In the 167h-sample they tend to form subhedral single-crystal grains. The compositions of the Fe-SiO grains range from ~30-75 wt% FeO (8 hours) and ~30-95 wt% FeO (30 & 167 hours) with two clusters at 35 and 52 wt% FeO of ferrosilite and fayalite grains, and an a third cluster at 70 wt% FeO of hematite, and possibly maghemite, grains. In addition to equigranular Mg-SiO material, the 167h-sample's yellow fraction is characterised by (I) randomly-distributed, euhedral magnesioferrite single-crystals (< 300 nm long; ~18 wt% MgO) and euhedral, single-crystal brucite, $Mg(OH)_2$, up to 50-100 nm in size and (II) smoke-like domains of subrounded grains that include (a) euhedral periclase (MgO) grains with a Mg-SiO mantle (~16-65 nm in diameter) and (b) core-free Mg-SiO grains (~9-60 nm in diameter).
<u>Fayalite and ferrosilite</u>. In both iron-rich olivine and pyroxene $Fe^{2+}/(Mg+Fe^{2+})$ = ~0.85 - 1.0. These silicates generally contain ferric iron, *viz.* $Fe^{3+}$ ions between 0.05 - 0.65 (calculated from stoichiometry), but mostly 0.05-0.10 (~70% of data). The $Fe^{2+}/(Fe^{2+} + Fe^{3+})$ ratios are 0.6-1.0 (olivine) and *fe* = 0.90-1.0 (pyroxene). In rare pyroxenes all iron is $Fe^{3+}$. We have not yet unambiguously identified laihunite (La) by electron diffraction but rare olivines in the 30h- and 167h-samples fit the structural formula of this 'ferrifayalite' mineral. These olivine are $Fo_{75}Fa_0La_{25}$ and $Fo_{54}Fa_0La_{46}$ (30 hours), and $Fo_5Fa_{90}La_5$ and $Fo_1Fa_{69}La_{30}$ (167 hours). We estimate log $fO_2$ between -15 and -10 atm. at the FMQ and HM buffers.

DISCUSSION. Autoannealing describes post-condensation solid-state transformations that occur in a vapor-condensed smoke [4]. It will be difficult to identify nanocrystals as part of the condensation history or of later thermal annealing. For example, fine-grained Mg-silicates in poorly-crystalline material of the 8h-sample might be due to autoannealing. Otherwise the increased grain size and quantities of nanocrystals, and the formation and growth of Fe-silicates, are consistent with prolonged heating. Contrary to the earlier findings [1], an Fe-contaminant in the present allocations did react with the Mg-SiO smoke during isothermal annealing. The Fe-silicates might have formed by reaction of Fe-vapor with Mg-silicates or via solid-state reactions. Considering the boiling points of metallic iron and of various Fe-oxides and the thermal annealing conditions, we presently favour the latter explanation. The Fe-contaminant was probably steel from the collector plate. We propose that enstatite reacted to form fayalite and ferrosilite, *viz.* (*a*) $MgSiO_3 + 2Fe + 1/2O_2 = Fe_2SiO_4 + Mg(g)$, (*b*) $2MgSiO_3 + 2Fe = Fe_2SiO_4 + 2Mg(g) + SiO(g) + 1/2O_2$, and (*c*) $MgSiO_3 + 3Fe + 2O_2 = FeSiO_3 + MgFe_2O_4$, whilst forsterite formed Fe-silicates according to (*d*) $2Mg_2SiO_4 + 2Fe = 2FeSiO_3 + 4Mg(g) + O_2$, and (*e*) $Mg_2SiO_4 + 2Fe = Fe_2SiO_4 + 2Mg(g)$.

The reactions *a*,*b*, *d*, & *e* produce a metallic-Mg vapor consistent with earlier evidence [1] for evaporative Mg-loss during annealing. Reaction *b* also produces SiO vapor. The Mg-bearing vapor condensed into euhedral MgO crystals possible as the result of the vapore reacting with liberated $_2O_2$. The euhedral MgO crystals indicate 3-dimensional growth at (local) high supersaturation ratio. They provided nuclei for Mg,Si-O deposition. Rare magnesioferrite spinel formed by reaction *c*. Magnesioferrite occurs naturally as a result of extreme and highly transient temperature gradients that yield disequilibrium mineral assemblages at a bulk scale but with domains of full thermodynamic phase equilibrium [5]. This type of environment is also conducive to laihunite formation via oxidation of fayalite wherein synthetic laihunite uniquely coexists with hematite and silica under atmospheric oxidation conditions [6,7]. Kinetically-controlled mineral formation rather than thermodynamic equilibrium for ultrafine asemblages also occurs during atmospheric entry flash-heating of micrometeorites wherein laihunite has also been observed [8,9]. The data support chaotic disequilibrium during isothermal annealing of an Fe-bearing, Mg-SiO smoke. After prolonged isothermal annealing, $Fe^{3+}$ is no longer accomodated in the silicates which induces the formation of nonstoichiometric Fe-silicates, such as laihunite, and there is evidence for partial evaporation and condensation to produce the distinctly fine-grained Mg(Si-O) smoke. Brucite is probably a post-annealing artifact due to reaction of MgO with atmospheric moisture.

CONCLUSIONS. We exploit the inadvertent contamination of an Mg-SiO smoke with Fe-metal grains. Fayalite and ferrosilite with variable fe-ratios, rare laihunite and magnesioferrite occur alongside existing forsterite, enstatite and tridymite. The Fe-minerals form from their Mg-counterparts as a function of annealing time at 1000°K with (partial) evaporation and condensation of a metallic-Mg vapor after prolonged annealing. When thermal annealing of dust in protostellar regions is an important process, it follows that this dust may contain variable proportions of Mg-rich and Fe-rich olivines and pyroxenes and accompanying MgO and Mg,Fe-oxide minerals. In addition to metamorphism of the dust, partial evaporation and condensation events could occur. The opacity of silicate dust in the near-IR region depends on their $Fe^{2+}/(Fe^0 + Fe^{2+} + Fe^{3+})$ ratio. This ratio might provide an important constraint on the aging of astrophysical dust [10]. We have shown that thermal annealing of Mg-silicates in the presence of an "Fe-donor phase" tends to produce high *fe*-ratios in a small fraction of the silicate grains. This type of AEM analyses of astrophysical dust analogs may help elucidate the details of dust evolution in environments such as the primitive solar nebula.

**REFERENCES**. 1. Rietmeijer FJM et al. (1986) Icarus 66, 211-222; 2. Bradley JP & Brownlee DE (1986) Science 231, 1542-1544; 3. Rietmeijer FJM (1991) EPSL 102, 148-157; 4. Rietmeijer FJM & Nuth JA (1991) Proc. LPS 21, 591-602; 5. Foit, Jr. FF (1987) Amer. Mineral., 72, 137-147; 6. Kondo, S et al. (1985) Amer. Mineral., 70, 737-746; 7. Kitamura, M et al. (1984) Amer. Mineral., 69, 154-160; 8. Keller LP et al. (1992) LPSC XXIII, 6765-676; 9. Rietmeijer FJM (1992) LPSC XXIII, 1151-1152; 10. Nuth JA & Hecht JH (1990) Astrophys. Space Sci. 163, 79-94.

This work was supported by NASA grant NAGW-3646

# AN ANALYTICAL ELECTRON MICROSCOPE [AEM] STUDY OF HYDROUS ALTERATION OF AMORPHOUS MAGNESIOSILICA SMOKES.

Frans J.M. Rietmeijer, Department of Earth and Planetary Sciences, University of New Mexico, Albuquerque, NM 87131, USA.

Hydrous alteration may affect amorphous silicates in the interstellar medium [1]. Thus, the ratio of hydrated versus anhydrous silicates is relevant to understand the early history of the primitive solar nebula [2,3]. For example, infrared [IR] spectral analyses of comets show that hydrated silicates are part of the ejected dust [4] while the dust compositions in comet P/Halley are consistent with ~8% of its dust as phyllosilicates [5]. These studies do not constrain the phyllosilicate origins, *i.e.* primary (interstellar dust) and secondary phases that formed *in situ* via hydrocryogenic and low-temperature aqueous alteration. Assuming that a fraction of chondritic interplanetary dust particles includes cometary debris, phyllosilicates in icy protoplanets have a largely secondary origin [6,7]. Experimentally determined hydration rates in amorphous Mg-SiO smokes indicate that significant hydration occurs in several months at 300K to several hours at 400-450K [3]. The rates are established based on changes in several features of the IR spectra. These changes in relative strengths of the features are indicators of changes in the Mg-SiO system but not of the diagnostic mineralogy [2,3]. This study monitors the mineralogical and textural changes in the Mg-SiO smokes used to develop the kinetic model [3]. Leaching and solid-state diffusion are probably the rate limiting steps in protophyllosilicate formation during hydration of vapor-condensed amorphous magnesiosilica materials.

I use a Jeol 2000FX AEM operated at 200 keV that allows determination of the chemical properties and the crystalline or amorphous nature of areas ~10-20 nm in diameter. The samples include (1) the starting material, (2) four samples heated in contact with liquid water at 357K for 48, 72 and 96 hours and at 368K for 9.1 hours, and (3) two samples in contact water at 378K for 3 and 7.5 hours (for details, cf. ref. [3]). A small portion of each sample is embedded in epoxy to obtain ultrathin (80-100 nm) sections for AEM analyses.

OBSERVATIONS. The original smoke contains three distinct textural units: (I) large (40-160 nm) opal-A spheres with tridymite domains ($\phi \simeq$ 1-3 nm), and radial shrinkage features. They are a kinetically-controlled late condensate [8] that occurs in all samples, (II) fluffy silica smoke with limited coagulation of its spherical units ($\phi$ = 27.5-85.7 nm; mean = 56.6 nm), and (III) fluffy Mg-SiO smoke with well-identified spherical units ($\phi$ = 4.7-34.0 nm; mean = 19.35 nm). The recognisable units of the silica smoke become smaller ($\phi$ = 7.7-68.5 nm; mean = 38.1 nm) with hydration time (densification?). There is also increased blurring of these units into patches of nonporous silica material. After 96 hours (357K) the originally distinct silica and Mg-SiO smokes become entangled due to collapse of the smoke texture. Silica smokes are not recognised in hydrated samples at 378K. The original Mg-SiO smoke texture is present in all samples but compact, nonporous patches (40-70 nm in size) occur after 48 hours (357K). After 72 hours many areas of the original smoke collapse into nonporous patches with > 25 Mg el.wt%. The samples after 96 hours (357K), and 3-7.5 hours (378K), also contain ragged spheres ($\phi \simeq$ 20 - 215 nm) with > 25 Mg el.wt%. All silica and magnesiosilica materials are amorphous.

Table 1 shows the compositions (Mg el.wt%) of the hydrated Mg-SiO smokes as a function of time and temperature. The bimodal distribution after 72 hours is real but remains unexplained at this time. Bimodality is not observed in samples heat-treated at 378K which show the same full range as the sample after 72 hours (357K). The mean compositions and ranges delineate the liquid immiscibility region in the $MgO-SiO_2$ phase diagram. The maximum values match the enstatite-crystobalite eutectic which is consistent with $Mg_6Si_8O_{22}$(or, $Mg_6Si_8O_{20}(OH)_4$, *i.e.* talc, kerolite, or saponite. For this qualitative comparison the Mg-SiO condensate represents the "quenched liquid" while leached silica precipitates as opal-A rather than cristobalite.

Protophyllosilicates. After 48 hours (357K), and 3-7.5 hours (378K), the nonporous patches and ragged spheres display a tangled network of phyllosilicates that are typically one or two basal units thick. After 73 hours (357K) extremely rare crystallites are up to five basal units thick. The basal lattice fringes range from 1.0 - 3.4 nm (mean = 1.86 nm; $N$=72). The spacings show no statistically significant differences among the hydrated samples. The most common spacings are between 1.2 nm and 2.2 nm with a distinct mode at 1.87 nm (range 1.6-2.16 nm). The fringe spacings support saponite. After 7.5 hours (378K) rare nanocrystals with 0.9 nm basal fringes suggest that talc, or kerolite, forms in addition to smectite.

TABLE 1: The mean and range ($R$) of Mg-contents (el. wt%) in hydrated magnesiosilica materials as a function of time and temperature.

| Temp ($^{o}$K) | Time (hours) | mean | $R$ | $S$ |
|---|---|---|---|---|
| starting material | | 14.7 | 6.4-20.0 | -0.575 |
| 357 | 48 | 16.3 | 2.5-29.4 (NO) | |
| 357 | 72 | 6.9 | 2.5-12.7 | -0.64 |
| | | 23.6 | 13.3-36.9 | |
| 357 | 96 | 7.8 | 2.2-18.8 | |
| 368 | 9.1 | 21.5 | 2.5-34.6 | -0.67 |
| 378 | 3 & 7.5 | 25.4 | 9.7-34.5 | |

Note: Populations are normal distributions at 95% significance level unless otherwise indicated (NO in the table). In case of non-Gaussian distributions the skewness value (S) is indicated.

DISCUSSION. The textures, sizes, and compositions of the units support mobilisation of silica as a function of hydration time. Leaching mimics liquid immiscibility in the MgO-$SiO_2$ phase diagram. That is, particular bond configurations are stable in the hydrated amorphous materials prior to phyllosilicate formation. The phyllosilicates spacings are similar to primitive clays in volcanic and synthetic glasses where a prominant 0.3-0.33 spacing may be attributed to the Si-O bond [9]. This spacing times eight is similar to the mean maximum spacing, 2.8 nm, in the hydrated samples. Protophyllosilicates only form in areas with a eutectic composition. While the bulk Mg/Si ratios do not match saponite or talc, spinodal fluctuations may induce nucleation. The magnesium diffusion coefficient in "enstatite-like material" at 298K, $10^{-20}$-$10^{-21}$ $m^2$/sec [10] suggests that diffusion will not restrict protophyllosilicate growth in the samples. Hydrated samples obtained after longer heat-treatment periods are under investigation. It is anticipated that layer silicates will be pervasive in these samples.

CONCLUSION. Hydration of the magnesiosilica smokes is characterised by leaching and solid-state diffusion that allows protophyllosilicate formation in amorphous, nonporous smoke areas. The IR features clearly reflect hydration of the magnesiosilica materials but not the actual form of protophyllosilicates. The results of the previous IR study [3] and this AEM analysis show that primitive saponite and talc (or, kerolite) may be present in interstellar dust, comet nuclei, and outer belt asteroids.

REFERENCES. 1. Knacke RF & Kratschmer W, Astron. Astrophys. 292, 281-288, 1980; 2. Nuth JA et al., JGR 91 (B4), D533-D537, 1986; 3. Nelson R et al., JGR, 92 (B4), E657-E662, 1987; 4. Sandford SA, Fundam. Cosmic Phys. 12, 1-73, 1987; 5. Jessberger EK et al., Nature 332, 691-695, 1988; 6. Rietmeijer FJM, EPSL 102, 148-157, 1991; 7. Rietmeijer FJM. Trends Mineral. 1, 23-41, 1992; 8. Rietmeijer FJM & Nuth JA, Proc. LPSC 21, 591-599, 1991; 9. Tasaki K et al., Clays Clay Miner. 37, 348-354, 1989; 10. Luce RW et al., GCA 36, 35-50, 1972.

The samples for this study are provided by Joe Nuth (NASA-GSFC).
This work is supported by NASA grant NAGW-3646.

# AN ANALYTICAL ELECTRON MICROSCOPE [AEM] STUDY OF HYDROUS ALTERATION IN A SMOKE OF MODAL FORSTERITE COMPOSITION

Frans J.M. Rietmeijer, Department of Earth and Planetary Sciences, University of New Mexico, Albuquerque, NM 87131, U.S.A.

Many studies have simulated vapor phase condensation in astrophysical environments such as the solar nebula. They generally investigated simple (Mg,Fe)-SiO vapors that yielded fine-grained amorphous and/or crystalline smokes with pyroxene and olivine compositions. A typical study matched infrared [IR] spectra of these smokes with those of astrophysical dusts but AEM analyses of smokes at the level of their constituents were rarely attempted. These analyses of the condensation event, including autometamorphism [1], and thermal alteration and hydration are necessary to constrain the onset of mineralogical activity in the solar nebula [2-4], in particular the nature of protophyllosilicates. Infrared spectroscopy, X-ray diffraction, scanning electron microscopy and AEM are the most common techniques for smoke characterization. The fact that IR spectroscopy is sensitive to different properties than AEM, for example, is not always appreciated, *e.g.* AEM analyses of hydrated Mg-SiO smokes with distinct IR features for layer silicates [2] showed small amounts of proto-phyllosilicates restricted to domains with the appropriate $MgO/SiO_2$ ratio [4]. I report the ongoing effort of AEM characterization of experimentally hydrated Mg-SiO smokes with a resolution that allows comparisons with AEM studies of interplanetary dust particles [IDPs] and undifferentiated meteorite matrices. A JEOL 2000FX AEM operating at 200 keV was used to determine the chemistry, and crystalline or amorphous nature, of individual smoke particles. Three samples include the Mg-SiO smoke that was the used for hydration at 423°K (22 hours) and 573°K (74 hours). A small volumes of each sample was embedded in epoxy to prepare ultrathin (80-100 nm) sections for AEM analyses.

**OBSERVATIONS.** The constituent compositions in the starting material, but for two distinct gaps, range from pure $SiO_2$ to pure MgO [Figure 1]. As constituents may be smaller than the section thickness individual analyses may be compromised. The ranges of the populations are slightly misleading because the variations in $MgO/SiO_2$ ratios may in part be an experimental artifact, particularly the texturally distinct end-members.

The hydrated samples do not show the complete range of $MgO/SiO_2$ ratios which may be due to heterogeneity at a larger scale than the sample volumes selected for ultrathin sectioning. This effect seems most likely for the silica-rich materials, that is a related study of hydrated Mg-SiO smokes showed that silica leached from the original smoke precipitated in distinct location in the sample [4].

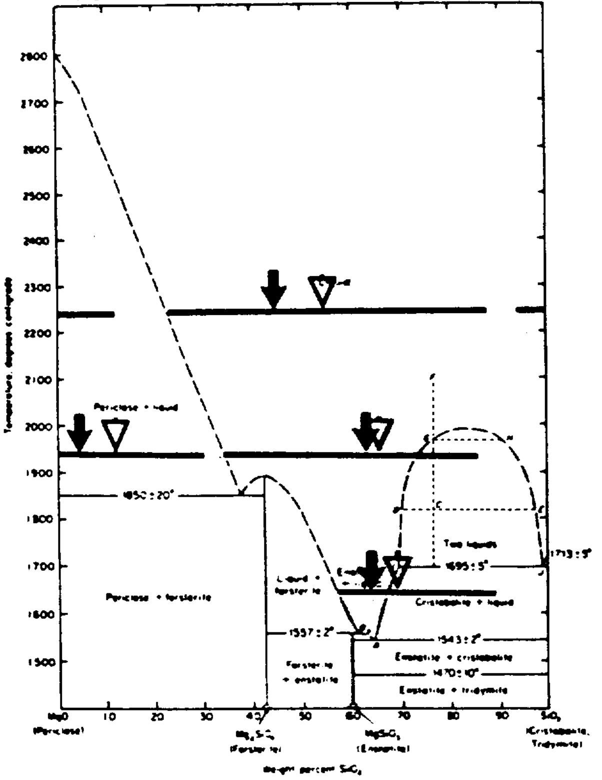

FIGURE 1: The binary phase diagram $MgO-SiO_2$ [reproduced from E.G. Ehlers, The Interpretation of Geological Phase Diagrams (1972) W.H. Freeman and Company, San Francisco] showing from top to bottom the MgO wt% ranges of (1) the starting material, (2) the hydrated sample at 423°K, and (3) the hydrated sample at 573°K for 74 hours. The modal (solid arrows) and mean values (open arrowheads) are also indicated.

## Hydrous Alteration of Forsterite Smoke: Rietmeijer, F.J.M.

The starting material is a porous smoke with pure silica particles and coagulated particles with MgO between the mean and modal values. The smoke includes (1) amorphous particles, $SiO_2$ > 65 wt%, with a well-defined grain boundary ($\phi$ = 30-60 nm) and rare ordered domains of tridymite or cristobalite, and (2) ragged (coagulated) particles (up to ~200 nm in size), MgO > 35 wt%, with scattered (sub)circular electron-opaque domains ($\phi \simeq 6$ nm). The domains are single-crystal forsterite that invariably occur in particles of mean MgO content, and higher. Particles of both morphological types contribute to the population with 12-78 wt% MgO. Forsterite, and possibly periclase (MgO), domains occur in particles with MgO > 90 wt%, while those in coagulated grains, MgO $\simeq$ 37 wt%, may also include enstatite.

During hydration the porous smoke has collapsed into a dense amorphous material with 14.5 - 65 wt% MgO with patches showing 0.7 nm lattice fringes (cristobalite?) (423/22) and MgO = 12 - 42 wt% in the 573/74-sample. This material is dominated by tangled networks and sinuous protophyllosilicate grains that are typically two to three basal layers thick. They are most abundant when the Mg-contents is close to the mean MgO value. The density of these protophyllosilicates, that may show turbostratic stacking, is much higher in the 573/74-sample compared to the sample hydrated at 423°K. The former also contains spikey (1-2 basal layers thick) and large (up to 600 x 100 nm) protophyllosilicate grains. In both samples the lattice fringe spacings and chemistry support the talc hydrate, kerolite, ($d_{002}$ = 0.99 nm; $d_{001}$ = 1.9-2.1 nm) and smectite with an average basal spacing of 1.6 nm (range: 1.3-1.9 nm).

The 423/22-sample has many tabular pure-Mg grains (< 60 nm thick). A protophyllosilicate that is two 1.7 nm basal layers thick covers the planar surfaces of the pure-Mg grains. The grain interior shows a mottled chessboard texture of domains with a 2.6 nm fringe spacing. The electron diffraction data support brucite, $Mg(OH)_2$ but with incipient damage caused by the incident electron beam. Some diffraction maxima fit both brucite and periclase (MgO) and are probably an experimental artifact. A few relic forsterite domains remain.

**DISCUSSION.** The collapsed condensate texture and formation of distinct end-member domains indicate that leaching was the rate limiting step in the mineralogical development of hydrated samples [*cf*.4]. The mean and modal MgO values of the starting material are close to the forsterite composition. The Ostwald Step Rule thus favors metastable growth of this olivine during autoannealing of the quenched Mg-SiO melt and possibly also MgO. Hydration of the Mg-SiO matrix yielded the saponite: $4\ Mg_2SiO_4 + 4\ H_2O.SiO_2 + nH_2O = Mg_6Si_8O_{20}(OH)_4.nH_2O + 2\ Mg(OH)_2$ and kerolite, *viz*. $4\ Mg_2SiO_4 + 4\ H_2O.SiO_2 + 2\ H_2O = Mg_6Si_8O_{20}(OH)_4.2H_2O + 2\ Mg(OH)_2$. Silica saturation during hydration is shown by formation of these metastable protophyllosilicates matching the mean and modal MgO matrix contents instead of serpentine, $Mg_6Si_4O_{10}(OH)_8$. The kinetically controlled co-precipitation of saponite and kerolite reflects the variable availability of water during these hydration experiments. The temperatures in both hydration experiments were high enough that diffusion was not a limiting factor for growth of these protophyllosilicates and brucite from nanometer sized forsterite. Brucite or MgO were not found in AEM analyses of carbonaceous chondrite matrix. A porous mass of periclase occurs in one Mg-rich, saponite dominated, IDP [5]. From this work it appears that formation of MgO or $Mg(OH)_2$, saponite and talc, or kerolite, is restricted to the pure $MgO-SiO_2$ system. Trace amounts of impurities, *e.g.* Al, may affect the product phases of hydration. Hence, MgO or brucite are probably rare minerals in meteorite matrix and IDPs.

**CONCLUSIONS.** Hydration of an Mg-SiO condensate under silica-saturated conditions favors protophyllosilicates with high Si/Mg ratios instead of serpentine. The resulting saponite and talc hydrate, or kerolite, reflect kinetically favored growth controlled by the availability of water for hydration. The results support that serpentine-rich chondritic IDPs are rare among the most primitive, hydrated solar system materials.

**REFERENCES.** [1] Rietmeijer FJM & Nuth JA (1991) Proc. Lunar Planet. Sci. 21, 591-599; [2] Nelson R et al. (1987) JGR, 92 (B4), E657-E662; [3] Rietmeijer FJM et al. (1986) Icarus 66, 211-222; [4] Rietmeijer FJM (1995) LPS XXVI, 1163-1164; [5] Zolensky ME & Lindstrom DJ (1992) Proc. Lunar Planet. Sci. 22, 161-169.

The samples were provided by J.A Nuth (NASA-GSFC). This work was supported by NASA Grant NAGW-3646.

# A FIRST RESULT OF ISOTHERMAL ANNEALING OF AN FE-SIO SMOKE

Jim M. Karner and Frans J.M. Rietmeijer, Department of Earth and Planetary Sciences,
University of New Mexico, Albuquerque, NM 87131, USA

Laboratory studies of thermally annealed smokes will advance the understanding of silicate dust evolution in O-rich protostellar environments. Previous condensation experiments on (Mg,Fe)-SiO vapors yielded amorphous solids of approximately olivine and pyroxene compositions [1,2]. Condensation in refractory Al-SiO, Fe-Al-SiO, and Fe-SiO vapors similarily produced amorphous solids but with cation proportions fixed at discrete values of existing Al, Fe-silicates [3]. Thermal annealing of an MgSiO smoke at 1000 °K for up to 30 hours showed increased crystallinity and coarsening of forsterite and tridymite grains prior to the formation of thermodynamically stable enstatite [4]. In a related isothermal annealing study of an Fe-bearing MgSiO smoke, fayalite and ferrosilite formed at 1000 °K from their Mg-counterparts [5]. After 167 hrs., this study documented partial evaporation of the smoke and recondensation of a metallic-Mg vapor [5]. These studies showed that thermal metamorphism of smokes produced metastable high-temperature end members of the appropriate solid solution.

This study represents the first data from a thermally annealed FeSiO condensate at 1000 °K for 4 hrs. first studied in 1991[6]. Ultramicrotomed thin sections (80-100 nm thick) of the annealed sample were prepared for analytical electron microscopy (AEM) for quantitative thin film analyses using a JOEL 2000 FX analytical microscope (AEM) equipped with a TN 5500 energy dispersive spectrometer for analysis of elements with $Z > 11$. The crystallographic nature (amorphous or crystalline) of smoke particles was determined by High Resolution imaging and Selected Area Electron Diffraction (SAED). Grain sizes were measured on TEM negatives with a relative error of ~7% (~80% have circular cross-sections; the remainder have an aspect ratio of ~0.75). Iron was calculated as FeO but it is more likely that it occurs as ferric iron [6].

RESULTS. The annealed sample has a typical texture of small (< 70nm) isolated grains, and contained in chains and clusters, as well as (rare) larger grains up to 285 nm. The grains are mostly amorphous, but some ordering is present. The compositions for individual grains (N= 272) show normal distributions with means at 0, 9, and 28 wt.% FeO at a 90% confidence limit. The sample is described by four distinct mineralogical, chemical, and morphological groups:

I. **(Rare) Pure (100 wt.%) $SiO_2$ droplet shaped grains** (131 nm to 285 nm in diameter) typically have a very smooth surface texture.

II. **97-99 wt.% $SiO_2$ nonspherical grains** (18- 90 nm in longest dimension, with aspect ratios ~0.75) have irregular outlines resulting from coagulation of individual grains. Their electron diffraction data are consistent with tridymite. Small (~6 nm) opaque domains are dispersed within these grains. These domains are assumed to be "Fe" grains as they might account for 1-3 wt.% FeO in these silica grains. The nature of the "Fe" phase remains undetermined.

III. **4-14 wt.% FeO silica grains** are circular to subcircular in shape, have a smooth texture, and are contained in clusters or chains of several grains. Individual grains are 5 nm to 17 nm in diameter. The SAED patterns show strong maxima consistent with tridymite.

IV. **15-43 wt.% FeO silica grains** are subcircular to elongate in shape (aspect ratio ~ 0.7) and range in size from 4 nm to 27 nm. These grains are found to be isolated or in small chains, as well as in dense clusters wherein individual grains are fused together. Their SAED patterns show strong diffraction maxima consistent with tridymite.

**Grain size distributions.** 222 individual grains with a 5-43 wt.% FeO show a log-normal size distribution (R= 0.99) for grains ranging from 4 nm to 27 nm. The mean size of these grains is 13 nm. Similarly 45 nonspherical silica grains from 18 - 90 nm show a log-normal distribution (R= 0.98). These grains have an average size of 35 nm.

DISCUSSION. The condensed material had a fluffy morphology with the grains <100 nm in size. Locally the sample contained pure silica clusters and globules up to 450 nm in diameter. The annealed sample is similar to the original smoke in overall morphology, and the presence of clusters and globules. The annealed sample uniquely contains pure silica droplet shaped grains. Both the original smoke and annealed samples showed trimodal distributions for the compositions of individual grains (Table 1).

FeSiO Smokes: Karner J.M. and Rietmeijer F.J.M.

Table 1. Comparison of original and annealed FeSiO smokes.

| | Unannealed smoke<br>[Ref. 6] | Annealed smoke at 1000 $^{0}$K for 4 hrs. [this report] |
|---|---|---|
| General morphology | Highly porous texture with grains <100 nm but up to 450 nm in clusters and globules | Porous morphology with grains <100 nm but up to 285 nm in smooth droplet grains |
| Chemical distributions | Trimodal with peaks at zero wt.%,<br>27.5 (range 12-60%) and<br>87.5 FeO wt.%. | Trimodal with peaks at zero wt.%,<br>9 (range 4-14%) and<br>28 (range 15-43%) FeO wt.% |
| Morphological and chemical groupings | 1) pure tridymite grains w/ simple and polysynthetic twinning<br>2) High-Fe silica grains (12-60%), include. rare dumbbell shaped grains<br>3) Maghemite grains +/- a mantle of amophous silica | 1) pure silica droplet shaped grains<br>2) 97-99% non-spherical silica grains<br>3) 4-14% Fe silica grains<br>4) 15-43% Fe silica grains |
| Crystallographic properties | Fringes and patterns matching tridymite in pure silica grains and high Fe silica grains. Fringes and patterns match maghemite in Very-high Fe silica grains | Diffraction patterns match tridymite for pure silica irregular edged grains and 4-43% Fe silica grains |
| Grain size distributions | 1)Silica grains show log-normal distribution<br>2) High-Fe silica grains show poor fit to a log-normal distribution<br>3) Maghemite grains range from 41 to 65 nm. Skewed distribution with mean of 38 nm and mode of 45 nm | 1) 4-43% Fe silica grains show a log - normal distribution<br>2) Nonspherical silica grains show a log normal distribution<br>3) Pure silica droplet grains range from 131 nm to 285 nm with mean size of 202 nm |

We did not locate grains with highest FeO contents in the annealed sample. The population of grains with FeO from 4-43 wt.% in the annealed sample actually included two distinct populations at 9 and 28 wt.% FeO. Both samples show approximate log-normal size distributions for silica grains (< 3 wt.% FeO) and high-Fe silica grains with similar size ranges for silica grains in both samples. The high-Fe silica grains (12-60 wt.% FeO) in the original sample were larger than those in the annealed sample; viz. maximum size ~120 nm and mean of 47 nm compared to a max of 27 nm and a mean of 13 nm.

In the original smoke an apparent high abundance of crystalline material was explained as post-condensation transformations, or autoannealing [6]. We do not find a similar high abundance of crystalline material in the annealed sample. For example, the original smoke contained large (sub) spherical grains of chemically pure tridymite that formed by coagulation of smaller droplets and vitrification during autoannealing. Tridymite is the stable silica polymorph between 1140-1743 $^{0}$K. Isothermal annealing at 1000 $^{0}$K raised these grains above the metastable extension of the liquidus and induced fusion (vitrification) of these grains but without melting proper. They transformed into smooth droplet shaped grains (Table 1). The mottled texture of high-Fe silica grains in the original smoke was explained as possible spinodal decomposition by autoannealing into a maghemite-like phase and a low-Fe silica material [6]. In the annealed sample the "Fe" grains in nonspherical silica grains may have a similar origin. The $Fe_3O_4$ - $SiO_2$ phase diagram has a eutectic between the two liquid and cristobalite - liquid fields at ~5 wt.% $Fe_3O_4$, or ~4.5 wt.% FeO. According to this equilibrium phase diagram isothermal annealing of this quenched condensate compositions at ~9 wt.% FeO (Table 1) might decompose this material into tridymite and Fe-oxide, hematite or magnetite.

**CONCLUSIONS.** First results of this isothermal annealing experiment on an Fe-SiO smoke showed that (1) the initial condensates are quenched melts predicted by the equilibrium phase diagram, and (2) metastable high-temperature polymorphs with appropriate endmember compositions, e.g. Pure $SiO_2$, may undergo fusion (vitrification) below the glass transition temperature. This first experimentally obtained result on thermally annealed anhydrous analogs of circumstellar dusts has predictive power to constrain the mineralogical constituents of dusts in astrophysical environments.

**REFERENCES:** 1. Day K.L., Astr. J. 246, 110-112 (1981). 2. Day K.L. & Donn B., Astr. J. 222, L45-L48 (1978). 3. Rietmeijer FJM, & Nuth J.A., LPS, 1017-1019 (1990). 4. Rietmeijer FJM et al., Icarus 66, 211-222 (1986). 5) Fu G. & Rietmeijer FJM, LPS, 493-494. (1994). 6) Rietmeijer FJM, and Nuth J.A., Proc. Lunar Planet Sci., 591-599 (1991). The samples were provided by Joe Nuth (NASA-GSFC). This work was supported by NASA Grant NAGW-3646.

# PRELIMINARY ELECTRON MICROBEAM ANALYSES OF LIGHTNING INDUCED EVAPORATION AND GAS PHASE MIXING

Jim M. Karner[1], Peter J. Wasilewski[2], Frans J.M. Rietmeijer[1], and Joseph A. Nuth[2]. [1] Department of Earth and Planetary Sciences, University of New Mexico, Albuquerque, NM 87131; [2] NASA Goddard Space Flight Center, Code 681, Greenbelt, MD 20771.

Transient high-energy events such as reconnecting magnetic fields, chemical energy in amorphous solids, frictional heat (infall model) and lightning are invoked for the formation of chondrules in the solar nebula. It remains an open question whether any single one of these events, or a combination of them, is responsible for the variety of chondrule properties in meteorites. We used the Langmuir Laboratory's Triggered Lightning Research Facility on South Baldy Mountain near Socorro (New Mexico) to conduct an exploratory experiment on lightning induced alteration of refractory materials in conjunction with an ongoing experiment to study the formation of lodestone in natural deposits. Blankets of glass wool (~1 cm thick) were placed in a cylindrical container as separations between three samples of natural magnetite. The samples were placed perpendicular to its axis and were about 1 cm thick. The lightning strike passed through the container from top to bottom thereby passing through the three samples and two intervening blankets of glass wool.

LIGHTNING. The passage of the lightning strike through the container left a hole in each blanket with $\phi \simeq 1$ cm. The hole's wall in the blanket between the samples of pure magnetite sample and magnetite with some amounts of (Mg,Fe,Ca)-silicates and calcite shows an orange-brown discoloration. A spray pattern with similar discoloration occurred on this blanket surface surrounding the hole. Several millimeter-sized black spheres and (rare) black fragments were located around the hole where the lightning strike exited the blanket.

AEM ANALYSES. A JEOL 2000FX AEM equipped with a TN-5500 Tracor Northern energy dispersive spectrometer for *in situ* determination of elements with atomic number $> 11$ was used for mineralogical and chemical characterization of crushed samples of (1) black spheres ($\phi < 1$ mm), (2) black fragments (± 1 mm), (3) discolored wall of the hole, (4) the blanket surface at ~20 mm and ~40 mm from the hole, (5) the blanket interior far away from the hole, and (6) glass wool from the stock that provided the blankets. The crushed samples were dispersed onto clean holey carbon thin films on Cu TEM grids. All samples, including a sample from the stock, contain unexpectedly high abundances of mineral impurities that are associated with the fibres. These fibres, 42 wt% $SiO_2$ and 58 wt% $Al_2O_3$, are mostly amorphous. Some degree of devitrification is shown by weakly-developed polycrystalline electron diffraction patterns with a symmetry typical of fibrous material.

Compositions of the hollow to highly vesicular black spheres and the black fragments are shown in a ternary diagram $SiO_2$-$Al_2O_3$-$Fe_2O_3$ (wt%) [Figure 1]. The spheres and fragments are silica-rich compared to the glass wool fibres. Pure $Al_2O_3$ occurs as patches in the (Al,Fe)-SiO material and as individual grains. The high $Fe_2O_3$ contents coincide with the skeletal growth texture at the sphere surface. This texture is reminiscent of iron-oxide dendrites in meteorite fusion crusts [*e.g.* ref. 1]. The only other Fe-bearing aluminosilica materials (< 2 wt% $Fe_2O_3$) were from the blanket surface at ~20 mm from the hole. Porous vapor phase condensate domains are scattered among the spheres. The compositions of this "rutile" smoke are clustered at $TiO_2$ = 81.6 wt%, $SiO_2$ = 17.1 wt% and CaO = 1.3 wt% but are up to $TiO_2$ = 53 wt% and $SiO_2$ = 47 wt%. One crystalline sphere fragment was identified as mullite, $SiO_2$ = 37 wt%, $Al_2O_3$ = 58 wt% and CaO = 5 wt% [Figure 1]. The impurities make up ~15% of each sample. They include euhedral Ti-oxide grains (< 200 nm) closely associated with the fibres, dense clusters (~200 nm in size) of sub- to euhedral Ti-oxides ($\phi \simeq 30$ nm), Au-Ag-Te fragments and spheres (< 500 nm), Ca-phosphates (< 400 nm) with measurable concentrations of Ce, Nd, La and Th in their center, and a nanometer sized Co [Fe,Ni,Cr] particle. All samples contain amorphous silica spheres ($\phi$ = 100-250 nm). In general, there are no obvious mineralogical and chemical differences among these different samples. It does not appear that the impurities were affected by the lightning strike with the exception of the production of a "rutile" smoke from the Ti-oxide impurities.

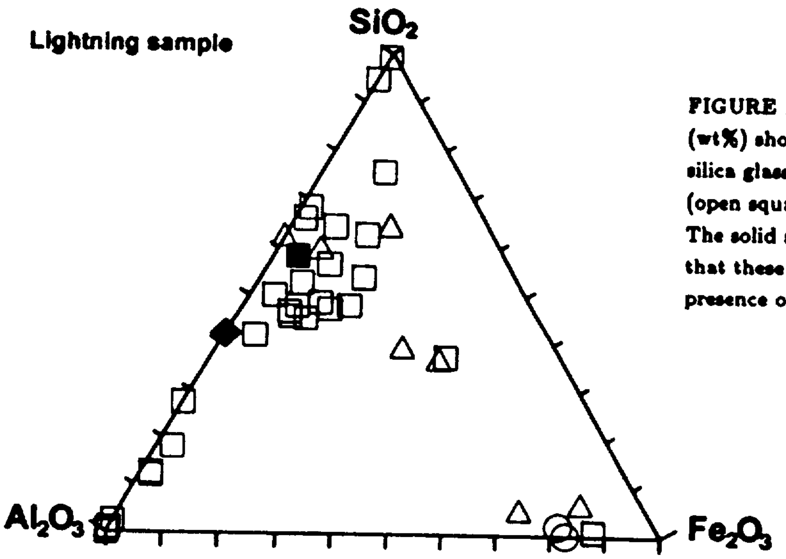

**FIGURE 1:** The ternary diagram $SiO_2$-$Al_2O_3$-$Fe_2O_3$ (wt%) showing the bulk composition of the alumino-silica glass wool (solid diamond), the black spheres (open squares) and black fragments (open triangles). The solid square is mullite. The open circles indicate that these Fe-rich phases were recalculated for the presence of $TiO_2$ grains.

**DISCUSSION.** The evidence that the lightning strike interacted with the aluminosilica glass wool blanket and magnetites consist of a penetration hole, the orange-brown discoloration, highly vesicular to hollow (Al,Fe,Si)-O spheres, "rutile" smoke particles, and crystalline mullite. The spheres and smoke particles suggest that evaporation and condensation occurred as a result of the lightning strike. The compositions of the black spheres and fragments show a distribution pattern in the $SiO_2$-$Al_2O_3$-$Fe_2O_3$ (wt%) diagram similar to those for individual condensate droplets in an Al,Fe-SiO smoke [2]. Condensation of this vapor at canonical solar nebula pressures produced a fluffy smoke of dense spherical grains [2]. The lightning experiment was conducted at atmospheric pressure which promotes formation of hollow spheres as, for example, during efficient firing of natural coals at high temperatures [3]. The spheres in typical coal fly-ash are condensates of mineral impurities in natural coals. The black spheres in the sample formed from an Al,Fe-SiO vapor due to lightning induced melting and evaporation of magnetite slabs and aluminosilica glass wool at atmospheric pressure. Assuming mullite in the spheres represents a quenched equilibrium melt, its presence suggests temperatures of 1700-1800°C in the $SiO_2$-$Al_2O_3$-CaO (wt%) phase diagram. Cotectic melting of aluminosilica glass wool suggests temperatures of ~1850°C based on the system $SiO_2$-$Al_2O_3$-$Fe_3O_4$ (wt%). Melting of Ti-oxides (assuming $TiO_2$) occurs between 1830-1850°C. The small size of Ti-oxide grains may allow melting at slightly lower temperatures. Quenching of this melt occurs at ~1800°C in the system $SiO_2$-$TiO_2$-CaO (wt%). These temperatures imply that the impurity elements probably made no contributions to the vapor phase (for example, the boiling points of Au, Ag and Ni are between 2100 and 3200°C, at P=1 atm).

**CONCLUSIONS.** This experiment was a first attempt to investigate the use of triggered lightning to form new phases via melting and evaporation of analogs of natural materials that might reflect conditions in the solar nebula. Samples were chosen for this experiment in order to investigate the possibility of forming lodestone via lightning strikes in natural ore deposits. We took the opportunity of placing glass wool blankets between the samples to investigate vapor phase effects. The lightning strike produced Al,Fe-SiO and Ti-SiO vapors from magnetite, glass wool fibres and Ti-oxides, plus a small amount of CaO vapor, at 1700-1800°C. It is encouraging that this first attempt not only shows unambiguous evidence of vaporization and condensation but also efficient vapor phase mixing. Future experiments will be conducted under much more controlled conditions.

**REFERENCES.** [1] Blanchard MB & Cunningham GG (1974) J. Geophys. Res. 79, 3973-3980; [2] Rietmeijer FJM & Nuth JA (1990) Lunar Planet. Sci XXI, 1017-1018; [3] Henry WM & Knapp KT (1980) Environ. Sci. Techn. 14, 450-456.

This work was supported by NASA grant NAGW-3646.

# BUCKYCARBONS AND FULLERENES IN INTERPLANETARY DUST PARTICLES BASED ON EVIDENCE FROM A TRANSMISSION ELECTRON MICROSCOPE (TEM) STUDY OF VAPOR CONDENSED CARBONS WITH VARIABLE C/H RATIO.

Frans J.M. Rietmeijer[1], Alessandra Rotundi[2,3], L. Colangeli[3], V. Mennella[3], P. Palumbo[2] and E. Bussoletti[2]. [1]Department of Earth and Planetary Sciences, University of New Mexico, Albuquerque NM 87131, USA; [2]Istituto di Fisica Sperimentale, Istituto Universitario Navale, Via A. de Gasperi 5, I-80133, Naples, Italy; [3]Osservatorio Astronomico di Capodimonte, Via Moiariello 16, I-80131, Naples, Italy.

Extraterrestrial buckminsterfullerene ($C_{60}$) was identified in the Allende meteorite [1] and an impact crater on the LDEF satelllite [2]. The X-XANES analyses of interplanetary dust particle (IDP) L2008F4 have not yet found $C_{60}$ [3]. Amorphous and poorly graphitised carbons, PAHs, and rare graphite and hexagonal diamond in IDPs were determined by a range of experimental techniques [4], including TEM. Following the discovery of $C_{60}$, fullerene-related carbons such as 'buckyonions', 'bucky(nano)tubes', and polyhedral structures of concentric (002) layers were indentified [5] and the concentric circular, poorly graphitised carbons in the Allende meteorite [6] were reinterpreted as 'buckycarbons'. Similarly, 'buckyonions', 'buckytubes', and loop-in-loop rings that are cross-sections of compound 'buckyonions' [*cf.* ref. 7], also occur in some chondritic IDPs [8,9]. We note that polycrystalline, or 'ring', selected area electron diffraction patterns for carbon blacks and samples of 'buckycarbons', when using a field limiting aperture larger than the modal size in the sample, show the same broad (*hkl*) 002, 10*l*, and 11*l* rings. Electron diffraction alone cannot distinguish these morphologically unique pre-graphitic carbons. An identification as poorly graphitised carbons implies that they are the products of prograde thermal metamorphism of hydrocarbons while the information carried by 'buckycarbons' is fundamentally different, *i.e.* they may be vapor phase condensates.

OBSERVATIONS. Our TEM study of C/H carbon smokes produced in atmospheres ranging from pure Ar to $Ar/H_2=7/3$ has found several carbon structures, *viz.* (*i*) carbon smoke, (*ii*) tangled networks of fine-grained [1-3 (002) layers] and coarse-grained (~2 - 5.5 nm) (002) ribbons, (*iii*) a profusion of 'buckyonions' and hollow 'buckytubes' ranging from needles to stubby units closed at both ends by curved, polygonal and cone shaped caps [10], (*iv*) coarse-grained polyhedral 'buckyonions' with up to 30-40 concentric (002) layers and 'buckytubes' with complex internal ('traversing' [5]) layer growth morphology [ref. 7], (*v*) open and compact, polyhedral scroll-type structures (~50-100 nm in diameter) of (002) ribbons with increasing thickness (~1-10 nm) from the center outwards, (*vi*) featureless polyhedral plates < 90 nm, and (*vi*) hexagonal, single-crystal carbon plates (< 500 nm) with an *a*-axis of 0.52 nm.

The polyhedral plates, the compact scroll-type structures and the hexagonal single-crystal plates occur in very low-hydrogen carbons that were produced by (*i*) condensation in a $H_2$-free atmosphere, and (*ii*) thermal annealing at 800°C of H-bearing carbons to drive off hydrogen [11]. The polygonal plates recrystallised at 700-800°C to hexagonal plates. The presence of other carbon structures is not obviously affected by the C/H ratio. The carbon interrelationships in the samples support that condensation of the coarse-grained polyhedral 'buckycarbons' and scrolls was followed by amorphous carbons that developed into the tangled networks. Rare 'buckyonions' have an amorphous carbon rim. We also analysed $C_{60}$ and $C_{70}$ samples (provided by D. Heymann) that consist of hexagonal single-crystal plates. The measured $C_{60}$ unit cell data match the reported values [12] for this molecular carbon.

DISCUSSION. A summary of literature data suggests to us that thermal annealing of carbonized carbons may take different tracks depending on whether the starting materials are hydrocarbons or pure carbons. The former was well studied by XRD and TEM studies [*cf.* 13]. The latter received considerable interest as part of the ongoing research on fullerene-related carbons. During the initial stages of heat treatment both types of starting materials develop similar tangled networks of graphitic ribbons of only a few basal layers thick that coarsen with continued heat treatment [13,14]. With further thermal annealing, a carbon soot developed (sub)circular closed loops of 2-8 carbon shells, at 1700°/1 h 'buckyonions' with polyhedral cross-sections at 2400°/4 min, and nanotubes closed at both ends [14]. Nanotubes are polygonized as a function of tubule thickness [15]. Polygonization of the fullerene-related carbons is due to (1) defects in the growth of aromatic layers by insertion of a pentagon or heptagon [15,16] and introduction of $sp^3$ bonds, either locally to relieve strain of the trigonal $sp^2$ state [7] or linear arrays [5] that causes bending at 60° and 120° angles in polygonal 'buckycarbons'.

A vapor condensed smoke consists of kinetically-controlled, high-temperature solids, *e.g.* tridymite in $Si_xO_y$ smokes [17] that formed during condensation proper and autoannealing of quenched liquid condensates. Iijima [7] suggested that the hollow center of concentric circular structures (*i.e.* 'buckyonions') is due to the liquid to solid carbon volume change but it is not clear how this interpretation explains the varied morphologies of 'buckytubes'. To evaluate the presence 'buckycarbons' in vapor-condensed carbons, it is germane to consider the thermal annealing of carbon soot [14] suggesting that 'buckycarbons' may be a high-temperature carbon allotrope with an effective volume much closer to the liquid than to that of the solid. If our interpretation is correct 'buckycarbons' will be a favored phase in pure carbon smokes.

The experimentally produced carbon structures (*ii*), (*iii*) and (*iv*) co-occur in chondritic IDPs [8,9] and support they condensed from pure to low-$H_2$ carbon vapors. The scroll-type carbons are pure carbons wherein growth defects in the aromatic layers introduced during rapid (molecular?) growth caused polygonization. Autoannealing of compact scrolls yielded polygonal sheets or platey hexagonal single-crystals in the thermally annealed sample. A simple interpretation of their unit cell parameters assumes a linear correlation between *a*-axis of graphite, $C_{60}$ and $C_{70}$, or $C_n$ where *n* is the number of atoms. This two-point correlation supports $n = 23 \pm 3$ in the hexagonal plates. We note that $C_{20}$ was proposed as a precursor to $C_{60}$ formation whereby the $C_{20}$ structure, *viz.* a closed cage, a cap, or a ring, is a function of the formation temperature [18]. The cap structure of five hexagons surrounding one pentagon is considered the seed upon which other fragments attach to form a complete closed $C_{60}$ shell [18]. $C_{20}$ may have formed in our experiments at temperatures conducive to the cap structure at about 725°C, but the duration and/or temperatures of the experiments precluded $C_{60}$ formation. It remains possible that curved PAHs, the intermediates in the conversion of planar PAH-type structures to curved fullerene-related structures, are necessary for $C_{60}$ formation [19].

**CONCLUSIONS.** In our AEM study of vapor condensed carbons with variable C/H ratio we found abundant 'buckyonions', 'buckytubes' and loop-in-loop carbon structures that are similar to those in several chondritic IDPs. The introduction of defects during continuous rapid growth in the experiments produced the scrolls of carbon ribbons that were precursors to hexagonal $C_{20}$ plates but that could not grow to form $C_{60}$. When our experiments indeed simulate carbon condensation under astrophysical conditions, our data support that in chondritic IDPs $C_{60}$ will be rare but $C_{20}$ could be a common pure carbon phase. Buckyonions and 'buckytubes' may abound and their presence does not constrain C/H ratios in the range we investigated. Post-accretion thermal annealing, *i.e.* dynamic pyrometamorphism, may be required to produce $C_{60}$ in pure elemental carbons in chondritic IDPs.

**REFERENCES.** [1] Becker L et al. (1994) Nature 372, 507; [2] Radicati di Brosolo F (1994) Nature 369, 37-40; [3] Bajt S et al. (1996) LPS XXVII, 57-58; [4] Keller LP et al., (1994) AIP Conf. Proc. 310, 159-164; [5] Harris PJF et al. (1993) J. Chem. Soc. Faraday Trans. 89, 1189-1192; [6] Smith PPK & Buseck PR (1991) Science 212, 322-324; [7] Ijima S. (1980) J. Cryst. Growth 50, 675-683; [8] Rietmeijer FJM & Mackinnon IDR (1985) Nature 316, 733-736; [9] Rietmeijer FJM (1992) GCA 56, 1665-1671; [10] Iijima S et al. (1992) Nature 356, 776-778; [11] Mennella V et al. (1995) Ap. J. Suppl. Ser. 100, 149-157; [12] Krätschmer W et al. (1990) Nature 347, 354-358; [13] Jenkins GM & Kawamura K (1976) Polymeric carbons-carbon fibre, glass and char. Cambridge Univ. Press, 178p; [14] de Heer WA & Ugarte D (1993) Chem. Phys. Lett. 207, 480-486; [15] Iijima S (1991) Nature 354, 56-58; [16] Clinard C et al. (1994) J. Phys. Chem. Solids 55, 651-657; [17] Rietmeijer FJM & Nuth JA (1991) Proc. Lunar Planet. Sci. 21, 591-599; [18] Brabec CJ et al. (1992) Phys. Rev. B 46, 7326-7328; [19] Becker L et al. (1995) LPS XXVI, 87-88. This work was supported by NASA Grant NAGW-3646.

# WORKSHOP ON
# PARENT-BODY AND NEBULAR MODIFICATION OF CHONDRITIC MATERIALS

Edited by

M. E. Zolensky, A. N. Krot, and E. R. D. Scott

Held at
Maui, Hawai'i

July 17–19, 1997

Hosted by
Hawai'i Institute of Geophysics & Planetology
University of Hawai'i

Sponsored by
Lunar and Planetary Institute
University of Hawai'i
National Aeronautics and Space Administration
NASA Integrated Systems Network

Lunar and Planetary Institute 3600 Bay Area Boulevard Houston TX 77058-1113

LPI Technical Report Number 97-02, Part 1
LPI/TR--97-02, Part 1

# ALTERATION OF PRESOLAR DUST BASED ON TRANSMISSION ELECTRON MICROSCOPE/ANALYTICAL ELECTRON MICROSCOPE STUDIES OF CHONDRITIC INTERPLANETARY DUST PARTICLES AND NONEQUILIBRIUM SIMULATION EXPERIMENTS.

F. J. M. Rietmeijer, F. Guofei, and J. M. Karner, Department of Earth and Planetary Sciences, University of New Mexico, Albuquerque NM 87131, USA.

Chondritic interplanetary dust particles (IDPs) collected in the lower stratosphere include porous (CP) to less porous chondritic filled (CF) aggregates and compact hydrated chondritic IDPs. Aggregate IDPs are typically dominated by anhydrous minerals, but they may contain small amounts of layer silicates, carbonates, and sulfates to indicate incipient aqueous alteration. Two important observations on the nature of CP and CF IDPs are (1) their morphologies, textures, and ultrafine-grained minerals and mineral assemblages are unique and not found in any conventional meteorite [1] and (2) their infrared spectra closely resemble those of the P and D outer-belt asteroids and comet nuclei [2]. Thus, they are associated with protoplanets containing the least-altered solar nebula dusts that are not sampled by conventional meteorites. Chondritic IDPs from short-period comets may include vestiges of presolar and interstellar dusts among their constituents. Anhydrous IDPs are classified as olivine- and pyroxene-rich CP, whereas CF IDPs and hydrated IDPs are classified as serpentine- and smectite-rich IDPs. These layer silicates are secondary phases due to postaccretion aqueous alteration, and at least part of this IDP classification scheme relies on secondary mineral properties.

The grain sizes of Mg,Fe olivines and Mg,Fe pyroxenes in the smallest recognizable textural units in CP and CF IDPs range from 2 nm to ~50 nm in diameter, occasionally up to ~500 nm. All IDPs enter the Earth's atmosphere at kilometer-per-second velocities and experience a brief (5–15 s) period of flash heating (up to ~1000°C). Based on nucleation and growth theory alone, a typical thermal profile of this event will be conducive to form these Mg,Fe silicates in an amorphous precursor. There is no proof that these ultrafine olivines and pyroxenes, or a fraction of them, formed in this manner. Their formation does not require a sustained thermal regime. It is possible that they are also secondary minerals.

**Observations:** CP and CF IDPs are typically made up of subcircular units between ~100 nm and ~500 nm in diameter. The first type of unit, "granular units (GUs)," consists of ultrafine-grained

Mg,Fe olivines, Mg,Fe pyroxenes, and Fe,Ni sulfides in an amorphous C and hydrocarbon matrix [3]. To these were added C-free "polyphase units (PUs)" of amorphous to holocrystalline, Ca,Al-bearing ferro-magnesiosilica materials. They include (1) coarse-grained PUs that consist of Mg,Fe olivine and Mg,Fe pyroxene (En,Fo = 0.75–1.0), Ca-bearing aluminosilica materials, and an Fe,Ni sulfide [4] and (2) ultrafine-grained PUs consisting of Mg,Fe olivines and Mg,Fe pyroxenes, plus Fe,Ni sulfides, Fe,Ni metals, or Fe oxides in an amorphous ferro-magnesiosilica matrix. The bulk compositions range from Mg/(Mg + Fe) (el. wt%) = 0.3 to 0.75 [4,5]. They were mislabeled "tar balls" [6], but are now known as GEMS [7]. They occur as S-bearing and S-free units. Sulfur may be lost during atmospheric entry heating [5]. Concentric circular 1.2-nm smectite lattice fringes may occur in ultrafine-grained PUs in addition to anhydrous minerals [5]. A third unit consists of low-atomic-number elements only. Although sheets of carbonaceous materials occur in CP and CF IDPs [8], there is still little evidence for discrete carbonaceous units that may fuse more readily than other units, including GEMS.

The chondritic IDPs are mixtures of these units plus micrometer-sized silicates and Fe,Ni sulfides [10]. None of the units is chondritic for all major elements. In a diagram Mg-Fe-Si (el. wt%) C-free units define two trends: (1) ultrafine-grained units along the Mg,Fe serpentine dehydroxylate, $(Mg,Fe)_3Si_2O_7$, line, and (2) coarse-grained units along the Mg-rich part of a smectite dehydroxylate line, $(Mg,Fe)_6Si_8O_{22}$. Two models to explain the petrological properties of C-free units are (1) preaccretion irradiation and amorphization of silicates and sulfides [7] and (2) closed-system crystallization and phase separation within isolated amorphous precursors [4,5]. The presence of typically nonchondritic amorphous materials as precursors to layer silicates, (rare) feldspars, and plagioclase that do not occur as discrete subspherical units in chondritic IDPs was already recognized [cf. 3]. These amorphous materials could be fragments of coarse-grained PUs.

The analytical and transmission electron microscope (AEM/TEM) data revealed two critical properties of the chondritic IDPs: (1) the common presence of amorphous materials with discrete Mg-Fe-Si ratios and Ca-bearing aluminosilica materials and (2) the ultrafine size of their constituent minerals. Both properties cause a high level of free energy that will be available during alteration. Our simulation studies constrain these properties assuming a critical role of nonequilibrium vapor phase condensation in the formation of amorphous materials. We note that amorphous silica and tridymite were prominent phases in the early stages of thermal annealing and hydration and that micrometer-sized silica grains occur in at least one CP IDP [3].

**Experiments:** We analyzed ultrathin sections of analog samples in the same manner as the IDPs. These analogs included vapor phase condensates (smokes) in the system $MgO\text{-}Fe_2O_3\text{-}SiO_2$ [10]. Binary smoke samples were produced in the Flow Condensation Apparatus at 500°C in an $H_2$ atmosphere at a pressure of ~80 torr. Silicon and O are introduced as $SiH_4$ and $O_2$. The starting materials for Fe silicates are liquid $Fe(CO)_5$ entrained in H gas fed through the liquid before mixing with $SiH_4$ and excess $H_2$ in a mixing bulb. This gas then flowed to an alumina furnace tube. Magnesium vapor is produced by heating solid Mg in a graphite crucible in the furnace tube. The mixed gases flow from the furnace (where some condensation occurs) to the cooler collection chamber wherein the remaining vapor condenses. Smokes are scraped from a collector plate located near the gas outlet of the appperatus. We also studied thermal annealing of Mg,Fe,SiO and MgSiO smokes and the hydration of MgSiO smokes.

The condensation study showed that the compositions of the individual smoke grains coincide with metastable eutectic points in the binary equilibrium phase diagrams. The metastable eutectic points in the $MgO\text{-}SiO_2$ system match serpentine and smectite dehydroxylates. Eutectic points in the $FeO\text{-}Fe_2O_3\text{-}SiO_2$ system at Fe/(Fe + Si) (el. wt%) = 0.4 and 0.15 do not match Fe silicates. During thermal annealing *in vacuo* fayalite and ferrosilite (~20 nm in diameter) formed after 8 hr at 725°C in amorphous ferromagnesiosilica material. After 167 hr these grains were 100–200 nm. After 167 hr Mg vapor reacted with Fe oxide to magnesioferrite ($MgFe2O_4$) with local periclase condensation [11]. Forsterite + tridymite had reacted to thermodynamically stable enstatite after 30 hr annealing. In the initial stages of MgSiO smoke hydration, discrete amorphous silica globules formed in the smokes. Only regions that evolved stoichiometric Mg/Si ratios showed kerolite and/or saponite protophyllosilicates and associated $Mg(OH)_2$ [12].

**Discussion:** The bulk compositions of ultrafine-grained units plot along the serpentine dehydroxylate line. Its termination on the Mg-Si join of the ternary diagram is constrained by vapor phase condensation. Since Fe during FeSiO condensation was oxidized, we found no metastable eutectic points matching the Fe serpentine dehydroxylate composition (assuming it is allowed in the equilibrium phase diagram). Fayalite and ferrosilite and intermediate phases readily formed during thermal annealing *in vacuo*. This result supports that as long as the Fe oxidation remains in the FeO stability field, $Mg_3Si_2O_7$ condensate may evolve to its Fe end member within the limits of the equilibrium phase diagram, i.e., Mg/(Mg + Fe) ratio <0.85, which matches the highest ratios for pyroxenes and olivines in GEMS. The O fugacities of the environment wherein they evolved were characterized by wustite. Formation of either olivine or pyroxene will be a function of heating rate [13]. Once started, their formation is linked to local supersaturation and formation of an Fe,Ni phase.

The bulk compositions of coarse-grained PUs plot on lines connecting the metastable eutectic points on the Fe-Si join and the metastable smectite dehydoxylate eutectic on the Mg-Si join. This relationship supports that they condensed at more oxidizing conditions than GEMS. The subsequent crystallization and phase separation into Fe,Mg silicates and amorphous Ca-bearing aluminosilica materials proceeded in the FeO stability field.

The mineralogy of coarse-grained units is presented by two generic reactions

$$\begin{gathered}\mathrm{Mg_3Fe_3Si_8O_{22}(+Al,Ca)amorph.} = \\ 2\ \mathrm{(Mg_{1.5}Fe_{1.5}Si_2O_7)amorph.} + 4\ \mathrm{SiO_2(+Al,Ca)amorph.}\end{gathered}$$

and

$$2\ \mathrm{(Mg_{1.5}Fe_{1.5}Si_2O_7)amorph.} = \mathrm{MgFeSi_2O_6} + 2\ \mathrm{MgFeSiO_4}$$

When the original composition was more Fe rich, the sulfides associated with these units formed by sulfidation according to

$$\begin{gathered}1.5\ \mathrm{Mg_2Fe_4Si_8O_{22}(+Al,Ca)amorph.} + 3\ \mathrm{H_2S} = \\ \mathrm{Mg_3Fe_3Si_8O_{22}(+Al,Ca)amorph.} + \\ 4\ \mathrm{SiO_2(+Al,Ca)amorph.} + 3\ \mathrm{FeS} + 3\ \mathrm{H_2O}\end{gathered}$$

followed by either one or both of the above reactions. The units show no evidence (yet) for hydration, but $H_2O$ produced in this fashion could be used to form kaolinite, e.g.

$$(Al_2Si_2O_7)\text{ amorph.} + 2\ H_2O = Al_2Si_2O_5(OH)_4$$

Similar reactions describe the mineralogical properties in GEMs that may contain saponite.

**Conclusions:** The C-free units are amorphous condensates that underwent thermal annealing in a closed system, but its timing is not constrained by the observations on IDPs. Sulfide formation requires an open system involving $H_2S$ in the solar nebula and also causes incipient aqueous alteration. The data do not invalidate a model of preaccretion irradiation and amorphization, but this model does not account for the origin of preexisting silicates and sulfides.

The amorphous smoke grains that formed directly as solids from the vapor may be regarded as quenched liquids with metastable eutectic points probably at ~500°C. Subsequent thermal annealing and hydration at comparable temperatures promoted phase relations at metastable extensions of equilibrium phase boundaries. Under highly kinetically controlled conditions alternative metastable behavior is to be expected. Thus, alteration products in IDPs will be chaotic, largely unpredictable assemblages until the free energy has dropped to levels commensurate with their local environments.

**Acknowledgments:** Samples were provided by J. Nuth and his team at NASA Goddard Space Flight Center. This work was supported by NASA Grants NAGW-3626 and NAGW-3646.

**References:** [1] Mackinnon I. D. R. and Rietmeijer F. J. M. (1987) *Rev. Geophys., 25,* 1527. [2] Bradley J. P. et al. (1992) *Astrophys. J., 394,* 643. [3] Rietmeijer F. J. M. (1992) *Trends Mineral., 1,* 23. [4] Rietmeijer F. J. M. (1997) *LPS XXVIII,* 1173. [5] Rietmeijer F. J. M. (1996) *LPS XXVII,* 1073. [6] Bradley J. P. (1988) *GCA, 52,* 889. [7] Bradley J. P. (1994) *Science, 265,* 925. [8] Thomas K. L. et al. (1993) *GCA, 57,* 1551. [9] Rietmeijer F. J. M. (1997) *LPS XXVIII,* 1169. [10] Karner J. M. (1997) M.Sc. thesis, Univ. of New Mexico. [11] Fu G. and Rietmeijer F. J. M. (1994) *LPS XXV,* 493. [12] Rietmeijer F. J. M. (1996) *LPS XXVII,* 1069. [13] Rietmeijer F. J. M. (1996) *Meteoritics & Planet. Sci., 31,* A114.

# PHASE EQUILIBRIUM IN A TRIGGERED LIGHTNING STRIKE EXPERIMENT

by

Frans J.M. Rietmeijer(1),

Jim M. Karner(1),

Joseph A. Nuth III(2), and

Peter J. Wasilewski(2)

(1): Department of Earth and Planetary Sciences, University of New Mexico,
Albuquerque, NM 87131, USA.

(2): NASA Goddard Space Flight Center, Code 681, Greenbelt, MD 20771, USA.

Submitted to

The European Journal of Mineralogy

October 1997

# ABSTRACT

This study describes the phase relations in a triggered lightning strike experiment that consisted of a stacked assemblage of magnetite discs and silica glass wool blankets. The very nature of this process yields ultra-fast heating and quenching rates. The strike produced millimeter sized black spheres wherein the compositions of reaction products defined cotectic crystallization in the $SiO_2$ - $Al_2O_3$ - $Fe_3O_4$ (wt %) equilibrium phase diagram at atmospheric pressure. Maximum heating temperatures were ~1750°C with a ternary minimum melt of ferri-cordierite glass at ~1400°C and $Al_2O_3$-$Fe_2O_3$ phase compositions at 1300–1400°C and high (>1 atm.) $pO_2$. Equilibrium phase diagrams also defined the compositions of the sillimanite dendrites and mullite glass. The import finding is that nanometer-sized minerals formed in thermal events of very short (micro-) second duration are constrained by the equilibrium phase relationships.

# INTRODUCTION

We are interested in the petrological phase relationships that result from ultra-fast heating and quenching. Diffusion in these short events will be the rate-limiting process. The results will be ultrafine-grained mineral assemblages and (partially) devitrified quenched melts. Natural occurrences characterized by ultra-fast excursions from ambient to high pressures and/or temperatures, followed by a similar rapid return to ambient conditions, include (1) fulgurites that are yellowish brown colored vitreous silica tubes and crusts formed in quartz sands, soil and rock due to lightning strikes (Galliot, 1980), (2) volcanic melt ejecta and plume condensates, (3) meteorite impact craters and the meteorite parent bodies (asteroids) (Stöffler *et al.*, 1988), and (4) meteorite fusion crusts. When a meteor's orbital velocity (km $s^{-1}$) is reduced by collisions with air molecules in the upper atmosphere, its kinetic energy is mostly transformed into heat. For a 'conventional' meteorite, this ablation and melting process results in a black, millimeter thick, fusion crust that consists of a quenched melt layer overlain by an iron-rich crust that is a mixture of reduced and oxidized iron-nickel phases (Ramdohr, 1967). Underneath the fusion crust the meteorite maintains its pre-entry temperature. In micrometer-size objects (typically ~10 μm) slowing down in the atmosphere to cm $s^{-1}$ the interior reaches thermal equilibrium with the surface. The duration of this flash heating and quenching event is 5-15 s (Love & Brownlee, 1991) with heating and cooling rates on the order of $10^5$-$10^6$ degrees $s^{-1}$. The peak heating temperatures in unmelted micrometeorites (or, interplanetary dust particles) range from 300-500°C to 1,150°C (Nier & Schlutter, 1992, 1993; Rietmeijer, 1992, 1996a). The resulting dynamic pyrometamorphic alteration generally involved kinetically controlled, mostly diffusion-less, oxidation reactions and (partial) melting. For example, the formation of laihunite (Keller et al., 1992) and cellular precipitates of iron-oxides in Mg,Fe-olivines (Rietmeijer, 1996a). During ultra-fast quenching and extreme supercooling, ultrafine (<30 nm) silicates and oxides formed in a melted micrometeorite via nucleation-controlled devitrification (Rietmeijer, 1996b). Cristobalite in fulgurites (Galliot, 1980) is probably due to devitrification. Anthropogenic processes with ultra-fast, or at least very-high, heating and cooling rates include vapor phase condensation experiments (e.g. Rietmeijer & Nuth, 1991) and coal-burning that produces fly ash spheres of mostly mullite compositions (e.g. Hulett *et al.*, 1980; Rietmeijer & Janeczek, 1997).

Natural shock metamorphism includes solid-state mineral alteration and melt vein formation (Stöffler *et al.*, 1988). High-pressure, high-temperature minerals crystallize in these high-density melts (Chen *et al.*, 1996). Although the duration of a typical impact event, including relaxation of the peak shock pressure, is only a few microseconds to several seconds, Chen *et al.* (1996) postulated that equilibrium liquidus phase relations constrain the shock peak temperature and pressure. We were prompted by our interest to use a triggered lightning experiment to explore the petrology of highly transient processes. Natural lightning creates conditions of both high temperatures and dynamic heating and cooling regimes. Attempts to better understand lightning strikes have persisted since the late 1700s when Benjamin Franklin showed lightning to be an electrical phenomenon.

Lightning strikes are very common high-energy events occurring on Earth at a rate of ~100 strikes per second delivering $10^9$ J per flash (Borucki & Chameides, 1984). With air temperatures reaching up to ~30,000°C materials struck by lightning can melt or vaporize in microseconds (Essene & Fisher, 1986). They reported metal-silicate liquid immiscibility and extremely reduced mineral phases on a micrometer to centimeter scale from a fulgurite in a carbon-rich soil. Extreme reduction was possible due to efficient vaporization of oxygen at very high temperatures of ~2,300°C based on thermodynamic equilibrium calculations (Essene & Fisher, 1986). There is little data on the nature of silicates and oxides, the scale of petrological heterogeneity and chemical fractionation in short-duration (μs to s) events. We report here the first-of-a-kind experiment examining ultra-fast thermal alteration on a nanometer scale under oxidizing conditions.

# EXPERIMENTAL

The Langmuir Laboratory for Atmospheric Research near Socorro (New Mexico, USA) is dedicated to the study of cloud physics, precipitation, and lightning. Its location on top of South Baldy Mountain in the Magdalena range is ideal for these experimental studies because frequent isolated summer storms are often small and stationary. Initially, this triggered lightning experiment was undertaken to explore alteration of magnetite under conditions of transient high-energy input in an attempt to duplicate conditions forming lodestone in natural environments (reported elsewhere). The experiment entailed placing three discs of magnetite (pure magnetite and magnetite with minor amounts of unidentified Mg,Fe,Ca-silicates and calcite) separated by blankets of silica glass wool in a cylindrical container. The aluminosilica glass wool (42 wt % $SiO_2$; 58 wt % $Al_2O_3$) contained single-crystal titanium oxide impurities (~200 nm in size). The discs and blankets (each ~1 cm thick) were placed perpendicular to the container axis. A rocket connected to the container by a copper wire was fired into an overhead cloud to induce a lightning strike. The lightning flowed down the wire and through the container from top to bottom thereby passing through all discs of magnetite and intervening glass wool blankets. The passage of the lightning strike through the glass wool left a hole with a diameter of ~1 cm and many smaller offshoots. An orange-brown discoloration occurred on the silica glass wool on the inside of the main hole. A spray deposit of similar discoloration formed on the blanket surface surrounding the hole. Several millimeter-sized black spheres and (rare) fragments were located around the main hole where the lightning strike exited the blankets.

Black spheres of ~1 mm in diameter were randomly picked from the glass wool and embedded in an epoxy (Spurrs) for preparation of serial ultra-thin (80-100 nm) sections using a Reichert-Jung Ultramicrotome E that operated at a diamond knife speed between 0.3 and ~0.6 mm $s^{-1}$. The sections were placed on a holey carbon thin-film supported by a standard Cu mesh grid for analyses using a JEOL 2000FX analytical electron microscope (AEM) operating at an accelerating voltage of 200 keV. The AEM was equipped with a Tracor-Northern TN-5500 energy dispersive spectrometer (EDS) for *in situ* chemical analysis of elements with atomic number >11 using a probe size ~20 nm in diameter for individual spot analysis. Quantitative analyses were obtained using the Cliff-Lorimer (1975) thin-film correction procedure with *k*-factors experimentally determined on natural standards. The phases were characterized by a combination of transmission electron microscope (TEM) imaging, EDS and selected area electron diffraction (SAED) data.

## OBSERVATIONS

When a slight pressure was applied, the spheres broke apart suggesting they were hollow objects. The chemical analyses showed that the spheres were mixtures of phases defined by an Al-Si-Fe-oxide ternary system. Most materials typically contained a few percent titanium with the highest amounts (up to 7 wt. % $TiO_2$) in domains of cordierite glass. Titanium was derived from the single-crystal titanium oxide impurities in the glass wool. Rare porous structures of titanium oxides (smokes) imply that titanium oxide vapors were produced during the event. This condensed smoke was a pervasive contaminant of the samples. We assumed that titanium does not occur in solid solution with the reaction products. The results of the experiment that was conducted in air are presented in the ternary diagram $SiO_2$-$Al_2O_3$-$Fe_3O_4$ (wt %) [Fig. 1] although variable $FeO/Fe_2O_3$ ratios probably existed due to small scale variations in oxygen fugacity as a function of location and time during the experiment.

The cluster centered at $SiO_2 = 60$ wt %, $Al_2O_3 = 39$ wt %, and $Fe_3O_4 = 1$ wt % represents main sphere compositions in the mullite field. The absence of diffraction maxima supports a glass phase. Its average composition matches the metastable eutectic point that straddles the equilibrium and spinodal solvi in the $SiO_2$-$Al_2O_3$ phase diagram (MacDowell & Beall, 1969). A cluster at $SiO_2 = 47$ wt %, $Al_2O_3 = 18$ wt %, and $Fe_3O_4 = 35$ wt % represents small domains of ferri-cordierite glass, $Al_{1.4}(Fe^{3+})_{2.9}[Si_{5.1}Al_{0.9}O_{18}]$ wherein $(Mg,Fe^{2+})$ and some Al were replaced by ferric iron, *viz.* $3Al + 2Fe^{2+} = 1.4Al + 2.9Fe^{3+}$. A third cluster on the $Fe_3O_4$-$Al_2O_3$ join is due to inclusions, ~530 nm in length and 300-450 nm wide, in mullite glass [Fig. 2]. Their compositions are within the $hem_{ss} + Al_2O_3.Fe_2O_3$ stability field at partial pressures >1 atm. They are single-crystal hercynite from dendritic growths of spinel in mullite glass. Dendritic growths also formed on the surface of the magnetite discs. Rare dendrites of single-crystal sillimanite with prominent 0.5 nm (*hkl*) (110) lattice fringes occurred in mullite glass. The dendrites are up to 300 nm long with branches extending out from the main trunk to ~80 nm [Fig. 3].

# DISCUSSION

This triggered lightning strike experiment offered insight in the petrological phase relations that formed during ultra-rapid heating up to ~1750°C and subsequent ultra-fast quenching at approximately atmospheric pressure in an oxidizing atmosphere. Oxidizing conditions were supported by the presence of ferri-cordierite glass and spinel phases. Triggered lightning induced melting and evaporation of magnetite, aluminosilica glass wool and nanometer sized titanium oxide impurities. The scattered data points in the mullite field and on the cotectic line between the corundum and spinel solid solution fields include both variable quenched melt compositions and contaminated spot analyses. Despite the short duration of the transient thermal event, the equilibrium phase diagram offers an internally consistent interpretation of the resulting phase relations. That is, along the path of the lightning strike aluminosilica glass wool decomposed into mullite glass and an $Al_2O_3$ residual melt. The glass composition matches the metastable eutectic composition in the $SiO_2$-$Al_2O_3$ equilibrium phase diagram. Similar behavior occurred during ultra-fast condensation of Al-SiO vapors at ~500°C (Karner, 1997). Spinel compositions on the $Fe_3O_4$-$Al_2O_3$ join of the equilibrium phase diagram supported peak heating temperatures up to 1750°C. The ferri-cordierite glass composition defines a ternary minimum melt in the $SiO_2$-$Al_2O_3$-$Fe_3O_4$ diagram at ~1400°C. Aluminum oxide and $Fe_2O_3$ (melts?) reacted to $hem_{ss}$ + $Al_2O_3.Fe_2O_3$ spinels at 1300-1400°C based on the $Al_2O_3$-$Fe_2O_3$ equilibrium phase diagram (Eitel, 1965).

Dendrites represent non-equilibrium growth. Yet, the equilibrium phase diagram defined the observed subsolidus phase compositions. That is, sillimanite formed on Al-rich solvus limb in the mullite phase field (cf. MacDowell & Beall, 1969). Symplectites of spinel and glass are common in meteorite fusion crusts. They resulted from rapid heating and quenching under oxidizing conditions whereby reduced and oxidized iron phases co-occur on small spatial scales (Blanchard and Cunningham, 1974). Less oxidizing conditions may have occurred (locally?) during hercynite formation, $0.6\ Fe_2O_3.Al_2O_3 = 0.4\ FeAl_2O_3 + (0.8\ Fe^{3+} + 0.9\ O_2)$ which precipitated from the vapor phase (cf. Rietmeijer and Nuth, 1991) and account for the orange-brown discoloration on the blankets. We note that similar highly-oxidized minerals, *e.g.* iron cordierite, and hercynite associated with mullite, formed in terrestrial pyrometamorphic rocks in response to rapid heating (at least when measured on a geological time scale) to 1020 - 1400°C (Cosca et al., 1989).

## CONCLUSIONS

A triggered lightning strike induced melting and evaporation of refractory materials. Flash heating to 1750°C and ultra-fast quenching produced highly oxidized phases. The resulting phases and textures were constrained by the $SiO_2$-$Al_2O_3$-$Fe_3O_4$ equilibrium phase diagram and included cotectic crystallization and minimum melt formation. Glass and subsolidus phase compositions matched metastable eutectic compositions. The reactions in this ultra-fast transient, high-energy event were kinetically controlled. Yet, the nanometer-size reaction products mimic melt equilibrium conditions. The presence of metastable eutectic compositions highlights the complexity involved in the proper interpretations of thermal conditions. More experiments at the Langmuir Laboratory for Atmospheric Research are planned.

## ACKNOWLEDGMENTS

We thank the staff at the Langmuir Laboratory for Atmospheric Research. The AEM analyses were performed at the Electron Microbeam Analysis Facility in the Department of Earth and Planetary Sciences (UNM) where Fleur Rietmeijer-Engelsman provided technical assistance. This work was supported by NASA grants NAGW-3646 and NAGW-3626 [to FJMR].

## REFERENCES

Blanchard, M.B. & Cunningham G.G. (1974): Artificial ablation studies: olivine. *J. Geophys. Res.*, **79**, 3973-3980.

Borucki, W.J. & Chameides, W.L. (1984): Lightning: estimates of the rates of energy dissipation and nitrogen fixation. *Rev. Geophys. Space Phys.*, **22**, 363-372.

Chen, M., Sharp, T.G., El Goresy, A., Wopenka, B., Xie, X. (1996): The majorite-pyrope + magnesiowüstite assemblage: Constraints on the history of shock veins in chondrites. *Science*, **271**, 1570-1573.

Cliff, G. & Lorimer, G.W. (1975): The quantitative analysis of thin specimens. *J. Microscopy*, **103**, 203-207.

Cosca, M.A., Essene, E.J., Geissman, J.W., Simmons, W.B., Coates, D.A. (1989): Pyrometamorphic rocks associated with naturally burned coal beds, Powder River Basin, Wyoming. *Amer. Mineral.*, 74, 85-100.

Eitel, W. (1965): *Silicate Science, Vol. II, Dry silicate systems*. Academic Press Inc., New York, New York, 553 p.

Essene, E.J. & Fisher, D.C. (1986): Lightning strike fusion: Extreme reduction and metal-silicate liquid immiscibility. *Science*, 234, 189-193.

Galliot, M.P. (1980): "Petrified lightning" A discussion of sand fulgarites. *Rocks and Minerals*, Jan/Feb, 13-17.

Hulett, Jr., L.D., Weinberger, A.J., Northcutt, K.J., Ferguson, M. (1980): Chemical species in fly ash from coal-burning power planets. *Science*, 210, 1356-1358.

Karner, J.M. (1997): Mineralogy, morphology and chemistry of vapor condensed silicate dust analogs. MSc. thesis, University of New Mexico, 148 p.

Keller LP, Thomas KL, McKay DS (1992) Thermal processing of cosmic dust: Atmospheric heating and parent body metamorphism (abstract). *Lunar Planet Sci*, XXIII, 675-676.

Love, S.G., & Brownlee, D.E. (1991): Heating and thermal transformation of micrometeoroids entering the Earth's atmosphere. *Icarus*, 89, 26-43.

MacDowell, J.F. & Beall, G.H. (1969): Immiscibility and crystallization in $Al_2O_3$-$SiO_2$ glasses. J. Amer. Ceram. Soc., 52, 17-25.

Nier, A.O. & Schlutter, D.J. (1992): Extraction of helium from individual interplanetary dust particles by step-heating. *Meteoritics*, 27, 166-173.

—, — (1993): The thermal history of interplanetary dust particles collected in the Earth's stratosphere. *Meteoritics*, **28**, 675-681.

Ramdohr, P. (1967: Die Schmelzkruste der Meteorieten. *Earth Planet.Sci. Lett.*, **2**, 197-209.

Rietmeijer, F.J.M. (1992): Mineralogy of primitive chondritic protoplanets in the early solar system. *Trends in Mineralogy*, **1**, 23-41.

— (1996a): Cellular precipitates of iron-oxide in extraterrestrial olivine in a stratospheric interplanetary dust particle. *Mineral Mag.*, **60**, 877-885.

— (1996b): The ultrafine mineralogy of a molten interplanetary dust particle as an example of the quench regime of atmospheric entry heating. *Meteoritics Planet. Sci.*, **31**, 237-242.

Rietmeijer, F.J.M. & Janeczek, J. (1997): An analytical electron microscope study of airborne industrial particles in Sosnowiec, Poland. *Atmos. Environ.*, **31**, 1941-1951.

--- & Nuth J.A. (1991) Tridymite and maghemite formation in an Fe-SiO smoke. *Proc. Lunar Planet. Sci. Conf. 21st* (G. Ryder & V.L. Sharpton, eds.), pp. 591-599. Lunar and Planetary Institute, Houston (TX).

Stöffler, D., Bischoff, A., Buchwald, V., Rubin, A.E. (1988): Shock effects in meteorites. *in* "Meteorites and the Early Solar System", J.F. Kerridge & M.S. Mathews, eds. University Arizona Press, Tucson, Arizona, 165-202.

Figure 1. The $SiO_2$ - $Al_2O_3$ - $Fe_3O_4$ (wt %) equilibrium phase diagram at atmospheric pressure showing the compositions of the aluminosilica glass wool and magnetite starting compositions (stars). Open circles show the Ti-free glass sphere compositions and those corrected for 1-10 wt % $TiO_2$ are shown by open squares. Sillimanite dendrites (dots), hercynite inclusions (corrected for 1-7 wt % $TiO_2$) (solid diamonds) and $Al_2O_3$ inclusions (solid triangles) are shown. Dashed lines are the liquidus phase relations (cf. Eitel, 1965).

Figure 2. Transmission electron microscope image showing single-crystal hercynite inclusions in the glass matrix of black spheres. The inset shows the SAED pattern viewed along the $[0\bar{1}1]$ zone axis.

Figure 3. Transmission electron microscope image showing a sillimanite dendrite in mullite glass of black spheres with the corresponding SEAD pattern of sillimanite viewed along the [001] crystallographic axis.

Fig 2

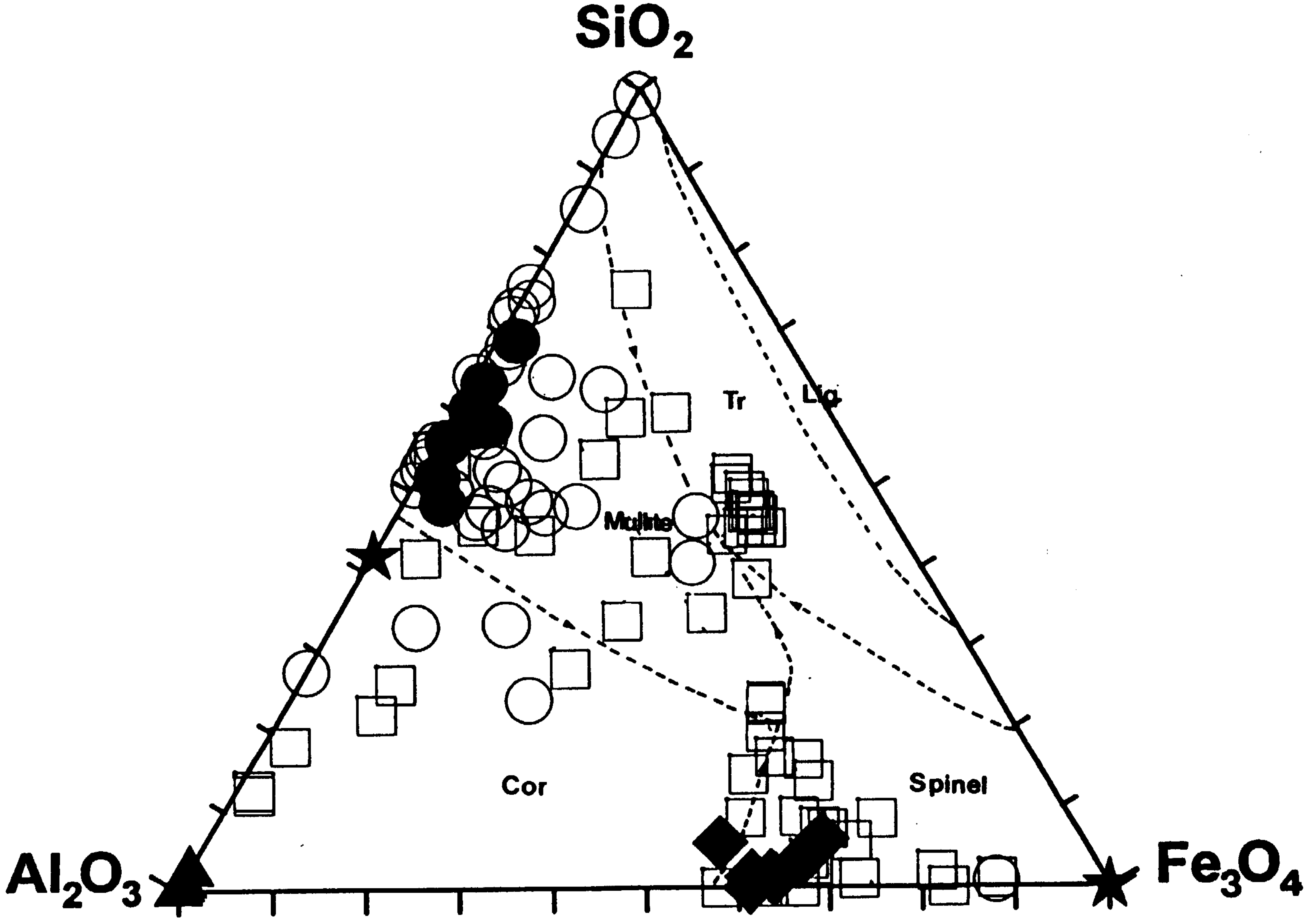

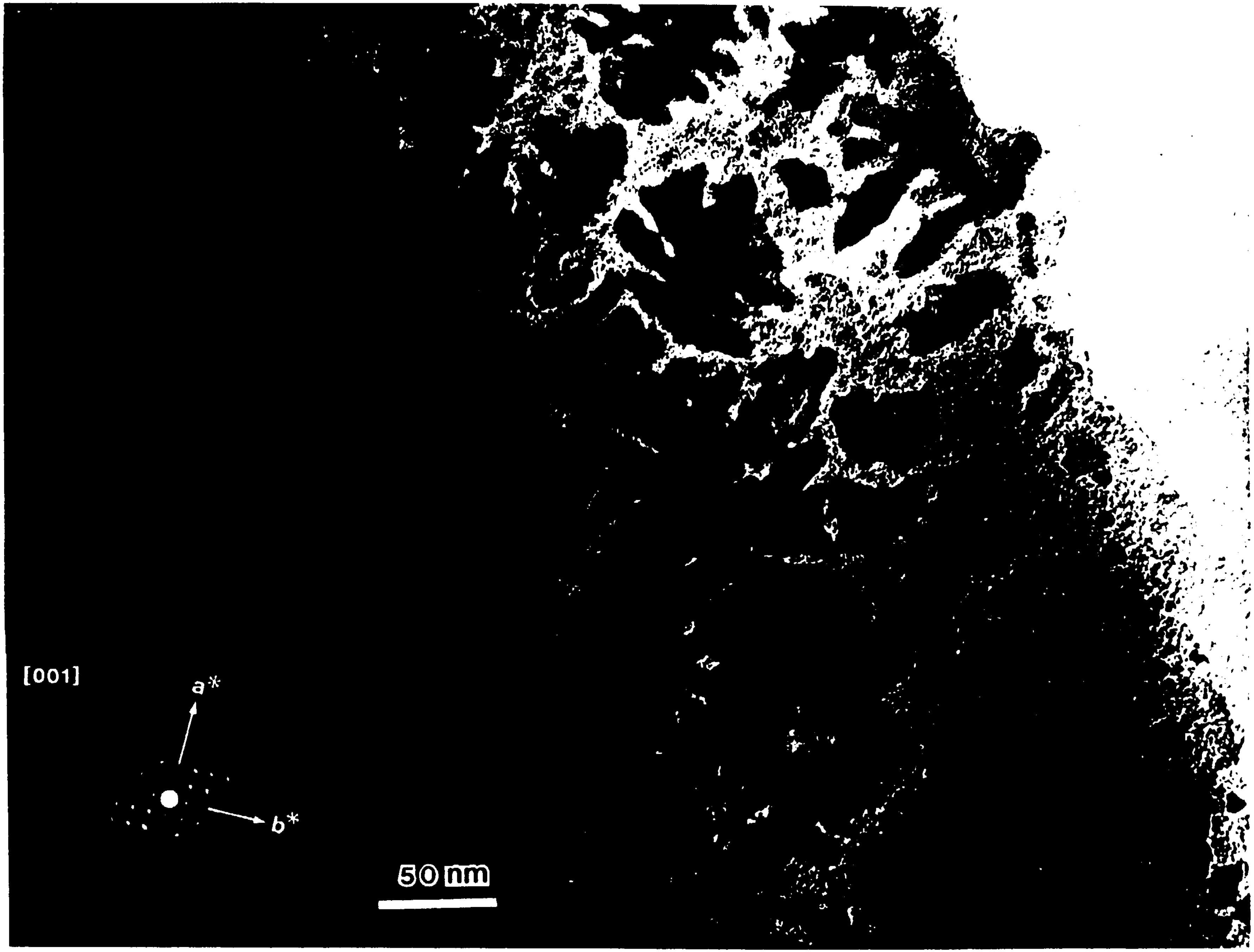
[001]
a*
b*
50 nm


[0$\bar{1}$1]
100nm

**A&A manuscript no.**
**(will be inserted by hand later)**

**Your thesaurus codes are:**
**(08.03.1)(08.03.4)(09.04.1)**

**ASTRONOMY**
**AND**
**ASTROPHYSICS**
**18.2.1997**

# Evidence of inherent forms of carbon in soot materials of astrophysical interest

**A. Rotundi**[1,2], **F.J.M. Rietmeijer**[3], **L. Colangeli**[2], **V. Mennella**[2], **P. Palumbo**[1,2], **E. Bussoletti**[1]

[1] Istituto di Fisica Sperimentale, Istituto Universitario Navale, via A. De Gasperi 5, I-80133 Napoli, Italy
[2] Osservatorio Astronomico di Capodimonte, via Moiariello 16, I-80131 Napoli, Italy
[3] Department of Earth and Planetary Sciences, University of New Mexico, Albuquerque, New Mexico 87131, USA

Received ; accepted

**Abstract.** We determined the carbon structures in condensed soot samples of variable C/H ratio using scanning and transmission electron microscopy. We observed several types of carbon structures, viz (1) Chain-like Aggregates, (2) Poorly Graphitized Carbon, (3) Graphitic Carbon Ribbons, (4) "bucky-carbons" and (5) Single-crystal Carbon Platelets. The Chain-like Aggregates dominate all the samples. Poorly Graphitized Carbon includes various inherent forms of carbon, not influenced by the C/H ratio and related to both condensation process and auto-annealing. "Bucky-objects" are properly produced by condensation. After these observations we can conclude that the UV spectral response of condensed soot samples of variable C/H ratio, e.g. the shift of the absorption peak position (Mennella et al. 1995a), depends on the Chain-like Aggregates and is not affected by the other inherent forms of carbon (~~de Heer & Ugarte 1993~~). Moreover, our results suggest that carbons in interplanetary dust particles could be condensed carbon structures.

Various found

**Key words:** Stars: carbon, circumstellar matter - dust, extinction - IDPs - Laboratory

## 1. Introduction

Fine-grained refractory particles are observed in circumstellar environments, the interstellar medium and in the solar nebula. Circumstellar dust condenses directly from a cooling gas phase (e.g. Lattimer & Grossman, 1978; Nuth & Donn, 1982) before being ejected into the interstellar medium. Since direct monitoring of dust formation and evolution in these environments cannot be performed, production, processing and analysis of laboratory analogues represent an effective approach to understand the evolution of dust in astrophysical environments. Thermal annealing can be considered a first approximation of dust processing which occurrs in interstellar environments. Laboratory experiments show that vapor phase condensates are generally XRD (X-ray diffraction) and IR amorphous solids, while crystalline phases generally indicate post condensation annealing. On the other hand, analytical electron microscope studies of chondritic interplanetary dust particles (IDPs) showed that they initially consisted of amorphous ferromagnesiosilica and aluminosilica materials (Rietmeijer 1992; Thomas et al. 1995) that subsequently - probably in protoplanetary bodies - became partially crystalline solids. These chondritic IDPs are among the most carbon-rich, ultrafine-grained extraterrestrial materials. They include amorphous and poorly-graphitized carbons and hexagonal diamond (Rietmeijer 1992). As far as the interstellar dust is concerned, the actual interpretation of the 217.5 nm bump in the interstellar extinction curve is strongly related to the intrinsic nature of solid carbons present in space. This feature was initially attributed to the presence of small spherical graphite grains (e.g. Girla 1972; Draine & Lee 1984). The difficulty to produce pure graphite in astronomical environments was evidenced by Mathis & Whiffen (1989). Hecht (1986) considered hydrogen-free carbon grains as the carrier of the UV bump. Dehydrogenation process in the diffuse medium, due to UV radiation, cosmic rays and annealing, induced by shocks (Sorrell 1990), may also be involved in

---

*Send offprint requests to*: A. Rotundi

the formation of the 217.5 nm peak (Hecht 1986). The existence of hydrocarbon grains in interstellar and circumstellar regions was supported by the meteoritic record (e.g. Nuth 1985), laboratory simulations (e.g. Bussoletti at al. 1987; Sakata et al. 1983; Colangeli et al. 1993) and models based on astronomical observations (e.g. Duley & Williams 1983). Laboratory experiments on submicron hydrogenated amorphous carbon grains subjected to thermal annealing, UV and ion irradiation (Mennella et al. 1995a; 1996a; 1996b) showed that the UV spectral response depends on the hydrogen content of the analogues. Mennella et al. (1995b) inferred that the internal structure of the carbon grains determines the UV extinction properties.

In order to support interpretations of astrophysical data and laboratory work to date, it becomes important to study the morphology and the structure of cosmic dust analogues produced by vapour phase condensation. In fact, to interpret variations detected in the spectral response of different soot samples, it is necessary to follow their structural and/or morphological modifications (Koike et al. 1994, Papoular et al. 1996, de Heer & Ugarte 1993).

In the present work we investigated in detail the carbon forms that we produced in a typical simulation experiment to document the morphologies and structures of soot samples with different hydrogen content. The aim was to establish their interrelationships during the "proper" condensation process and subsequent auto-annealing as part of this process (cf. Rietmeijer & Nuth 1991). Since we found several inherent forms of carbon in typical soot materials, the question rises on how their presence affects, if at all, the UV spectral response.

## 2. Experimental

In order to analyse soot samples characterised by different hydrogen content, we considered two sets of samples: (1) condensed samples and (2) thermally annealed condensates. The carbon material was produced by arc-discharge between two amorphous carbon rods, at a pressure of 10 *mbar*, and collected on UV grade fused silica substrates (for more details see Mennella et al. 1995a). In the production phase the only variable parameter was the composition of the ambient atmosphere. We produced six samples in atmospheres characterized by variable proportions of argon and hydrogen: 1) Ar = 100%; 2) Ar = 99.6% and $H_2$ = 0.4%; 3) Ar = 99.2% and $H_2$ = 0.8%; 4) Ar = 90% and $H_2$ = 10%, 5) Ar = 70% and $H_2$ = 30%; 6) $H_2$ = 100%. They are labelled respectively: ACAR, ACH2(0.4), ACH2(0.8), ACH2(10), ACH2(30), ACH2-a. The second set of samples consists of ACH2 samples annealed at different temperatures: 415 °C, 700 °C and 800 °C, labelled respectively AC415, AC700, AC800. Thermal annealing was performed for 3 hours in vacuum ($p < 10^{-5} mbar$), (for more details see Mennella et al. 1995a). The two sets of samples reported in Table 1, i.e. ACAR to ACH2-a and AC800 to ACH2-b are comparable: they consists of carbon samples with an increasing ammount of hydrogen.

In the present work the samples were analysed by means of two different techniques: (1) field emission scanning electron microscopy and (2) transmission electron microscopy. The 3-D morphology was determined using a Stereoscan 360 - Cambridge Field Emission Scanning Electron Microscope (FESEM) operating at a maximum accelerating voltage of 25 keV and with a spatial resolution of 2 nm. In order to check for the presence of contaminants in the soot samples we used an Energy Dispersive X-ray (EDX) detection system, attached to the FESEM, that was able to detect elements down to Be (i.e. $Z > 4$).

The characterisation of the structural units was performed using a JEOL 2000FX Transmission Electron Microscope (TEM) operating at an accelerating voltage of 200 keV and with a spatial resolution of 0.32 nm in the TEM mode. Rietmeijer (1995) described the experimental conditions we used in this study including those for selected area electron diffraction (SAED) analyses. Each condensed sample was embedded in epoxy (Spurrs). Serial ultrathin (80 nm - 100 nm) sections were prepared using a Reichert-Jung Ultramicrotome E that was operated at a diamond knife speed between 0.3 and 0.6 mm/s. Ultrathin sections were placed on a holey carbon thin-film supported by a TEM grid and housed in a Gatan low-background, double-tilt specimen holder for TEM analyses. For the thermally annealed samples a small portion of material from each sample was scraped off the collecting substrates and deposited directly onto a holey-carbon thin film supported by a Cu-grid. The FESEM analyses were performed directly on the collecting substrates that were attached to FESEM aluminium pin stubs by a conductive silver paste. These analyses were useful to define the spatial distribution of different morphologies within the condensed samples. In order to characterise the morphology at higher resolution, FESEM measurements were repeated on small fractions of dust dispersed onto properly smooth silicon wafers attached with conductive silver paste to the aluminium pin stubs. The EDX measurements were performed separately on materials dispersed onto smooth carbon pin stubs in order to look for contaminant particulates in the samples. In a few samples (both annealed and condensed) we detected traces of Si. In order to identify the cause of Si contamination we cross-checked the EDX results for ACH2 samples with fragments of both fresh and used-up carbon rods mounted with silver paste on Al stubs. For comparison, ACH2 soot was collected directly during the arc-discharge onto carbon stubs. We concluded that silica contamination results from scraping off soot samples from their collecting substrate.

## 3. Observations

Typical FESEM and TEM images of examined samples are reported in this section with the aim of evidencing their main morphological and structural features. FESEM images for all samples display a fluffy morphology of fine-grained (diameter ~ 7 up to about 15 nm) spheres organised in agglomerates that arrange themselves in necklaces together with individual spheres (Fig. 1). TEM analyses of these typical Chain-like Aggregates (CLA) show round discs of amorphous carbon grains (Fig. 2) – actually spheres, as shown by FESEM analysis – with values of sphericity S = 0.9–1.0. All the samples are dominated by CLA carbon. In addition to the CLA texture, FESEM analyses showed that the samples contain micron-sized (up to 20x20 microns) patches characterized by more compacted CLA with abundant whiskers and lesser amounts of irregularly shaped platelets (Fig. 3).

TEM analyses of the condensed and thermally annealed samples allowed us to characterise five additional structures. The detection of different structures in the analysed samples is summarised in Table 1. Samples produced in atmosphere with different $H_2$ amount (from ACAR to ACH2-a) and samples annealed at different temperatures (from AC800 to ACH2-b) form two sets with the common characteristic of an increasing hydrogen content (see previous section). Poorly graphitized carbon (PGC) is arranged as isolated domains of loops or rings on smooth carbon sheets. Thin sheets of fused condensate grains are present in all samples wherein they form irregular patches within the CLA smoke. Occasionally these sheets are up to several micrometers in size. These sheets typically contain several isolated ring-like structures that are delineated by a single graphite basal plane lattice fringe (Fig. 2, 4). The shape of these structures suggests that fusion of loops occurred prior to formation of this lattice fringe. When the density of loops becomes sufficiently high, the result is a network of tangled loops (Fig. 2, 5). While this network of thin rings is common to all samples, a similar network of coarser loops (Fig. 6) is also present in most samples. The thickness of the single graphite layer forming the loops is markedly dinstinct in both networks. The coarser network may also occur in micrometer-sized patches.

All samples also contain compact irregular masses of well-defined concentric circular units and tubes, or "bucky-onions" with diameters in the range of 10 - 40 nm (average = 22 nm), and "bucky-tubes" up to about 100 x 10 nm in size (Fig. 3 and 7). These tubes typically have a high aspect ratio distinct from stubby "bucky-tubes" that co-occur with these common "bucky-carbon" forms. The typical onion shell morphology is formed by distinct basal graphitic lattice fringes. Narrow ribbons (about 5 to 15 nm) of similarly well-developed fringes occur among the "bucky-carbons". They tend to form concentric units with either circular or polyhedral shapes (Fig. 8). While a well-defined size cut-off is not evident, the smallest units are about 30-40 nm in diameter. Spherical grains, with several (up to about 5) graphitic layers along the grain boundary, are also present among these "bucky-carbons" in most samples.

In addition, TEM analyses also revealed rare and broad graphitic carbon ribbons (GCR) within the smoke of the thermally annealed samples (Table 1). The margin of these sheets is delineated by broad (~ 10 up to ~ 125 nm) ribbons with graphitic basal lattice fringes (Fig. 2, 9), and extremely rare Single-crystal Carbon Platelets (SCPs), that occur as micrometer-sized sheets embedded in the dominant CLA carbon material (Table 1). The sheets consist of well-defined, hexagonal single-crystal platelets about one nanometer thick. The SAED data support a hexagonal carbon phase.

In summary, the carbon forms identified in our samples are (see Table 1): CLA (Chain-like Aggregates), PGC (Poorly Graphitized Carbon), GCR (Graphitic Carbon Ribbons), "bucky-carbons" ("bucky-tubes" and "bucky-onions") and SCPs (Single-crystal Carbon Platelets).

We attempted qualitative estimates of relative abundances of the different carbon forms in our samples based on their distribution in 40 - 50 individual ultrathin sections of each sample. Typical CLA smoke is the predominant carbon in all the samples. In the samples condensed in an atmosphere containing hydrogen sub-micrometer patches of "bucky-carbons" are more common than tangled network carbons (PGC). In samples that were thermally annealed above 415 °C both "bucky-carbons" and PGC occur in distinctly lower abundances relative to CLA than in the condensed samples. Only in the ACAR sample is PGC more abundant than "bucky-carbons".

## 4. Discussion

The occurrence of different types of textures in carbon soot samples with different hydrogen content, obtained by condensation and thermal annealing, is directly related to, and indigenous to, their formation from the gas phase. The formation of the CLA, dominating each sample, is typical of vapour phase condensation and occurs in both carbon and silicate smokes (Stephens & Kothari 1978). In fact, the condensation process produces a quenched liquid which cools rapidly through the glass transition temperature to the ambient temperature.

The tubes and concentric circular units are similar to "bucky-tubes" and "bucky-onions" produced by arc-discharge of graphite in a He atmosphere (Harris et al. 1993) and in vapor-deposited amorphous carbon films (Iijima 1980). We interpret these structures as products of the condensation process "proper". Coagulation and fusion during auto-annealing produced the contiguous amorphous carbon sheets that developed graphitic loops (PGC). They often delineate original condensate grain boundaries. Variations in the density of these loops locally result in compact patches of this particular PGC structure. Condensation process "proper" and auto-annealing are intimately linked. They occur within the production chamber as a result of the overall condensation process. While both processes are directly connected with the soot production, the "bucky-tubes" and "bucky-onions" have a fundamentally different origin than the PGC loops. In fact, while "bucky-carbons" condensed as they are observed, the graphitic loops of the PGC formed thanks to a pre-existing substrate. The substrate (amorphous carbon) is a condensate while the loops formed during the relaxation of the thermal energy. Yet all these different structures are considered to be inherent forms of carbon produced during vapor phase condensation.

The formation of very rare pre-graphitic ribbons (GCR) is limited to the AC415 and AC700 samples and could be explained in terms of a continuous graphitization as a function of the thermal annealing temperature. This poorly graphitised carbon phase is similar to the wavey ribbons that develop during heat treatment of pre-graphitic graphitisable carbons (Bonijoly et al. 1982).

The origin of the very rare SCPs structure remains enigmatic. It could be the result of peculiar chemico-physical conditions (i.e. distribution of the hydrogen and temperature of the substrate) during soot production. We note that the elongated and twisted graphitic loops (nanotube-like), the concentric circular units and the loops on smooth carbon sheets in our samples are similar to those reported for poorly-graphitized carbons in chondritic IDPs (Rietmeijer and Mackinnon 1992, Rietmeijer 1992), shown in Fig. 10, and in acid residues of carbonaceous chondrites (Smith and Buseck 1981, Lumpkin 1981).

Our results suggest that all carbons we observe are inherent. All of them, but CLA, appear insensitive to the carbon to hydrogen content. ~~CLA shows structural variations dependent on the C/H ratio, which deserve an in depth analysis,~~ subject of a forthcoming paper (Rotundi et al. 1997). These conclusions have an impact in the interpretation of the UV extinction properties of carbon ~~grains. In~~ particular, we are able to isolate CLA as the structure responsible for the UV extinction bump shift as a function of C/H ratio (Mennella et al. 1995a, 1995b). This is furtherly supported by de Heer & Ugarte (1993) who noticed that the other inherent carbons we observed, while seemingly affecting the peak width and shape, do not affect the peak position.

→ don't do this. This caused the Question asked by the Reviewers.

## 5. Conclusions

We were able to monitor morphologies and structures in carbon soots differently processed and characterized by different C/H ratios. We found several types of textures. The Chain-like Aggregates (CLA) are strictly related to the condensation processes and dominates all the samples. The inherent Poorly Graphitized Carbon (PGC) and "bucky-carbons" are related to both the condensation processes and to auto-annealing, but they are not influenced by the different C/H ratio. Very rare graphitic ribbons are probably due to the graphitisation during thermal annealing; and the very rare SCPs of uncertain origin.

Structures similar to the PGC carbons, due to both the condensation process "proper" ("bucky-things") and to auto-annealing, occur in chondritic interplanetary dust particles. This result supports a possible primary origin, rather than a parent body processing. The inherent carbons we observed, except for CLA, are insensitive to the carbon to hydrogen ratio and do not affect the position of the UV peak (de Heer & Ugarte 1993). We conclude that the predominant CLA texture is responsible for the UV extinction bump shift depending on the C/H ratio of the soot samples. This is the dominant texture in all the samples and it is a "proper" condensation product. More TEM observations are needed to investigate the structural variations that can occur within the CLA due to the variable C/H ratio.

We believe that the present paper sheds light on the actual structure of carbon soot which are among the candidates to simulate the astronomical features commonly attributed to cosmic carbon dust (e.g. Papoular et al. 1996).In addition, the comparison of our images and those relative to interplanetary dust particles gives an interesting clue on the formation process of IDPs. After our results, in fact, we can conclude that carbons in IDPs could be condensed carbon structures.

*Acknowledgements.* We thank, S. Inarta, N. Staiano and E. Zona for their technical assistance during sample preparation and analyses. We thank R. Trentarose for his technical assistance during images preparation. We warmly thank Prof. A. Blanco and Prof. S. Fonti for their contribution in the preparation of one of the samples. This work was supported by ASI, MURST, CNR and GIFCO grants. The TEM analyses were performed in the Electron Microbeam Analysis Facility of the Department of Earth and Planetary Sciences at UNM, where Jim Karner and Fleur Rietmeijer-Engelsman provided technical assistance. The

SEM and EDX analyses were performed at the Cosmic Physics Laboratory of Naples. FJMR was supported by NASA grants NAGW-3626 and NAGW-3646.

## References

Bonijoly, M., Oberlin, M., Oberlin, A., 1982, Intern. J. Coal Geol.,1, 283
Bussoletti E., Colangeli L., Borghesi A., Orofino V., 1987, A&A Suppl 70, 257
Czyzak, S.J., and Santiago, J.J., 1973, Ap&SS, 23, 443
de Heer, W.A. and Ugarte, D., Chem. Phys. Lett., 207, 480, 1993
Draine, B., and Lee, H.M., 1984, Ap. J., 285, 89
Duley, W.W., and Williams, D.A., 1983, M.N.R.A.S., 205, 67
Gilra, D.P., 1972, in Scientific Results from the Orbiting Astronomical Observatory OAO 2. ed. A.D. Code (NASA SP-310)
Harris, P.J.F., Green, M.L.H., Chi Tsang, S., 1993, J. Chem. Soc. Faraday Trans. 89(8), 1189
Hecht, J.H., Holm, A.V., Donn, B., Wu, C.C., 1984, Ap. J., 280, 228
Hecht, J.H., 1986, Ap. J., 305, 817
Iijima, S., 1980, J. Crystal Growth, 50, 675
Koike, C., Kaito, C., Shibai, H., Mon. Not. R. Astron. Soc., 268, 321, 1994
Lattimer J.M. and Grossman L., 1978, Moon Planets, 19, 169
Lumpkin, G.R., 1981, Proc. Lunar Planet. Sci., 12B, 1153
Mathis, J.S., and Whiffen, G., 1989, Ap. J., 341, 808
Mennella, V., Colangeli, L., Blanco, A., Bussoletti, E., Fonti, S., Palumbo, P., Mertins, H.C., 1995a, Ap. J., 444, 288
Mennella, V., Colangeli, L., Bussoletti, E., Monaco, G., Palumbo, P., Rotundi, A., 1995b, Ap. J. SS., 100, 149
Mennella, V., Colangeli, L., Palumbo, P., Rotundi, A., Schutte, W., Bussoletti, E., 1996a, Ap. J. Lett., 464, L191
Mennella, V., Baratta, G., Colangeli, L., Palumbo, P., Rotundi, A., Bussoletti, E., Strazzulla, G., 1996b, AP. J., in ~~press~~
Nuth J.A. and Donn B., 1982 , Ap. J., 257, L103
Nuth J.A., Nature, 318, 166, 1985
Papoular, R., Conard, J., Guillois, O., Nenner, I., Reynaud, C., and Rouzaud, J.-N., 1996, A&A, 315, 222
Rietmeijer, F.J.M., Mackinnon, I.D.R., 1987, Nature, 326, 162
Rietmeijer, F.J.M., Nuth, J., 1991, Lunar Planet. Sci. 21 (Eds. G. Ryder and V.L. Sharpton), 591
Rietmeijer, F.J.M., 1992, Geochim. Cosmochim. Acta., 56, 1665
Rietmeijer, F.J.M., 1995, Carbon, 33, 827
Rotundi, A., Rietmeijer, F.J.M., Colangeli, L., Mennella, V., Palumbo, P., Bussoletti, E., 1997, in preparation ← don't do this
Sakata, A., Wada, S., Okutsu, Y., Shintani, H., and Nakada, Y., 1983, Nature, 301, 493
Smith, P.P.K., Buseck, P.R., 1981, Science, 212, 322
Stephens, J.R. and Kothari, B.K., 1978, The Moon and the Planets, 19, 139
Sorrel, W.H., 1990, MNRAS, 243, 570
Thomas, K.L., Keller, L.P., McKay, D.S., Meteoritics, 30, 587, 1995
Wright, E.L. 1989, ApJ, 346, L89

# FIGURE CAPTIONS

**FIGURE 1** Field emission scanning electron micrograph of sample ACH2 showing the fluffy morphology of the CLA smoke. In the bottom left frame a high-resolution image shows the single grains arranged in agglomerates.

**FIGURE 2** Transmission electron micrograph of sample AC415, dispersed onto a holey carbon thin-film, showing CLA carbon in the lower right-hand corner (black arrow), thin carbon sheets with isolated loops (PGC) that evolved locally into a tangled network (open arrows), and rare GCR (solid white arrow).

**FIGURE 3** Field emission scanning electron micrograph (left) showing in the ACAR sample a micron-sized patch characterized by more compacted CLA (upper right) with abundant whiskers ( "bucky-tubes") and lesser amounts of irregularly shaped platelets (lower right).

**FIGURE 4** High-resolution transmission electron micrograph of single loops in an ultrathin section of sample ACAR. In this image, rare loops (PGC) consist of several graphitic lattice fringes (arrow) while a closed "buckytube" is shown on the right.[NOTE: The grey background in the transmission electron micrographs of ultrathin sections represents the embedding epoxy. This amorphous material contains a trace amount of chlorine which allows positive identification that prevents it from being identified as sample material. Many figures also show the holey carbon thin-film supporting the ultrathin sections during electron microbeam analyses].

**FIGURE 5** Transmission electron micrograph of the fine-grained tangled network (PGC) in an ultrathin section of sample ACH2(0.8). The darker areas on the right side and in the upper left-hand corner of the figure are dense concentrations of "bucky-carbons".

**FIGURE 6** Transmission electron micrograph of the coarse-grained tangled network (open arrow) in an ultrathin section of sample ACAR with a fine-grained network in the lower right-hand portion of the figure (PGC).

**FIGURE 7** Transmission electron micrograph of concentric circular "bucky-onions" and closed "bucky-tubes" with variable aspect ratios (black arrows) in an ultrathin section of sample ACAR.

**FIGURE 8** Transmission electron micrograph of open loops on the left-hand side, both concentric circular and polyhedral "bucky-carbons" (arrows) from the top-left to the bottom-right corners of the figure, including a complex polyhedral loop structure, in an ultrathin section of sample ACAR.

**FIGURE 9** Transmission electron micrograph of graphitic carbon ribbons (GCR) (open arrow) in an ultrathin section of sample ACH2(0.4) along with concentric circular and polyhedral "bucky-onions" and "bucky-tubes".

**FIGURE 10** A transmission electron micrograph of poorly graphitized carbon in an ultrathin section of an interplanetary dust particle showing the thin carbon sheets with scattered loops (open arrow), "bucky-onions" (black arrow) and "bucky-tubes" closed at both ends. Reproduced from Rietmeijer (1992) by the courtesy of Geochimica et Cosmochimica Acta.

This article was processed by the author using Springer-Verlag LaTeX A&A style file *L-AA* version 3.

**TABLE 1** Summary of the different structures observed in the analysed samples. Samples annealed at different temperatures (from AC800 to ACH2-a) and samples produced in atmosphere with different $H_2$ amount (from ACAR to ACH2-b) form two sets with the common characteristic of an increasing hydrogen content.

| | SAMPLE | CLA(c) | PGC(d) | BUCKY ONIONS | BUCKY TUBES | GCR(e) | SCPs(f) |
|---|---|---|---|---|---|---|---|
| 1st set of samples (a) | ACAR | yes | yes | yes | yes | no | yes |
| | ACH2(0.4) | yes | yes | yes | yes | no | very rare |
| | ACH2(0.8) | yes | yes | yes | yes | no | no |
| | ACH2(10) | yes | yes | yes | yes | no | no |
| | ACH2(30) | yes | yes | yes | yes | no | no |
| | ACH2-a | yes | yes | yes | yes | no | no |
| 2nd set of samples (b) | AC800 | yes | yes | rare | no | no | very rare |
| | AC700 | yes | yes | not observed | not observed | very rare | no |
| | AC415 | yes | yes | yes | yes | very rare | no |
| | ACH2-b | yes | yes | yes | yes | no | no |

(a) Ultrathin section
(b) Scraped off on TEM grids
(c) Chain-like Aggregates
(d) Poorly Graphitized Carbon
(e) Graphitic Carbon Ribbons
(f) Single-crystal Carbon Platelets

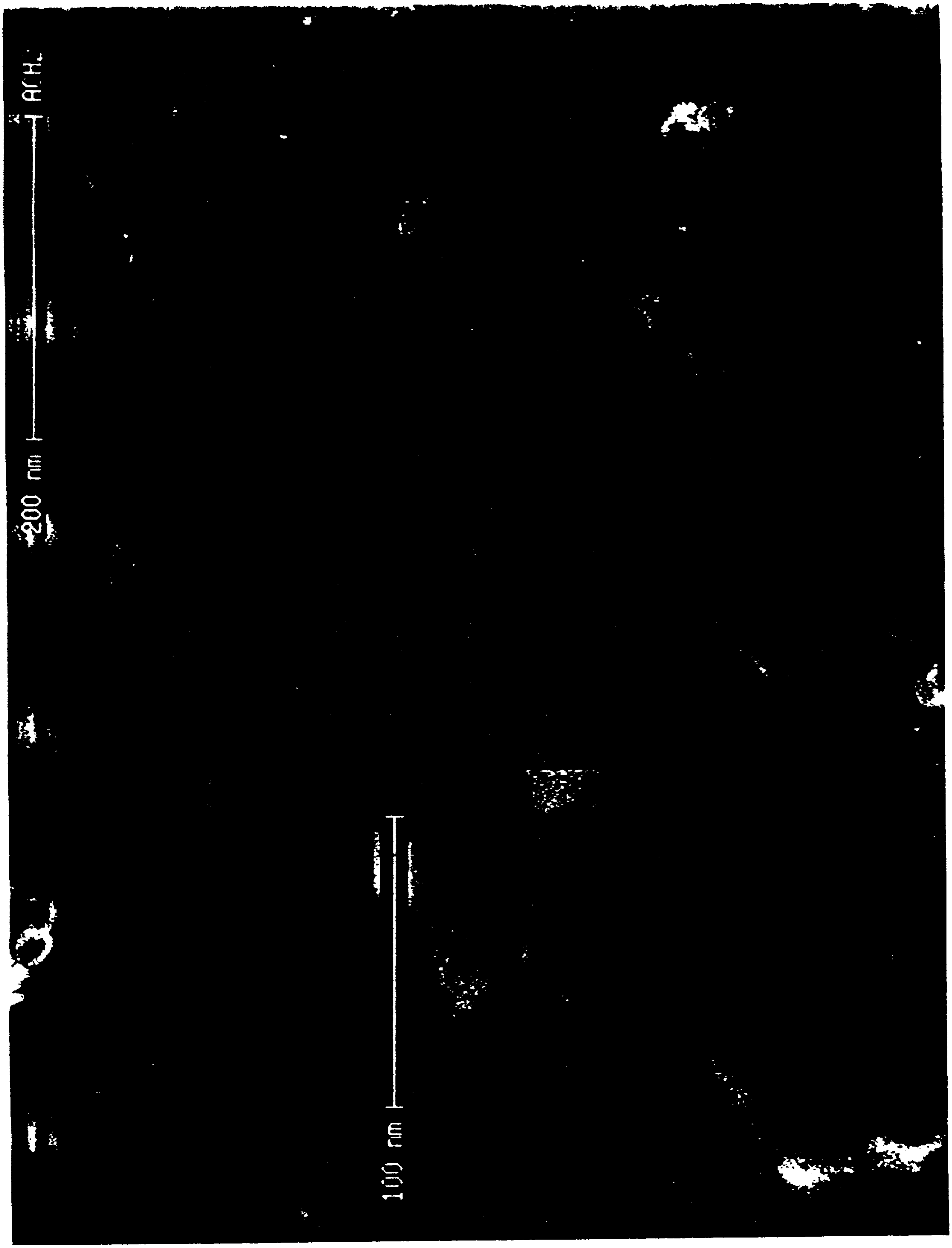
Ar:H2
200 nm
100 nm

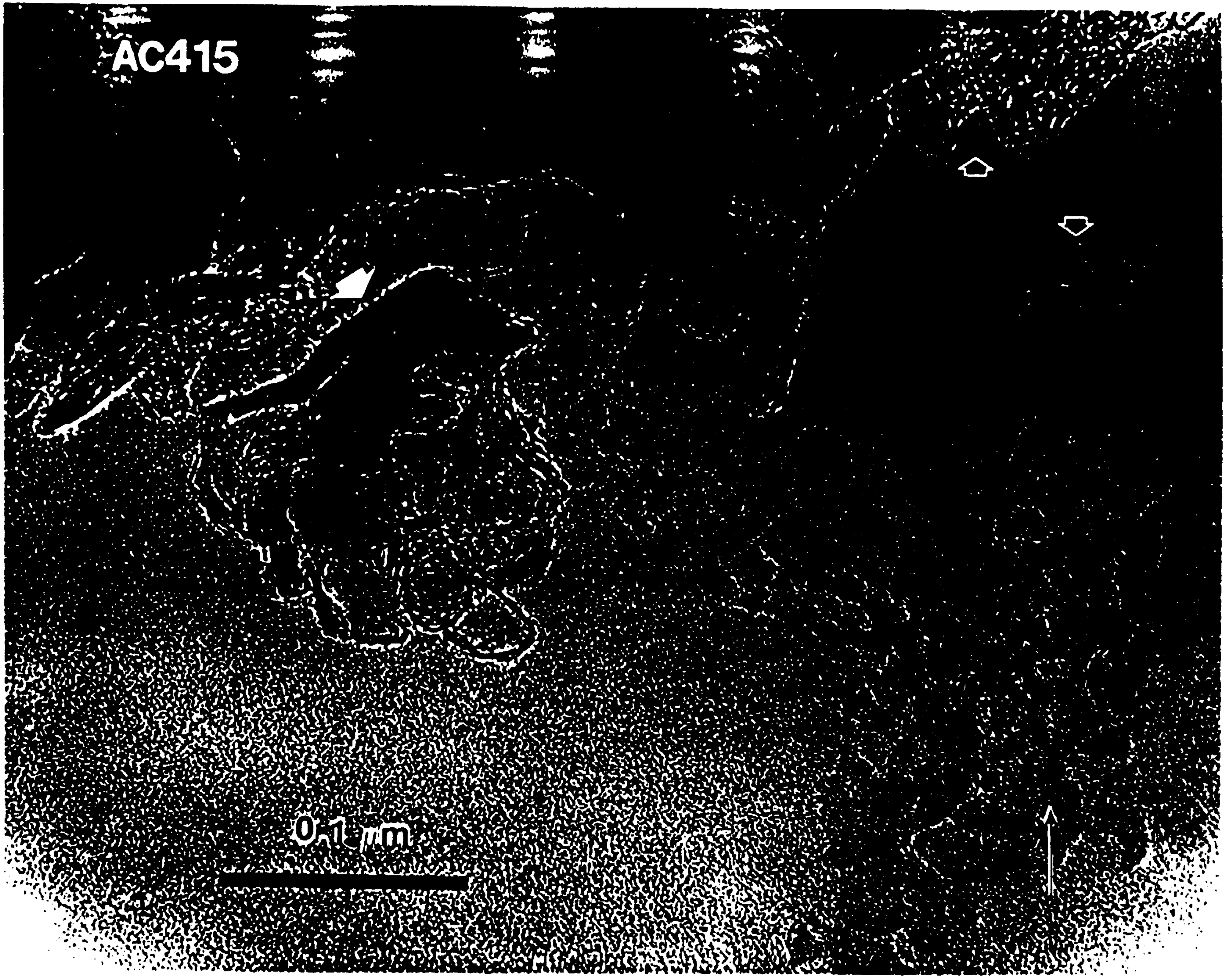

2.3

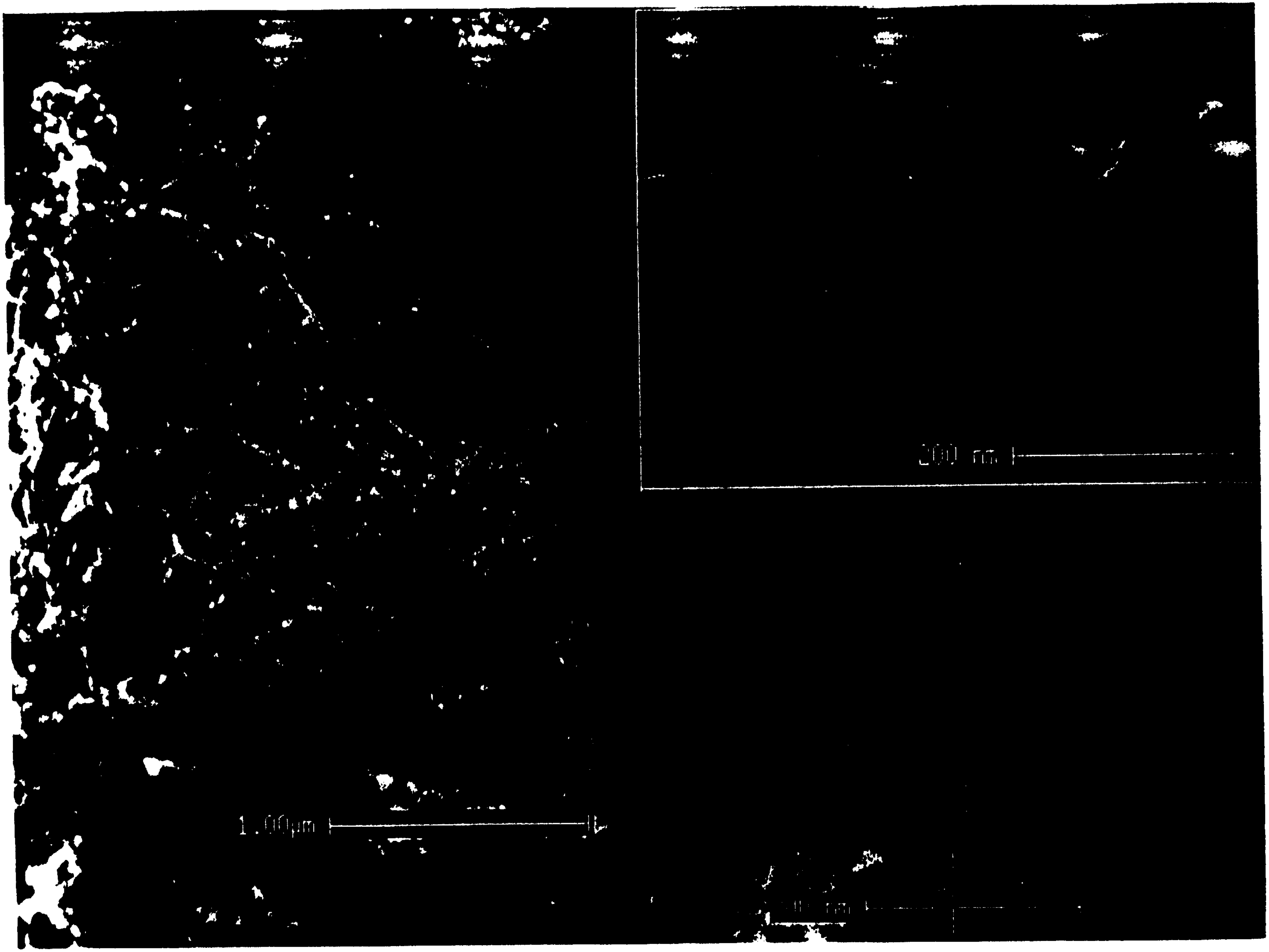

Fig 3

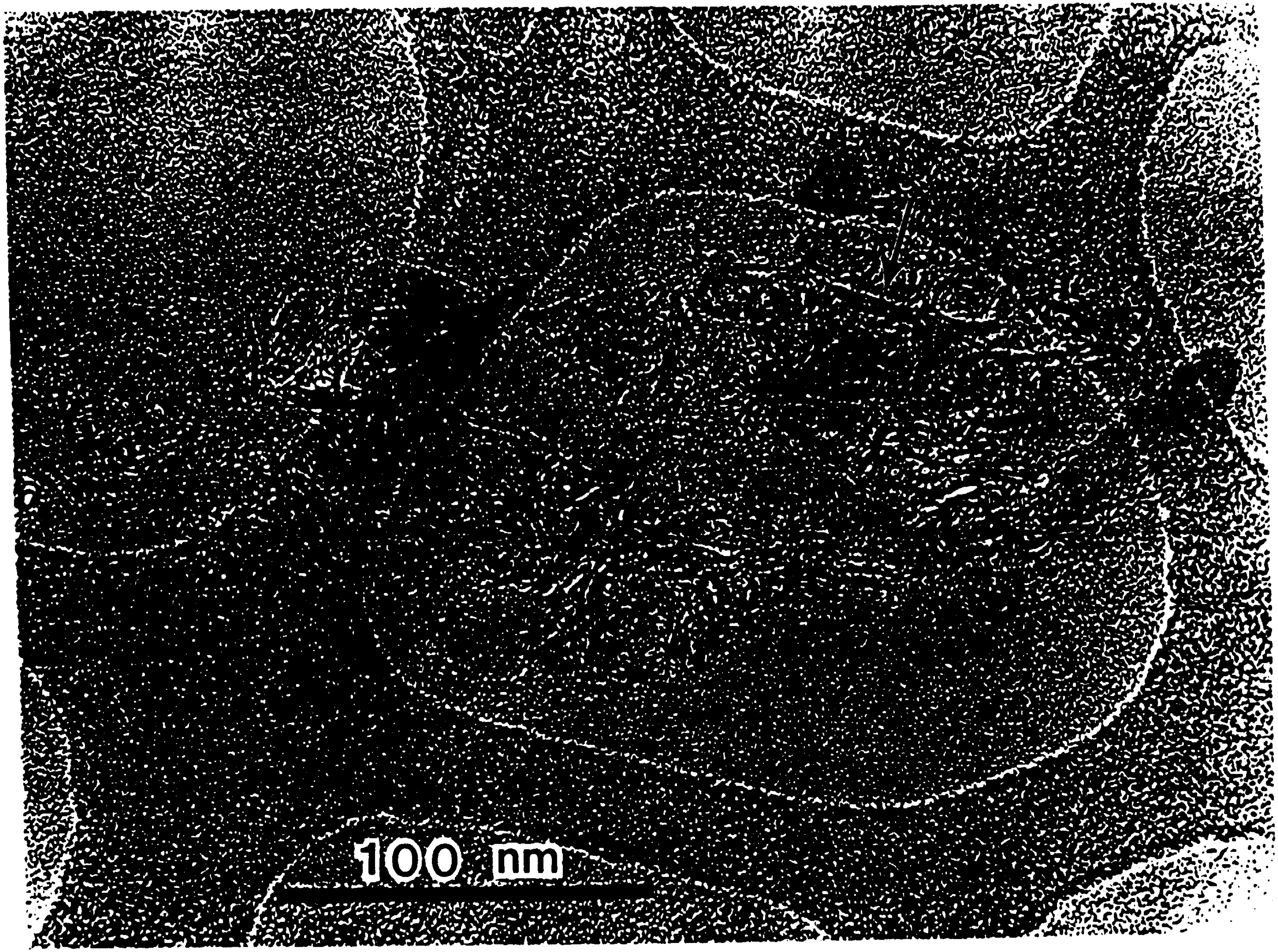

Fig. 4

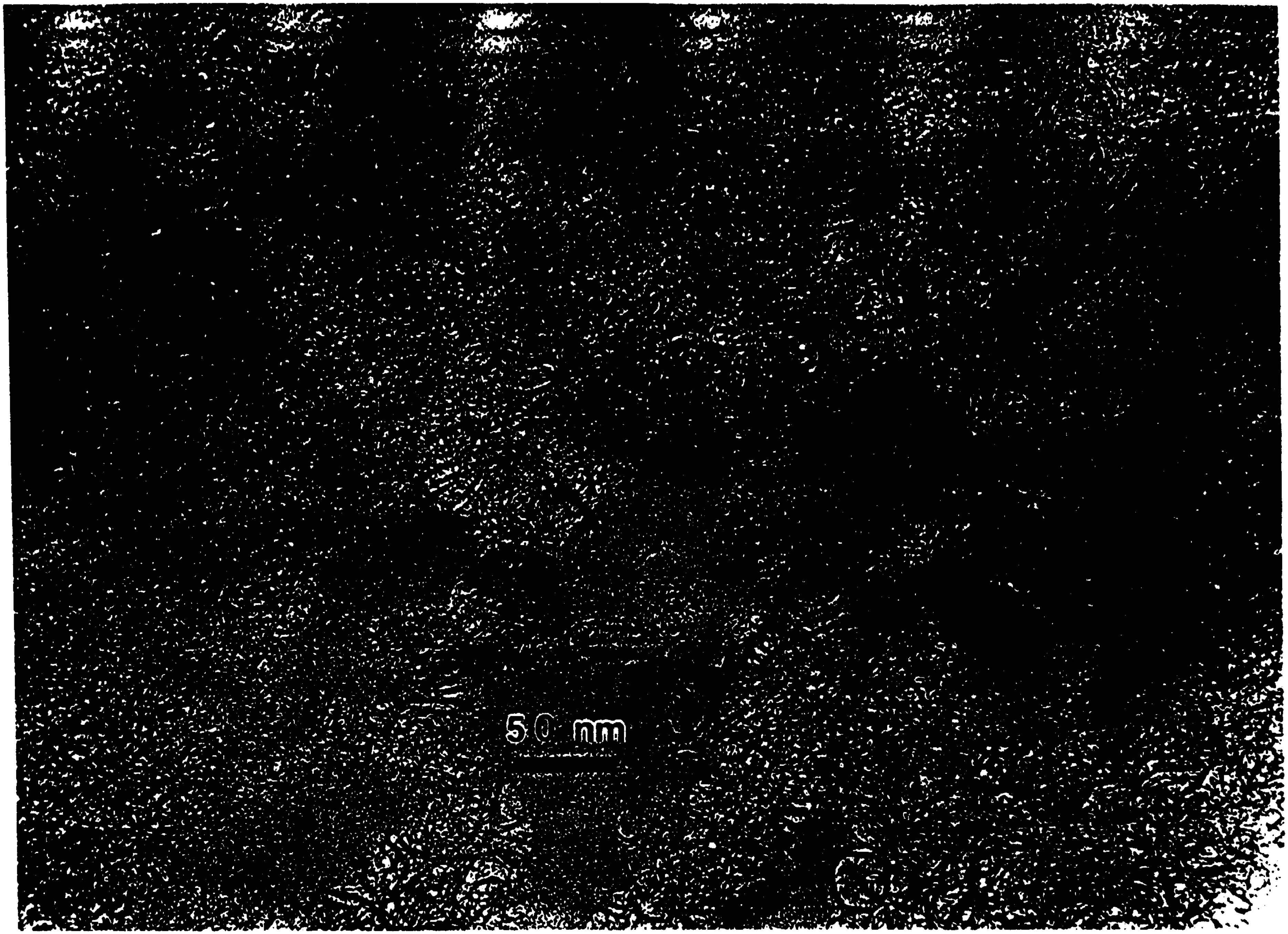

Fig. 5

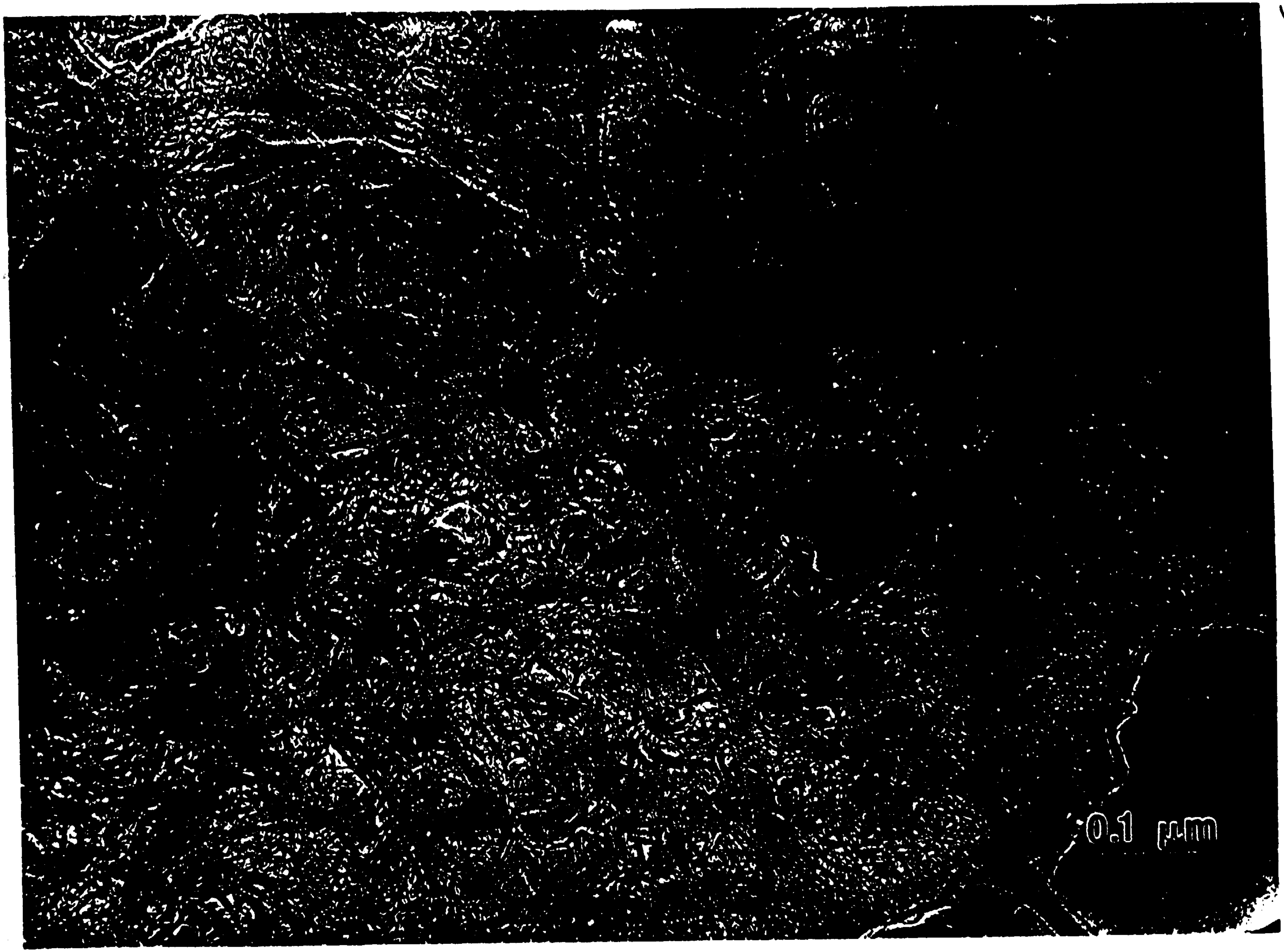

Fig. 6

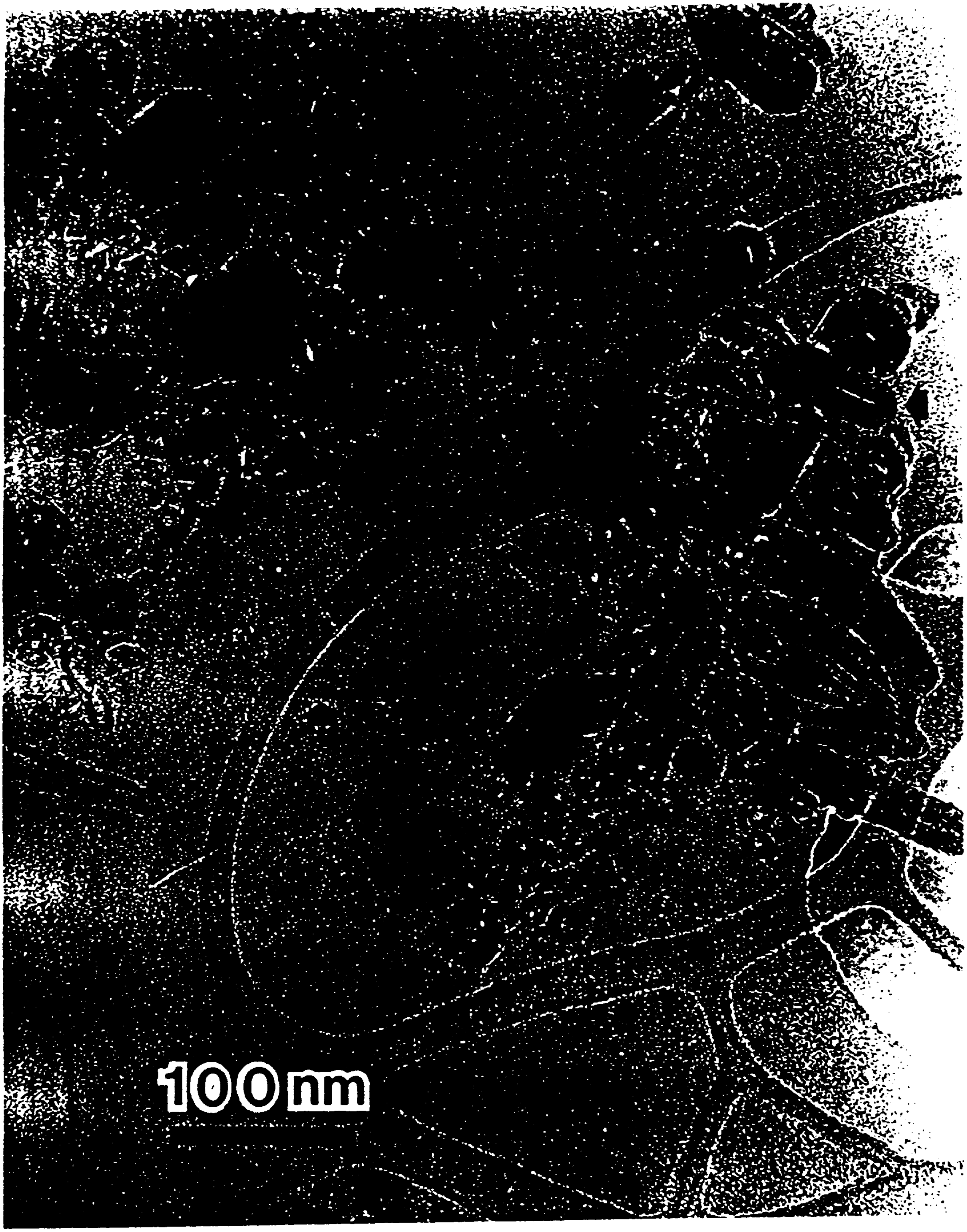

Fig. 7

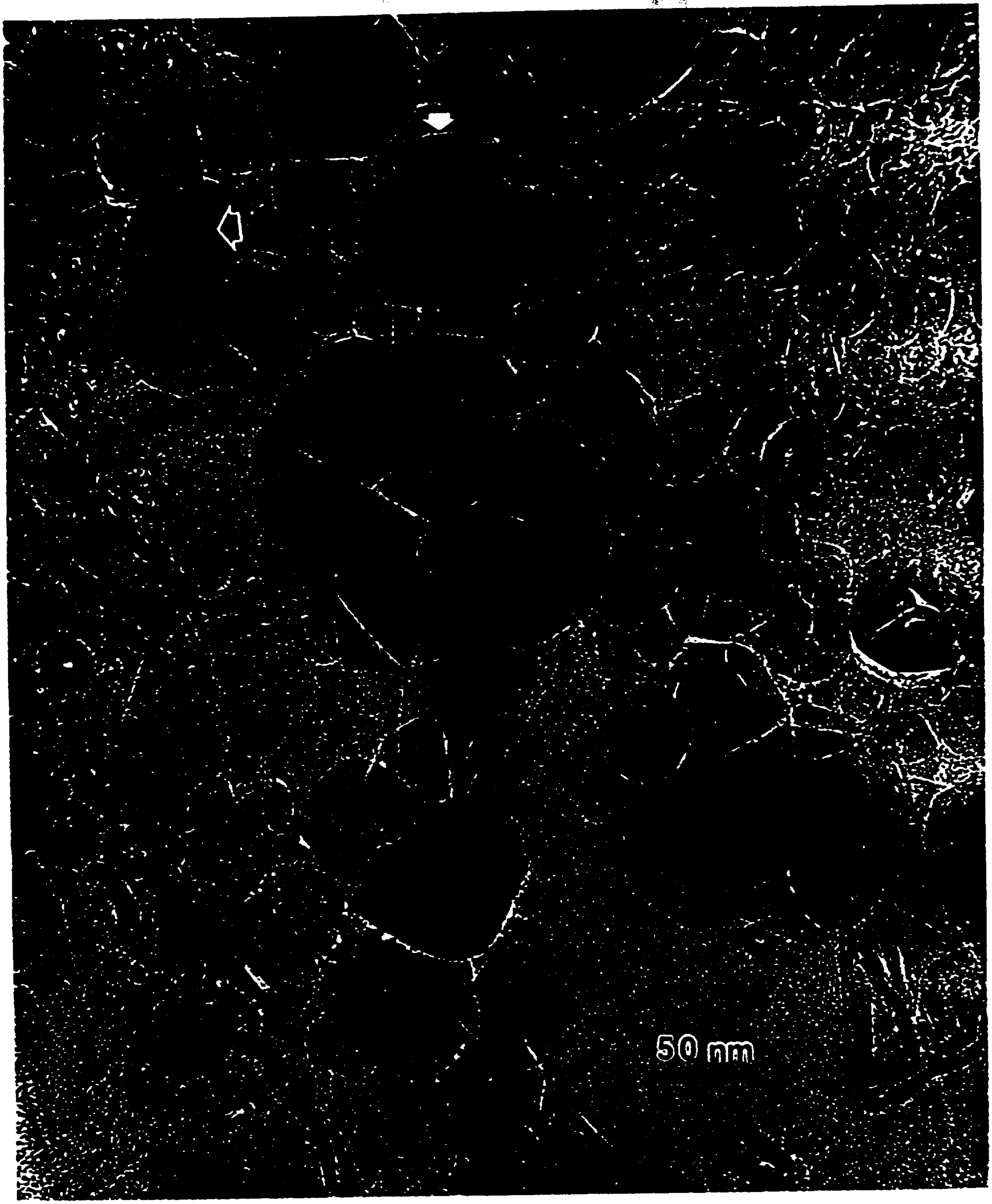

Fig. 8

Fig. 9

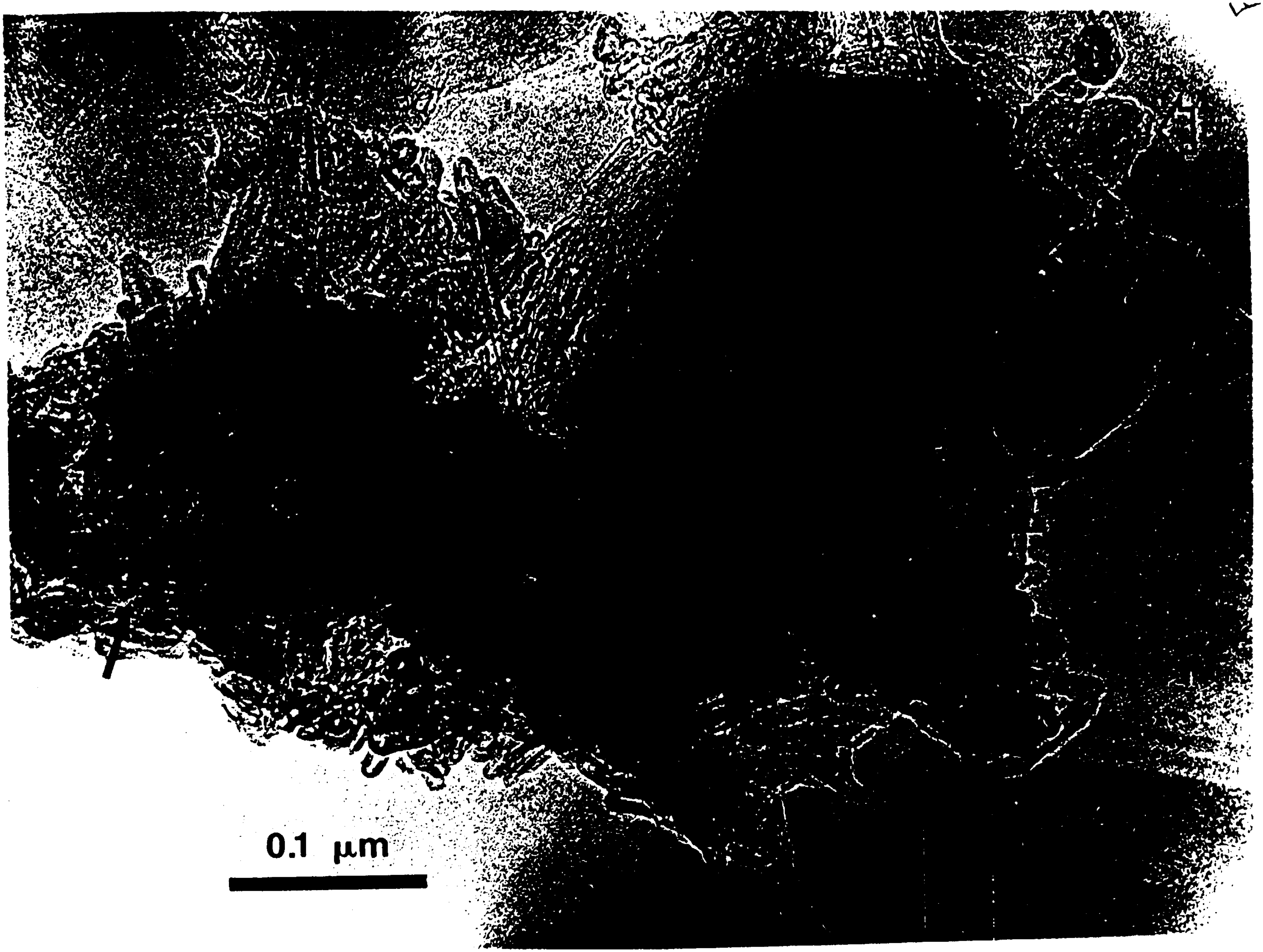

Fig 10

# METEORITICS & PLANETARY SCIENCE

Volume 31 SUPPLEMENT 1996 July

# 59th Annual
# Meteoritical Society Meeting
## Humboldt-University
## July 22–26
## 1996

## BERLIN

PUBLISHED BY
THE METEORITICAL SOCIETY
THE LUNAR AND PLANETARY INSTITUTE

## AEM, XRD, AND IR ANALYSES OF AN AlSiO CONDENSATE ANNEALED FOR TWO HOURS AT ROOM TEMPERATURE UP TO 1100°C.

J. M. Karner[1], F. J. M. Rietmeijer[1], and J. Janeczek[2], [1]Department of Earth and Planetary Sciences, University of New Mexico, Albuquerque NM 87131, USA, [2]Department of Earth and Planetary Sciences, Silesian University, Miekzarskiego 60, 41-200 Sosnowiec, Poland.

The fluffy texture of vapor phase condensates will isolate its individual entities that during thermal annealing will behave as chemically closed systems [1]. To test this hypothesis we annealed an AlSiO condensate at 100°, 210°, 300°, 500°, 600°, 700°, 800°, and 1100°C, each for 2 hr. Assuming relevant diffusion rates in the $Al_2O_3$-$SiO_2$ system, and considering the small size (30–150 nm) of individual entities, diffusion-controlled reactions will be established during this time. If our hypothesis is correct, dusts in O-rich circumstellar environments may show a wide range of chemical signatures determined by allowable stable configurations in the $Al_2O_3$-$SiO_2$ system.

The original condensate was dominated by Al-O bonds and minor SiO features but, when the sample became fully oxidized during annealing in air, the IR data show changes in the length and bending modes of O-Si-O bonds and at 1100°C semicrystalline $SiO_2$ features. All samples are overwhelmingly X-ray amorphous except for tiny amounts of cristobalite between 210° and 500°C, but all traces of crystalline materials disappeared above 600°C. AEM analyses were performed on the original condensate and the sample annealed at 1100°C. All chemical and size data were submitted to statistical treatment in order to assess similarities and differences between the samples. Both samples have a fluffy texture consisting of (sub)circular grains with compositions ranging from 0 to ~70 wt% $Al_2O_3$. Two distinct types of grains are recognized in both samples.

1. Amorphous grains, 0–12 wt% $Al_2O_3$, have a well-defined 8.5-nm-thick rim of 0.7-nm lattice fringes (probably cristobalite). The rimmed grains, 32–79 nm (mean = 54 nm), have log-normal size distributions. Both samples have elongated strands of fused grains but with a single rim. Isolated rimmed grains in the unannealed sample have 0 and 6.9 wt% $Al_2O_3$, but in the annealed sample they occur mostly in clusters (~9 wt% $Al_2O_3$) wherein individual grains are only somewhat discernable.

2. The compositions of mottled grains show peaks at 23, 38.5, 51, and 59.5 wt% $Al_2O_3$ in the condensate and rare entities with a stoichiometric mullite composition (70 wt% $Al_2O_3$). Annealed mottled grains show peaks at 23, 39, and 58.5 wt% $Al_2O_3$. Mottled grains (30–150 nm) in both samples have log-normal size distributions with a mean of 90 nm. The grains are generally amorphous except for scattered diffraction maxima in grains with 40–60 wt% $Al_2O_3$ that are consistent wth sillimanite.

The grain size distributions, morphology, and chemistry in the condensate and the sample annealed at 1100°C are very similar. Differences between the samples include a compositional peak at 51 wt% $Al_2O_3$ and a higher abundance of mottled grains <60 nm, both in the condensate. We attribute the disappearance of this peak and the smallest grains to thermal annealing. The presence of two morphologically distinct grains can be explained using the $SiO_2$-$Al_2O_3$ equilibrium binary phase diagram [2] wherein compositions of the rimmed grains match those of the liquidus surface between pure $SiO_2$ and the eutectic composition at ~10 wt% $Al_2O_3$. The liquidus surface also constrains mottled grain compositions on the liquidus of the phase diagram between the eutectic composition and the mullite stability field. The compositional peaks in the condensate match those of the putative equilibrium and spinodal solvi postulated in this phase diagram. It suggests that condensation of liquid droplets occurred at preferred $Al_2O_3/SiO_2$ configurations during the gas-liquid transition. The preservation of compositional peaks in the annealed sample (1100°C) confirms that isolated entities were prevented from reacting to match compositions of the solvus crests. Subsolidus phase decomposition into sillimanite nanocrystals and an amorphous silica-rich aluminosilica matrix during autoannealing was preserved during thermal annealing.

**Conclusion:** Amorphous phase relationships during condensation of fluffy aluminosilica materials and subsequent thermal annealing are predictable by the phase diagram. These amorphous materials are observed in interplanetary dust particles, which suggests that these dusts could occur in O-rich circumstellar environments.

**Acknowledgments:** We thank J. Janik and J. Nuth for IR analyses. This work was supported by NASA grant NAGW-3646.

**References:** [1] Rietmeijer F. J. M. (1996) *LPS XXVII*, 1071–1072. [2] MacDowell J. F. and Beall G. H. (1969) *J. Am. Ceram. Soc.*, 52, 17.

# Mineralogy, Morphology and Chemistry of Vapor Condensed Silicate Dust Analogs

by

James Karner

B.S., Geology, Bemidji State University, 1994

THESIS

Submitted in Partial Fulfillment of the
Requirements for the Degree of

Master of Science
Earth and Planetary Sciences

The University of New Mexico
Albuquerque, New Mexico

August, 1997

# Acknowledgements

I would like extend a special thanks to Dr. Frans Rietmeijer, my research advisor, for the many patient hours he spent teaching and advising me in the work of this thesis. I also thank my committee members Drs. Jim Papike, Cornelis Klein, and Albert Kudo for their time and efforts in producing a final work. I would also like to thank Dr. Joseph Nuth III and his coworkers at the NASA Goddard Space Flight Center for providing me with the smoke samples. I also thank Dr. Jerzy Janik (Dept. of Chemistry, UNM) for performing, and Dr. Nuth for interpreting, the IR analyses. Dr. Janusz Janeczek at the Silesian University (Sosnowiec, Poland) performed the XRD analyses during his extended residence at the Dept. of Earth and Planetary Sciences. Dr. Rhian Jones, (IOM) assisted with thermal annealing experiments on the Al-Si-O samples in her laboratory. Sample analyses were performed in the Electron Microbeam Analysis Facility (EMAF) at the University of New Mexico and I thank Dr. Lumin Wang and the staff for their technical support and willingness to help me with any problems I encountered. I also thank Dr. Dieter Stoffler and the Meteoritical Society committee which awarded me a student travel stipend in order to present a portion of this research at the annual meeting in Berlin, Germany 1996.

A special thanks also to my family who supported me through this endeavor and encouraged me when tasks seemed overwhelming.

I would also like to sincerely thank NASA as this work was supported by the NASA Origins of Solar Systems project and NASA grant NAGW- 3646 [FJMR]. I also thank the New Mexico Space Grant committee in awarding me a fellowship which supported the finishing of this thesis.

# Mineralogy, Morphology and Chemistry of Vapor Condensed Silicate Dust Analogs

by
James Karner

## ABSTRACT OF THESIS

Submitted in Partial Fulfillment of the
Requirements for the Degree of
Master of Science
Earth and Planetary Sciences

The University of New Mexico
Albuquerque, New Mexico

August, 1997

# Mineralogy, Morphology and Chemistry of Vapor Condensed Silicate Dust Analogs

Jim Karner

B.S. in Geology, Bemidji State University, 1994

M.S. in Earth and Planetary Sciences, University of New Mexico, 1997

## ABSTRACT

Silicate dust analogs are produced by vapor phase condensation of binary and ternary metal oxide mixtures of Fe, Mg, Si, and Al. These elements are chosen because they make up the bulk of amorphous materials found in meteorite matrices and Interplanetary Dust Particles (IDPs). The objectives of this study are to investigate vapor phase condensation in circumstellar environments, and determine whether condensation is an equilibrium or nonequilibrium process, but still defined by existing phase diagram.

Condensation in the Fe-Si-O system produces amorphous grains along with crystalline grains of tridymite ($SiO_2$) and maghemite (ġ- $Fe_2O_3$). The mottled texture of FeSiO grains may be due to spinodal phase decomposition into silica and iron-rich phases during autoannealing. Thermal annealing produces little change in the original condensate except for the fusion of tridymite phases above the metastable extension of the liquidus (glass-transition).

Mg-Si-O condensation produces grains ranging from pure $SiO_2$ to pure MgO. Diffraction data supports the occurrence of tridymite, forsterite, ortho- and clino-enstatite, and periclase, along with amorphous grains. The condensed grains show a strong link

between composition and morphology. The compositional peaks of the grains appear to be predictable using the $MgO$-$SiO_2$ phase diagram.

Fe,$MgSiO_x$ grains are morphologically and compositionally very similar to those found in the binary systems of this study. Silica condenses in many forms including clusters, globules, patchy materials, and rimmed grains. Clusters of cristobalite, in which all the grains are in the same orientation, support the idea that crystallization is a post-condensation process.

Smooth grains and rimmed grains in an Al-Si-O condensate show compositional peaks that follow the topology of the liquidus in the phase diagram. Thermal annealing preserves textures and compostions of grains owing to the fluffy nature of the condensates.

Vapor phase condensation is a nonequilibrium process that produces amorphous to poorly crystalline grains that are < 100 nm in diameter and show log-normal size distributions. Crystalline grains may mostly be a post-condensation experimental artifact. This implies that amorphous materials in meteorite matrices and IDPs are the most representative of circumstellar solids, while crystalline grains in these materials represent a secondary process, possibly annealing of amorphous precursors.

# Table of Contents

## Table of Contents (continued)

## List of Figures

## List of Figures (continued)

# List of Tables

# CHAPTER 1. INTRODUCTION AND EXPERIMENTAL METHODS

## 1.1 INTRODUCTION

The chemical composition of circumstellar and interstellar dust grains has been the subject of debate since the 1950s (Nuth, 1981). These grains are thought to condense from cooling gases around stars (e.g. circumstellar environments) before being ejected into the interstellar medium. Chemically, circumstellar environments have been classified as oxygen-rich (i.e., silicate formation) and carbon-rich (i.e., formation of elemental carbons and carbides, SiC, etc). While astronomers agree that certain emission and absorption peaks in the Infrared (IR) and Ultraviolet (UV) are from dust grains, including silicates, the exact compositions, sizes, structures, and morphologies of these dust grains are still unknown. For example, an IR absorption peak at 10 μm is attributed to the Si-O stretching and bending modes in silicates (Ney, 1977), but the question remains whether this peak is due to crystalline phases such as olivine [$(Mg,Fe)_2SiO_4$] or pyroxene [$(Mg,Fe)SiO_3$], or due to amorphous phases of similar compositions (Day, 1974). Because formation of dust by condensation in a cooling circumstellar gas cannot be directly observed, theoretical and laboratory simulations of condensation in cosmochemically relevant vapors are the best approach to understand details of dust evolution in astronomical environments such as envelopes of cooling stars and the interstellar medium. The objectives of this study are to investigate vapor phase condensation in circumstellar environments, and to determine whether condensation is an equilibrium or nonequilibrium process.

## 1.2 EQUILIBRIUM CONDENSATION MODELS

The first models of the condensation of grains in circumstellar environments approached the problem theoretically using equilibrium thermodynamics. These models assumed an appropriate gas phase composition, pressure and temperature for a particular circumstellar environment, such as the solar nebula. For example, the calculations by Lattimer and Grossman (1978) for condensation in cooling supernovae ejecta used the twelve most abundant elements in chemical zones around a supernova ( H, C, N, O, Na, Mg, Al, Si, S, Ca, Ti, Fe,) at temperatures ranging from 1730$^0$ C to 430$^0$ C, and pressures between $10^{-8}$ and $10^{-3}$ atm. By using equilibrium thermodynamics, the condensation sequence of mineral phases from a cooling gas were then calculated. The exercise begins at a high temperature, that is inferred from solar nebula models at which all constituents occur in the gas phase. The temperature of the system is allowed to drop until the first mineral species condenses. The reaction proceeds to completion until this mineral gas phase species is depleted in the cooling gas. The composition of the remaining vapor is then recalculated and a pressure decrease due to adiabatic expansion and condensation is taken into account. The system is then allowed to cool until the next solid species condenses-and so on. An example of a calculated condensation sequence in a gas of solar composition at $10^{-4}$ atm, was done by Grossman and Larimer (1974) and is as follows: the first condensate containing a major element is corundum ($Al_2O_3$) which condenses at 1406 °C. The condensation sequence proceeds, via:

| | |
|---|---|
| perovskite ($CaTiO_3$) and mellilite ($Ca_2Al_2SiO_7$) | 1227 °C |
| diopside ($CaMgSi_2O_6$) | 1114 °C |
| metallic Fe with Co and Ni. | 1102 °C |
| forsterite ($Mg_2SiO_4$) | 1097 °C |
| enstatite ($MgSiO_3$) | 1050 °C |
| Ca-feldspar ($CaAl_2Si_2O_8$) | 1027 °C |
| Na-K feldspars [$(Na,K)AlSi_3O_8$] | 927 °C |
| fayalite ($Fe_2SiO_4$) and ferrosilite ($FeSiO_3$) | 477 °C |
| troilite (FeS) | 427 °C |
| magnetite ($Fe_3O_4$) | 132 °C |

Equilibrium models have been proposed for grains formed in the atmospheres of stars (Gilman, 1969), super nova shells (Lattimer and Grossman, 1978), and the solar nebula, (Wood, 1963; Lord, 1965; Grossman and Larimer, 1974). Within these calculations there are five important assumptions, which are:

(1) reactions occur at thermodynamic equilibrium

(2) reactions proceed directly from gas to solid

(3) condensation products are stoichiometric crystalline phases

(4) condensation products include "complex" solids (e.g.silicates), and

(5) reactions are not kinetically inhibited

## 1.3 NONEQUILIBRIUM CONDENSATION MODELS

Theoretical considerations cast doubt on these assumptions in the thermodynamic models. Donn (1979) noted that vapor phase condensation produced metastable condensates, had a strong temperature dependence, and occurred under disequilibrium arising from low cloud densities. He concluded that the condensation of gases does not follow an equilibrium path but instead is controlled by kinetics. Blander and Katz (1967) calculated that the surface energies of solid grains would be high, and high degrees of vapor supersaturation were needed, for a gas phase species to condense. This supersaturation requirement could alter the predicted condensation sequence of the thermodynamic models and also alter the composition of species formed at lower temperatures (Nuth, 1981). Further theories predicted a gas-liquid-solid transition with the products of condensation being amorphous solids rather than crystalline phases (Donn et al., 1981). The predicted condensation of silicates was also questioned, as these complex solids do not exist as gas phase molecules (Donn et al., 1981). Also, other kinetic factors indicated that the predicted formation of hydrated magnesium silicates from crystalline olivine and pyroxene grains would take ~ 10 times longer than the present age of the solar system for grains with a radius of ~100 nm (Fegley, 1987).

## 1.4 EXPERIMENTAL CONDENSATION

The controversy over condensation theories led scientists to explore vapor phase condensation experimentally. Some workers thought natural materials found on earth (e.g. meteorites) could contain vapor phase condensates, while others began to produce condensates in the laboratory. The fundamental question was still; "What is the nature of the products of vapor phase condensation?"

### 1.4.1 CI and CM meteorites and condensation

A first attempt to identify and characterize the composition of circumstellar dusts concentrated on the study of meteorites, in particular the CI and CM chondrites, which are chemically the most primitive meteorites we know. Cameron (1973) conjectured that they may also be the most representative of interstellar solids. Grossman and Larimer (1974) suggested that the chemistry and mineralogy of carbonaceous chondrites was established during the condensation of the solar system. CM meteorites consist mainly of coarse-grained silicate mineral assemblages termed chondrules, and a fine-grained matrix. The matrix is a two-component mixture of 1) angular, micron sized, altered olivines and pyroxenes supposedly derived from chondrule fragmentation and 2) nonangular nanometer sized hydrous silicates, carbonates, sulfides, various sulfates, magnetite, amorphous material, and carbon as carbonates and organic phases. CI meteorites have no chondrules and are composed of only fine-grained matrix. Although the chemical makeup of CI and

CM chondrites is very primitive, the mineral components suggest that secondary processes such as thermal metamorphism and aqueous alteration have taken place (Zolensky and McSween, 1988). For example, a fine-grained matrix and chondrules with a forsterite composition ($Mg_2SiO_4$) have been partially or wholly replaced by phyllosilicates, such as serpentine [($Mg_3Si_2O_5(OH)_4$] as a result of aqueous alteration. Furthermore, the grain sizes of minerals in the CI carbonaceous chondrites are in the range of 50- 600 nm for the fine-grained matrix (Mackinnon and Kaser, 1988) and 100 microns to 1 millimeter in chondrules (Fujimara et al., 1983). These grain sizes are larger and have a much greater range than the nanometer sized grains predicted by vapor phase condensation theories and observed in experiments. Also, the pressure and temperature history of meteorite grains as well as the compaction processes in parent body environments is not well understood. In short, the conditions of meteorite formation are not well constrained, and the identification of pristine, interstellar and circumstellar, condensates in CI and CM chondrites was not successful. Scientists realized that if there were any pristine condensate grains in meteorites, they would be contained in the fine-grained, low-temperature matrix, which had a lower temperature history than the other components, and thus may have retained part of its presolar record. The problem was that the matrix is very fine-grained and full of sticky organic matter, which deemed conventional mineral seperation methods unsuccessful (Anders and Zinner, 1993). With the improvement in mineral separation methods as well as analytical techniques, scientists in the mid 80s returned to search for interstellar and circumstellar grains in the matrices of chondritic meteorites. Destructive chemical separations, wherein undesirable matrix material is dissolved by appropriate reagents led to the discovery of four circumstellar components including micron sized SiC, graphite spherules, and corundum ($Al_2O_3$), and nanometer sized diamonds (Anders and Zinner, 1993-for a thorough review).

### 1.4.2 UOC meteorites and condensation

Further matrix studies concentrated on the fine-grained, opaque, Fe-rich component of unequilibrated ordinary chondrites. This opaque matrix or "Huss matrix" is composed of micron to submicron-sized silicate grains in an amorphous material along with nanometer sized NiFe metal, and sulfide grains. In a TEM study of "Huss matrix", Brearley et al. (1989) hypothesized that fine-grained olivines and pyroxenes contained in amorphous Fe-rich material could be derived by the annealing of amorphous presolar or nebular condensates. The olivine and pyroxene grains ranged from 20-200 nm in diameter and were in loosely consolidated clusters. These grains are very similar to those produced by the annealing of amorphous silicate smokes (Table 1.1). It may be that the amorphous silicate components of ordinary chondrite matrices are interstellar and circumstellar condensates (Brearley et al., 1989). Recently, a new source of possibly more primitive extraterrestrial material has become available with the collection of interplanetary dust particles (IDPs) (Bradley et al., 1988). IDPs may provide a better look at the initial amorphous materials produced by condensation.

**Table 1.1 Comparison of condensate properties in theoretical models, meteorite matrices, CP IDPs, interstellar grains, and representative experimentally produced analogs. Abbreviations: x = mean, OL= olivine, PYX = pyroxene. 1- Brearley et al. 1989. 2- Rietmeijer and Mackinnon, 1986. 3- Anders and Zinner, 1993. 4- Stephens and Kothari, 1978. 5- Rietmeijer et al., 1986. 6- Salpeter, 1974. 7- Donn et al., 1981. 8- Grossman and Larimer, 1974.**

| | **Morphology** | **Grain Sizes** | **Mineralogy and Structure** |
|---|---|---|---|
| **Ordinary chondrite matrices[1]** | -subrounded grains in loose clusters | 20-200 nm | -crystalline olivine within Fe-rich amorphous to poorly ordered matrix |
| **CP IDPs[2]** | -aggregated fluffy grains | 2-100 nm | -olivines and pyroxenes in amorphous matrix with sulfides |
| **Interstellar grains in meteorites[3]** | -diamonds, euhedral<br>-SiC, platey, cubic<br>- graphite, spherules<br>-corundum | -diamonds, x = 1nm<br>- SiC, 0.5 -20 μm<br>- graphite, 0.8- 7 μm<br>-corundum, 1-3 μm | -diamond, crystalline<br>-SiC-β, crystalline<br>-graphite-bucky balls, semicrystalline<br>-$\gamma Al_2O_3$, crystalline |
| **Dust analogs[4]** | -Fe,Ni alloy-chains of spheres<br>-SiC- euhedral, chains<br>- spherical<br>-OL + PYX- chains of spheres<br>-Carbon-irregular chains | -Fe,Ni, x= 15 nm<br>-SiC, x= 20 nm<br>-$Al_2O_3$, x= 30 nm<br>-OL + PYX, x= 20 nm<br>-Carbon, x=20 nm | -Fe,Ni alloy-crystalline<br>-SiC-β -crystalline<br>- $\gamma Al_2O_3$- crystalline<br>-OL + PYX-amorphous<br>-Carbon-amorphous |
| **Dust analogs[5], MgSiO** | -chains, crude bulky network. Annealed-well defined fluffy clusters | -Condensed, x= 30 nm<br>-2 hrs x= 31 nm<br>-4 hrs, x= 35 nm<br>-Si plates 200-250 nm | -condensed material amorphous to poorly ordered<br>-Annealed-tridymite, forsterite, enstatite |
| **Theoretical predictions-kinetic theory[4,6,7]** | -chains of grains, collisional growth | -nucleation size ~ 1 nm<br>-coagulation leads to grains from 15-100 nm | - amorphous grains of mixed composition will form and not minerals |
| **Theoretical predictions-equilibrium theory[8]** | - not specified | - sizes not specified | - sequence of minerals-<br>$Al_2O_3$, $CaTiO_3$, $Ca_2Al_2SiO_7$, $CaMgSi_2O_6$, $Mg_2SiO_4$, $MgSiO_3$, $CaAl_2Si_2O_8$, $(Na,K)AlSi_3O_8$, etc. [cf. Sect. 1.2] |

### 1.4.3 Interplanetary Dust Particles and condensation

IDPs are collected from the earth's stratosphere and are thought to be derived from outer belt asteroids (P and D type) (Zook and McKay, 1986) and cometary dusts (Fraundorf et al, 1982). Spectra from P and D type asteroids reveal that they have high carbon contents and possibly ice in their interiors (Bell et al., 1988). Along with comets, P and D type asteroids are considered to be the most primitive bodies in the solar system because of their lack of internal heat sources. The chondritic porous (CP) IDPs have a fluffy porous nature and are believed to have cometary origins (Fraundorf et al., 1982). The fluffy porous nature is believed to be derived from ice grains that originally filled in the pore spaces between dust aggregates. The CP IDPs are mainly nonequilibrium assemblages of <100 nm grains of olivine and pyroxene and sulfides in an amorphous ferromagnesiosilicate matrix. It could be that the crystalline grains are derived by the annealing of the amorphous phases (Rietmeijer, 1992). Mackinnon and Rietmeijer (1987) noted a wide variety of organic phases, and enstatite whiskers and platelets, and concluded that CP IDPs contain mineral assemblages and textures different from any known meteorite class. Furthermore, the formation of whiskers and platelets in these CP IDPs could support with growth from the vapor phase (Bradley et al., 1983). These IDPs are considered likely to contain unaltered solar nebula or even pre-solar dust (Bradley, 1988).

### 1.4.4 Experimentally produced condensates

Laboratory efforts in the early 1970s produced condensate grains (smokes) from mixtures of elements assumed to be abundant in circumstellar environments such as Mg, Si,C, O, Fe, and Al, in binary and ternary gas mixtures at temperatures ranging from 300 - 750 °C and pressures from 1 to 80 Torr. Ultraviolet and Infrared spectral properties such as emission and absorption of the condensates were then measured and compared with astronomical measurements of interstellar and circumstellar dusts to constrain the nature of these natural dusts. The analogs also presented the opportunity to study the size, chemistry, mineralogy and structure of grains produced from condensation. Secondary processes such as thermal annealing could also be performed on the condensates to simulate processes such as bombardment by energetic photons and electrons (Nuth and Hecht, 1989) affecting silicate dust after being ejected into the interstellar medium.

The first condensed particles were produced by evaporation in an electric arc (Lefevre, 1970). Grains of iron, carbon, silicon carbide and silica were produced with sizes from 10 to 200 nm in diameter. The silica particles had spherical shapes with diameters from 10 -100 nm, and occurred as chains. Similar results were reported for grains of iron, elemental carbon, iron-oxide and silica produced by Kamijo et al. (1975) using a gas evaporation technique. These grains were 4 to 100 nm in diameter and also formed chainlike morphologies. Both studies noted iron and iron-oxide grains appeared crystalline, while silica and carbon grains appeared to be amorphous.

Day and Donn (1978a) described the condensation of the thermodynamically unstable $Si_2O_3$ from an Si-O gas. The $Si_2O_3$ was identified by IR spectra. The X-ray and electron diffraction data showed that the grains were amorphous. Adding Mg to the system produced amorphous nonstoichiometric condensate grains with a compositional range from high Mg/Si to almost pure silica (Day and Donn, 1978b). The IR spectrum of the amorphous magnesium silicates showed a strong resemblance to the 10 μm feature observed from astronomical sources. When annealed at 500 and 1000 $^0$C the material always crystallized to form forsterite ($Mg_2SiO_4$). Thermodynamic theory predicted condensation in this system at 1100 $^0$C (Grossman and Larimer, 1974), but this experiment revealed that condensation was temperature-dependent, occurring only after temperatures dropped to 300 $^0$C. Day and Donn (1978b) attributed the temperature dependence of condensation to the high surface energy of the silicates which prevented nucleation until high supersaturation of the vapor phase. These experiments were important as they demonstrated the nonequilibrium nature of the condensation process-that is, not only producing amorphous solids at much lower temperatures than predicted, but also producing phases that were not the most thermodynamically stable in the system, relative to equilibrium conditions.

By means of a pulsed laser, Stephens and Kothari (1978) evaporated samples of olivine, pyroxene, nickel-iron alloy, $Al_2O_3$, carbon, calcium carbonate and silicon carbide. The condensates were studied by transmission electron microscopy (TEM) and electron diffraction and found to be glassy, spherical grains in chain-like structures with median diameters of ~20 nm in all samples. Calcium carbonate typically formed grains 60 nm in diameter. Olivine, pyroxene, nickel-iron alloy, carbon, and calcium carbonate condensed as amorphous grains while $Al_2O_3$ and SiC were crystalline.

Rietmeijer et al. (1986) used analytical electron microscopy (AEM) to study an Mg-Si-O condensate previously characterized by IR and X-ray diffraction (XRD). They found amorphous to poorly-ordered grains in the condensate. Annealing these grains at 727 $^0$C for 4 hours produced forsterite and tridymite grains, that with further annealing, reacted to form the thermodynamically stable phase enstatite ($MgSiO_3$) after 4 hours. The formation of a thermodynamically unstable mixture of forsterite and tridymite was due to the large surface free energy of the nanometer sized grains, which inhibited the reaction of tridymite and forsterite to enstatite.

Condensation in the Fe-Si-O system produced amorphous grains ranging from 2-130 nm in size, in chains and cluster morphologies (Rietmeijer and Nuth, 1991). Rare polycrystalline tridymite globules were up to 450 nm in diameter. Simple crystalline oxides, such as tridymite and maghemite ( $\gamma$-$Fe_2O_3$), were found. The high abundance of crystalline material was explained as post-condensation transformations, or autoannealing (Rietmeijer and Nuth, 1991). Autoannealing is thought to be a thermal damping of the system whereby "hot" condensates convert excess thermal energy to structural ordering. Rietmeijer and Nuth (1991) hypothesized that there were two stages in the evolution of condensed materials - (1) simple metal oxide condensates are more likely to nucleate from the vapor than complex silicates, and (2) autoannealing will produce crystalline mono-metal oxides first, and further thermal annealing may produce complex silicates, or bi(tri)-metal oxide compounds.

To summarize, theoretical and experimental data shows that vapor phase condensation is a nonequilibrium process that produces amorphous to poorly ordered grains that are generally < 100 nm in size but can be as large as 450 nm in clusters and globules that result from coagulation during condensation. The small (< 100 nm) grains are often contained in branching chain-like morphologies and clusters that define a fluffy, or "smoke" texture. Metastable high temperature phases are the first to form, but the most thermodynamical stable phase can often be produced by thermal annealing of the system.

## 1.5 SAMPLES OF THIS STUDY

In this study of silicate dust analogs, *IDPs are used as a ground truth base* for circumstellar and interstellar dusts. The dust analogs in this study are constrained by the compositions of the amorphous materials found in IDPs (from: Rietmeijer, 1992), which are:

Magnesiosilica materials
(Na-rich), ferromagnesio-aluminosilica (both high and low $Al_2O_3$) materials
Silica-rich materials
Chondritic (approximately) materials

This study will detail the mineralogy, chemistry and morphology of individual grains and their interrelationships in vapor condensed silicate analogs of interstellar and circumstellar dust. I will document grain sizes, size distributions, and the phases produced by the condensation of binary and ternary oxide gas phase mixtures and their subsequent thermal annealing. By performing these analyses I hope to gain a better understanding of silicate dust evolution, from its formation to incorporation into primitive solar system bodies such as IDPs.

This project provides data that are currently lacking because data on the mineralogical, morphological and chemical properties of silicate dust condensates nanometer scale are scarce, and because sample preparation has recently been greatly improved with the use of ultrathin sections. With these advances in analytical techniques I anticipate to perform a more thorough and complete study on silicate dust analogs using TEM imaging, electron diffraction, and energy dispersive spectrometry than has been done previously. While spectral studies are needed to ultimately match signatures of dust analogs to astronomical observation, there is also a need for an AEM study to characterize the nanometer size particles to answer fundamental questions concerning the vapor phase process. That is, what phases and particles sizes are stable via the condensation event and subsequent thermal annealing. This study will also contribute to an experimental data base of petrologic observations of silicate dust, and along with spectral studies will add to our knowledge and understanding of silicate dust and its evolution.

## 1.6 EXPERIMENTAL METHODS

Samples of vapor condensed silicate dust analogs were obtained from Dr. J.A. Nuth at the NASA Goddard Space Flight Center in Greenbelt, MD. The vapor condensed analogs are produced in the condensation flow apparatus described by Nelson et.al. (1989) and shown in Figure 1.1.

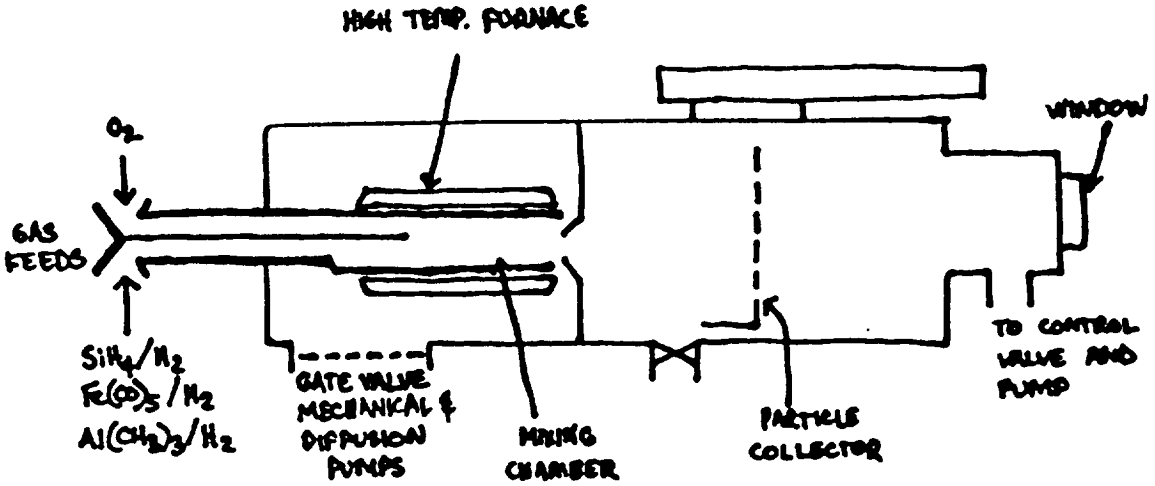

Figure 1.1 Schematic diagram showing the condensation flow apparatus used in the manufacture of the samples. Si, Al, and Fe vapors are premixed before introduction into the mixing chamber while $O_2$ enters the center of the mixing chamber from a different inlet. Solid Mg metal is vaporized in a small graphite boat within the furnace (not shown). The diameter of the mixing chamber is ~ 2.5 cm. (Drawing not to scale) Modified from Nuth et al. (1988).

The experiment entails condensing binary oxide systems, such as Fe-Si-O, Mg-Si-O, Al-Si-O, and ternary oxides, Fe-Mg-Si-O in $H_2$ at a temperature of ~ 500 $^0$C and pressure of ~ 80 torr. The experiment starts by entraining all constituents as gas phase molecules in a alumina reaction tube heated by a graphite furnace. Iron and aluminum are contained in liquid $Fe(CO_5)$ and $Al(CH_3)_3$ and are introduced as gas by bubbling hydrogen gas through the liquid. Silicon and oxygen are introduced as the gases $SiH_4$ and $O_2$, respectively. Magnesium vapors are produced by heating solid magnesium metal in the furnace. Once all the constituents are in the vapor phase, condensation is induced by the flow of cool $H_2$ gas through the furnace into a collection chamber kept at 25 $^0$C. The collection chamber is lined with aluminum foil and condensate grains are scraped from a collector plate and the chamber walls for TEM/AEM analysis. A typical experiment produces ~ 0.5 grams of material.

Samples were sent to the University of New Mexico where I embedded them in epoxy blocks and prepared them for serial ultramicrotome thin sectioning using a Riechert-Jung ultramicrotome E equipped with a diamond knife (Figure 1.2). Thin sections were obtained with a knife speed of 0.5 to 0.8 mm/sec. In reflected light the sections appeared silver to gold indicating 80-110 nm thicknesses. Sections were mounted onto holey-carbon substrates supported by standard 200-mesh Cu grids in preparation for investigation by (TEM), Energy Dispersive Spectroscopy (EDS), and Selected Area Electron Diffraction (SAED). All these techniques utilize an electron beam (probe) size (~15 nm) comparable to the smallest particles studied, and allow for detailed chemical and physical information of nanometer sized materials.

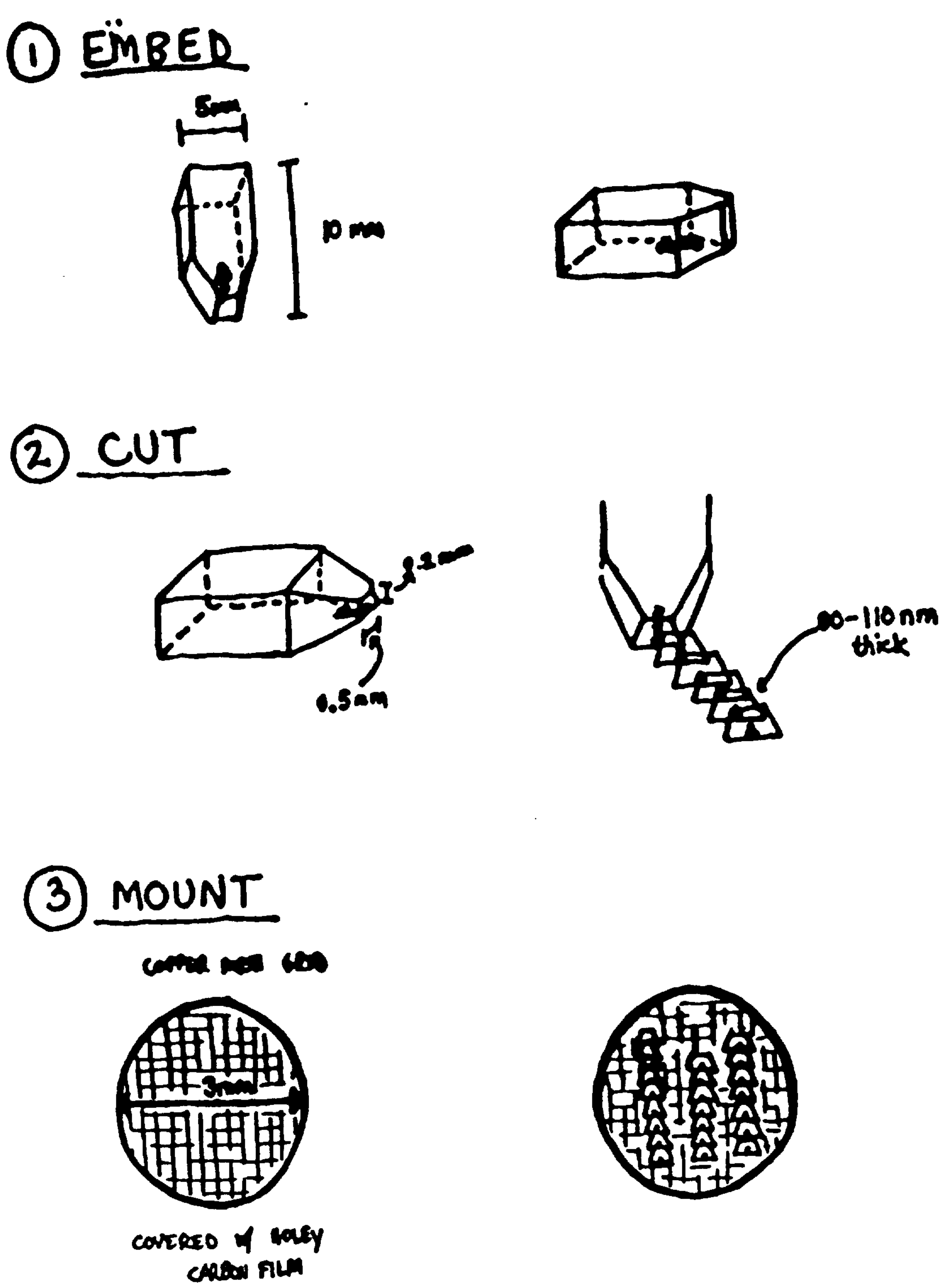

Figure 1.2 Three steps in preparing samples for TEM analysis. 1) Grains are embedded in an epoxy block. 2) The epoxy block is fashioned with razor blades and glass knives until a small trapezoidal face is formed with the grains directly below the epoxy surface. Thin sections are then cut with a diamond knife. 3) Thin sections are then mounted on copper grids. Note that *all* sections containing sample is the ideal case.

All analyses were performed on a JEOL 2000FX Analytical Electron Microscope, equipped with a TN-5500 Energy Dispersive Spectrometer, in the Electron Microbeam Analysis Facility at the University of New Mexico. The AEM operates by using a series of magnetic lenses to focus an accelerated electron beam (200 kV) under high vacuum, through an ultra-thin (80 nm to 110 nm thick) specimen (Figure 1.3).

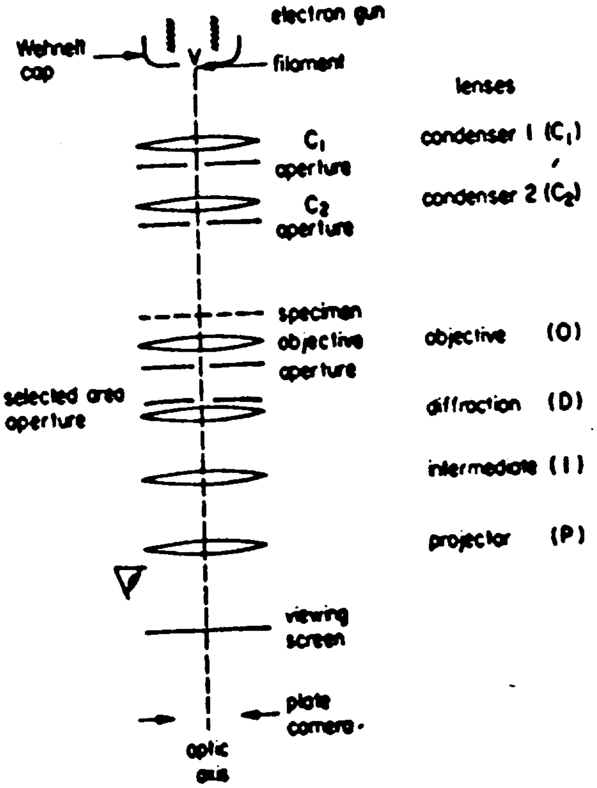

**Figure 1.3** A schematic diagram showing the important components of the electron microscope. Taken from Eddington (1976).

An image or diffraction pattern is obtained from the specimen on a flourescent screen using a multi-lens magnification system. Image contrast can be enhanced using an objective aperature, and the area for diffraction may be selected via a selected area aperature. The image is focussed using the objective lens and magnification is controlled by the excitation of the intermediate and/or diffraction lens. The great advantage of the electron microscope is its point-to-point resolution. A general equation for maximum resolution is,

$$\Delta r_{min} = \lambda^{3/4} C_s^{1/4}$$

where r is the minimum distance able to be resolved between two points, $\lambda$ is the wavelength of the electron beam, and $C_s$ is the spherical abberation constant for an objective lens, usually 1 or 2 mm. This microscope has a resolution of about 0.3 nm. This value represents an ideal value and image quality is greatly controlled by alignment factors including alignment of the objective lens, adjustments to minimize objective astigmatism, and illumination conditions as well as centering of the specimen on the optic axis. The high resolution of the instrument is very useful in the study of nanometer sized grains such as dust grains. The AEM is also ideal for this study because it has operation modes which allow for *in situ* imaging, diffraction and chemical analysis.

Bright Field imaging in the AEM is obtained by utilizing transmitted beams to produce an image on a viewing screen below the sample. High resolution images use both transmitted and diffracted beams together, and can provide information on sub-unit cell structures and defects. Bright Field imaging was used to determine grain size and morphology at various calibrated magnifications from 68,000 to 850,000 times. Grain sizes were measured directly from micrographs and expressed as the root-mean square (rms) size according to the equation,

$$rms = (a^2 + b^2)^{1/2}$$

where a and b are two orthogonal diameters. Grain sizes are then submitted to statistical treatment in order to obtain ranges, averages, standard deviations, populations, and grain size distributions.

Deviations from true grain size can occur from improper alignment of the microscope and measurement error. Proper alignment of the microcope has the specimen axis and optic axis intersecting at an exact point, known as the eucentric position. Deviations from the eucentric position result in beam shift across the sample and elongation of the image. The eucentric position of this microscope is arbitrarily fixed at an objective lens setting of 7.09. Ideally images were taken at this setting, but some were not, and thus a small but calibrated error was introduced, but grains sizes reported here were corrected for this error. Error in size measurement at the eucentric position was obtained by measuring identical grains at different magnifications and obtaining a mean size at each magnification. By comparing these mean sizes a relative error of ~7 % per measurement was calculated (Table 1.2).

Selected Area Electron Diffraction is obtained for grains by focusing the transmitted and diffracted beams on the back focal plane of the objective lens to form a spot or ring diffraction pattern. A ring pattern is obtained from polycrystalline materials while a spot pattern usually comes from a single crystal. The pattern is produced by constructive interference of diffracted beams from crystal planes in addition to the

**Table 1.2 Grain size error analysis**

| Plate 4554 | Plate 4556 | Plate 4614 | Plate 4613 |
|---|---|---|---|
| 250K | 500 K | 500 K | 250K |
| rms (nm) | rms (nm) | rms (nm) | rms (nm) |
| 24.63 | 27.73 | 26.84 | 29.22 |
| 24.23 | 22.8 | 26.87 | 29 |
| 23.84 | 22.86 | 27.31 | 28.97 |
| 23.96 | 22.73 | 27.29 | 28.78 |
| 24.36 | 22.8 | 27.86 | 29.13 |
| 24.36 | 22.67 | 26.16 | 29.09 |
| 24.36 | 22.93 | 26.6 | 29.35 |
| 24.63 | 22.67 | 26.66 | 29.61 |
| 24.49 | 22.8 | 27.11 | 29.66 |
| 24.49 | 22.86 | 26.09 | 29.25 |
| 24.38 | 22.73 | 27.13 | 29.51 |
| 24.36 | 22.81 | 27.08 | 29.51 |
| 24.75 | 22.86 | 26.59 | 29.76 |
| 24.35 | 22.8 | 26.97 | 28.94 |
| 24.35 | 22.73 | 26.85 | 29.51 |
| x = 24.35 | x = 22.79 | x = 26.89 | x = 29.29 |

(24.35-22.79) / 24.35 x 100 = 6.4%

(29.29- 26.89) / 29.29 x 100 = 7.3%

Relative error = (6.4 + 7.3)/ 2

**Relative error = 6.85%**

transmitted beam spot at the center of the pattern. The distance from a diffraction maximum or ring, R, to the transmitted beam spot can be measured directly from electron micrographs. These measurements can be processed using the equation,

$$d = \lambda L / R$$

where $\lambda L$ is the camera constant calculated by the wavelength of the electron beam ($\lambda$) multiplied by the camera length (L), and d is the interplanar spacing of the measured spot. A series of calculated d-spacings from a pattern can be checked against tables of d-spacings to determine the crystalline phase in question. SAED patterns from grains at 340,000 to 850,000 times magnification with an aperture of ~1 µm were taken to determine the amorphous (no diffraction maxima) or crystalline nature of the grains. Efforts were taken to obtain patterns from single grains when possible, but due to the very fine-grained nature whereby grains were smaller than the section thickness, and clustering of the condensates, most patterns were obtained for at least 5 to 10 grains (Figure 1.4). The error for polycrystalline (or "ring") electron diffraction patterns was obtained by measuring selected patterns twice, and then comparing the measurements. A relative error of up to ~ 6% was calculated (Table 1.3).

Chemical EDS analysis of the condensed grains used a 15 nm probe size, as measured from electron micrographs. An EDS detector measures the energy of continuum and characteristic x-rays given off by beam interaction with the sample. X-rays are counted to generate a spectrum on an attached CRT screen. This EDS detector has a beryllium window and is capable of measuring x-rays from elements with atomic number greater than 10. Magnifications of 400 to 850 K allowed for isolation of individual grains for analysis. A spot size of ~15 nm and counting times up to 200 seconds allowed for analysis of all but the smallest grains while still providing identifiable peak to background ratios. Because the samples qualify as thin foils, there is no absorption or x-ray fluorescence corrections (Figure 1.5), and I used the technique developed by Cliff and Lorimer (1975) which is:

$$I_a / I_b = k\,(C_a/C_b)$$

where $I_a$ and $I_b$ are the measured characteristic x-ray intensities or peak counts (minus continuum or background x-rays), and $C_a$ and $C_b$ are the weight concentrations of the elements in the sample. A *k*-factor is determined as a correction factor calculated from thin standards. In this study I have calculated compositions as weight percent of the oxides. Compositional peaks are statistically determined and tested for normality, range, mean, and standard deviation. Individual grains were analyzed at all possible times but "contamination" from ultrafine grains may occur because individual grain sizes are smaller than the sample thickness [cf. Fig. 1.4]. The relative error of individual analyses at the 95% confidence level is given by

$$\text{Error (\%)} = \pm \{[2(N_a)^{1/2} / N_a] + [2(N_b)^{1/2} / N_b]\} \times 100$$

where N is the number of x-ray counts for each element, a and b. When added to a typical *k*-factor error of ± 3% (Williams 1984), an error for $C_a/C_b$ is obtained, where C is the wt.% of each element. Thus, the error for each individual analysis in these samples is ~12% (Table 1.4).

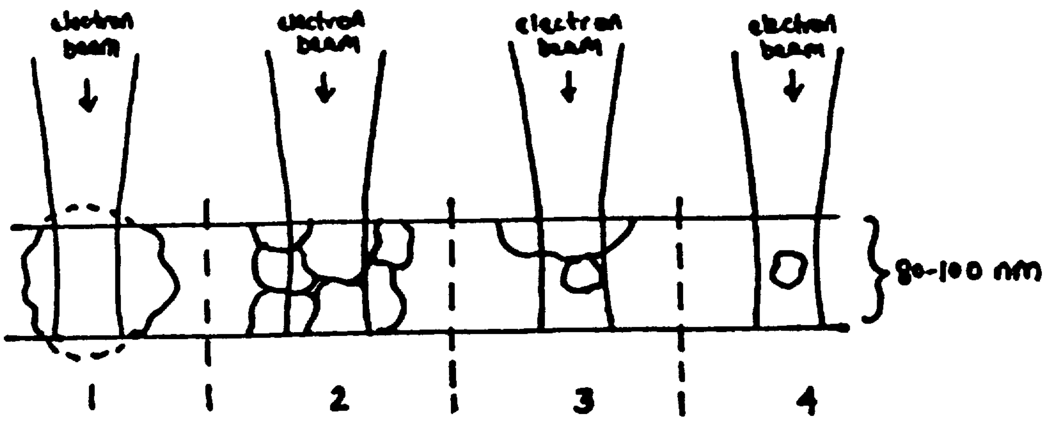

Figure 1.4. Schematic showing hypothetical sample configurations during EDS and electron diffraction analysis. 1) Single grain analysis in which the grain is larger than the sample thickness. 2) Analysis from several grains smaller than the sample thickness-a bulk analysis. Also, a bulk diffraction pattern in which diffracting grains are not identifiable. 3) Analysis of a single grain contaminated by underlying grain. 4) Analysis of a grain smaller than the sample thicknes

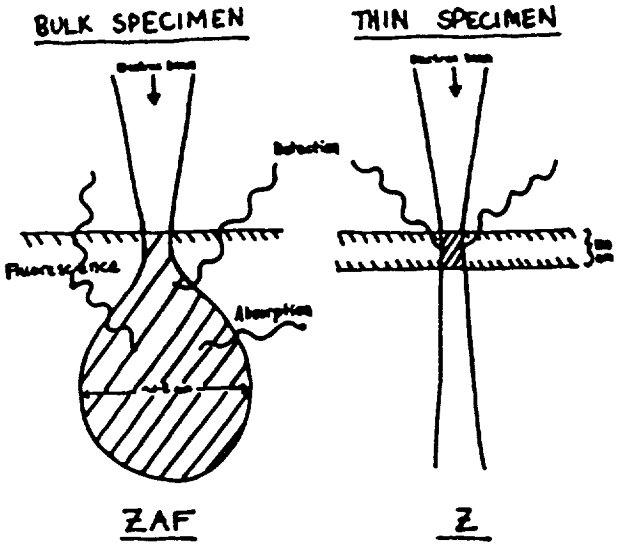

Figure 1.5. Schematic electron distribution in a bulk sample vs. a thin (~ 100 nm) specimen-i.e., foil. The probability of X-ray absorption or fluorescence is small in a thin specimen. Modified from Cliff and Lorimer (1975).

**Table 1.3 Diffraction pattern error analysis**

| Plate # | d= lL/R<br>d(nm)<br>1st measure | <br><br>2nd measure | % Error<br>(d1-d2)/ d1x100 |
|---|---|---|---|
| 0420 | 0.34 | 0.34 | |
| | 0.20 | 0.2 | |
| | 0.15 | 0.15 | |
| 0517 | 0.32 | 0.32 | |
| | 0.19 | 0.19 | |
| | 0.16 | 0.17 | ~5.8% |
| 0893 | 0.51 | 0.51 | |
| | 0.35 | 0.34 | ~2.9% |
| | 0.21 | 0.2 | ~4.8% |
| 1265 | 0.39 | 0.38 | |
| | 0.31 | 0.31 | |
| | 0.17 | 0.17 | |
| 0935 | 0.6 | 0.61 | ~2.6% |
| | 0.52 | 0.52 | |
| | 0.34 | 0.34 | |
| 1447 | 0.30 | 0.29 | ~3.3 |
| | 0.22 | 0.21 | ~4.5 |
| | 0.14 | 0.14 | |

**Table 1.4. EDS error analysis**

| analysis # | Si counts | Fe counts | 95% confidence error |
|---|---|---|---|
| 2 | 24054 | 0 | 1.2 |
| 3 | 12055 | 0 | 1.8 |
| 180 | 14605 | 0 | 1.7 |
| 182 | 6344 | 0 | 2.5 |
| 190 | 1017 | 281 | 18 |
| 191 | 323 | 87 | 33 |
| 192 | 1253 | 235 | 19 |
| 193 | 1226 | 278 | 18 |
| 194 | 1263 | 725 | 13 |
| 195 | 2077 | 1385 | 9.8 |
| 196 | 1991 | 1174 | 10 |
| 197 | 1527 | 1014 | 11 |
| 198 | 2388 | 1486 | 9.3 |
| 199 | 1821 | 1266 | 10 |
| 200 | 2396 | 1710 | 8.9 |
| 201 | 1671 | 1122 | 11 |
| 207 | 4208 | 2434 | 7.1 |
| 208 | 2453 | 1297 | 9.6 |
| 209 | 3880 | 2211 | 7.5 |
| 210 | 922 | 383 | 17 |
| 211 | 2682 | 1757 | 8.6 |
| 212 | 1493 | 656 | 13 |
| 213 | 1151 | 793 | 13 |
| 214 | 2364 | 1009 | 10 |
| 215 | 3831 | 2797 | 5.4 |
| 216 | 2660 | 2351 | 8 |
| 217 | 4570 | 3712 | 6.2 |
| 218 | 3023 | 2748 | 7.4 |
| 219 | 2313 | 1319 | 9.7 |
| 220 | 2900 | 2146 | 8 |
| 221 | 4167 | 3296 | 6.6 |
| 222 | 4513 | 3491 | 6.4 |
| 170 | 7530 | 116 | 21 |
| 171 | 8090 | 0 | 2.2 |
| 172 | 2352 | 2588 | 7.4 |
| 173 | 5678 | 3467 | 6.1 |
| 174 | 3437 | 2110 | 7.8 |
| 175 | 1348 | 755 | 13 |
| 176 | 3952 | 4478 | 6.2 |
| 177 | 2760 | 3058 | 7.4 |
| 151 | 12660 | 0 | 1.8 |
| 152 | 11342 | 0 | 1.9 |
| 153 | 12551 | 0 | 1.8 |
| 154 | 6453 | 0 | 2.5 |
| 155 | 5309 | 2861 | 6.5 |
| 156 | 6457 | 3095 | 6.1 |
| 157 | 3557 | 1713 | 8.2 |
| 158 | 1988 | 1458 | 8.3 |
| 159 | 4220 | 2776 | 6.9 |
| 160 | 4110 | 2291 | 7.3 |
|  |  |  | x = ± 8.88% |

Total relative error = k-factor error + counting stat error

Total Relative error = 3.3% + 8.88%

Total Relative error = ± 12%

## 1.7 MISCELLANEOUS

The TEM micrographs in the following chapters show condensate grains contained in a gray matrix material, which is the epoxy of the thin sections. The holey carbon film substrate that supports the thin sections is also visible in some micrographs. I will be as clear as possible in identifying the substrate when necessary.

Contrast differences in the micrographs whereby grains appear darker than other lighter grains may result from ( I ) some grains being composed of more material, such as clustered grains (thickness effects), ( II ) crystalline grains, having a more dense structure than amorphous grains of the same composition and thickness ( III ) crystalline grains in the optimum diffracting condition (Bragg condition), or 4) grains composed of elements with high Z (atomic number). When contrast differences are apparent in the micrographs I will explain the results with reference to these choices.

I use the terms "strong" and "weak" to describe diffraction maxima in the text and in the SAED patterns accompanying TEM images. These terms are relative to one another and describe the intensity of the maxima. "Weak" maxima may be the result of very small crystalline grains, while "strong" maxima may be due either to larger crystalline grains (more diffracting mass), or single-crystal grains. I also note that diffraction maxima presented for any particular grain type are a compilation of maxima measured from several polycrystalline SAED patterns of the same grain type. Single-crystal diffraction patterns are identified as such when shown.

# CHAPTER 2. CONDENSATION AND SILICATE DUST ANALOGS

## 2.1 INTRODUCTION

Theoretical and experimental evidence indicate that the nucleation and growth of solid grains from the vapor is a kinetically controlled process (Donn, 1979; Donn et al., 1981). Therefore, equilibrium thermodynamics can neither predict the size, shape, structure of condensed grains, nor metastable equilibrium phases among small (< 1 *um*) grains formed by vapor phase condensation (Stephens and Kothari, 1978). This chapter assesses the nucleation and growth theory of condensate grains and their properties; as such it provides the reader with a basic understanding of the descriptions and discussions of silicate dust analogs that will follow in subsequent chapters.

## 2.2 NUCLEATION AND GROWTH

The first grains to homogeneously nucleate from a gas should be approximately 1 nm in diameter (Abraham, 1974; Doremus, 1985). Salpeter (1974) calculates a similar "critical size" for nucleation of solid grains in stellar atmospheres, but predicts that these first grains are seed nuclei for further surface nucleation and thus final grain sizes will be approximately 30 nm in diameter. This size is consistent with previous studies of condensates, but is somewhat smaller than grains found in natural samples [cf. Table 1.1]. Nucleated grains grow by two processes (Stephens and Kothari, 1978) including 1) collisional growth of the ~ 1nm grains, and 2) monomeric addition of gas molecules to spatially seperated nuclei. While the condensation event probably involves both processes, it is postulated that dominant collisional growth produces chains of submicron grains (Stephens and Kothari, 1978). Silicate dust analogs in these experiments consistently show submicron grains in chains, chain-like, or necklace-like morphologies.

Principle growth forms of condensate grains are due to the relative supersaturations of the gas phases and can be described qualitatively. Low supersaturations combined with a substrate leads to whisker growth. At high supersaturations many nuclei are produced and crystals can be produced by three dimensional growth. This type of growth form is called a powder. Intermediate supersaturation is characterized by two-dimensional growth of platey grains. Silicate dust analogs are essentially powders, but there is some indication of platey grains [cf. Table 1.1], which indicate high to intermediate supersaturations of the vapor phases.

## 2.3 OSTWALD RIPENING

Individual grains of silicate dust analogs are in the range of ~ 5 nm up to 200 nm, and up to 400 nm in clusters and globules [cf. Table 1.1]. An average size is on the order of 100 nm. Size distributions of dust analogs tend to show log-normal distributions (Rietmeijer and Nuth, 1991; Rietmeijer and Nuth, 1988). A log-normal size distribution is consistent with a ripening and coalescence growth termed Ostwald ripening. Ostwald ripening is characterized by the simultaneous growth and dissolution of grains (Baronett, 1984). The tendency is to minimize the high surface free energy of small grains by dissolving them and growing larger grains.

## 2.4 STRUCTURE

The experiments on vapor phase condensation in the 60s, 70s and early 80s produced amorphous grains (Stephens and Kothari, 1978; Nuth and Donn, 1983; Donn et al., 1981; Lefevre, 1969; Kamijo et al., 1975). Crystalline silicates were only produced after thermal annealing of the original condensates. Later studies using electron microscopy revealed an "incipient crystalline nature" of condensed silicate dust analogs (Rietmeijer et al., 1986) as evidenced by electron diffraction. This incipient crystallinity could have been overlooked in previous studies, and it is undetectable when analysis techniques such as IR spectroscopy and XRD are used. Rietmeijer et al., (1986) used analytical electron microscopy to characterize Mg-Si-O condensates that had previously been studied by IR and XRD, and concluded that AEM should be the primary tool to detect budding crystallinity in vapor phase condensates. In a later study of a different binary system (Fe-Si-O), Rietmeijer and Nuth (1991) explained a high abundance of crystalline grains by autoannealing, whereby condensed grains convert high thermal and surface energies to structural ordering.

The condensed grains in this silicate dust analog study often show structural ordering, i.e.-crystallinity, as evidenced by electron diffraction maxima and high-resolution TEM images of lattice fringes. The SAED patterns are usually composed of "weak" maxima that correspond to interplanar spacings (*d*-spacings) of high-index planes (high *hkl* Miller indices) in minerals. Diffraction maxima matching low-index plane *d*-spacings are usually not present. This could be consistent with a theory that continued crystal growth allows for the development of low-index planes and implies "improved crystallinity" in the grains (Kraus,1985). While electron diffraction data and lattice fringes do not allow for definitive mineral identifications, they are evidence for crystalline domains within the smokes.

*Identification of mineral phases in this study* is made by combining SAED data and lattice fringe imaging in conjunction with the chemical compositions of the grains. The identifications of mineral phases may not always correlate with the stoichiometric chemical composition of the grains, which may be due to one or more of the possible configurations in Figure 1.5 during analysis. As an example I note the identification of "tridymite" diffraction from grains with compositions that include 12-60 wt.% FeO (Rietmeijer and Nuth, 1991). The diffracting grains in this work were nanometer sized crystallites of tridymite contained within larger grains, that is a mixture of $SiO_2$, FeSiO or FeO in some proportion with pure tridymite domains or grains. Also, tridymite can take some foreign cations into its structure. I stress it is not always possible to unambiguously identify crystalline grains in diffraction patterns that contain information on several grains. Also it is not always possible to identify "inclusion" grains (Figure 1.5) that may be the diffracting (crystalline) material. Thus, mineral identification in the nanometer smoke size particles requires a balanced judgement , and I will be as clear as possible in descriptions of defining how and why certain identifications are made.

## 2.5 METASTABLE PHASES

Building on the discussion of mineral phases I note the observation of metastable phases forming in vapor phase condensates. Nuth and Donn (1982) produced the metastable phase $Si_2O_3$ from a Si-O gas and Rietmeijer and Nuth (1991) found the high temperature $SiO_2$ polymorph tridymite in an FeSiO condensate. The presence of high temperature and/or high pressure phases forming outside their stability fields can be explained using the Ostwald Step Rule (Figure 2.1). This rule states that in any transformation or reaction the kinetically most favorable sequence of phases will form rather than those involving the greatest reduction in free energy (Putnis and McConnell, 1980). I refer to the example of tridymite forming from a silica glass. The glass is in a metastable state and the transformation to the stable form of quartz would constitute the greatest reduction in free energy, but this transformation would require a large activation energy. It requires a lesser activation energy and is therefore "easier" for the glass to crystallize into a tridymite phase first. It should be noted that the high surface free energy of the uniquely nanometer sized grains in this study make an important contribution to the free energy of the parent phase. The implication could be that either metastable phases or assemblages may persist because the high surface energies are a barrier to reaction towards equilibrium. Therefore, metastable minerals and assemblages that could form outside their fields can be present in vapor phase condensates. For example, in my samples I identify metastable phases such as tridymite, cristobalite, and sillimanite, and metastable mineral assemblages such as olivine together with a silica phase.

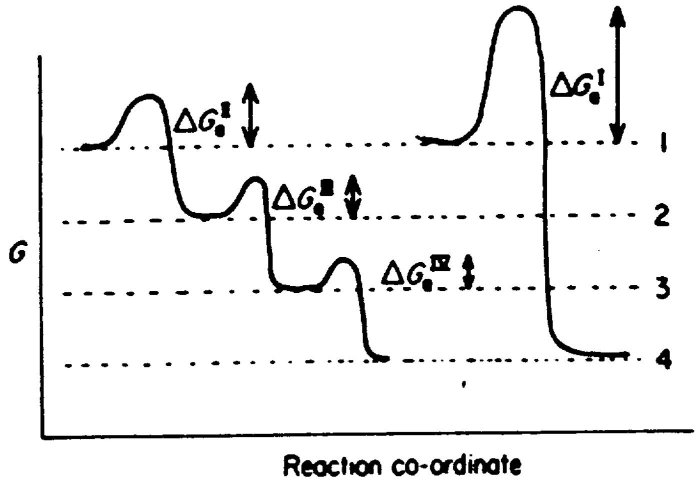

**Figure 2.1** Illustration of the Ostwald step rule where G = Gibb's free energy. The direct transformation from 1-4 involves a large activation energy (ΔG1) and may be slow. Transformations by a sequence of steps involving smaller activation energies may be more favorable. (Taken from Putnis and McConnell, 1980).

# CHAPTER 3. ISOTHERMAL ANNEALING OF AN Fe-Si-O SMOKE

* Parts of this chapter were presented as a poster at the 27th Lunar and Planetary Science Conference: Karner J.M., and Rietmeijer F.J.M. (1996) A first result of isothermal annealing of an FeSiO smoke. *Lunar and Planet. Sci. Conf. XXVII,* 647-648.

## 3.1 INTRODUCTION AND SAMPLE PREPARATION

This chapter reports data from an Fe-SiO condensate thermally annealed *in vacuo* at 727 °C for 4 hours. The original condensate, (Rietmeijer and Nuth, 1991), was produced in a condensation flow apparatus [cf. Figure 1.1] from a mixture of $SiH_4$, $Fe(CO)_5$, and $O_2$ in $H_2$ at a nominal temperature of 727 °C. The $Fe(CO)_5$ and $SiH_4$ were premixed in $H_2$ before entering the the furnace, while $O_2$ was added separately using a tube entering the center of the reaction chamber. Condensation occurs as the cool gas stream exits the furnace into a chamber kept at 25 °C. The temperature at which the smoke actually forms is not well defined because the mixture either reacts at the moment of entry in the furnace or well after it emerges from the high-temperature zone of the experiment (Rietmeijer and Nuth, 1991). Ultrathin sections of the annealed sample were prepared [cf. Section 1.6]. Grain sizes are reported as the longest diameter and not rms size [cf. Section 1.6] for better comparison with sizes reported for the original condensate grains by (Rietmeijer and Nuth, 1991). Iron was calculated as FeO but it is more likely ferric iron,- i.e. $Fe_2O_3$, because maghemite was found during condensation and/or autoannealing [cf. Rietmiejer and Nuth, 1991].

## 3.2 OBSERVATIONS

The annealed sample has a texture of small (< 70nm) isolated grains, contained in chains and clusters (Figure 3.1) as well as (rare) larger grains up to 285 nm. The compositions for 227 individual grains are presented in Figure 3.2. The compositions show normal distributions with means at 0, 9, and 27 wt.% FeO determined at a 90% confidence limit (Table 3.1). The grains are mostly amorphous, but some crystalline domains are present as indicated by weak diffraction maxima, shown in Table 3.2. The sample is described by four distinct mineralogical, chemical, and morphological groups:

**Ia. (Rare) Pure (100 wt.%) $SiO_2$ round droplet shaped grains** (Figure 3.3) range from 131 nm to 285 nm in diameter and typically have a smooth surface texture. Diffraction patterns from these grains either showed no diffraction maxima, or diffuse halos, which are both consistent with amorphous materials.

**Ib. 97-99 wt.% $SiO_2$ nonspherical grains** are 18- 90 nm in longest dimension, (aspect ratios ~ 0.75) and have irregular outlines resulting from coagulation of individual grains (Figure 3.4). Their combined electron diffraction data and chemistry are consistent with tridymite (Table 3.2). Small (~6 nm) round opaque domains are dispersed within these grains and correspond with probed areas that show 1-3 wt.% FeO.

**Table 3.1 Comparison of original and annealed FeSiO smokes. Abbreviations: N= observations, R= range, sd= standard deviation.**

| | **Unannealed smoke [Rietmeijer and Nuth,1991]** | **Annealed smoke at 727 °C for 4 hrs. [this report]** |
|---|---|---|
| **General morphology** | Highly porous texture with grains <100 nm but up to 450 nm in clusters and globules | Porous morphology with grains <100 nm but up to 285 nm in smooth round, droplet grains |
| **Chemical distributions** | Trimodal with peaks at zero wt.%,<br>27.5 (range 12-60%) and<br>87.5 FeO wt.% | Trimodal with peaks at zero wt.%, 9 (N=32, R= 4-18%, sd= 3.31) and 27 (N=141, R= 19-43%, sd=5.9) FeO wt.% |
| **Morphological and chemical groupings** | 1) pure tridymite grains w/ simple and polysynthetic twinning<br>2) High-Fe silica grains (12-60 wt.% FeO) include rare dumbbell shaped grains<br>3) Maghemite grains +/- a mantle of amorphous silica | 1) pure silica droplet shaped grains<br>2) 97-99 wt.% $SiO_2$ non-spherical silica grains<br>3) 4-14 wt.% FeO silica grains<br>4) 15-43 wt.% FeO silica grains |
| **Crystallographic properties** | Fringes and patterns matching tridymite in pure silica grains and high Fe silica grains. Fringes and patterns match maghemite in "Very-high Fe" silica grains | Diffraction patterns match tridymite for pure silica, irregular edged grains and 4-43 wt.% FeO silica grains |
| **Grain size distributions** | 1) Silica grains show log-normal distribution<br>2) High-Fe silica grains show poor fit to a log-normal distribution<br>3) Maghemite grains range from 41 to 65 nm. Skewed distribution with mean of 38 nm and mode of 45 nm | 1) Nonspherical silica grains show a log normal distribution<br>2) Pure silica droplet grains range from 131 nm to 285 nm with mean size of 202 nm<br>3) 4-43 wt.% FeO silica grains show a log-normal distribution |

Table 3.2 Diffraction interplanar spacings (nm) observed in FeSiO 1k/4h sample and interplanar spacings for silicate minerals that are possible in the FeSiO system from the JCPDS XRD files

| | | 0-5 wt.% FeO grains | 5-43 wt.% FeO grains | Tridymite ($SiO_2$) 14-260 | Fayalite ($Fe_2SiO_4$) 34-178 | Ortho-Ferrosilite ($FeSiO_3$) 29-721 | Clino-Ferrosilite ($FeSiO_3$) 17-548 | Maghemite ($\gamma$-$Fe_2O_3$) 25-1402 | |
|---|---|---|---|---|---|---|---|---|---|
| | | | | | | 0.904 | | | |
| | | | | | | | | 0.791 | |
| | | | | | | | | 0.694 | |
| | | | | | | 0.646 | 0.646 | | |
| | | | | | | | | 0.59 | |
| | | | | 0.543 | | | | | |
| | | | | | | | | 0.533 | |
| | | | | | 0.524 | | | | |
| | | | 0.51 | | | | | | |
| | | | | | | | | 0.482 | |
| | | | | | | 0.461 | 0.461 | | |
| | | | | 0.437-0.433 | 0.438 | | | | |
| | | | | 0.427 | | | | 0.429 | |
| | | | | 0.412-0.41 | | | | | |
| | | | | 0.408-0.40 | | | | | |
| | | | | | 0.397 | | | | |
| | | | | 0.387-0.38 | | | | | |
| | | | | | 0.378 | | | 0.373 | |
| | | | | 0.361 | | | | | |
| | | | | | 0.355 | | | | |
| | | | | 0.343-0.34 | | 0.343 | | 0.34 | |
| | | | | 0.337-0.33 | | | 0.335 | | |
| | | 0.32 | 0.32 | 0.328-0.323 | | 0.323 | 0.323 | 0.32 | |
| | | | | 0.316 | | | | | |
| | | | | 0.307 | 0.306-0.304 | 0.3 | 0.303 | | |
| | | | | 0.3-0.298 | | | | | |
| | | | | 0.295 | | 0.291 | 0.291 | 0.295 | |
| | | | | | 0.283 | 0.286 | | | |
| | | 0.27 | 0.27 | 0.276 | | 0.275 | | 0.278 | |
| | | | | | 0.263-0.26 | | 0.26 | 0.264 | |
| | | | | 0.259 | 0.257-0.25 | 0.259 | | 0.251 | |
| | | 0.24 | | 0.249-0.245 | 0.241 | 0.241 | 0.248 | 0.241 | |
| | | | | 0.233-.23 | 0.235-0.23 | 0.23 | | 0.232 | |
| | | | | | | 0.227 | | 0.223 | |
| | | | | | 0.219-0.215 | 0.216 | 0.216 | | |
| | | 0.21 | 0.21 | 0.213-0.209 | | | | 0.21 | |

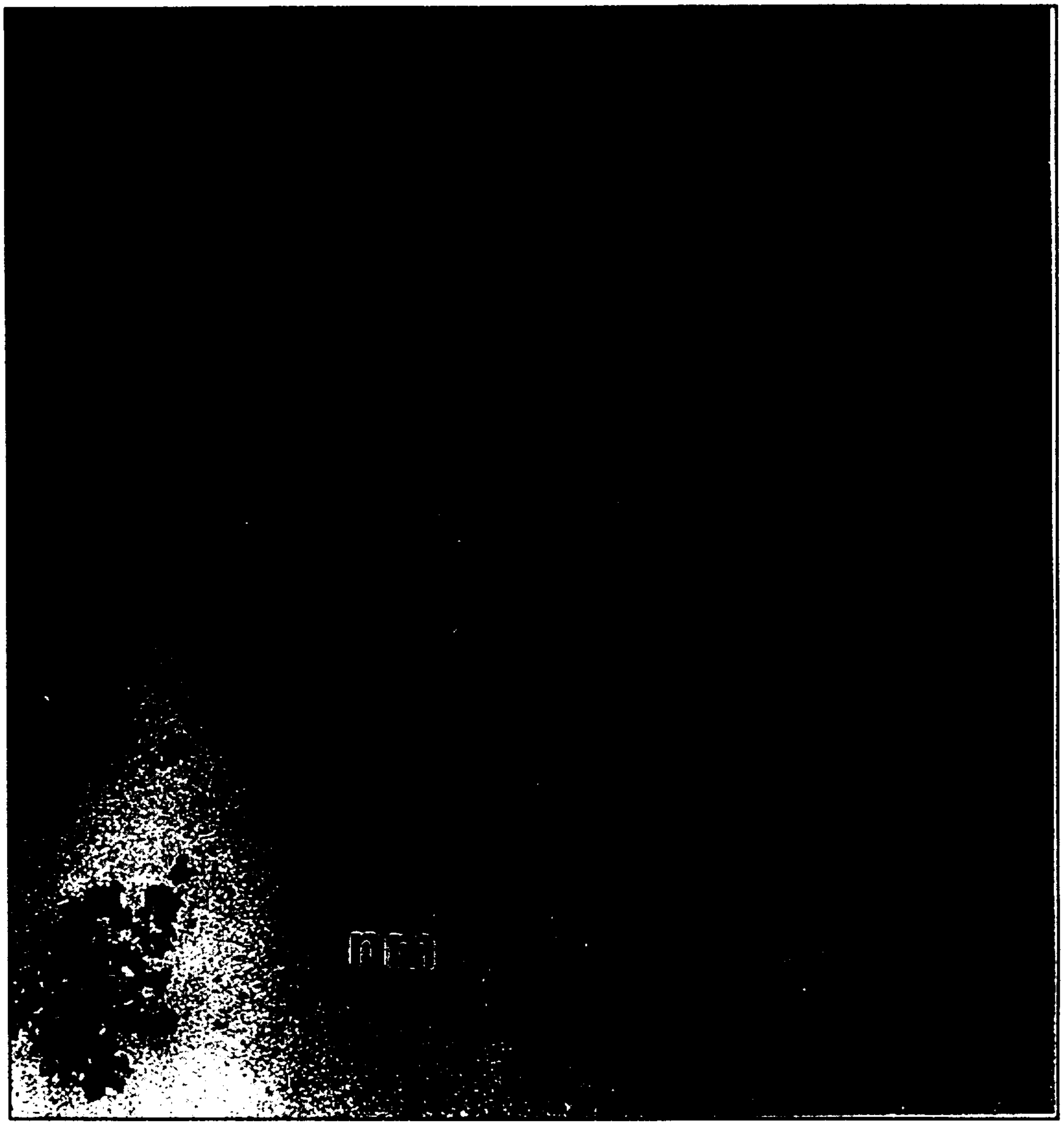

**Figure 3.1** Transmission electron micrograph of grains in chains and clusters in the annealed FeSiO sample. Two types of grains are apparent by their differing contrasts. The darker grains (left side of image) contain more clustered grains and/or higher FeO contents than the lighter grains (right side of diagram.

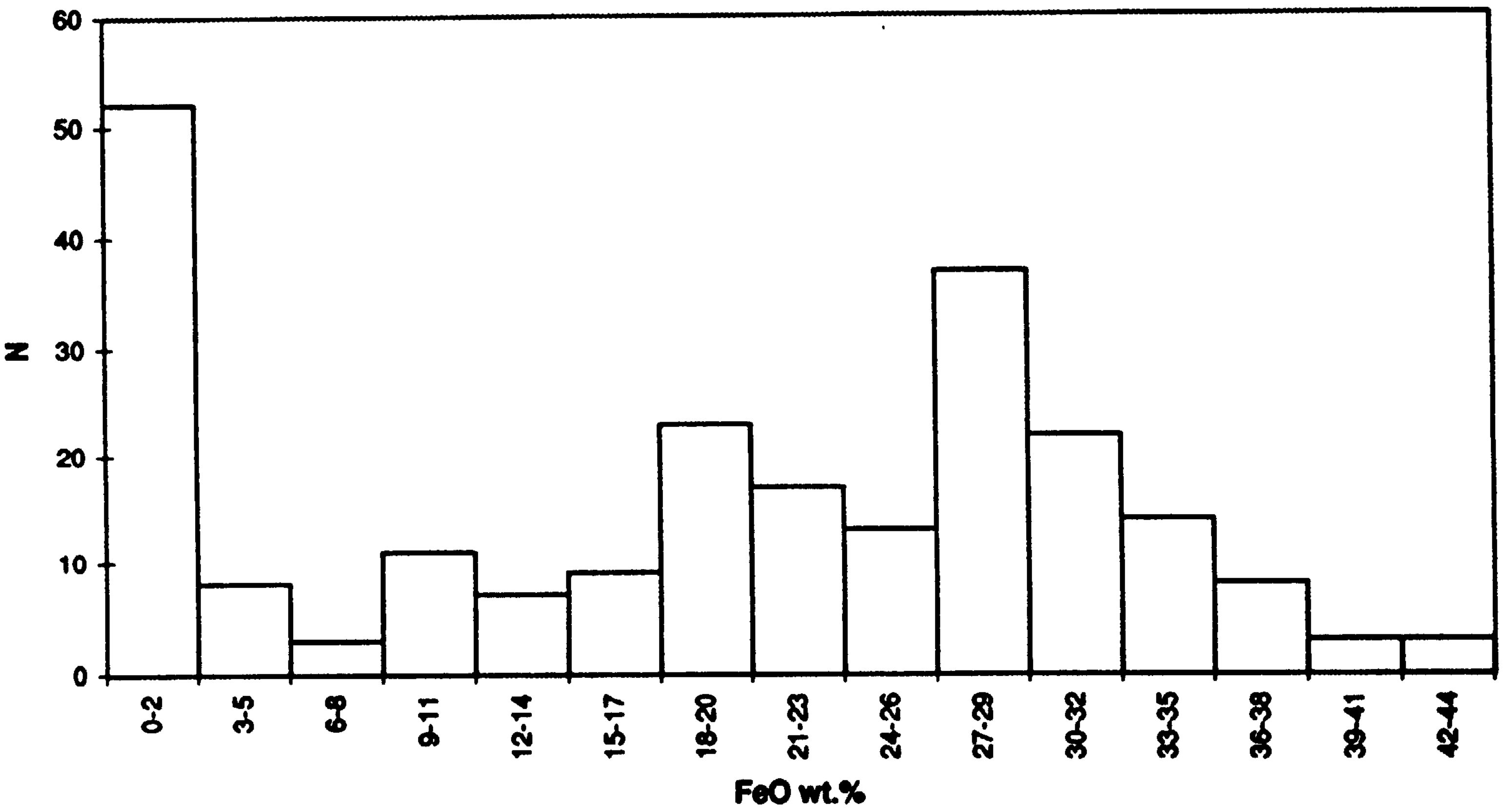

Figure 3.2 Histogram showing the FeO (wt.%) distribution for grains in the annealed FeSiO sample.

**Figure 3.3** Transmission electron micrograph of pure silica round, droplet shaped grains.

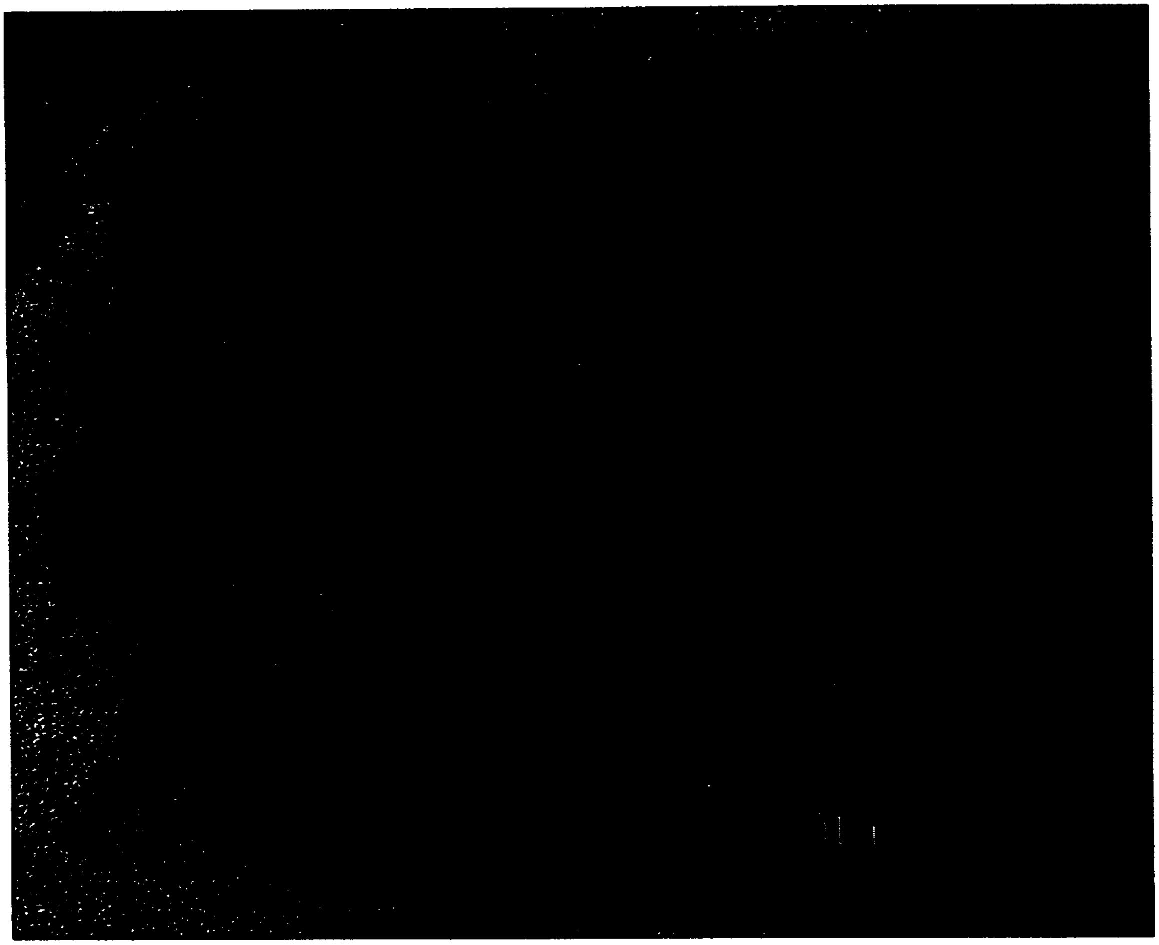

**Figure 3.4** Transmission electron micrograph of 97-99 wt.% $SiO_2$ nonspherical grains with small opaque domains.

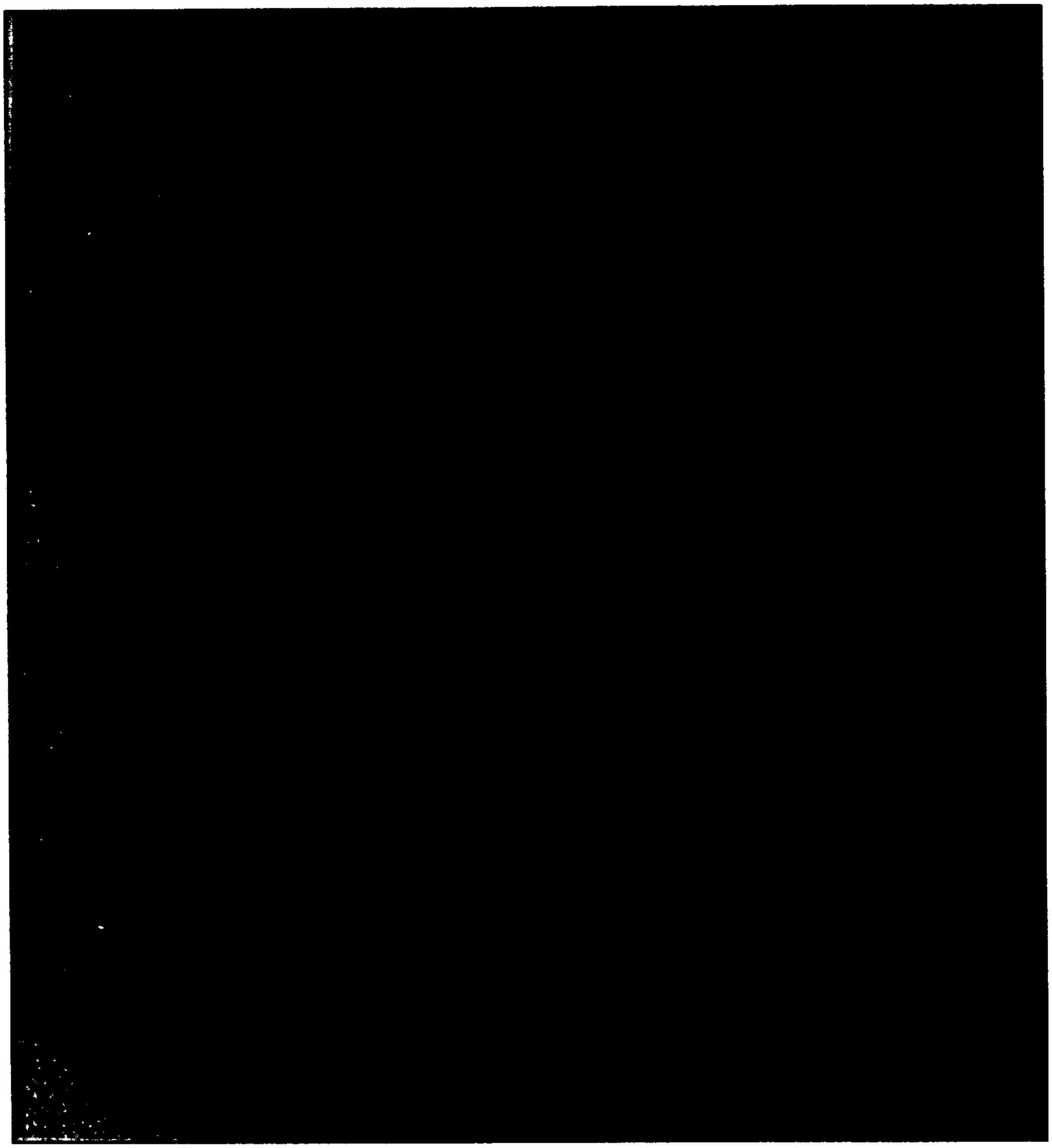

**Figure 3.5** Transmission electron micrograph of 4-14 wt.% FeO silica grains contained within branching chain-like morphologies. The darker grains are probably crystalline and in the optimum Bragg condition.

**II. 4-14 wt.% FeO silica grains** are circular to subcircular in shape, have a smooth texture, and were contained in clusters or chains of several grains (Figure 3.5). Individual grains are 5 nm to 17 nm in diameter. Combined with their compositions, the SAED patterns show maxima consistent with tridymite (Table 3.2). These grains make up the "9 wt.% FeO" population.

**III. 15-43 wt.% FeO silica grains** are subcircular to elongate in shape (aspect ratio ~ 0.7) and range in size from 4 nm to 27 nm. These grains are much "darker" during bright-field TEM imaging than the 4-14 wt.% FeO grains, and make up the "27 wt.% FeO" population. The grains are found to be isolated or in small chains, as well as in dense clusters wherein individual grains are fused together. Figure 3.6 shows 15-43 wt.% FeO grains clustered together in a silica rich matrix, wherein a mottled texture is apparent. Their SAED patterns show strong diffraction maxima that could support the presence of tridymite, fayalite ($Fe_2SiO_4$), and maghemite ($Fe_2O_3$) (Table 3.2).

**Grain size distributions.** 222 individual grains with 4-43 wt.% FeO show a log-normal size distribution ($R^2 = 0.98$) for grains ranging from 4 nm to 27 nm (Figure 3.7). The mean size of these grains is 13 nm. Similarly, 45 nonspherical silica grains from 18 - 90 nm show a log-normal distribution ($R^2 = 0.97$). These grains have an average size of 35 nm (Figure 3.8).

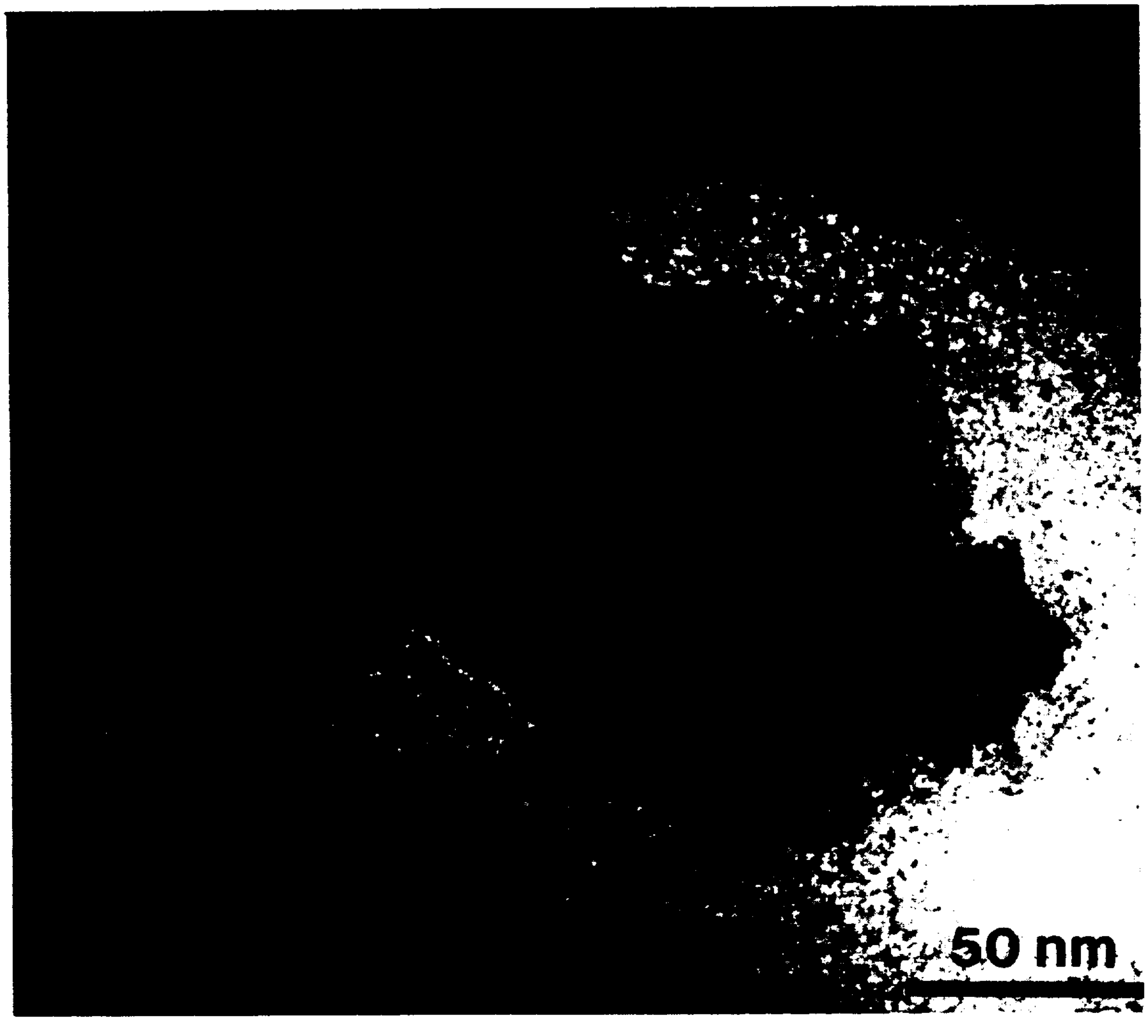

**Figure 3.6** Transmission electron micrograph of a cluster of dark 15-43 wt.% FeO grains in a silica rich matrix. The mottled texture could be due to subsolidus phase decomposition.

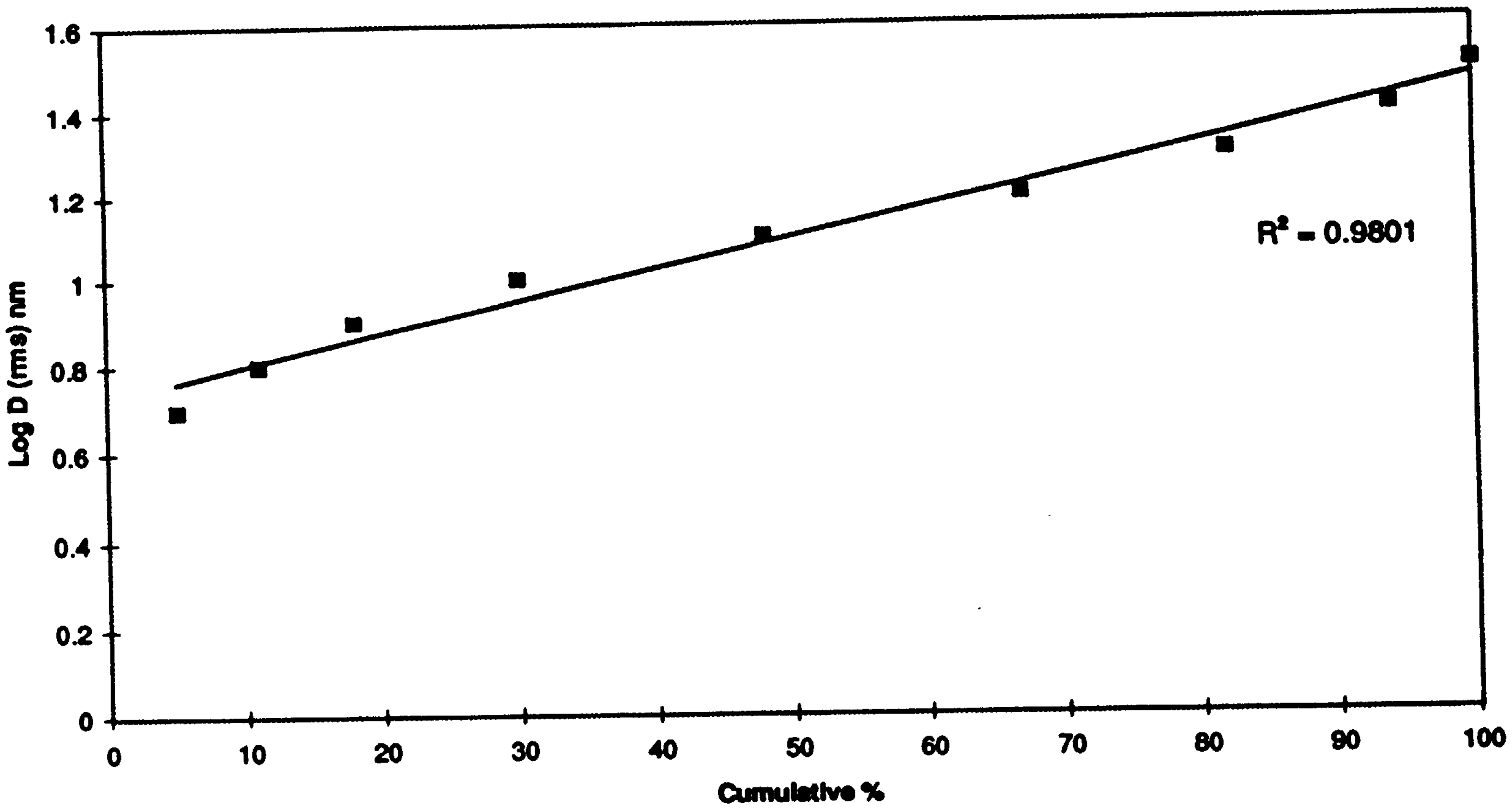

**Figure 3.7** Log D (size) distribution for 222 individual 4-43 wt.% FeO grains showing a good fit to a log-normal distribution.

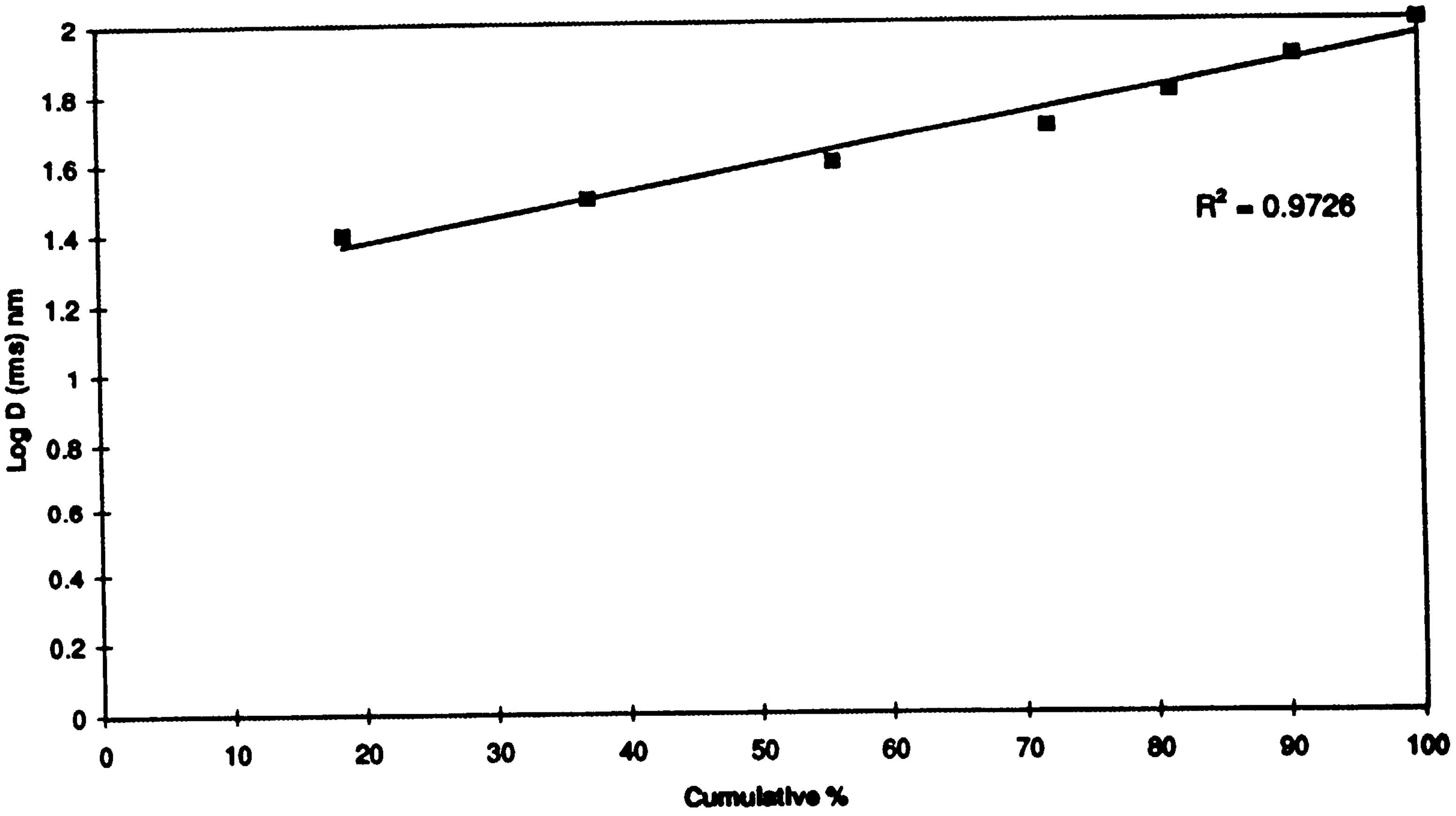

Figure 3.8 Log D (size) distribution for 45 nonspherical silica grains showing a good fit to a log-normal distribution.

## 3.3 DISCUSSION

In 1991 Rietmeijer and Nuth analyzed the unannealed FeSiO condensate using transmission electron microscopy. Comparisons between the unannealed and annealed samples are summarized in Table 3.2 (Karner and Rietmeijer, 1996). The condensed material was consistent with a highly porous, or fluffy morphology of grains less than 100 nm in size. Locally the sample contained pure silica globules and clusters up to 450 nm in diameter. In a plot of chemical distribution for individual grains Rietmeijer and Nuth (1991) found a trimodal distribution with peaks at 0, 27.5, and 87.5 wt.% FeO. A clear gap in their distribution occurs between 45 and 75 wt.% FeO, which includes the stoichiometric fayalite and ferrosillite compositions. Crystalline grains of tridymite ($SiO_2$) and large (sub)-spherical globules showing simple and polysynthetic twinning were identified in the condensate along with single crystal grains of maghemite ($\gamma$- $Fe_2O_3$). Grains ranging from 12-60 wt.% FeO showed polycrystalline diffraction patterns and small areas of lattice fringes consistent with tridymite.

The annealed sample is similar to the original smoke in overall morphology, and the presence of clusters and globules. The annealed sample uniquely contains pure silica round, droplet shaped grains. Both the original smoke and annealed sample show trimodal distributions for the compositions of individual grains (Table 3.1). The grains with FeO from 4-43 wt.% in the annealed sample actually include two distinct populations at 9 and 27 wt.% FeO. The population of grains at 9 wt.% FeO was not reported in the unannealed condensate, and is distinctly different in morphology than other FeO-silica grains in the annealed sample. I did not locate the grains with highest FeO contents in the annealed sample, which were identified as maghemite in the unannealed sample. The absence of these grains could be attributed to a sampling size problem, whereby high-iron grains are not present in selected ultrathin sections due to sample heterogeneity. The grains in the annealed sample are mostly amorphous but electron diffraction data show evidence for some crystalline domains. I identify tridymite in the 97-99 wt.% $SiO_2$ and 4-43 wt.% FeO grains from its diffraction data. Its presence here is consistent with the original condensate. The 4-43 wt.% FeO grains may also contain fayalite, and/or maghemite.

Both samples show log-normal size distributions for silica grains (< 3 wt.% FeO) and high-Fe silica grains with similar size ranges in both samples. A log-normal distribution supports the theory that grains coarsened by converting small grains into larger ones. The high-Fe silica grains (12-60 wt.% FeO) in the original sample were larger than those in the annealed sample; viz. maximum size ~120 nm and mean of 47 nm compared to a maximum of 27 nm and a mean of 13 nm. These differences may point to a heterogeneity of grain growth in the vapor phase (on a nanometer scale) that produces grains differing in size, but with similar compositions.

In the original smoke a high abundance of crystalline material was explained as post-condensation transformation, or autoannealing (Rietmeijer and Nuth, 1991). I do not find a similarly high abundance of crystalline material in the annealed sample. For example, the original smoke contained large (sub)-spherical grains of chemically pure tridymite (Figure 3.9) that formed by coagulation of smaller droplets and vitrification during autoannealing. Tridymite is the stable silica polymorph between 870-1470 $^0$C .

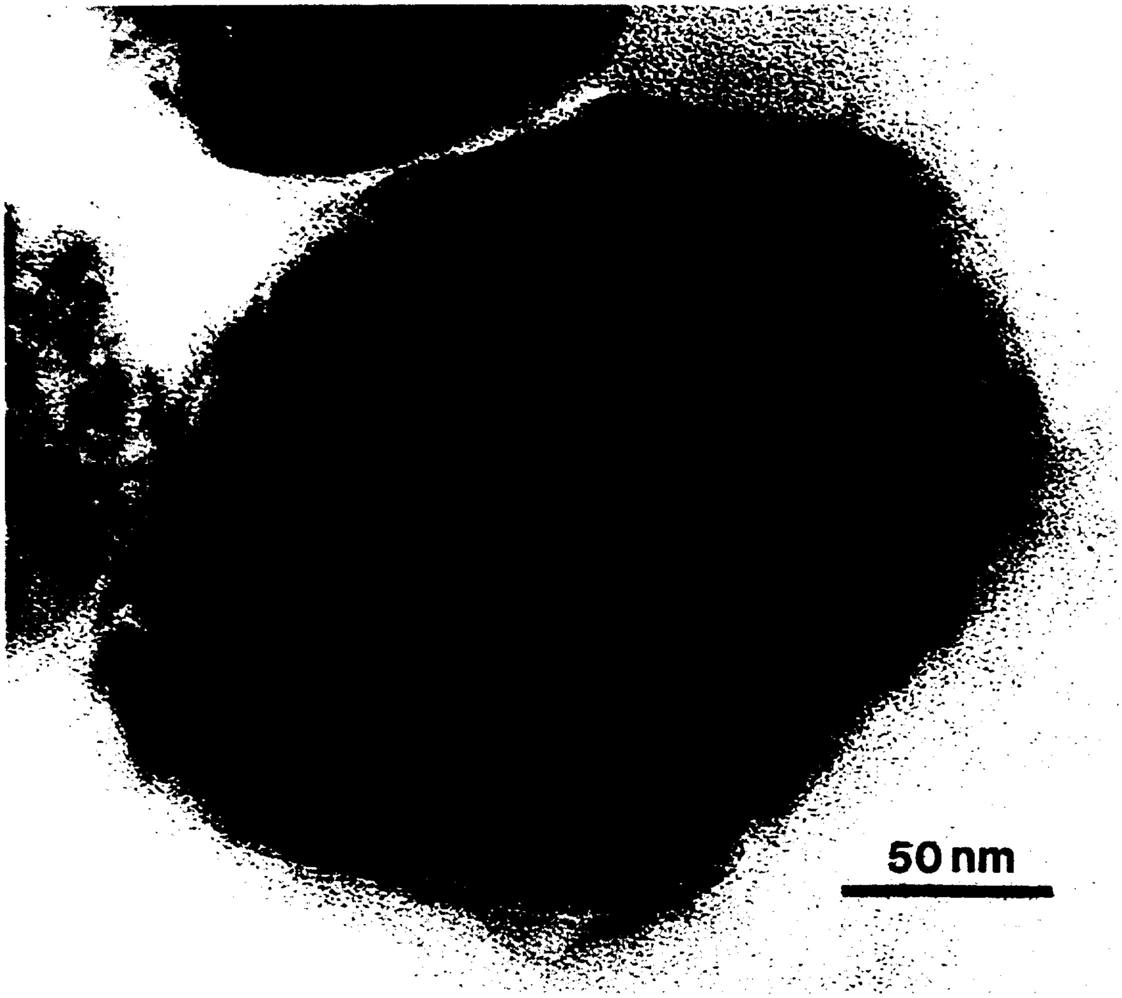

**Figure 3.9** Transmission electron micrograph of a large sub-spherical tridymite globule showing lattice fringes and polysynthetic twinning from the unnannealed FeSiO sample (From Rietmeijer, unpublished data).

Isothermal annealing at 727 °C raised these grains above the metastable extension of the liquidus and induced fusion (vitrification) but without melting *proper*. These condensed and coagulated grains transformed into the pure silica, smooth droplet-shaped grains in the annealed sample (Figure 3.3).

The mottled texture of high-Fe silica grains (27.5 wt.% FeO population) in the original smoke was explained as the result of possible spinodal decomposition by autoannealing into a maghemite-like phase and a low-Fe silica material (Rietmeijer and Nuth, 1991). In the annealed sample the 15-43 wt.% FeO grains show a similar decomposition texture and could have a similar origin. The "opaque" domains in the annealed nonspherical silica grains contribute a 1-3 wt.% FeO signal when probed. The nature of these Fe grains remains undetermined, but unlike the 15-43 wt.% FeO grains they may be Fe inclusions that predate silica condensation, and do not reflect post-condensation processes such as decomposition.

The equilibrium phase diagram $Fe_3O_4$-$SiO_2$ (Muan, 1957) (Figure 3.10) has a eutectic between the two liquid and cristobalite - liquid fields at ~ 5 wt.% $Fe_2O_3$. According to this equilibrium phase diagram isothermal annealing of this quenched condensate composition at ~9 wt.% FeO (Table 3.1) might decompose into tridymite and Fe-oxide. The compositional peak at ~ 27 wt.% FeO is puzzling because the phase diagram does not predict a mixed $Fe_3O_4$-$SiO_2$ here.

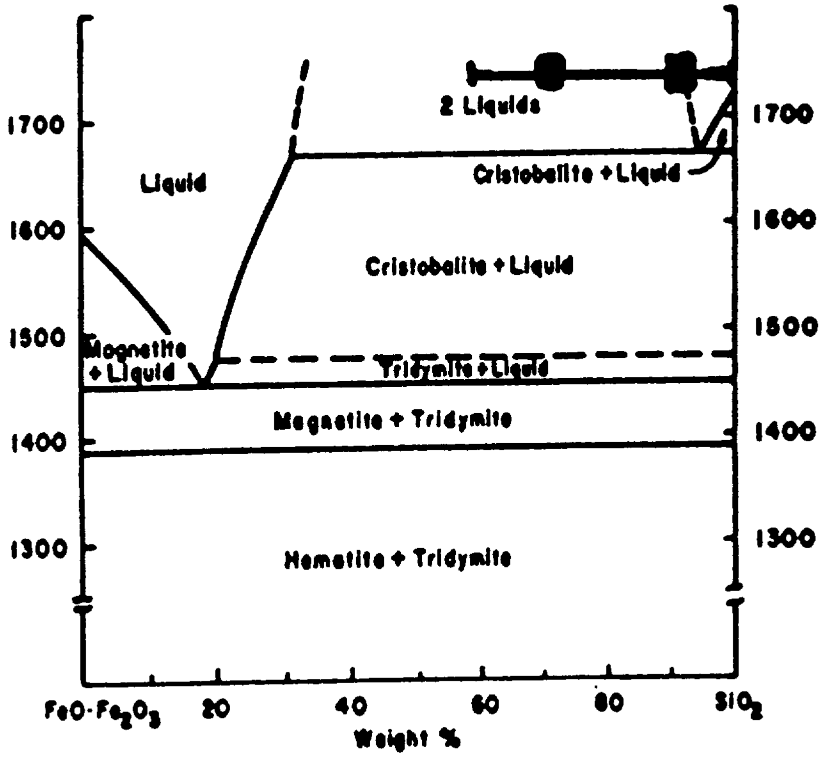

**Figure 3.10** Equilibrium phase diagram for the system $Fe_3O_4$ -$SiO_2$. The bold line represents the range of compositions for grains in the annealed FeSiO sample. The peaks at 9, and 27 wt.% FeO are marked by solid rectangles. Reproduced from Muan (1957).

## 3.4 CONCLUSIONS

The results of the isothermal annealing of an Fe-SiO smoke shows that (1) the condensates are quenched melts consistent with the equilibrium phase diagram, and (2) metastable high-temperature minerals, i.e.- tridymite, may undergo fusion (vitrification) at the glass transition temperature, and (3) autoannealing and subsequent thermal annealing may induce subsolidus phase decomposition, i.e., spinodal decomposition, that continues from the autoannealing phase of the condensation process.

# CHAPTER 4. CONDENSATION IN THE Mg-Si-O SYSTEM

## 4.1 INTRODUCTION

This chapter reports data from nine samples condensed in the Mg-Si-O system. They are divided into two suites as a function of slightly different experimental conditions. The second suite of samples is thought to have resulted from more efficient mixing in the vapor phase, thus producing more mixed MgSiO grains than the first suite.

## 4.2 SAMPLE PREPARATION

The samples were produced by the vapor phase nucleation of SiO and Mg vapors in a $H_2$ atmosphere at ~ 80 Torr and 500 °C. The experiment begins with the vaporization of Mg metal chunks contained in a graphite boat within the furnace [cf. Figure 1.1]. As the magnesium starts to vaporize, silane ($SiH_4$) and $O_2$ gases are introduced into the furnace. The hydrogen flow gas mixes the vapors and condensation occurs as the gases flow into a collection chamber kept at 25 °C. Ultrathin sections for TEM analyses were prepared [cf. Section 1.5]. In this chapter the grain sizes are reported as *rms* sizes.

## 4.3 OBSERVATIONS

### 4.3.1 Suite 1

The four samples of the first suite were labeled (1) "Brown MgSiO-no metal", (2) "Mix Mg MgSiO", (3) "Brown Mg metal" and (4) "Mg + MgSiO Collector". These labels were provided by the team that produced the samples and they refer to macroscopic properties (color and luster) of the condensates deposited on the collector surface. The first three samples consist of orange-brown to tan platey particles. Some fluffy white particles are also noticeable. The fourth sample (4), is distinctly different from the rest as it is composed of dark gray to greenish gray platey particles (Table 4.1).

In the AEM the samples mainly consist of patchy materials (Figure 4.1) wherein individual grains are indiscernible. In Table 4.1 I compare the morphological, chemical and mineralogical properties of this first suite of MgSiO samples. I should note that the peaks of pure silica materials in the following histograms are not representative of their true distribution. These phases are clearly identifiable by imaging and it is sufficient to analyze a small number of grains to characterize them. The emphasis on these samples was to characterize the mixed composition grains, because these are considered to better represent condensates in astronomical environments. The patchy material is ~100 wt.% $SiO_2$ (Figure 4.2) with some MgO grains as contaminants. Weak [cf. Sect. 1.7] polycrystalline diffraction maxima (Table 4.2) from the patchy material is consistent with tridymite. Areas near the patchy material contain fluffy, smooth grains (Figure 4.1) that average 60-70 nm in size. These grains are pure silica but show no diffraction maxima,

Table 4.1. Table comparing the properties of the four MgSiO samples in Suite 1. **Abbreviations:** Grain Size data (nm): N=sample size, R=range, x= mean, sd= standard deviation.

| | Br MgSiO - No Metal | Mix Mg MgSiO | Br Mg Metal | Mg+MgSiO - Collector |
|---|---|---|---|---|
| **General Morphology** | - Patchy material wherein grains indescernible<br>- Smooth grains in small areas | - Patchy material<br>- Smooth grains<br>- Euhedral, blocky, bright grains | - Patchy material<br>- Smooth grains, circular & tear shaped<br>- Bright grains in epoxy, almost undefinable perimeters | - Small irregular grains<br>- Patchy material<br>- Round grains |
| **Chemistry** | - Patchy material and smooth grains are ~100 wt.% $SiO_2$ | - Patchy material and smooth grains grains ~100 wt.% $SiO_2$<br>- Blocky bright grains are MgO but some $SiO_2$ contamination | -Patchy and smooth grains 100 wt.% $SiO_2$<br>- Bright grains<br>MgO grains w/ small amounts of $SiO_2$ | - Patchy& sm irregular grains ~ 100 wt.% $SiO_2$<br>- Round grains 50wt.% MgO |
| **Crystallographic Properties** | - Patchy material gives faint rings w/some spots | - Patchy and cluster grains give no diffraction or fringes.<br>- Blocky grains show diffraction | - Patchy grains faint rings, spots<br>- Bright MgO grains give polycrystalline diffraction and fringes | - Rounds-polycrystalline patterns<br>- Irregular and patchy |
| **Grain Sizes** | -Patchy material, arbitrary clusters<br>N= 48, R = 99, x = 65.2<br>- Smooth grains, individuals<br>N= 21, R= 68, x= 61, sd = 19.4 | - Smooth grains -> N=96 R=89, x=60, sd = 21.3<br>- MgO grains<br>N= 36 R= 133,x = 117, sd= 31 | - Smooth silica grains<br>N = 46, R = 83, x = 71, sd = 22<br>-Bright Mg grains - only a few<br>N=5, x = 41.5<br>- Smooth grains, cut shaped<br>N= 7, x = 489 | - Irregular silica grains<br>N = 48, R = 33, x= 22 sd =5.9<br>-MgSiO rounds<br>N=35, R=146, x=68.3 sd=31.8 |
| **Color and Texture** | - orange-brown to gray-tan brown - platey, chippy material | - orange-brown w/some white particles - (fluffy) | - orange-brown to tan, and white particles (fluffy) | - dark gray to greenish-gray (platey) |

**Table 4.2. Diffraction interplanar spacings (nm) for the first suite of MgSiO samples and interplanar spacings of minerals possible in the MgO-SiO2 system from the JCPDS XRD files.**

| Patchy ($SiO_2$) | Lg. Euhed. (MgO) | Rounds x=42% MgO | Tridymite ($SiO_2$) | Cristobalite ($SiO_2$) | Periclase (MgO) | Forsterite ($Mg_2SiO_4$) | Ortho-Enstatite ($MgSiO_3$) | Clino-Enstatite ($MgSiO_3$) |
|---|---|---|---|---|---|---|---|---|
| | | | 18-1170 | 11-695 | 4-829 | 34-189 | 22-714 | 35-610 |
| | | 0.51 | | | | 0.51 | 0.519 | 0.517 |
| | | 0.47 | | | | 0.47 | | |
| | | 0.44 | | | | | 0.443 | 0.441 |
| | | | 0.437-0.433 | | | 0.43 | | 0.437 |
| | | | 0.427 | | 0.421 | | | 0.429 |
| | | | 0.412-0.41 | | | | | |
| | | | 0.408-0.40 | 0.405 | | | 0.403 | 0.405 |
| | | 0.38 | 0.387-0.38 | | | 0.388 | | |
| | | | | | | 0.372 | | |
| | | | 0.361 | | | | | |
| | | 0.35 | | 0.352 | | 0.35 | | 0.353 |
| | | | 0.343-0.34 | | | 0.348 | | |
| | 0.33 | | 0.337-0.333 | | | | 0.331 | 0.332 |
| | | | 0.328-0.32 | | | | | 0.328 |
| 0.31 | | 0.31 | 0.316 | 0.314 | | | 0.318 | 0.317 |
| | | | 0.307 | | | 0.30-0.299 | | 0.304 |
| | | | 0.295-0.294 | | | | 0.295 | 0.298 |
| | | 0.28 | | 0.284 | | | 0.288-0.283 | 0.287-0.28 |
| | | | 0.276 | | | 0.277 | 0.271 | 0.277 |
| | | 0.25 | 0.259 | | | | 0.254 | 0.258-0.25 |
| | 0.24 | | 0.249-0.245 | 0.249-0.247 | 0.243 | 0.246 | 0.249-0.247 | 0.247-0.24 |
| | | | 0.237-0.23 | 0.234 | | 0.235-0.232 | 0.239-0.23 | 0.238 |
| | | | | | | 0.26-0.225 | 0.228-0.224 | 0.228-0.22 |
| | 0.21 | 0.21 | 0.213-0.209 | 0.212 | 0.211 | 0.216 | 0.212-0.21 | 0.214-0.21 |
| | | | 0.205 | 0.202 | | 0.203 | 2.03-0.199 | 0.209-0.2 |

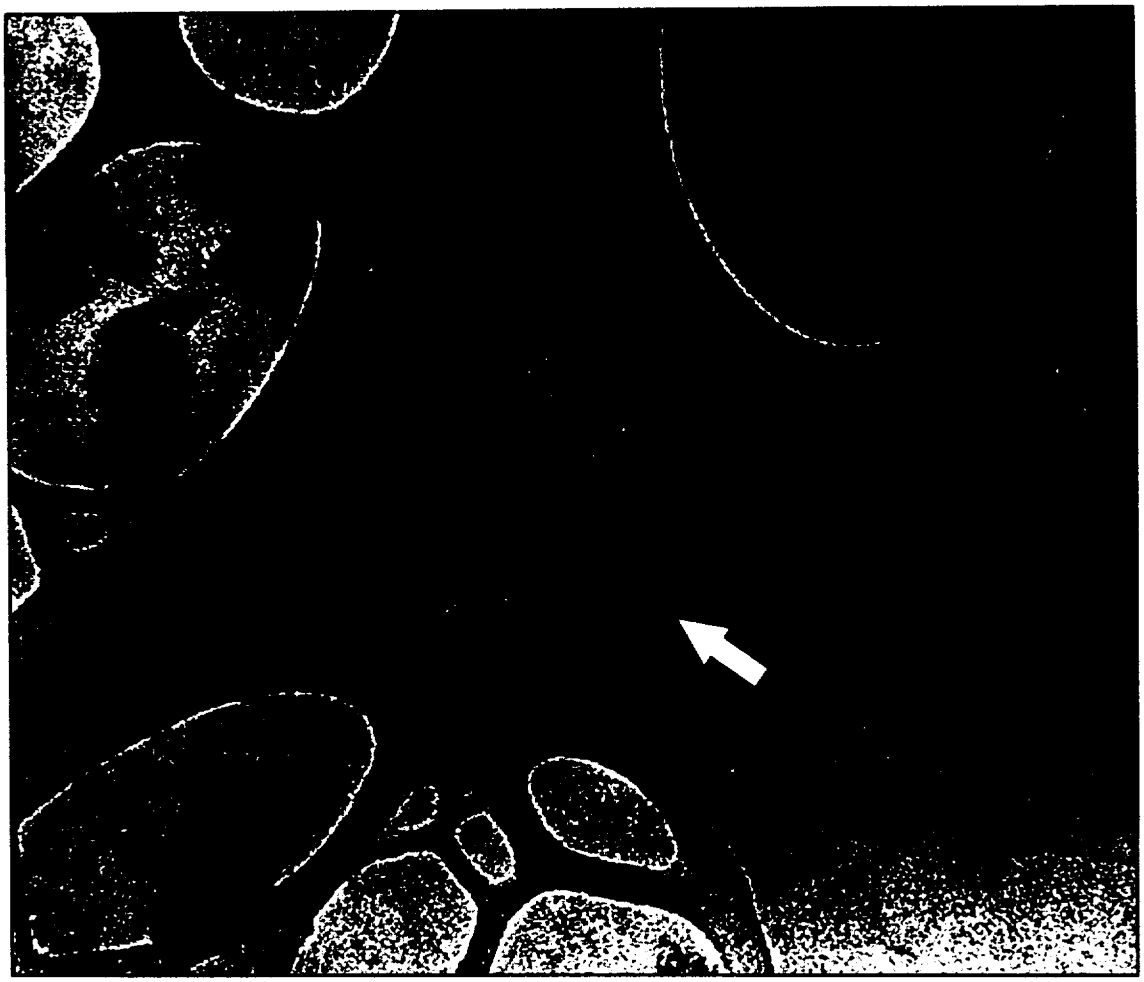

**Figure 4.1** Transmission electron micrograph of patchy silica material (white arrow) and smooth silica material (black arrow) in the "Brown Mg-no metal" sample of the first suite of MgSiO samples. The substrate is a holey carbon film.

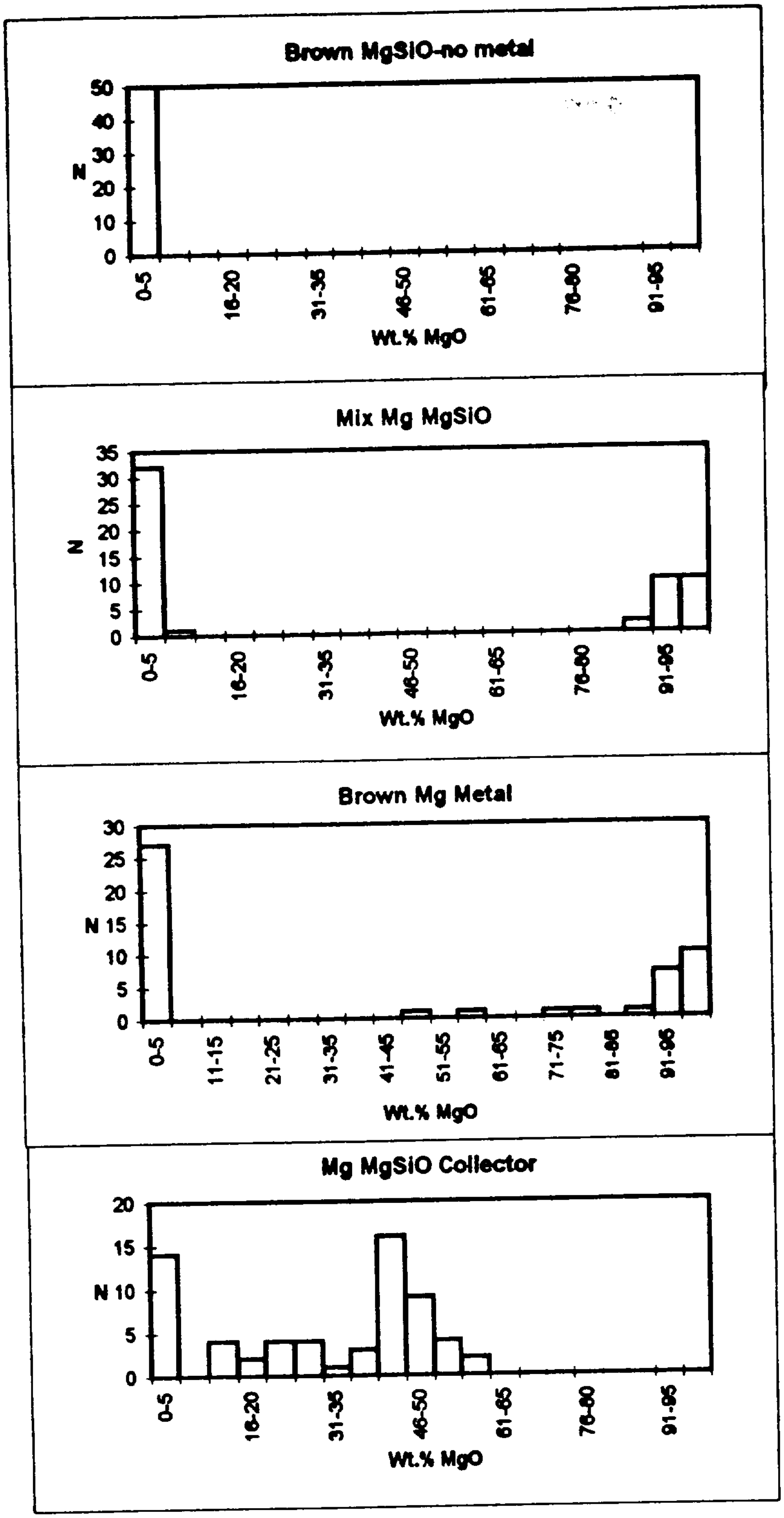

**Figure 4.2** Histogram showing the distributions of chemical compositions for grains in the first suite of MgSiO samples.

indicating they are amorphous. The samples also contain euhedral (~95 wt.% MgO) and subhedral ( ~85 wt.% MgO) high MgO grains. Polycrystalline SAED (Table 4.2) consistently show maxima matching the (111), (200), and (220) planes of periclase. Other maxima support the presence of possibly forsterite and/or enstatite. The euhedral grains have an average size of 117 nm while the subhedral grains have a mean of 41 nm.

The fourth sample in the first suite contains patchy silica material similar to the first three samples, grading into irregular silica grains 22 nm in size that give diffraction consistent with tridymite (Table 4.2). Round, droplet-shaped grains are also found in isolated areas within the sections. These grains range from 21-56 wt.% MgO with a mean at 42 wt.% MgO and have an average size of 68 nm. Polycrystalline patterns of strong diffraction maxima (Table 4.2) from these grains are accordant with forsterite, and/or either ortho-, or clinoenstatite.

The presence of mixed composition "round grains" in the fourth sample prompted a detailed study of five samples labeled $MgSiO_x$ #1-5. This sample was thought to have more efficient mixing of Mg and Si-(O) vapors before condensation, and that would have yielded a higher abundance of Mg-Si grains, whereas the other three were produced at experimental conditions that did not promote efficient mixing in the vapor phase.

### 4.3.2 Suite 2

These samples are all composed of granular to platey particles that are dark gray to greenish-gray in hand specimen, similar to the fourth sample in Suite 1. The samples consist mostly of round droplet-shaped grains and irregular-edged cluster grains in a highly porous texture wherein most grains are in contact with only a few others. Discrete locations within samples #1, 2, 4, and 5 contain subhedral grains and spherical grains in smoke-like textures. Samples #1, 2, and 5 also contain subhedral to euhedral grains that occur in groups of a dozen or more grains. Chemical analysis of individual grains reveal a range of compositions from 0 to 100 wt.% MgO in samples #2, and 4, while samples #1, 3, and 5 contain no pure silica materials (Figure 4.3).

The $MgSiO_x$ samples can be described by five morphologies. Each morphology has specific chemical and mineralogical properties that will be defined below. A combination of the five morphologies defines each sample. Table 4.3 compares all five $MgSiO_x$ samples according to their mineralogical, chemical, and morphological properties.

1. **Round grains (Figure 4.4)**- These grains are droplet-shaped and are found in samples #1-4, and are very similar to those in Suite 1 [cf. Section 4.3.1]. Some round grains have a homogeneous smooth texture while others show identifiable domains within their interiors. These domains have an average size of 19.8 nm and appear as aggregated inclusions within the centers of some round grains. The domains do not have differing chemistries from the bulk grain. Round grains range from 23-74 wt.% MgO with average compositions of 57, 56, 49, and 52 wt.% MgO in sample #1,2,3,4 respectively (Table 4.4). Polycrystalline diffraction data from these grains are consistent with forsterite, orthoenstatite, and clinoenstatite (Table 4.5). Lattice fringes measuring 0.83, 0.56, 0.4, and 0.31 nm are also found (Table 4.6).

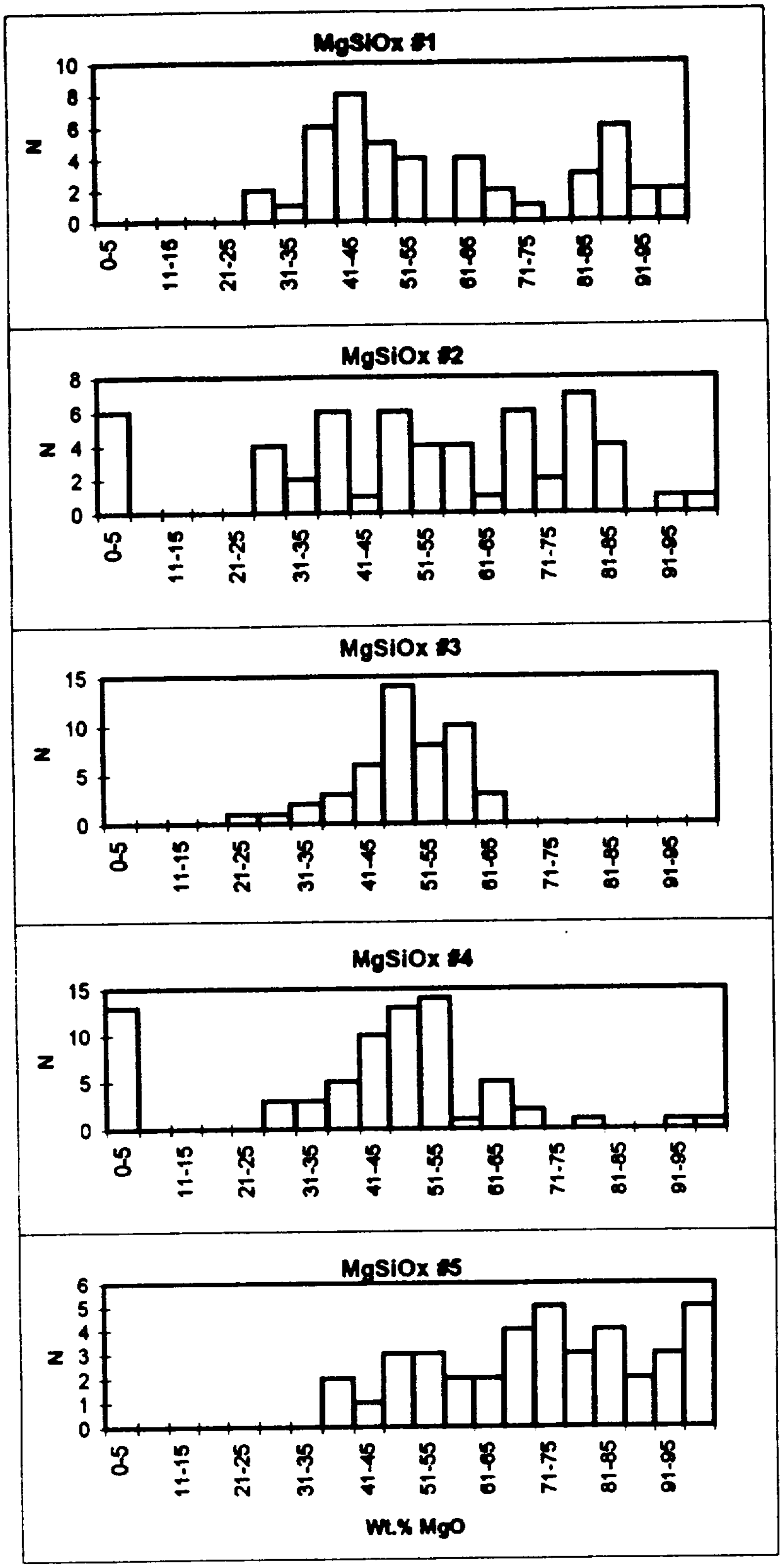

**Figure 4.3** Histograms showing the compositions of grains in the MgSiOx samples (Suite 2)

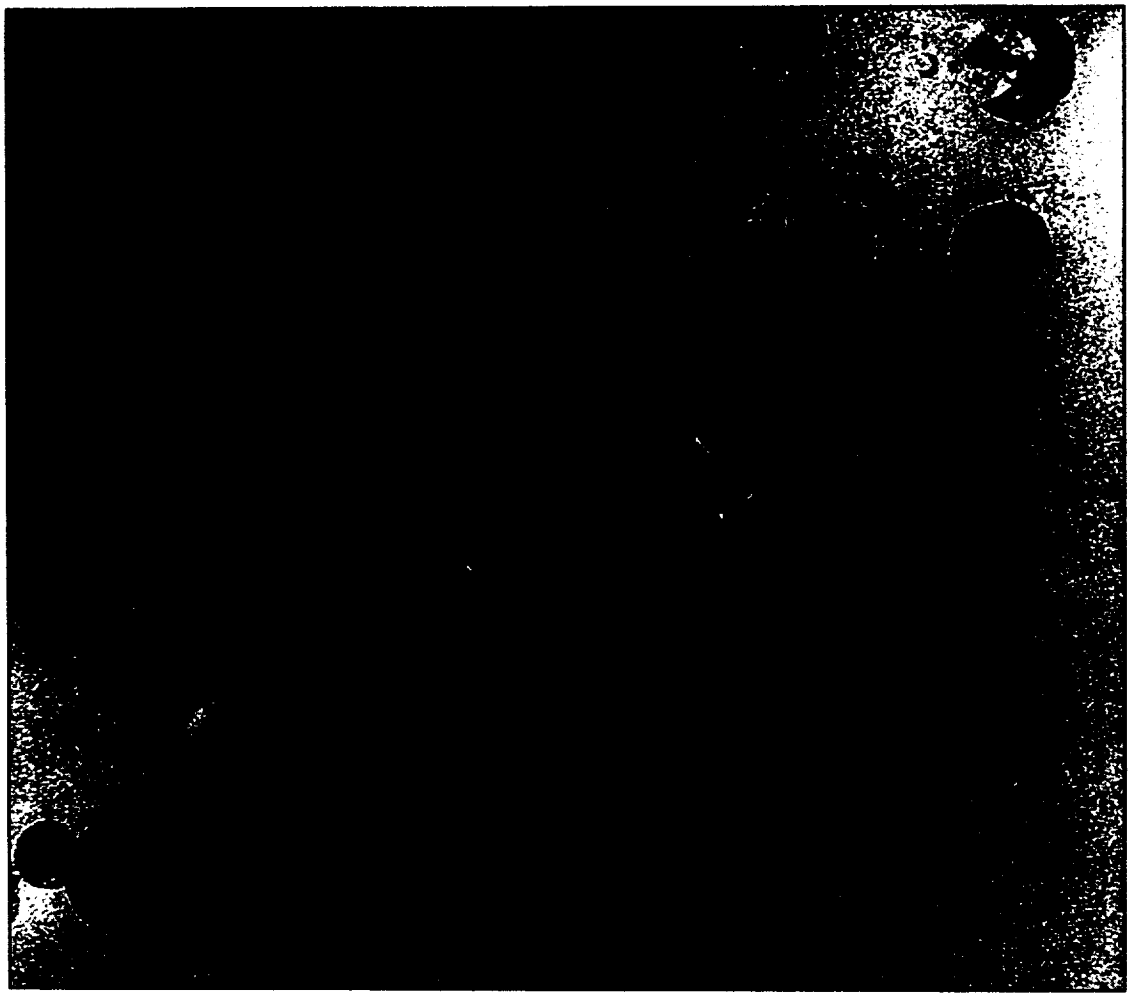

**Figure 4.4** Transmission electron micrograph showing the round grains in $MgSiO_x$ #3. The darker grains are crystalline and in the optimum Bragg condition.

Table 4.3 Properties of MgSiOx samples #1-5. Abbreviations: sm=small, lg=large, x=average (nm), diff.=diffraction.

| | MgSiO$_x$ #1 | MgSiO$_x$ #2 | MgSiO$_x$ #3 | MgSiO$_x$ #4 | MgSiO$_x$ 5 |
|---|---|---|---|---|---|
| **General Morphology** | - round grains<br>- irregular clusters<br>- sm bright subhedral<br>- large subhedral | - Round grains<br>- irregular clusters<br>- small bright subhedral<br>- large subhedral<br>- small chainy spheres<br>- fluffy circular grains (rare) | - round grains<br>- irregular clusters (rare) | - round grains<br>- irregular clusters<br>- small bright subhedral (rare)<br>- small chainy spheres | - irregular clusters<br>- small bright subhedral<br>- large subhedral |
| **Chemistry** | - round grains: X=57 wt.% MgO<br>- irregular clusters: X=42 wt.% MgO<br>- sm subhedral: X=88 wt.% MgO<br>- large subhedral: X= 96 wt.% MgO | - round grains: X=56 wt.% MgO<br>- irregular clusters: X=40 wt.% % MgO<br>- sm suhedral: X=81 wt.% MgO<br>- large subhedral: X= 94 wt.% MgO<br>- sm chainy spheres: 100 wt.% $SiO_2$<br>- fluffy grains: 100 wt.% $SiO_2$ | - round grains:X=49 wt.% MgO<br>- irregular clusters: X=52 wt.% MgO | - round grains: X=52 wt.% MgO<br>- irregular clusters: X=44 wt.% MgO<br>- sm subhedral: X=84 wt.% MgO<br>- sm chainy spheres: 100 wt.% $SiO_2$ | -irr. clusters: 40-75 wt.% MgO<br>-sm suhedral: X=89 wt.% MgO<br>- Lg subhedral: X=96 wt.% MgO |
| **Crystallo-graphic Prop** | - Rounds and clusters: diff. maxima and fringes<br>- Lg and Sm subhedral diff. maxima | - Rounds and clusters: diff. maxima<br>- Sm and Lg subhedral diff maxima<br>- sm chainy spheres diff. maxima<br>- fluffy circular: no maxima | - Round and clusters diff. maxima and fringes | - Rounds and clusters diff. maxima and fringes<br>- sm. subhedrah diff. maxima<br>- sm chainy spheres diff. maxima | - Irregular clusters diff. maxima and fringes<br>- Sm and Lg subhedral diff. maxima |
| **Grain Sizes** | - Rounds: X=62 nm<br>- Irr clusters: X=115 nm<br>- Sm subhedral: X=46 nm<br>- Lg subhedral: X=71 nm | - Rounds: X=69 nm<br>- Irr clusters: X=93 nm<br>- Sm subhedral: X=47 nm<br>- Lg subhedral: X=92 nm<br>- Sm chainy spheres: X=30 nm<br>- fluffy circular: X=100 nm | - Rounds: X=94 nm<br>- Irr clusters: X=100 nm | - Rounds: X=96 nm<br>- Irr clusters: X=130 nm<br>- Sm subhedral: X=47 nm<br>- Sm chainy spheres: X=32 nm | - Irr clusters: X=123 nm<br>- Sm subhedral: X=36 nm<br>- Lg subhedral: X=117 nm |
| **Color and Texture** | - dark grey to greenish gray, fine grained to platy | - dark grey to greenish gray, fine grained to platy. Some orange stuff | - dark grey to greenish gray, fine grained to platy | - dark grey to greenish gray, fine grained to platy | - dark grey to greenish gray, fine grained to platy |

**Table 4.4 Statistical data for the compositions of round grains, irregular clusters, and small subhedral grains in samples MgSiOx #1-5.**

**Round grains:**

| Sample | #1 | #2 | #3 | #4 | #5 |
|---|---|---|---|---|---|
| | N= 10 | N= 16 | N= 48 | N= 26 | |
| | R= 43-70 | R= 43-74 | R= 23-64 | R= 38-66 | |
| | x= 57 | x= 56 | x= 49 | x= 52 | |
| | sd= 9.3 | sd= 10.6 | sd= 9.1 | sd= 7.3 | |

**Irregular clusters:**

| Sample | #1 | #2 | #3 | #4 | #5 |
|---|---|---|---|---|---|
| | N=22 | N= 17 | | N= 27 | N= 23 |
| | R= 29-65 | R= 29-59 | | R= 26-56 | R= 36-76 |
| | x= 42 | x= 40 | | x= 44 | x= 60 |
| | sd= 7.8 | sd= 9.5 | | sd= 7.2 | sd= 12.6 |

**Small subhedrals grains:**

| Sample | #1 | #2 | #3 | #4 | #5 |
|---|---|---|---|---|---|
| | N= 11 | N= 9 | | N= 5 | N= 5 |
| | R= 81-96 | R= 77-94 | | R= 70-99 | R= 83-90 |
| | x= 88 | x= 81 | | x= 84 | x= 89 |
| | sd= 4.4 | sd= 5.5 | | sd= 11.9 | sd= 5.7 |

**Table 4.5. MgSiOx diffraction interplanar spacings (d, nm) for samples of Suite 2 and interplanar spacings of possible minerals in the MgO-SiO$_2$ system from the XRD files.**

| | | | | | | | | | Ortho- | Clino- |
|---|---|---|---|---|---|---|---|---|---|---|
| | | | | | Tridymite | Cristobalite | Periclase | Forsterite | Enstatite | Enstatite |
| Sm subhed | Sm chain | Lg Euhed | Round | Clusters | ($SiO_2$) | ($SiO_2$) | (MgO) | ($Mg_2SiO_4$) | ($MgSiO_3$) | ($MgSiO_3$) |
| ~85% MgO | ($SiO_2$) | >90% MgO | x=52% MgO | x=47% MgO | 18-1170 | 11-695 | 4-829 | 34-189 | 22-714 | 35-610 |
| | | | | 0.994 | | | | 1.02 | | 0.96 |
| | | | 0.85 | | 0.82 | | | | 0.885 | 0.882 |
| | | | | | | 0.69 | | | | |
| | | | | | | | | | 0.633 | 0.634 |
| | | | 0.58 | | | | | 0.59 | | |
| | | | | | 0.543 | | | | | |
| | | | 0.52 | 0.52 | | | | | | |
| 0.51 | | | | | | | | 0.51 | 0.519 | 0.517 |
| | | | | | | | | | | |
| | | 0.47 | 0.47 | | | | | 0.476 | | |
| | | | | 0.44 | | | | | 0.443 | 0.441 |
| 0.43 | | | 0.43 | | 0.437-0.433 | | | 0.43 | | 0.437 |
| | | | | | 0.427 | | 0.421 | | | 0.429 |
| | | | | | 0.412-0.41 | | | | | |
| | | | | | 0.408-0.40 | 0.405 | | | 0.403 | 0.405 |
| 0.4 | | 0.39 | | | | | | | | |
| | | | 0.38 | 0.38 | 0.387-0.38 | | | 0.388 | | |
| 0.37 | | | | | | | | 0.372 | | |
| | | | | | 0.361 | | | | | |
| | | | 0.35 | 0.35 | | 0.352 | | 0.35 | | 0.353 |
| | | | | | 0.343-0.34 | | | 0.348 | | |
| | | | | | | | | | | |
| | | | | | | | | | | |
| | | | | | 0.337-0.333 | | | | 0.331 | 0.332 |
| | | | | | 0.328-0.32 | | | | | 0.328 |
| 0.3 | 0.31 | | 0.31 | 0.31 | 0.316 | 0.314 | | | 0.318 | 0.317 |
| | | 0.3 | | | 0.3-0.298 | | | 0.30-0.299 | | 0.304 |
| | | | | | 0.295-0.294 | | | | 0.295 | 0.298 |
| | | | | | | 0.284 | | | 0.288-0.283 | 0.287-0.28 |
| 0.27 | | | 0.27 | 0.27 | 0.276 | | | 0.277 | 0.271 | 0.277 |
| | | | | | 0.259 | | | | 0.254 | 0.258-0.25 |
| 0.24 | | 0.24 | 0.24 | 0.24 | 0.249-0.245 | 0.249-0.247 | 0.243 | 0.246 | 0.249-0.247 | 0.247-0.24 |
| | | | | | 0.233-0.23 | 0.234 | | 0.235-0.232 | 0.239-0.23 | 0.238 |
| | | | | | | | | 0.226 | 0.228-0.224 | 0.228-0.22 |
| 0.21 | | 0.21 | 0.21 | 0.21 | 0.213-0.209 | 0.212 | 0.211 | 0.216 | 0.212-0.21 | 0.214-0.21 |
| | | | | | 0.205 | 0.202 | | 0.203 | 2.03-0.199 | 0.209-0.2 |
| | | | | | | | | | | |
| | | | | | | | | | | |

**Table 4.6 MgSiOx lattice fringe spacings and diffraction data, and (hkl) planes for forsterite, orthoenstatite, and clinoenstatite.**

| | | | | | |
|---|---|---|---|---|---|
| | | | JCPDS# | JCPDS# | JCPDS# |
| Irregular Cluster grains | | | 34-189 | 22-714 | 35-610 |
| | | | forsterite | O-enstatite | Cl-enstatite |
| | lattice fringes | electron diff. | hkl | hkl | hkl |
| | | 0.994 | 010 | | |
| | 0.65 | | | 210 | 210 |
| | 0.53-0.59 | | 100 | | |
| | | 0.51 | 020 | 001 | 001 |
| | | 0.44 | 011 | 020 | 020 |
| | | 0.39-0.38 | 120 | | |
| | | 0.35 | 111 | | 111 |
| | | 0.31 | 121 | 420 | 220 |
| Round grains | | | | | |
| | | | forsterite | O-enstatite | Cl-enstatite |
| | lattice fringes | electron diff. | hkl | hkl | hkl |
| | 0.83 | 0.84 | | 010 | 010 |
| | 0.56 | 0.58 | 100 | | |
| | | 0.52-0.51 | 020 | 001 | 001 |
| | | 0.48-0.47 | 001 | | |
| | 0.4 | 0.43 | 011 | 020 | 020 |
| | | 0.39 | 120 | | |
| | | 0.35 | 111 | | 111 |
| | | 0.33 | | 121 | 121 |
| | 0.31 | 0.31-0.3 | 121 | 420 | 300 |

Figure 4.5 shows three round grains (~58 wt.% MgO) with 0.31 nm lattice fringes and a single-crystal diffraction data that matches forsterite. The sizes of the round grains ranges from 30- 150 nm with an average of ~65 nm in samples #1,2, and ~95 nm in samples #3,4. Grain size distributions are log-normal for samples #1,2,3,4 with correlation coefficents of $R^2$ = 0.96, 0.92, 0.97, and 0.96 respectively (Figure 4.6).

**2. Irregular cluster grains (Figure 4.7).** These grains are found in all five samples and along with the round grains make up about 70% of each sample. Irregular cluster grains have a generally circular shape but their edges are irregular. Some grains look fairly homogenous but others reveal smaller individual grains aggregated to form the cluster. The irregular clusters are 26- 80 wt.% MgO with means of 42, 40, 55, 44, and 60 wt.% MgO in samples #1-5 respectively (Table 4.4). Polycrystalline SAED patterns show maxima (Table 4.5) that can be attributed to periclase, forsterite, and ortho- or clino-enstatite. Lattice fringes from cluster grains measure 0.65, and 0.53-0.59 nm (Table 4.6). The cluster grain in Figure 4.8 is approximately ~70 wt.% MgO and shows lattice fringes and diffraction maxima consistent with forsterite and periclase. The size of cluster grains is ~95 nm in samples #2,3, and ~115-130 nm in the three others [cf. Table 4.3]. The grains show log normal size distributions with a range of 40-170 nm, and $R^2$ values of 0.93. 0.95, 0.94, and 0.95 in samples #1,2,4, and 5 respectively (Figure 4.9).

**3a. Small subhedral grains (Figure 4.10)** are MgO rich. They show compositional peaks at 88, 81, 84, and 89 wt.% MgO in samples #1,2,4 and 5 respectively (Table 4.4). These grains are very similar to those found in Suite 1 [cf. Section 4.3.1]. Small subhedral

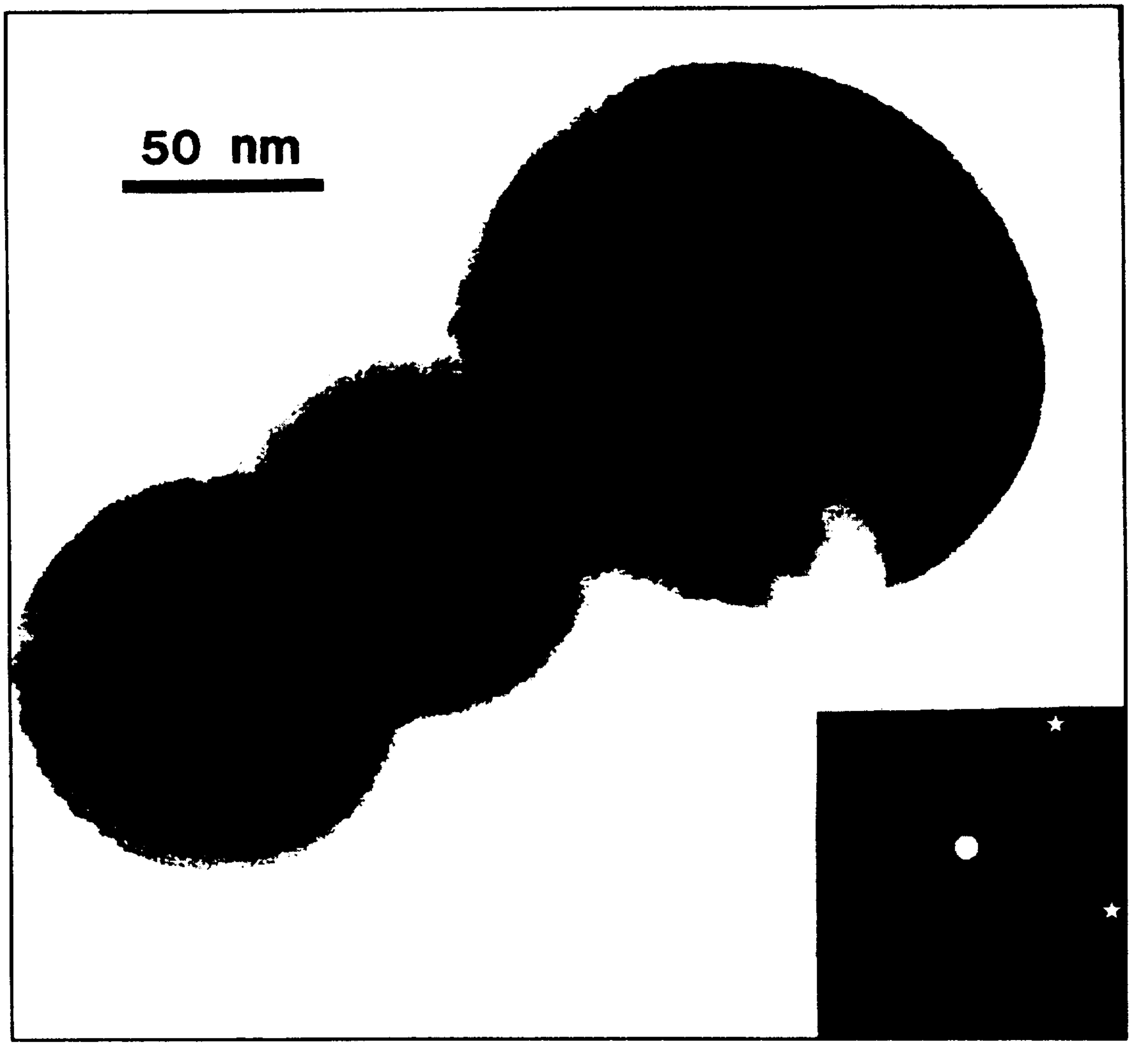

**Figure 4.5** Transmission electron micrograph showing three round grains with 0.31 nm lattice fringes. The corresponding single crystal SAED pattern indicates that the grain orientation is with the a-axis [100] of forsterite perpendicular to the page.

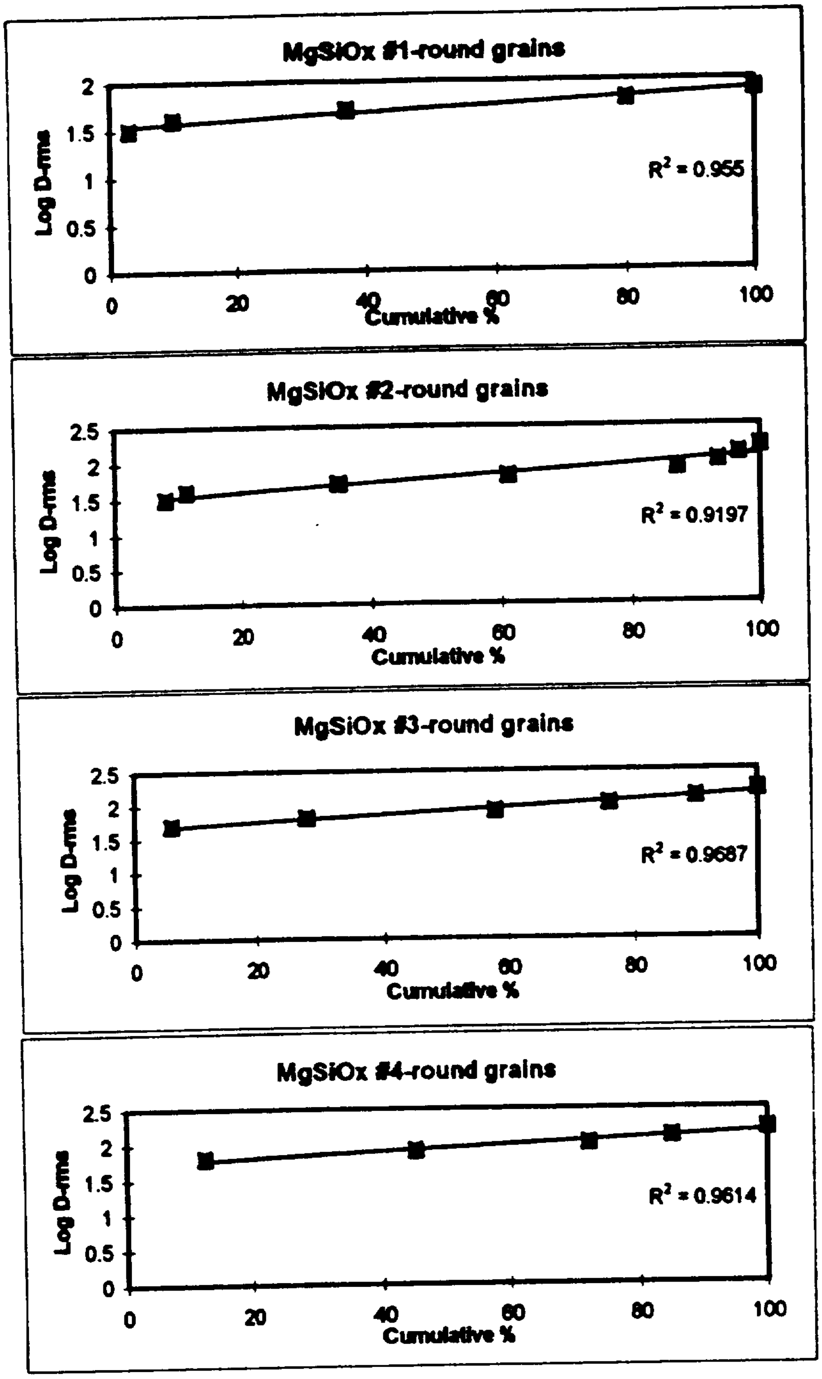

**Figure 4.6** Log D sizes of round grains fit to log-normal distributions.

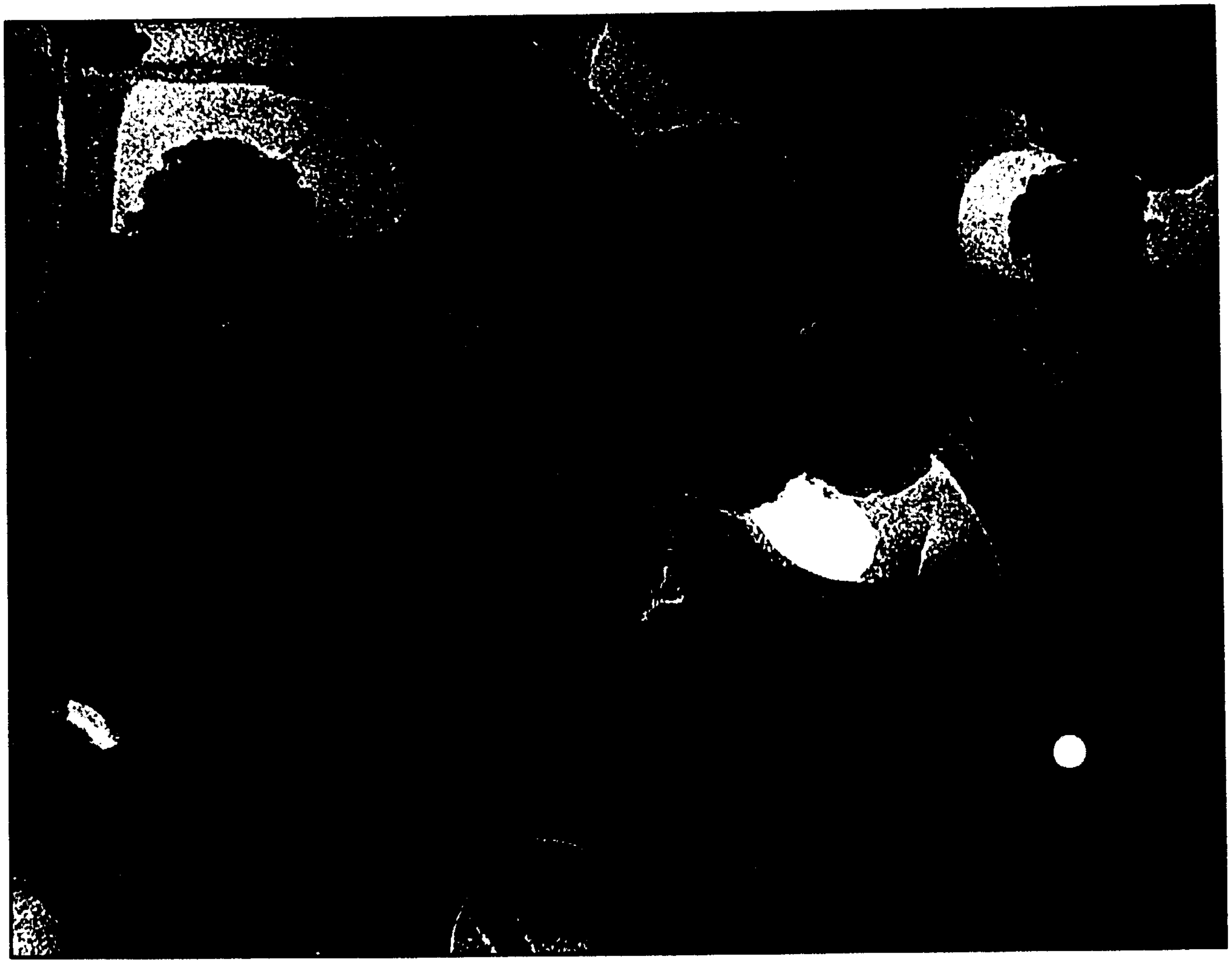

**Figure 4.7** TEM image of irregular cluster grains. The corresponding polycrystalline SAED pattern is from all the grains. Contrast differences are probably due to crystalline domains within the clusters.

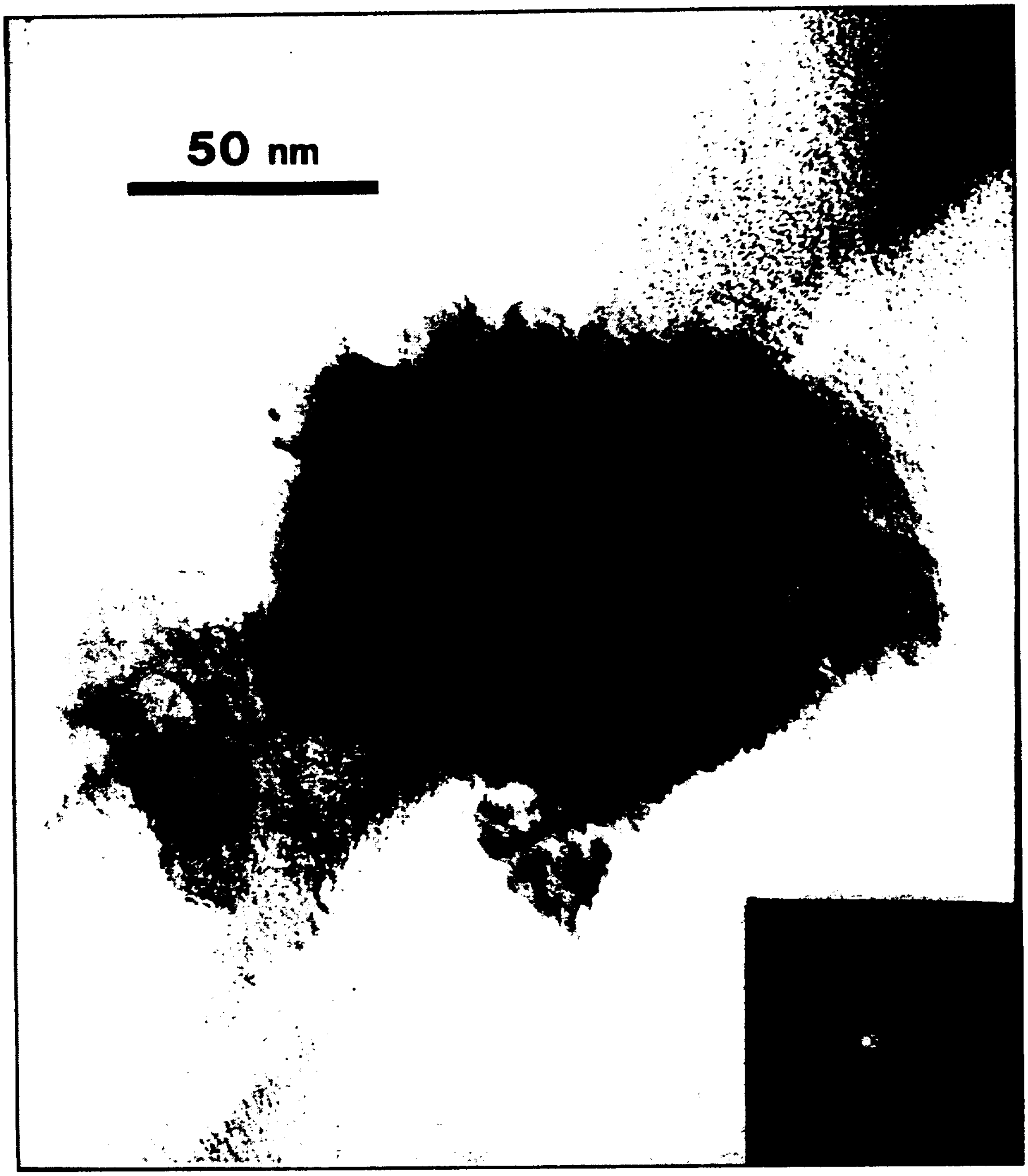

**Figure 4.8** Transmission electron micrograph of an irregular cluster grain that has a composition of 70 wt.% MgO showing 0.53 nm lattice fringes. Circled maxima in the corresponding polycrystalline SAED pattern supports evidence for periclase (111) and forsterite (101).

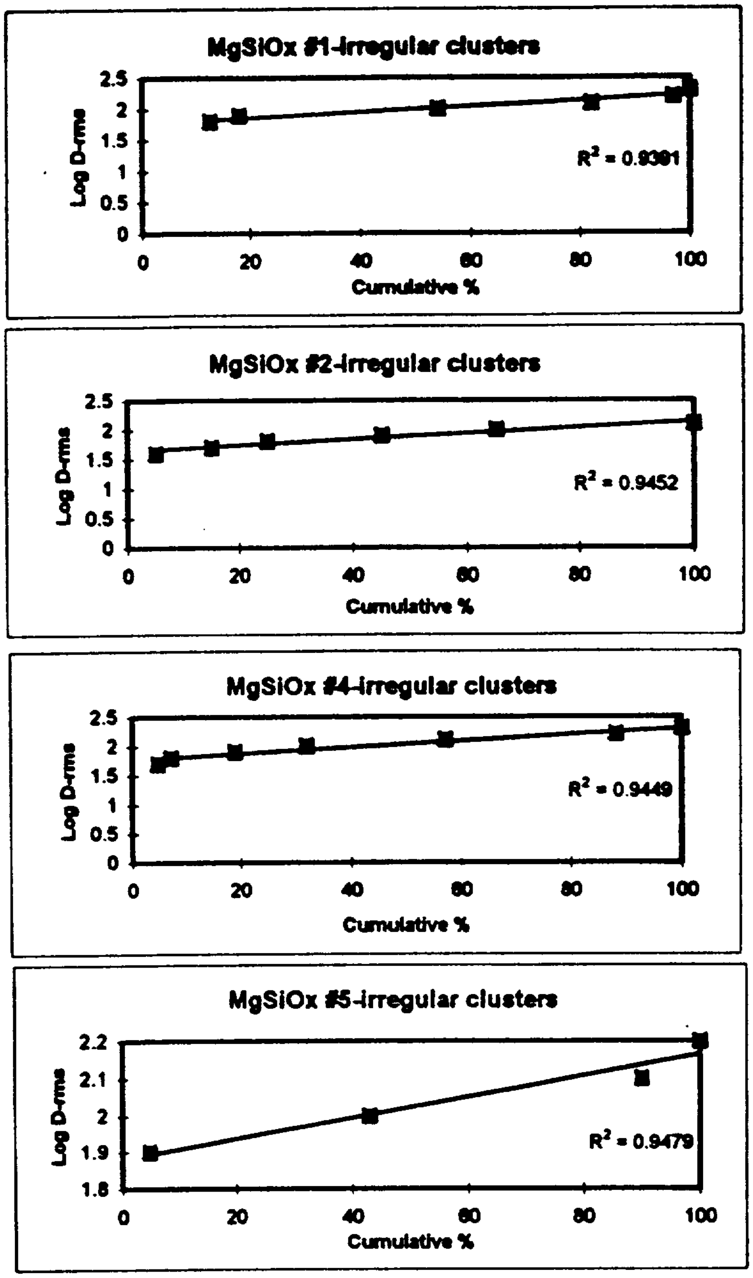

Figure 4.9 Log D sizes of irregular cluster grains in the MgSiOx samples showing log-normal distributions

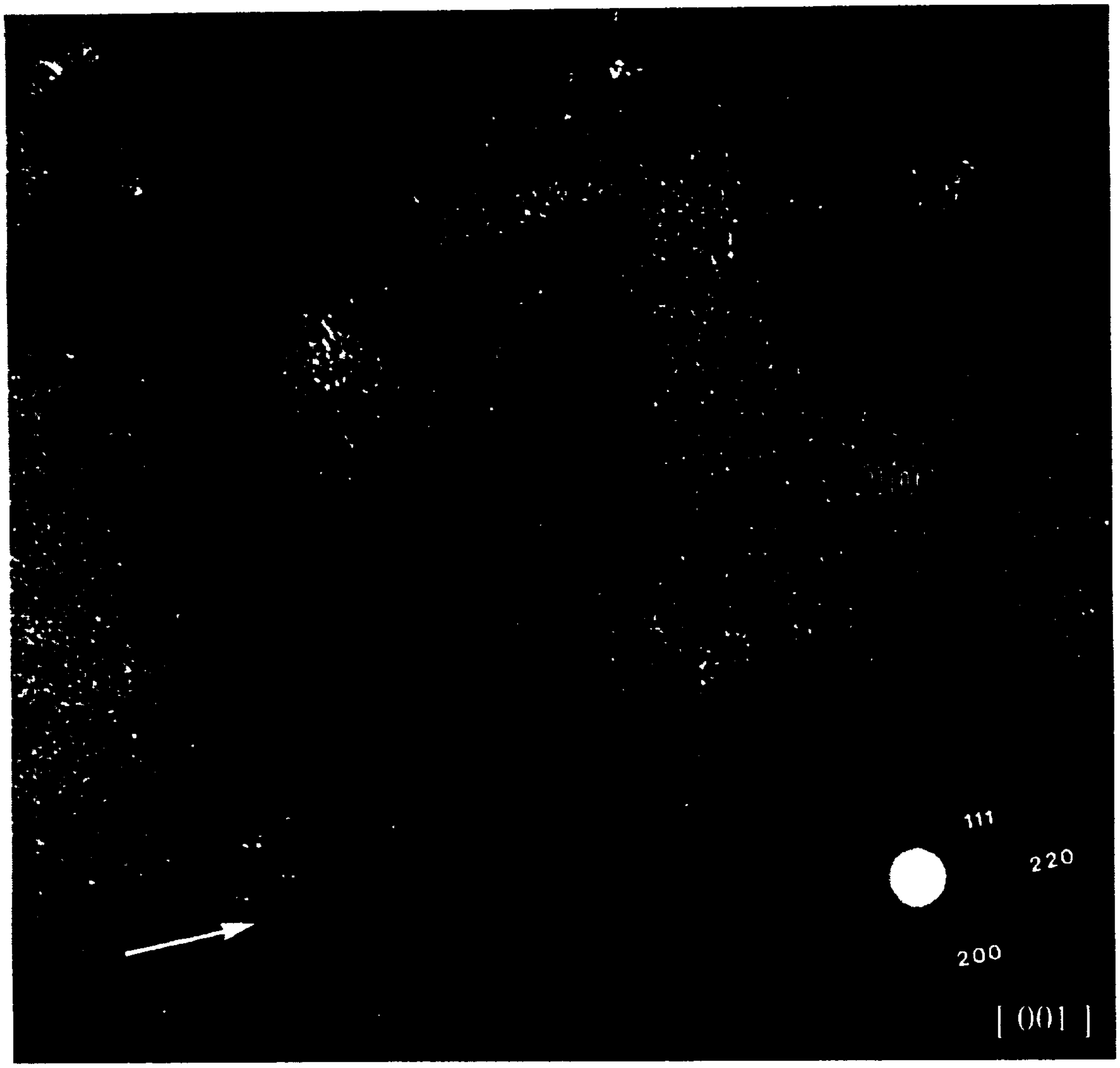

**Figure 4.10** Transmission electron micrograph of small subhedral and subrounded grains with a corresponding polycrystalline SAED pattern. The white arrow indicates a subrounded grain while the dark arrow indicates a subhedral grain. The darker grains reflect crystalline grains in the optimum diffracting (Bragg) condition. The circled maxima in the SAED pattern correspond to (111), (200), and (220) planes, and identify a single-crystal pattern projected down the c-axis of periclase.

grains are contained in smoke-like textures along with sub-rounded grains within samples #1, 2, and 5. Some subhedral grains appear very "dark" during bright field TEM imaging, probably due to the grains being crystalline rather than amorphous, thus possessing a greater electron density. Subhedral grains within the smoke texture are slightly more Mg-rich than the subrounded grains. Diffraction maxima (Table 4.5) consistently matches the (111), (200), and (220) planes of periclase (MgO). Diffraction data also shows maxima that may be consistent with forsterite, and/or enstatite. It could be that the dark subhedral grains are crystalline MgO, and the other grains within the smoke texture are an amorphous magnesio-silica mixture. The sizes of subhedral and subrounded grains range from 30 to 60 nm (Table 4.3) and show log-normal distributions with correlation coeffients of 0.95, 0.91, and 0.88 in samples #1,2, and 5. (Figure 4.11).

**3b. Large subhedral to euhedral grains (Figure 4.12)** have rectangular, hexagonal and octagonal shapes and are often isolated in groups of 5 to 10 grains and sometimes associated with small subhedral grains of 3a. They show high MgO contents (>90 wt.%) and diffraction patterns (Table 4.5 and Figure 4.12) that match periclase and/or an MgSiO phase. They range in size from 40 to 170 nm and have an average size of ~72 nm in the samples $MgSiO_x$ #1 and 2, and an average size of 117 nm in sample #5.

**4. Small chainy spheres (Figure 4.13)** occur in smoke-like textures in isolated areas of samples #2, and 4. The grains are 100 wt.% $SiO_2$ and show weak diffraction maxima

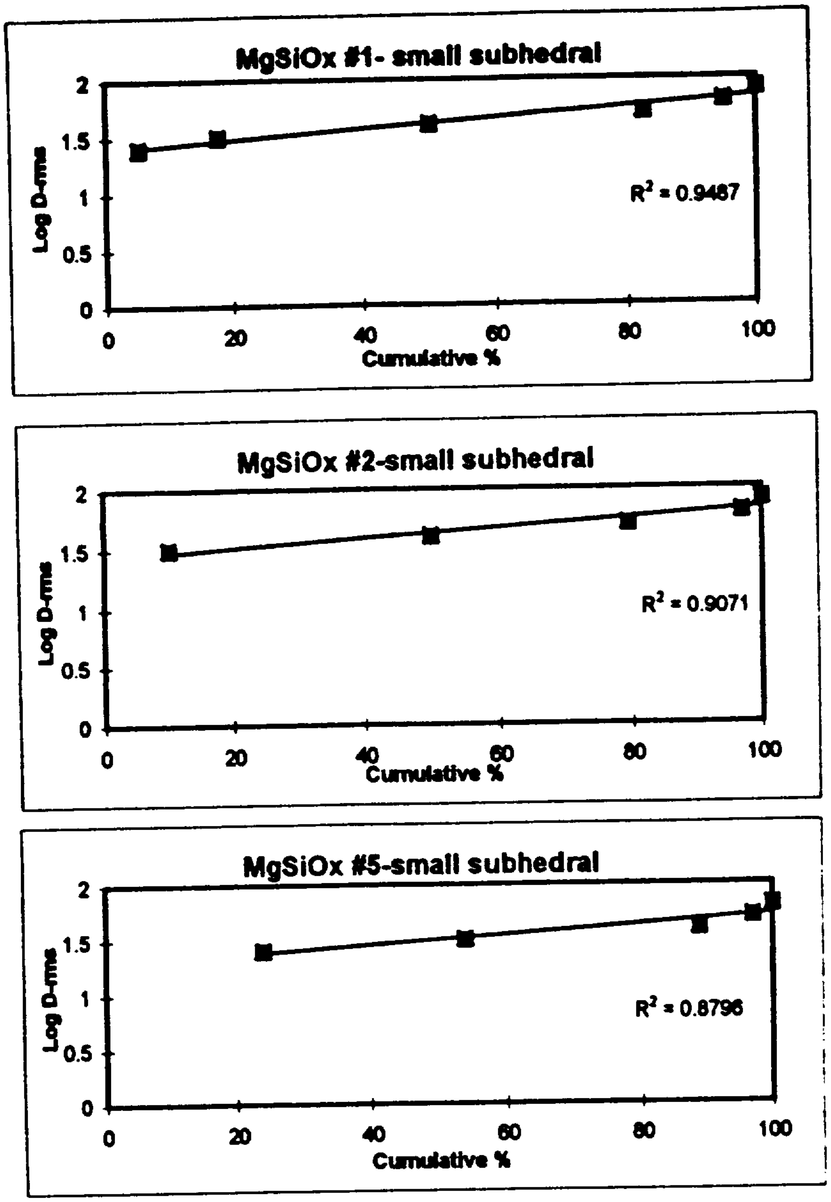

**Figure 4.11** Log D sizes of small subhedral grains fit to log-normal distributions.

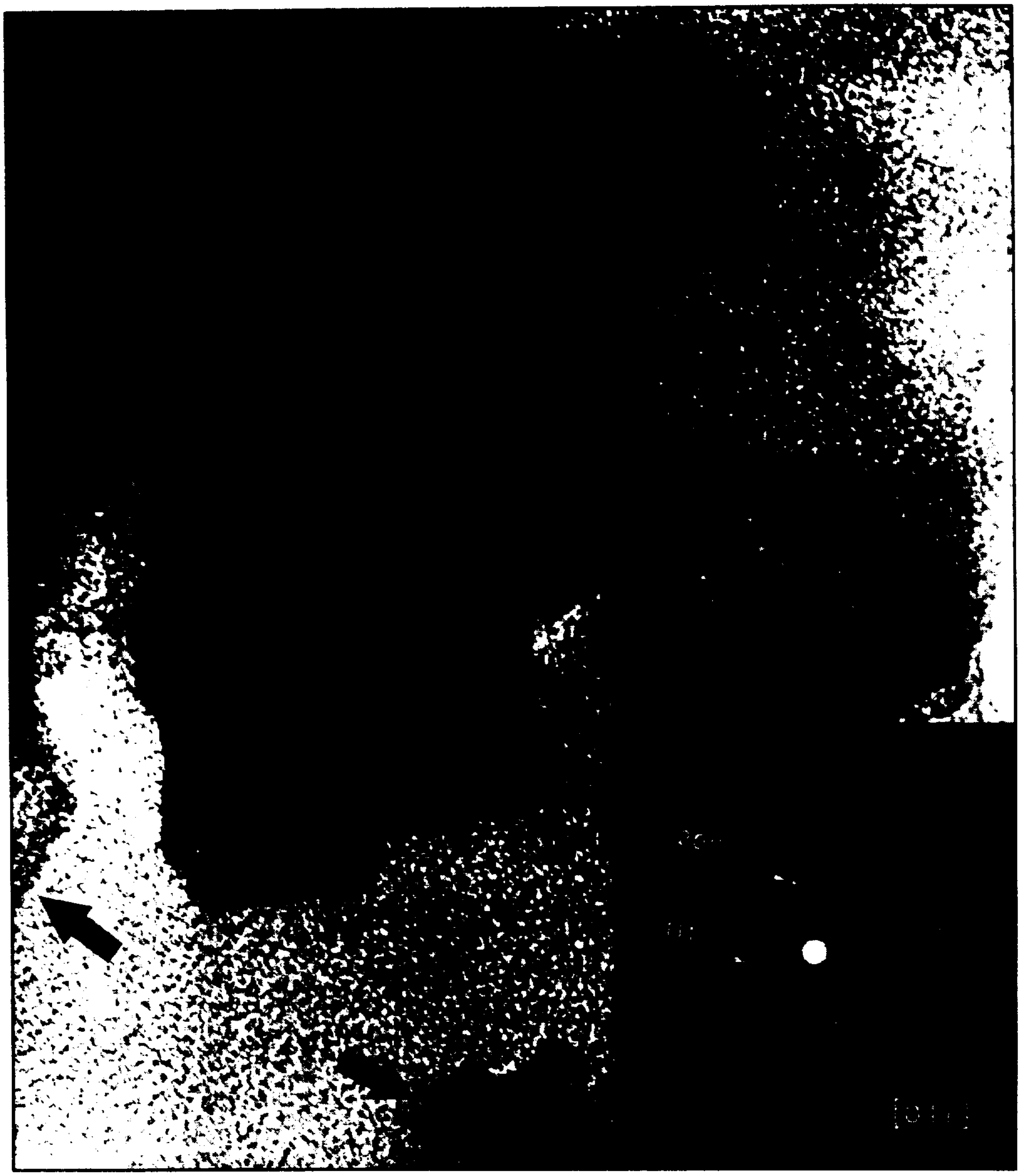

**Figure 4.12** Transmission electron micrograph of large euhedral MgO grains along with silica rich grains (black arrows). The corresponding SAED shows a single-crystal pattern looking down the [011] of periclase. The (111) and (200) maxima are also identified. Other maxima may be due to the silica phases.

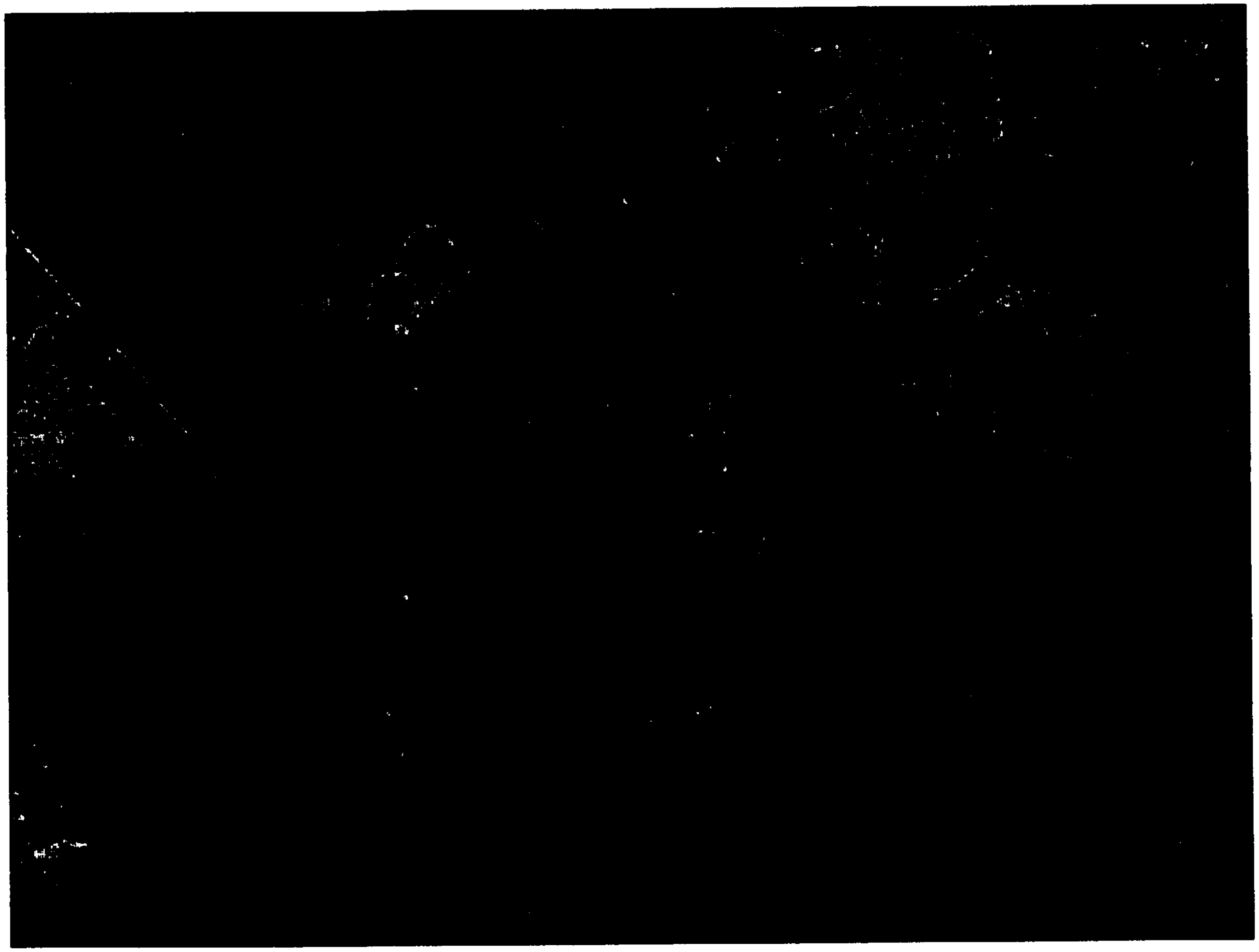

**Figure 4. 13** Transmission electron micrograph of smooth silica grains in an epoxy thin section atop a holey carbon film substrate. The darker clustered areas are thickness effects while dark individual grains are probably crystalline.

consistent with tridymite and/or cristobalite (Table 4.4). The grains range from 15-50 nm with a mean size of ~31 nm. The size distributions of the spheres are log-normal with $R^2 = 0.92$ and 0.96 in samples #2 and 4 respectively (Figure 4.14).

A sixth morphology is rare smooth fluffy pure silica grains similar to those found in Suite 1 [cf. Figure 4.1]. The grains show no diffraction maxima and are interpreted to be amorphous. They have an average size of 100 nm and only occur in sample #2.

## 4.4 DISCUSSION

Condensation in the $MgSiO_x$ system produces grains ranging in compositions from $SiO_2$ - MgO (Figures 4.2, 4.3). The bulk of the samples consist of round and clustered grains ranging from ~ 25 to 70 wt.% MgO. The remainder of the samples consist of (near) endmember composition grains with differing morphologies. A clear gap in the data occurs between 5 to ~ 30 wt.% MgO (Figure 4.15). The corresponding equilibrium phase diagram (Ehlers, 1972) predicts a liquid immiscibility region from ~ 3- 30 wt.% MgO (Figure 4.15). This could explain the absence of this compositional range in the samples of this study.

The compositional peaks of morphologically distinct grains in this $MgSiO_x$ sample can also be understood using the phase diagram. First, the irregular cluster grains and the round grains range from 23-80 wt.% MgO and show averages of 47, and 52 wt.% MgO respectively (Figure 4.16). The stable phases within this range are forsterite and enstatite,

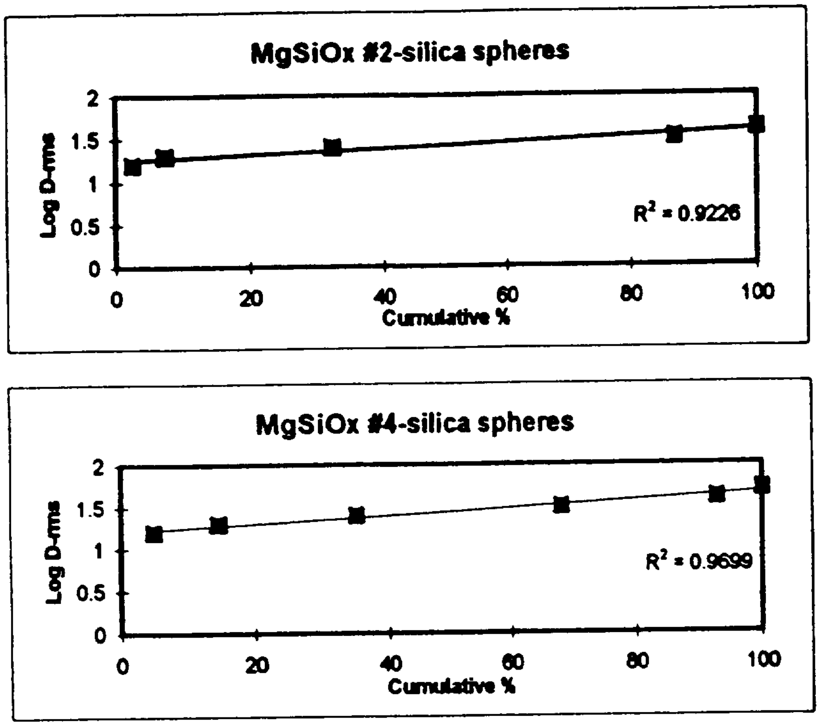

Figure 4.14 Log D sizes of silica spheres fit to a log-normal distribution.

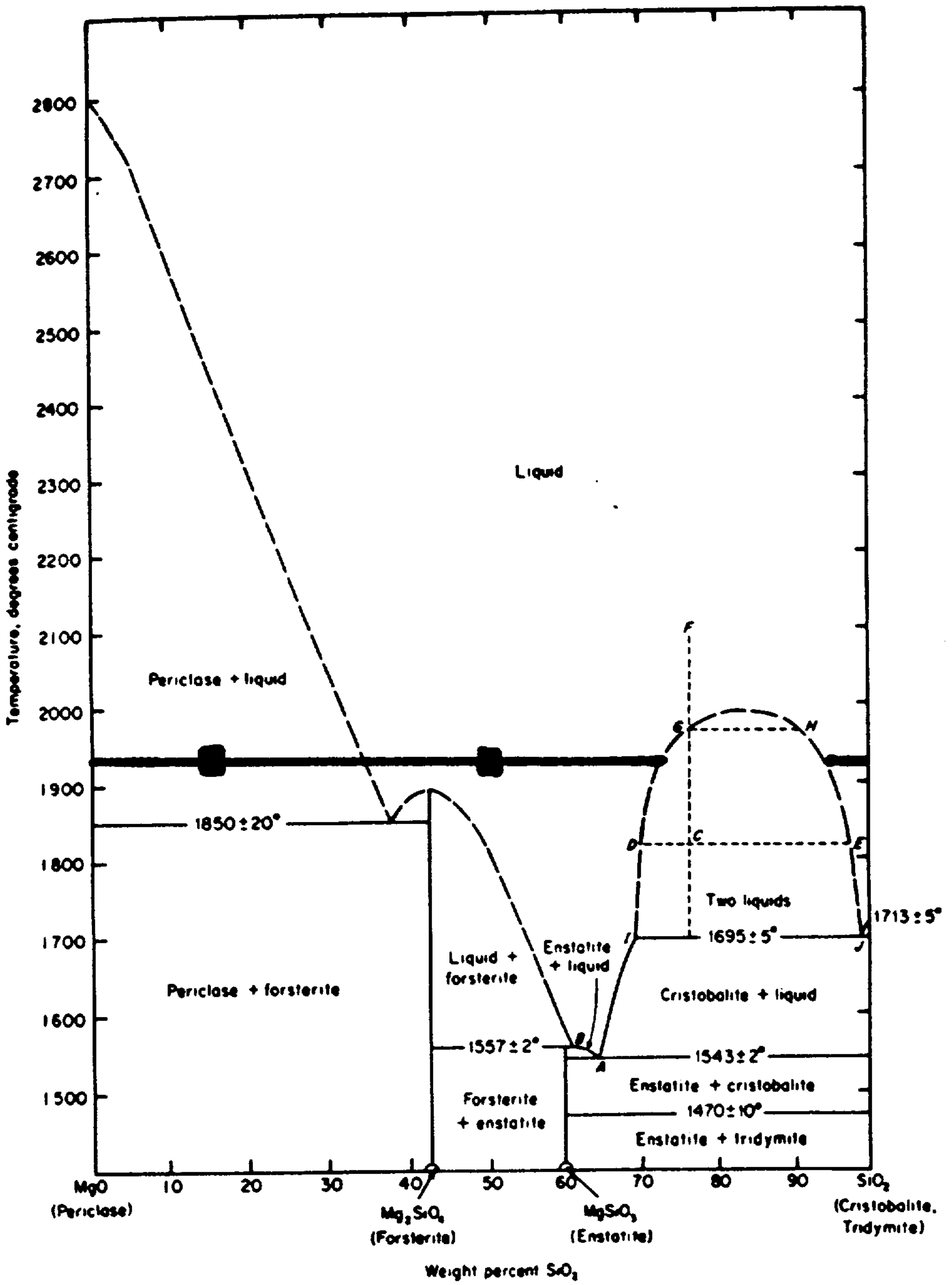

**Figure 4.15** MgO- $SiO_2$ equilibrium phase diagram showing the range of compositions of grains in the $MgSiO_x$ samples (bold line) in this study. The solid rectangles mark the average compositions of the round grains and irregular clusters (~50 wt.% MgO) and the small subhedral to large euhedral grains (~85 wt.% MgO). Reproduced from Ehlers (1972).

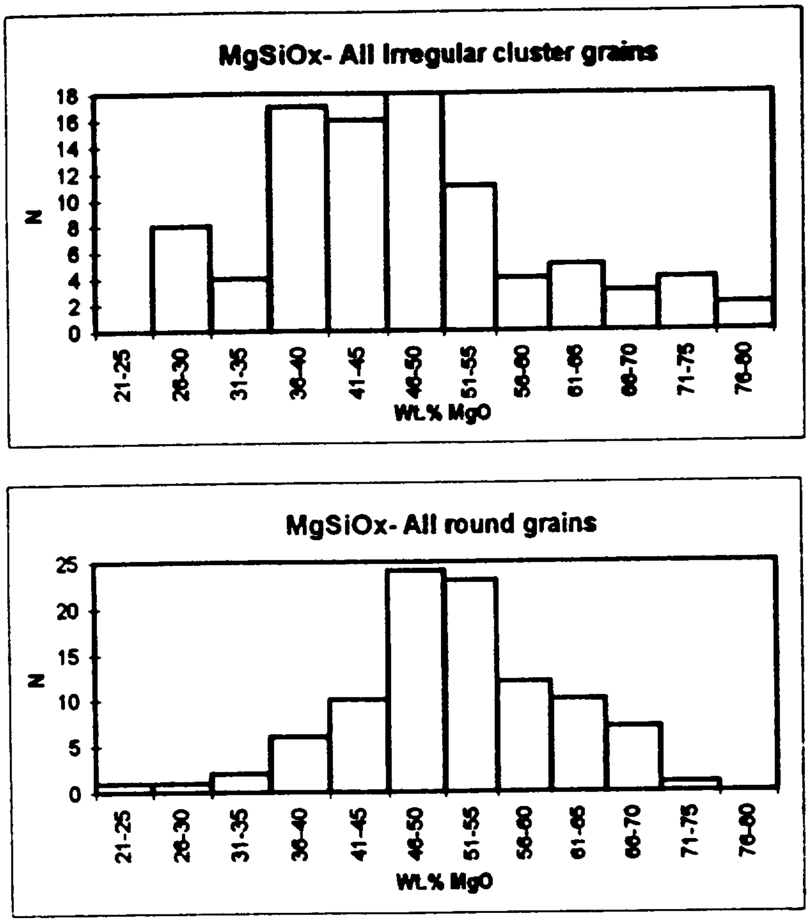

**Figure 4.16** Histograms showing the compositions of irregular cluster and round grains in the MgSiOx samples.

which correspond to electron diffraction and lattice fringe data for the round grains and irregular clusters. Secondly, the small subhedral to large subhedral to euhedral grains range from 70-100 wt.% MgO (Figure 4.15). They show diffraction data consistent with periclase and possibly forsterite, which is predicted by the phase diagram.

The MgSiO samples contain a large amount of crystalline material. The crystalline material could be attributed to autoannealing [cf. Sect. 1.4.2]. Subhedral to euhedral MgO-rich grains within the sample show rectangular, hexagonal and octagonal shapes. These different shapes are inconsistent with the identification that these grains are periclase-which is a macroscopic isometric mineral. This could be explained by the fact that grains dominated by kinetic processes do not have time to grow into an equilibrium shape of low index planes (i.e.- cubic). Therefore, small crystalline grains may grow by developing high-index planes that, given enough time, will grow out of existence, leading to equilibrium shapes (Doremus, 1985). Another possibility is that the grains are actually platey which is indicative of two-dimensional growth from intermediate supersaturations of the gas phases. Tilting experiments in the TEM were performed but did not produce conclusive results.

Another observation concerns the occurrence of grains with several different morphologies for the same chemical compositions. Silica grains are seen in clusters, patchy material, globules, smooth grains and rimmed grains. MgO grains may be subhedral and relatively small (50-60 nm) or euhedral and much larger (70 -100 nm). Round grains and irregular cluster grains also have similar compositions. Besides post-condensation processes, different morphologies for identical compositions may be due to processes and properties of the vapor phase such as supersaturation as a function of temperature and turbulence.

The log-normal size distributions of round grains, silica spheres, irregular clusters, and subhedral grains are accordant with the notion these grains grow by coagulation in which smaller grains combined to produce larger grains in a tendency to reduce high free energies.

## 4.5 CONCLUSIONS

(1) The presence of distinct chemical composition grains in discrete locations within the samples is consistent with a heterogeneous vapor phase at a nanometer-micron scale.

(2) Compositions of condensed grains follow the topology of the liquidus in the phase diagram for this system.

# CHAPTER 5. CONDENSATION IN THE Fe,MgSiO$_x$ SYSTEM

## 5.1 SAMPLE PREPARATION

This sample represents the first condensation study of a ternary-metal oxide condensate. The sample was produced by the vapor phase nucleation of SiO, Fe and Mg vapors in a $H_2$ atmosphere at ~ 80 Torr and 500 °C. The experiment proceeds similarly to that of the Mg-Si-O system which begins with the vaporization of Mg-metal chunks contained in a graphite boat within the furnace. As the Mg starts to vaporize, silane ($SiH_4$) and $O_2$ gases are introduced into the furnace. Fe vapors are introduced by bubbling hydrogen through $Fe(CO)_5$ liquid. The hydrogen flow gas mixes the vapors and condensation occurs as the gases flow into a collection chamber kept at 25 °C.

The chemical compositions of individual grains were calculated as combinations of $SiO_2$, MgO, and FeO (although there is diffraction evidence for ferric iron, $Fe_2O_3$, in this sample). Grain sizes are reported as *rms* sizes.

## 5.2 OBSERVATIONS

The condensed smoke is dominantly made up of chains of several small sub-circular grains that grade into more dense clusters. Some clustered areas (~1 *u*m in diameter) contain a dozen or more larger (~80 nm) round, droplet shaped grains. Isolated areas within the sample contain dark irregular shaped grains in dense clusters. Rare areas of the sample show subhedral to euhedral grains that are associated with clustered smoke grains.

The chemical compositions of individual grains are represented in the ternary diagram $SiO_2$-FeO-MgO as solid rectangles (Figure 5.1) The analyses cluster about the endmember compositions and areas on the joins between binary-oxide components including 50 wt.% MgO- 50 wt.% $SiO_2$, and 25 wt.% FeO - 75 wt.% $SiO_2$. The clusters of analyses are furthur constrained by morphological and mineralogical properties in the following summary:

### 5.2.1 High silica grains

1) 90-100 $SiO_2$ grains make up about 80% of the sample. This high-silica material condenses in a variety of morphologies including clusters, patchy material, globules, and both rimmed and smooth grains. The high-silica material invariably contains a small iron component (up to ~10 wt.% FeO), but any measurable MgO content (up to 2 wt.%) is rare. The clusters (Figure 5.2) have a fluffy texture and consist of smaller spherical grains that are aggregated together. The clusters are 100 to 97 wt.% $SiO_2$ and up to 3 wt.% FeO. The FeO component may be due to small (< 10 nm) dark domains within the cluster that give an Fe signal when probed. A second high-silica morphology is dense patchy material. These areas are compositionally up to 10 wt.% FeO and also show dark domains within the patchy material (Figure 5.3). A third and fourth morphology of silica-rich grains are rare rimmed grains and dense globules (Figure 5.4). The rimmed grains are ~100 wt.% $SiO_2$ while the dense globules contain up to 8 wt.% FeO.

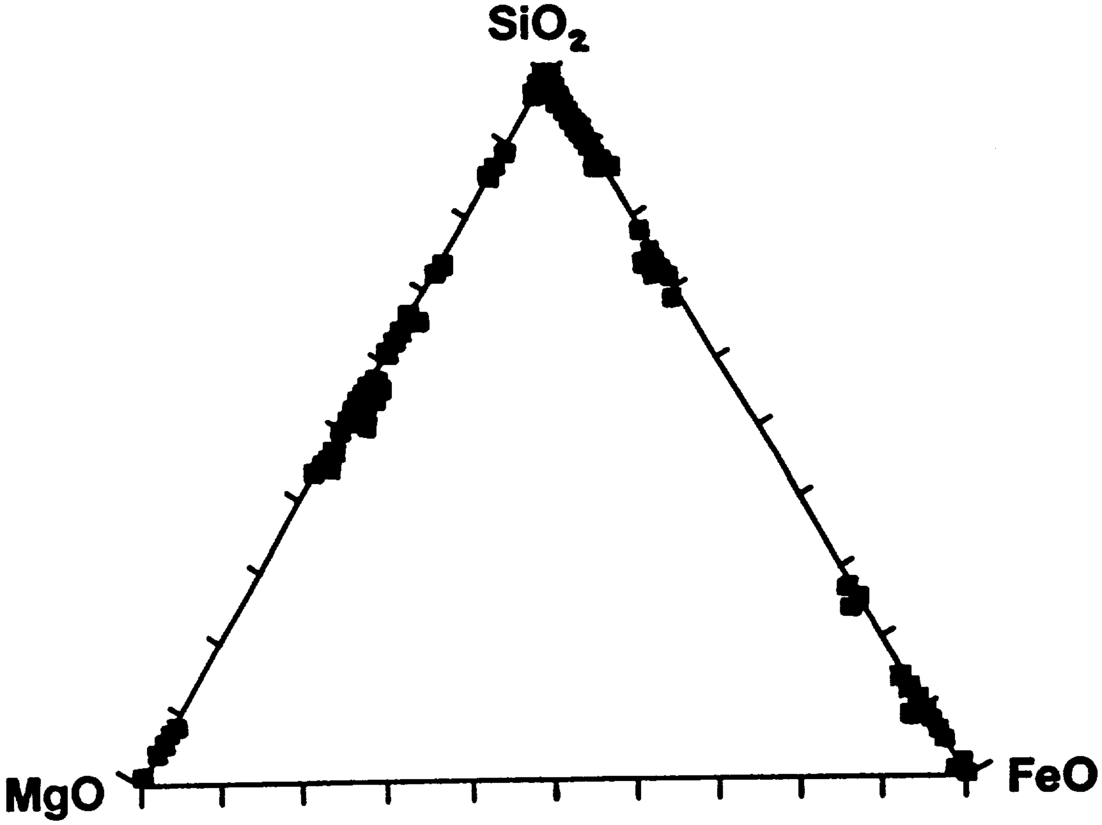

Figure 5.1 Ternary diagram $SiO_2$-FeO-MgO showing chemical compositions of grains in the Fe,$MgSiO_x$ sample.

**Figure 5.2** Transmission electron micrograph showing high-silica grains in dense clusters. The corresponding polycrystalline SAED pattern shows an orientation projected down the [2$\bar{2}$0] axis of cristobalite. The (111) and (113) maxima are identified.

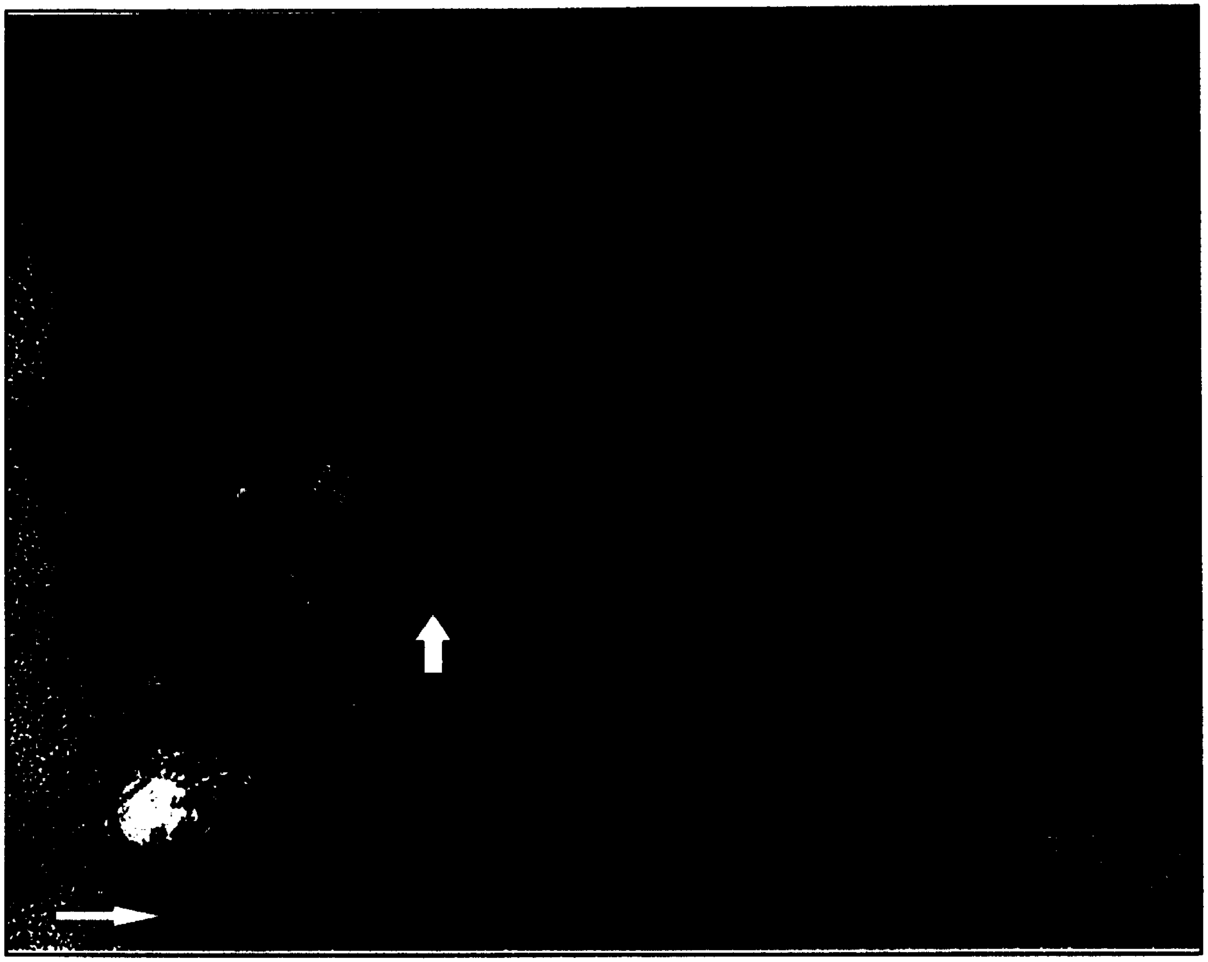

**Figure 5.3** Transmission electron micrograph showing patchy silica material. Dark domains are “Fe” grains (white arrows) within the silica materials.

**Figure 5.4** Transmission electron micrograph showing a high silica globule along with rimmed pure silica grains in epoxy on a holey carbon film substrate. The corresponding polycrystalline SAED pattern is from the globule only, and shows an orientation projected down the axis [220] of cristobalite. The (111) and (113) maxima are identified.

All the preceeding 90-100 wt.% $SiO_2$ materials give weak diffraction maxima that are consistent with an $SiO_2$ phase, probably cristobalite or tridymite, and possibly an "FeO" phase, either maghemite or magnetite (Table 5.1, col. A). SAED patterns also reveal that the high silica clusters and the globules consistently show weak maxima that corresponded to the (111) and (113) planes of cristobalite (cf. Figures 5.2, 5.4).

The fifth morphology of silica-rich material is rare, smooth (semi)-circular grains that are ~165 nm in diameter. The grains are pure silica and show no diffraction maxima, indicating an amorphous material.

### 5.2.2 FeSiO grains

**2. High-FeO FeSiO grains** range from 75 to 100 wt.% FeO (Figure 5.1). They occur in two morphologies in which the first is dense clusters of irregular FeO grains measuring ~34 nm in diameter that are contained within and around silica materials. These clusters give weak diffraction (Table 5.1, col. B) that is accordant with maghemite ($\gamma$- $Fe_2O_3$) or magnetite ($Fe_3O_4$). A second morphology of high-FeO grains is rare, large (up to 350 nm in diameter) isolated grains. Figure 5.5 shows a large ~88 wt.% FeO grain with a corresponding single-crystal diffraction pattern that matches magnetite.

**3. FeSiO grains** occur as small subhedral to subrounded grains in chain-like structures that are easily recognized throughout the sample (Figure 5.6). The chemistry of these grains is 70-78 wt.% silica and 22-30 wt.% FeO with an average composition at 26 wt.% FeO. Diffraction maxima from these grains may be consistent with a silica polymorph,

Table 5.1 Fe,MgSiOx- diffraction interplanar spacings (nm) and interplanar spacings for minerals along the binary joins of the Fe-Mg-Si-O system

| A. >90 wt.% $SiO_2$ | B. >95 wt.% FeO | C. Chainy 26% FeO | D. Round x=44% MgO | E. Subhedral MgO | Tridymite ($SiO_2$) 18-1170 | Cristobalite ($SiO_2$) 11-695 | Maghemite ($\gamma$-$Fe_2O_3$) 25-1402 | Magnetite ($Fe_3O_4$) 19-629 | Periclase (MgO) 4-829 | Forsterite ($Mg_2SiO_4$) 34-189 | Ortho-Enstatite ($MgSiO_3$) 22-714 | Clino-Enstatite ($MgSiO_3$) 35-610 | Fayalite ($Fe_2SiO_4$) 34-178 | Ortho-Ferrosilite ($FeSiO_3$) 29-721 | Clino-Ferrosilite ($FeSiO_3$) 17-548 |
|---|---|---|---|---|---|---|---|---|---|---|---|---|---|---|---|
| | | | | | | | | | | | | | | 0.904 | |
| | | | | | | | 0.791 | | | | | | | | |
| | | | | | | | 0.694 | | | | | | | | |
| | | | | | | | | | | | | | | 0.646 | 0.646 |
| | | | | | | | | | | | 0.633 | 0.634 | | | |
| | | | | | | | 0.59 | | | | | | | | |
| | | | | | 0.543 | | | | | | | | | | |
| | | | | | | | 0.533 | | | | | | | | |
| | | | 0.52 | | | | | | | | | | 0.524 | | |
| | | 0.51 | | | | | | | | 0.51 | | | | | |
| | | | | | | | 0.482 | 0.485 | | | | | | | |
| | | | | | | | | | | | | | | 0.461 | 0.461 |
| | | | | | | | | | | | 0.443 | 0.441 | | | |
| | | | | 0.43 | 0.437-0.433 | | | | | 0.43 | | 0.437 | 0.438 | | |
| | | | | | 0.427 | | 0.429 | | 0.42 | | | 0.429 | | | |
| | | | | | 0.412-0.41 | | | | | | | | | | |
| | | | | | 0.408-0.40 | 0.405 | | | | | 0.403 | 0.405 | | | |
| | | | 0.39 | | | | | | | | | | 0.397 | | |
| | | | | | 0.387-0.38 | | | | | 0.388 | | | | | |
| | | | | 0.37 | | | 0.373 | | | 0.372 | | | 0.378 | | |
| | | | | | 0.361 | | | | | | | | | | |
| | | | 0.35 | | | 0.352 | | | | 0.35 | | 0.353 | 0.355 | | |
| | | | | | 0.343-0.34 | | 0.34 | | | 0.348 | | | | 0.343 | |
| | | | | | 0.337-0.333 | | | | | | 0.331 | 0.332 | | | 0.335 |
| | 0.32 | | | | 0.328-0.32 | | 0.32 | | | | | 0.328 | | 0.323 | 0.323 |
| 0.31 | | | 0.31 | | 0.316 | 0.314 | | | | | 0.318 | 0.317 | | | |
| | | | | | 0.307 | | | | | | | 0.304 | 0.306-0.304 | 0.3 | 0.303 |
| | | | | | 0.3-0.298 | | 0.295 | 0.296 | | 0.300-0.299 | 0.295 | 0.298 | | 0.291 | 0.291 |
| 0.28 | | | | | | 0.284 | | | | | 0.288-0.283 | 0.287-0.28 | 0.283 | 0.286 | |
| | | 0.27 | | | 0.276 | | 0.278 | | | 0.277 | 0.271 | 0.277 | | 0.275 | |
| | | | | | | | 0.264 | | | | | | 0.263-0.26 | | 0.26 |
| | 0.25 | | 0.25 | | 0.259 | | 0.251 | 0.253 | | | 0.254 | 0.258-0.25 | 0.257-0.25 | 0.259 | |
| | | | | 0.24 | 0.249-0.245 | 0.249-0.247 | 0.241 | 0.242 | 0.243 | 0.246 | 0.249-0.247 | 0.247-0.24 | 0.241 | 0.241 | 0.248 |
| | | | 0.23 | | 0.237-0.23 | 0.234 | 0.232 | | | 0.235-0.232 | 0.239-0.232 | 0.238 | 0.235-0.23 | 0.23 | |
| | | | | | | | 0.223 | | | 0.226-0.225 | 0.228-0.224 | 0.228-0.22 | | 0.227 | |
| 0.21 | | | 0.21-0.20 | | 0.213-0.209 | 0.212 | 0.21 | | 0.211 | 0.216 | 0.212-0.21 | 0.214-0.21 | 0.219-0.215 | 0.216 | 0.216 |
| | 0.2 | | | | 0.205 | 0.202 | | 0.209 | | 0.203 | 0.203-0.199 | 0.209-0.2 | 0.207 | 0.208-0.203 | 0.204 |
| | | | | | | | | | | | | | | | |
| | | | | | | | | | | | | | | | |
| | | | | | | | | | | | | | | | |
| | | | | | | | | | | | | | | | |

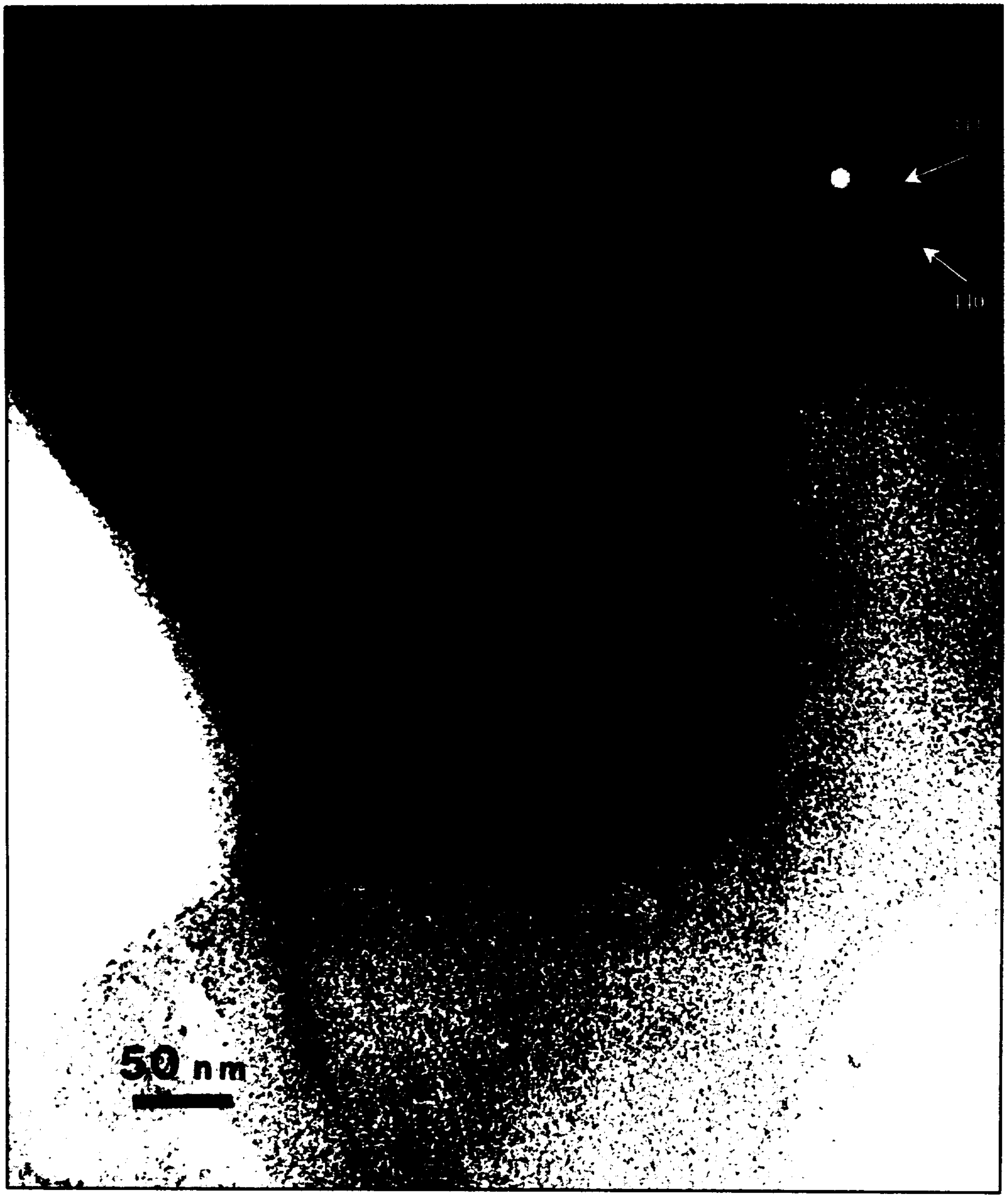

**Figure 5.5** Transmission electron micrograph showing a $\underline{8}8$ wt.% FeO grain with corresponding single-crystal pattern projected down the $[\bar{1}12]$ axis of magnetite. The (311) and (440) maxima are identified. The grain is contained in an epoxy thin section that is slightly folded to the left side of the grain.

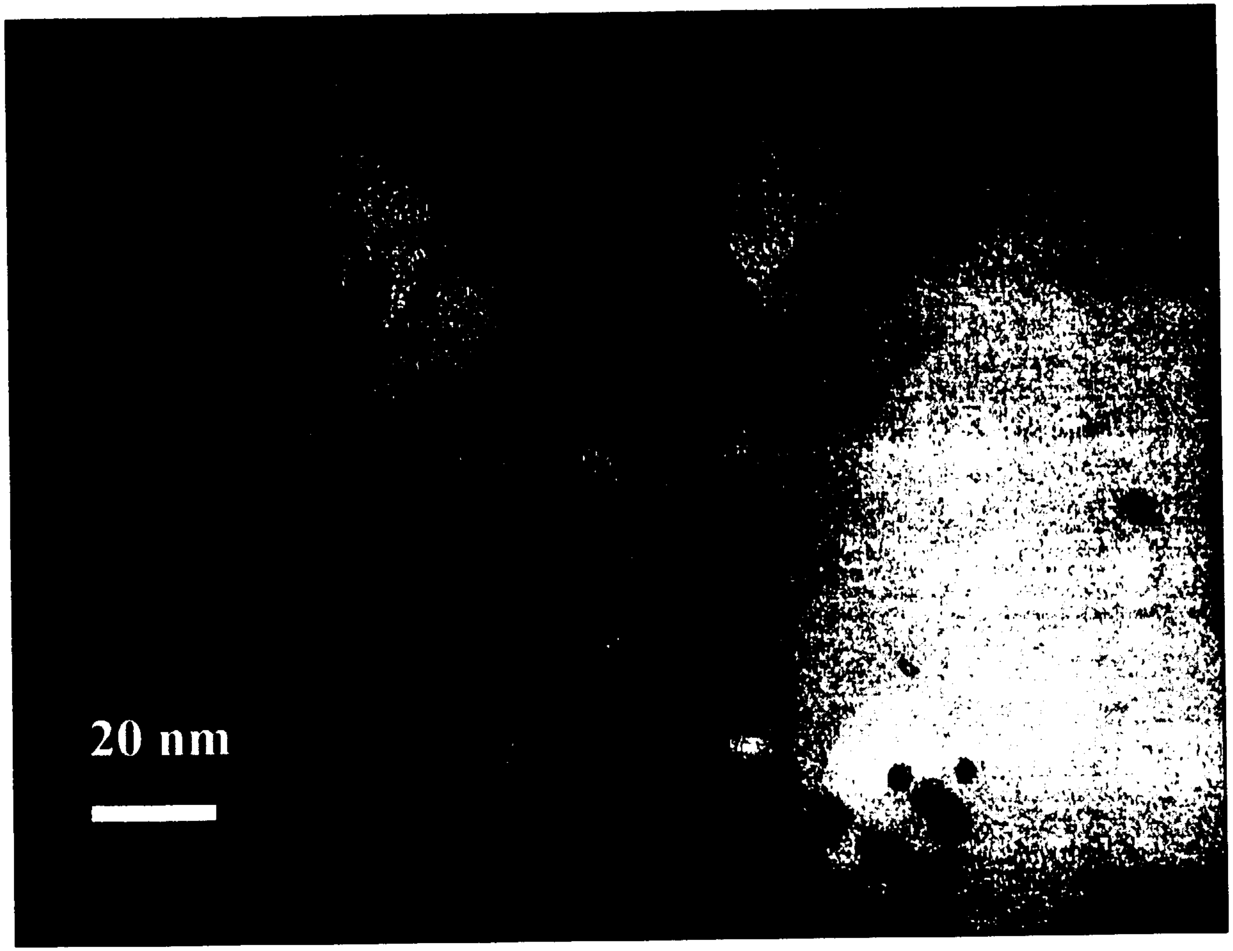

**Figure 5.6** Transmission electron micrograph of subhedral FeSiO grains in chain-like morphologies. The darker grains are crystalline and in the optimum Bragg condition.

tridymite or cristobalite, and/or an FeSiO phase, fayalite (Table 5.1, col. C). Individual grains range from 10 - 30 nm in size with a mean size of 17 nm. The grains fit a log-normal distribution with $R^2 = 0.91$ (Figure 5.7).

### 5.2.3 MgSiO grains

4. MgSiO grains are found in small areas of ~ 20 grains or more, throughout the sample. The grains appear as round droplets within and around high-silica fluffy material (Figure 5.8). The grains range from 45-73 wt.% $SiO_2$ and up to 55 wt.% MgO with an average composition of 43 wt.% MgO. Strong diffraction maxima are accordant with forsterite and clinoenstatite, or orthoenstatite (Table 5.1, col. D). The round grains are 40-130 nm in diameter with an average size of 78 nm. In a plot of log-size the grains show a normal distribution with $R^2 = 0.95$ (Figure 5.9).

5. Rare high-MgO grains (Figure 5.10) occur as subhedral to euhedral rectangular shapes that are ~100 wt.% MgO. The grains range from 70 - 140 nm in diameter and show diffraction maxima in agreement with periclase and forsterite (Table 5.1, col. E).

## 5.3 DISCUSSION

The abundance of end-member composition material in the $Fe,MgSiO_x$ sample is understandable. The previous samples in this thesis [cf. Chapters 3, 4] have shown that endmember grains are invariably present regardless of the chemical system. Previous results also show that mixing will take place between silica and magnesia [cf. Sect. 4.2]

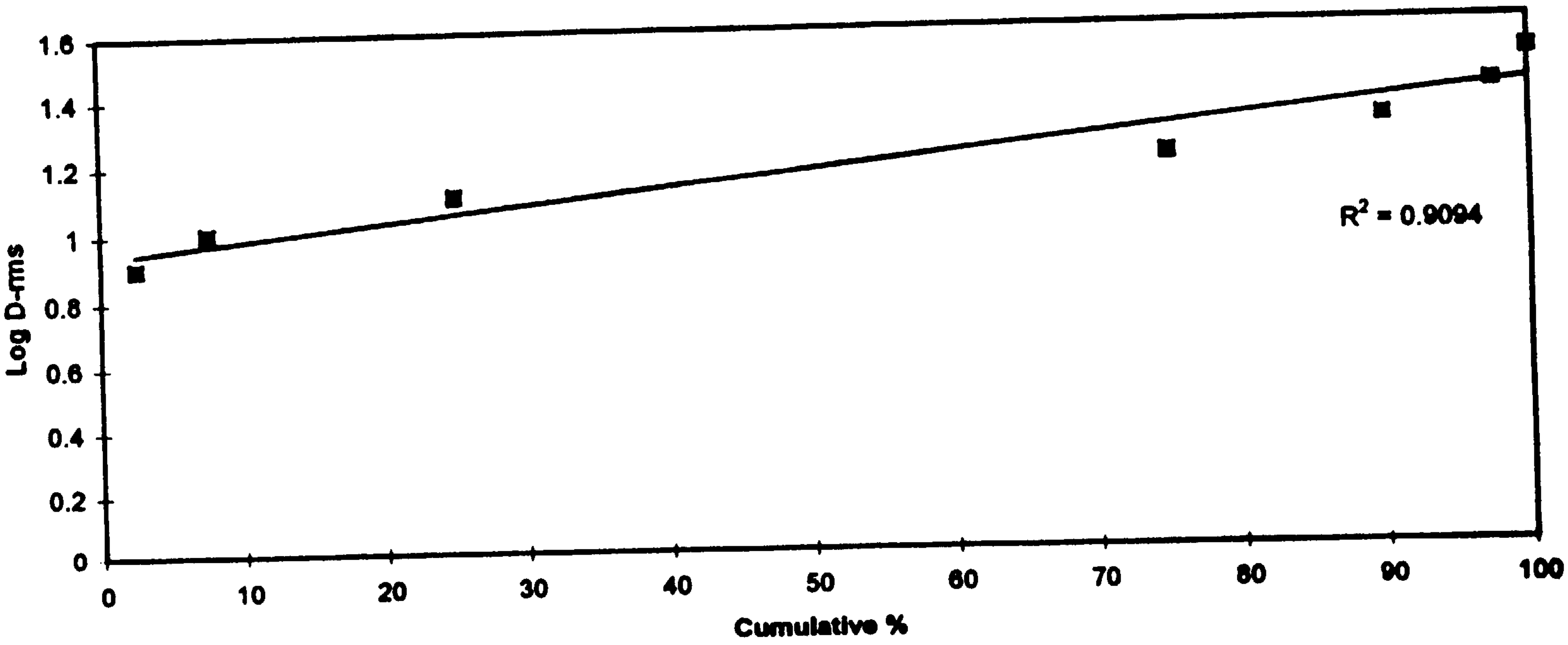

**Figure 5.7** Log D (size) distribution for 40 chainy FeSiO grains fit to a log-normal distribution.

**Figure 5.8** Transmission electron micrograph of round MgSiO grains within silica material (white arrows). The SAED pattern shows single crystal maxima of (020) and (131) planes of forsterite. Composite crystal maxima (open white arrow) are due to the silica material.

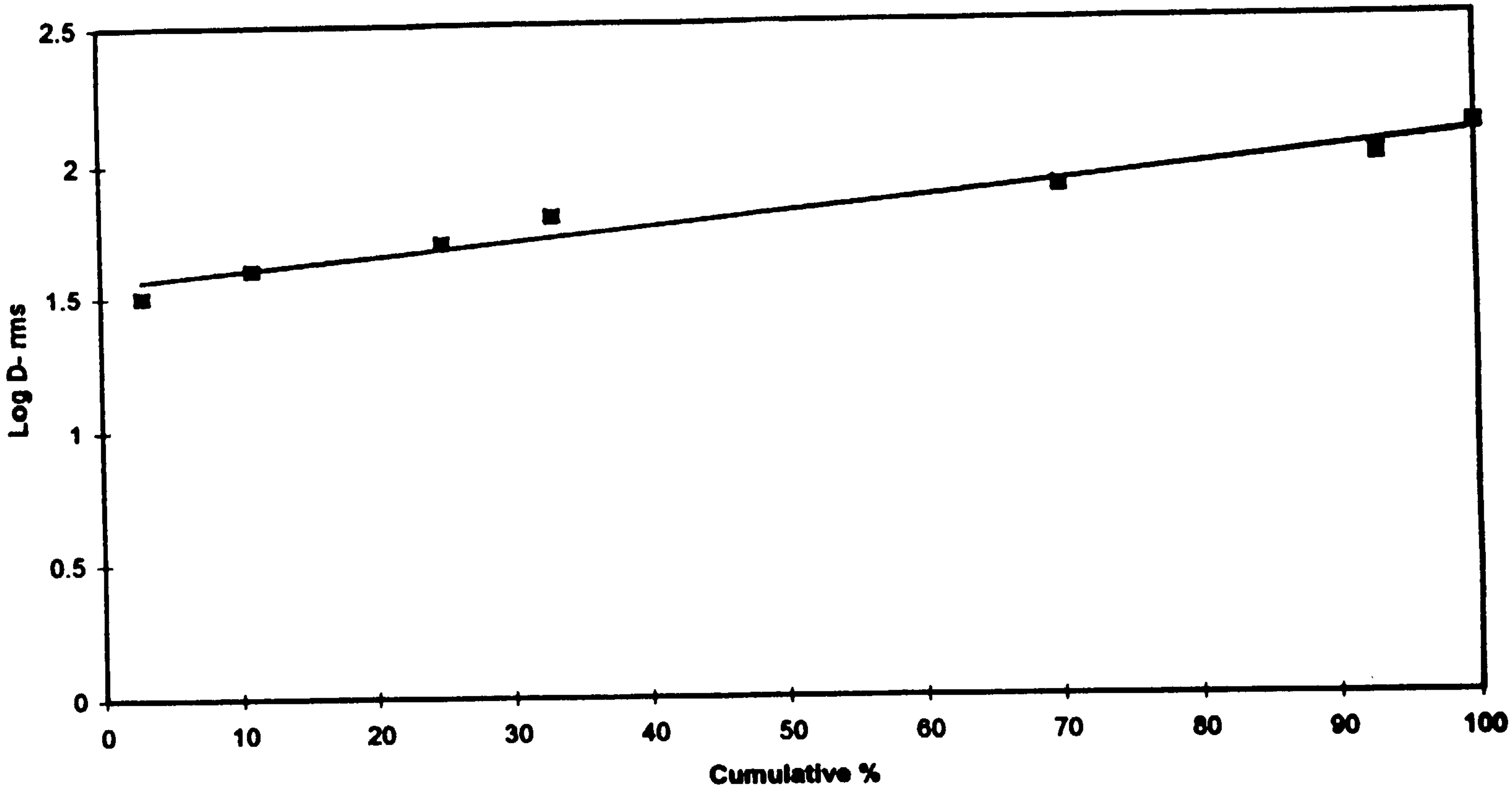

Figure 5.9 Log-D (size) of 30 round grains fit to a log-normal distribution.

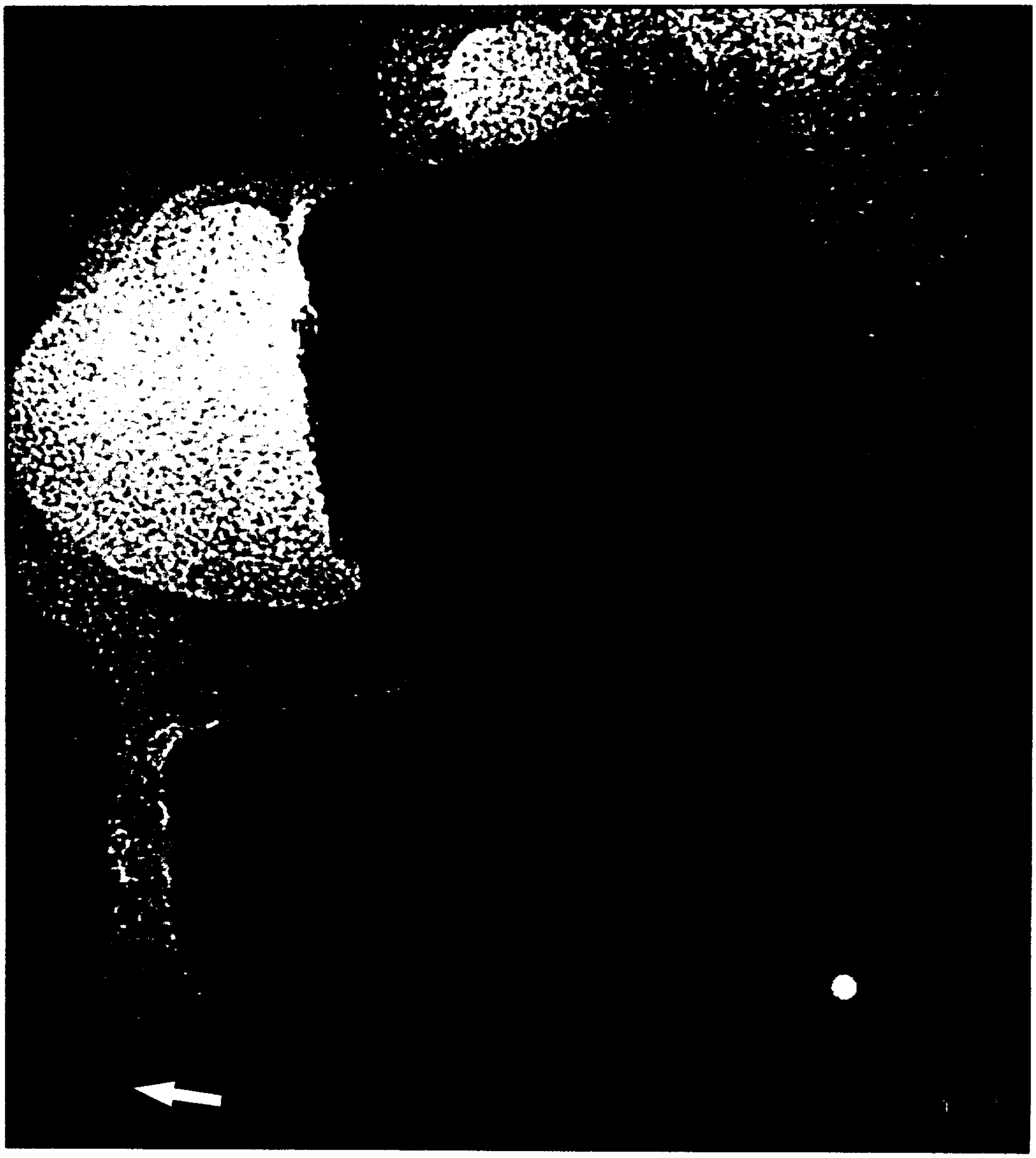

**Figure 5.10** Transmission electron micrograph of rare euhedral MgO grains and silica rich material (white arrow). The corresponding SAED pattern shows a single crystal pattern projected down the [1$\bar{1}$0] axis of periclase. The (111) and (220) maxima are identified.

and silica and iron vapors [cf. Sect. 3.2] we also see this type of mixing in the Fe,MgSiO$_x$ sample. Figure 5.11 shows the compositions of Fe,MgSiO$_x$ grains in the binary oxide sytems FeO-SiO$_2$, and MgO-SiO$_2$ for better comparison with the samples FeSiO and MgSiO [cf. Sect. 3.2, 4.2]. It is clear that the condensed grains in this Fe,MgSiO$_x$ sample mimic those in the binary oxide systems based on mineralogy, morphology and chemistry. First of all, the endmember grains in the Fe,MgSiO$_x$ are similar to those found in the previous samples. The FeO grains (maghemite or magnetite) are similar to those found in the original FeSiO sample [cf. Sect. 3.2], and the MgO euhedral grains (periclase) appear very much like those found in the MgSiO sample [cf. Sect. 4.2], and have grain sizes (i.e. 70-140 nm) within the range of those found in that sample. Also, the high-silica morphologies such as clusters, patchy material, and globules are accordant with silica morphologies in the MgSiO and FeSiO samples, and the dark domains within the silica clusters resemble those found in the FeSiO sample [cf. Sect. 3.2]. The mixed composition MgSiO and FeSiO grains also mimic those found in the binary oxide samples. The round Mg-SiO grains are similar in size, shape and composition (25-56 wt.% MgO) to the round grains in the MgSiO$_x$ samples [cf. Sect. 4.2]. Both show grain sizes from ~30 to 150 nm, have log-normal size distributions, and show diffraction maxima consistent with forsterite and orthoenstatite or clinoenstatite. Lastly, the subhedral to subrounded chainy silica-rich iron grains in this Fe,MgSiO$_x$ sample are similar to those seen in the FeSiO sample [cf. 3.2]. Both are contained in chain-like structures, have similar grain sizes, and give weak

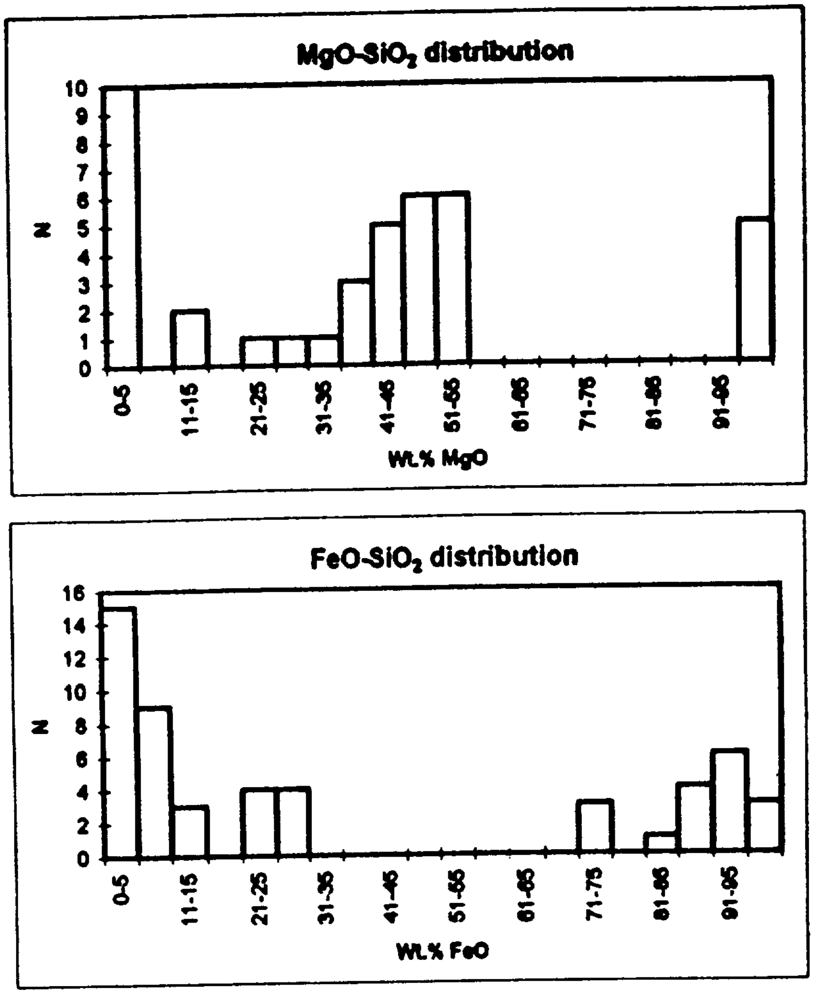

**Figure 5.11** Histograms showing the distributions of Fe,MgSiOx grains in the binary systems $MgO-SiO_2$ and $FeO-SiO_2$.

diffraction data corresponding to a silica phase, tridymite or cristobalite and a Fe rich phase, fayalite and/or maghemite, magnetite.

The absence of mixed iron and magnesium grains may be an experimental artifact. When the Fe vapors are introduced into the furnace they first encounter oxygen and silica gas. In the time it takes the iron vapor to reach the magnesium vapors, it is probably significantly depleted. Another possibility is that magnesium and iron condense in the furnace as metals, and become oxidized in the collection chamber. In a previous ternary-oxide study Fu and Rietmeijer (1994) analyzed a thermally annealed MgSiO smoke contaminated with Fe-metal grains. They found fayalite and ferrosillite with variable Fe-ratios, rare laihunite and magnesioferrite alongside or coexisting with forsterite, enstatite and tridymite. The Fe minerals formed from their magnesium counterparts as a function of annealing time at 727 °C with (partial) evaporation and condensation of a metallic-Mg vapor. The Fe,$MgSiO_x$ sample in this study does not reflect any reaction between Mg and Fe and suggests that thermal annealing might be necessary to promote the formation of iron magnesium silicates.

Regardless of the absence of iron-magnesium silicates, the compositions present in this Fe,$MgSiO_x$ sample behave according to the phase diagram MgO-$SiO_2$- $Fe_3O_4$ (Figure 5.12). First, all endmember compositions are present and the phases identified (cristobalite, periclase, magnetite and/or maghemite) are consistent with the phase diagram. The mixed-oxide binary compositions also obey the phase diagram. The round grains have an average of 44 wt.% MgO which falls very near the olivine and pyroxene stability fields, and diffraction from these grains suggest forsterite and enstatite, or

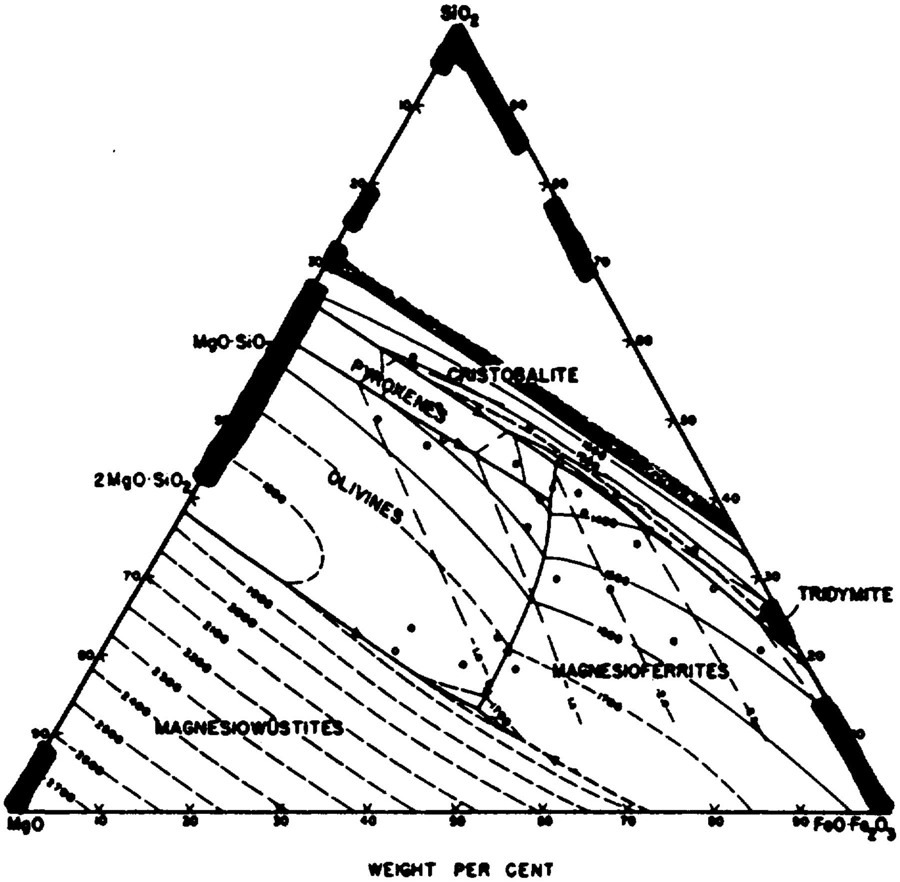

**Figure 5.12** The MgO-SiO$_2$- Fe$_3$O$_4$ ternary phase diagram with the compositions of Fe,MgSiO$_x$ grains indicated by solid black lines. Stippled dark areas are inferred two-liquid regions. Reproduced from Muan and Osborn (1956).

clinoenstatite. The FeSiO grains show compositional peaks at 9 and 26 wt.% FeO. These compositions fall within the cristobalite stability field, which is consistent with the SAED data for these grains.

Another important observation from this sample is that high silica clusters and globules show these crystalline grains all in the same diffracting orientation. If these grains condensed as crystals it is highly improbable that deposition into clusters would occur with a preferred orientation. Instead it is more likely that crystallization was a post-condensation event (autoannealing), occurring after the grains were deposited into clusters and globules.

## 5.4 CONCLUSIONS

Conclusions for the Fe,MgSiO$_x$ system are as follows: 1) end-member grains readily form along with mixed MgSiO and FeSiO grains. Mixed Mg and Fe grains do not form and this could be explained as an experimental artifact wherein Fe vapors are depleted before reaching Mg vapors, and 2) Condensed grains show similar chemical, mineralogic and morphologic properties to condensate studies in binary metal-oxide systems suggesting vapor phase condensation experiments are repeatable, and 3) the condensed grains are again constrained by the appropriate phase diagrams.

# CHAPTER 6. AEM, XRD, AND IR ANALYSES OF AN Al-Si-O CONDENSATE ANNEALED FOR 2 HOURS AT ROOM TEMPERATURE UP TO 1100° C

* The research described in this chapter was given as an oral presentation at the 59th Annual Meteoritical Society Meeting in Berlin, Germany: Karner J.M., Rietmeijer F.J.M., and Janeczek J. (1996) AEM, XRD, and IR analyses of an AlSiO condensate annealed for two hours at room temperature up to 1100 °C. *Meteoritics and Planet. Sci. 31*, A69.

## 6.1 SAMPLE PREPARATION

The sample was produced in the condensation flow apparatus [cf. Figure 1.1] by mixing $SiH_4$ and the liquid $Al(CH_3)_3$ with $O_2$ in a $H_2$ atmosphere at approximately 80 Torr and a temperature of ~ 500 °C. The $SiH_4$ and the $Al(CH_3)_3$ were premixed in $H_2$ before entering the furnace, while $O_2$ was added separately using a tube entering the center of the mixing chamber. Condensation is induced by a cool stream of $H_2$ flowing into a collection chamber kept at 25 °C. The annealed samples were produced by thermally annealing in air at 100, 210, 300, 500, 600, 700, 800, and 1100° C, each for two hours.

Infrared (IR) analysis was performed by Dr. Jerzy Janik, (Department of Chemistry, UNM), and interpreted for the first author by Dr. Joe Nuth (NASA Goddard Space Flight Center). X-ray diffraction (XRD) data was collected and interpreted by Dr.

Janusz Janeczek when he was a "visiting scholar" at the Department of Earth and Planetary Sciences, UNM). IR and XRD analyses were performed on all samples. AEM analyses were performed on the original condensate and on the sample annealed at 1100° C for 2 hours.

## 6.2 OBSERVATIONS

### 6.2.1 XRD and IR data

The IR data show the original condensate is dominated by Al-O bonds and minor SiO features. Oxidation during annealing in air is reflected by changes in the length and bending modes of O-Si-O bonds. At 1100 °C semi-crystalline $SiO_2$ features are seen in the IR spectra. All samples are x-ray amorphous except for low intensity peaks at d = 0.252-0.255 nm which may be related to tiny amounts of cristobalite between 210 to 500 °C. Above 600 °C the crystalline component diminishes and is absent in samples above 700 °C. Figure 6.1 shows the XRD spectra from the unannealed and 300 °C samples, and Table 6.1 summarizes IR, XRD, and selected area electron diffraction data (SAED).

### 6.2.2

### AEM data

The original condensate and the 1100 °C sample have a typical smoke texture (Figure 6.2) consisting of (sub)-circular grains with compositions ranging from 0 to ~70

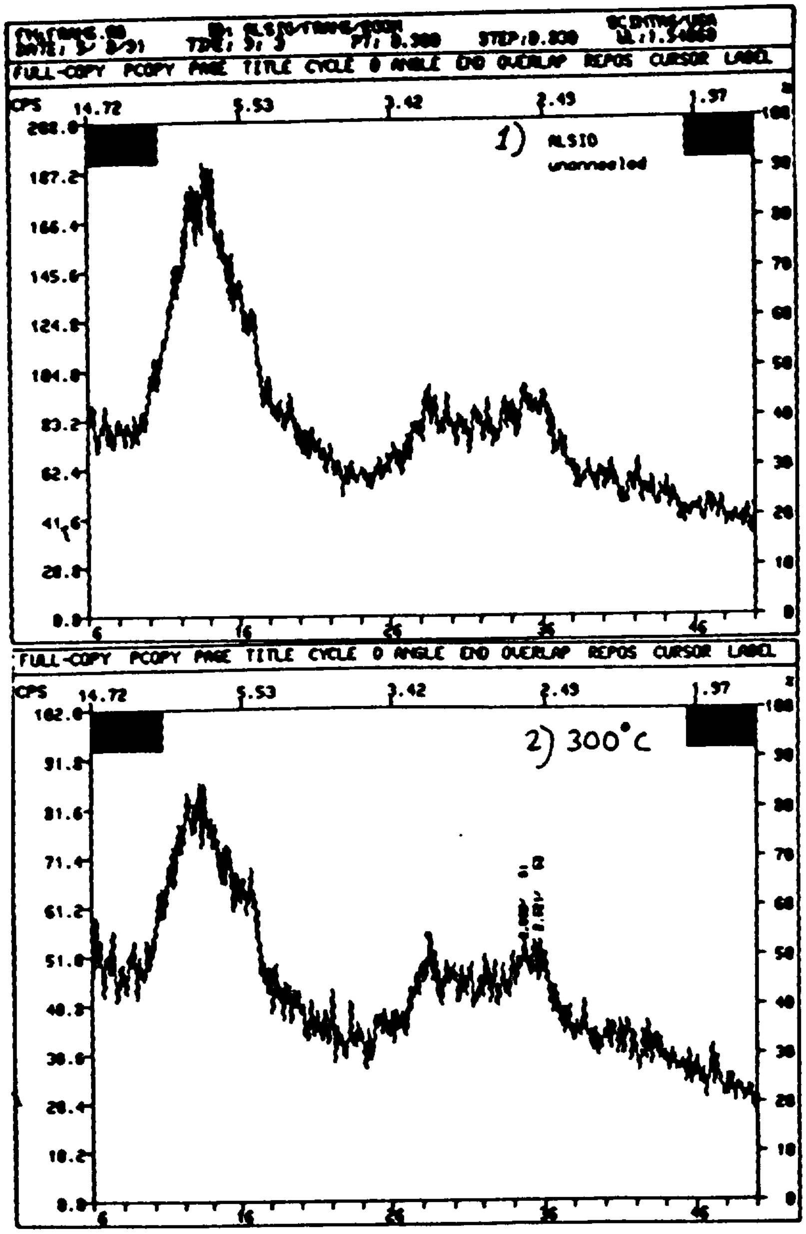

**Figure 6.1** X-ray diffraction spectra from the 1) unannealed sample and 2) the sample annealed at 300 °C. Both spectra show a predominantly x-ray amorphous material, although the spectra of the annealed sample shows a peak at 2.52- 2.58 that can be attributed to small amounts of cristobalite.

**Table 6.1** Comparison of IR, XRD and SAED data for the AlSiO samples.

| AlSiO sample | IR | XRD | SAED |
|---|---|---|---|
| Unannealed | Al-O bonds, minor Si-O features | Amorphous | Cristobalite, tridymite, and sillimanite, mullite |
| 100 °C to 800 °C | Changing in length and bending modes of O-Si-O bonds | Small amounts of cristobalite between 210 to 500 °C | No data |
| 1100 °C | Semi-crystalline $SiO_2$ features | Amorphous | Cristobalite, tridymite, and sillimanite, mullite |

wt.% $Al_2O_3$ (Figure 6.3). The bulk of both samples is mottled grains in fluffy clusters that grade into loose chains. Small chains of rimmed grains occur between, and sometimes connect, mottled grains (Figure 6.4) and makeup the rest (~15 %) of the sample. Mottled and rimmed grains are chemically and morphologically distinct and occur in both the unannealed and 1100 °C sample.

(1) Rimmed grains (0-12 wt.% $Al_2O_3$) are amorphous except for a well-defined 8.5 nm thick rim of 0.7 nm lattice fringes (Table 6.2) that are consistent with the β-cristobalite *hkl* plane (001) (Figure 6.5). The rimmed grains, 32 - 79 nm (mean = 54 nm), have indistinguishable log-normal size distributions (Figure 6.6). Both samples have elongated strands of fused grains that are sometimes outlined by a continuous single rim. Isolated rimmed grains in the unannealed sample have 0 and 6.9 wt.% $Al_2O_3$, but in the annealed sample they occur mostly in coagulated clusters (~9 wt.% $Al_2O_3$) wherein individual grains are only somewhat discernable (Figure 6.5). Electron diffraction from the rimmed grains (Table 6.2) show weak maxima that are consistent with cristobalite-although the presence of tridymite cannot be ruled out.

(2) Mottled grains (Figure 6.7) show compositional peaks at 23, 38.5, 51, and 59.5 wt.% $Al_2O_3$ in the unannealed condensate and rare entities with a stoichiometric mullite composition (70 wt.% $Al_2O_3$). Mottled grains in the 1100 °C sample show peaks at 23, 39, and 58.5 wt.% $Al_2O_3$. Table 6.3 shows the histograms based on the mottled grains populations in the two samples. Mottled grains (30-150 nm) in both samples have log-normal size distributions with a mean of 90 nm (Figure 6.8). The grains are generally

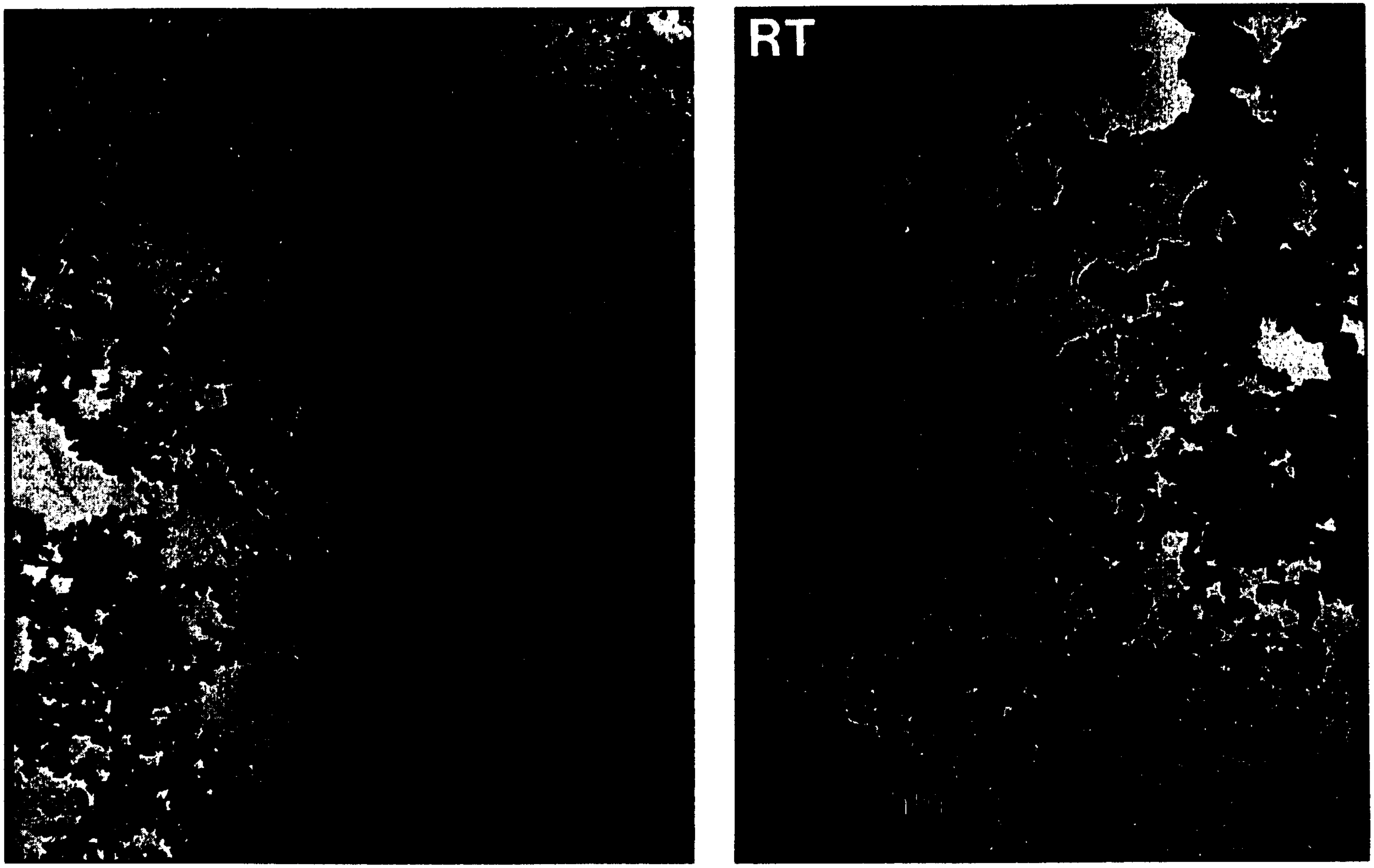

**Figure 6.2** Transmission electron microscope image of the original AlSiO (RT) condensate with a fluffy texture of nanometer size grains in chains and clusters. The right and left panels show the condensate is heterogeneous in grain size and morphology on a nanometer scale. The folded substrate is a holey carbon film in the left hand panel. RT denotes Room Temperature.

**Table 6.2** AlSiO unannealed and 1100 C/2h electron diffraction and lattice fringe interplanar spacings (nm) and interplanar spacings of possible minerals in the Al-Si-O system from the XRD files.

| Rimmed grains | | Mottled grains | | Tridymite | Cristobalite | Mullite | Sillimanite | Corundum |
|---|---|---|---|---|---|---|---|---|
| 0-12 wt.% $Al_2O_3$ | | 40-60 wt.% $Al_2O_3$ | | $(SiO_2)$ | $(SiO_2)$ | $(Al_6Si_2O_{13})$ | $(Al_2SiO_5)$ | $(Al_2O_3)$ |
| | | | | 14-260 | 11-695 | 15-776 | 22-18 | 10-173 |
| | | | | 0.82 | | | | |
| 0.7 (fringes) | | | | | | 0.76-0.75 | 0.767-0.75 | |
| | | | | | 0.69 | | | |
| | | | | | | | 0.577 | |
| | | | | 0.543 | | | | |
| | | 0.53 | | | | 0.539 | 0.536 | |
| | | | | | | | | 0.476 |
| | | | | | | | 0.458 | |
| | | | | 0.437-0.433 | | | | |
| | | | | 0.427 | | | | |
| | | | | 0.412-0.41 | | | | |
| | | | | 0.408-0.40 | 0.405 | | | |
| | | | | 0.387-0.38 | | | | |
| | | | | | | 0.377 | 0.374 | |
| | | | | 0.361 | | | | |
| | | | | | 0.352 | | | |
| | | 0.34 | | 0.343-0.34 | | 0.343 | 0.342 | 0.348 |
| | | | | 0.37-0.33 | | 0.339 | 0.337 | |
| | | | | 0.328–0.32 | | | 0.32 | |
| 0.31 | | 0.31 | | 0.316 | 0.314 | | | |
| | | | | 0.307 | | | | |
| | | | | 0.299-0.294 | | | | |
| 0.28 | | 0.28 | | | 0.284 | 0.289 | 0.29-0.285 | |
| | | | | 0.276 | | | | |
| | | | | | | 0.269 | 0.268 | |
| | | | | 0.259 | | 0.254 | 0.254 | 0.256 |
| 0.24 | | 0.24 | | 0.249-0.245 | 0.249-0.247 | 0.243 | 0.242 | |
| | | | | 0.233-0.23 | 0.234 | 0.239-0.23 | 0.232-0.29 | 0.238 |
| | | | | | | 0.221 | 0.22 | |
| | | 0.21 | | 0.213-0.21 | 0.212 | 0.212 | 0.211 | 0.217 |

**Table 6.3** Statistical data for the mottled grain populations (medians) in the unannealed and 1100 °C samples. All data in wt.% $Al_2O_3$. N=observations, R= range, x= average, sd= standard deviation

| AlSiO sample | Populations (medians) |
|---|---|
| **Unannealed** | **23** N= 12, R= 15-32, x= 27, sd= 4.5 |
| | **38.5** N= 37, R= 33-47, x= 41.4, sd= 3.9 |
| | **51** N= 31, R= 48-58, x= 52.3, sd= 3.0 |
| | **59.5** N= 22, R= 58-72, x= 62.5, sd= 3.8 |
| **1100 °C** | **23** N= 34, R= 15-33, x= 25.4, sd= 4.7 |
| | **39** N= 68, R= 34-54, x= 41.6, sd= 6.9 |
| | **58.5** N= 31, R= 55-69, x= 60.4, sd= 4.8 |

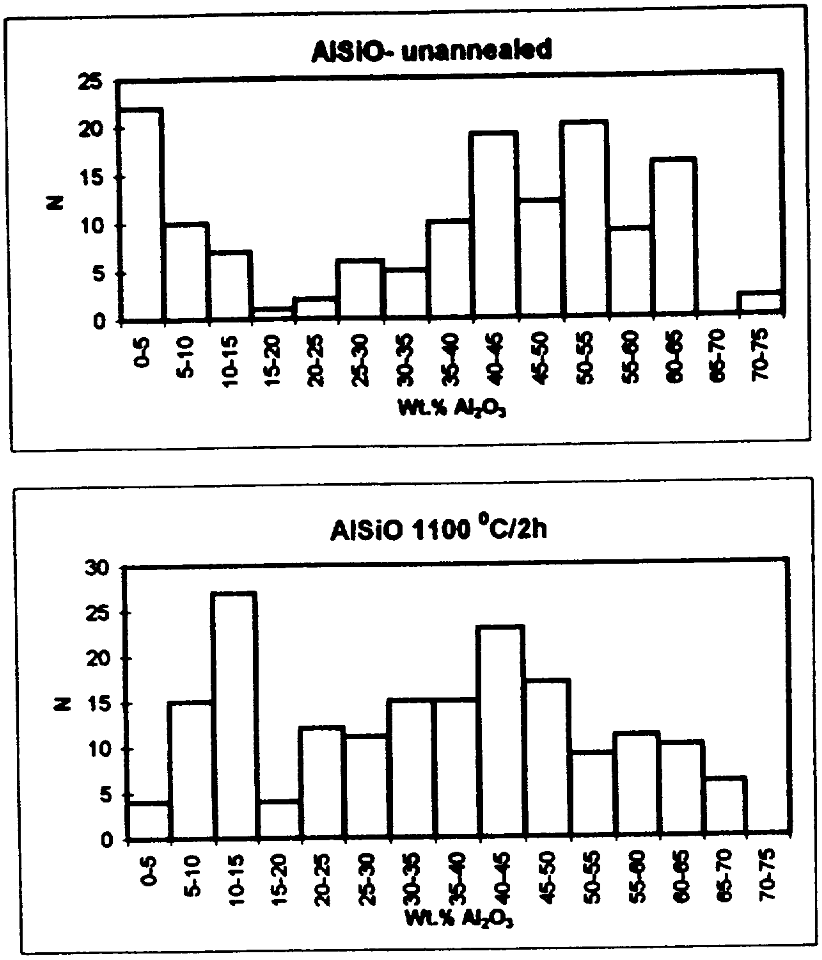

**Figure 6.3** Histogram showing the chemical distributions of grains in the condensed and annealed AlSiO samples.

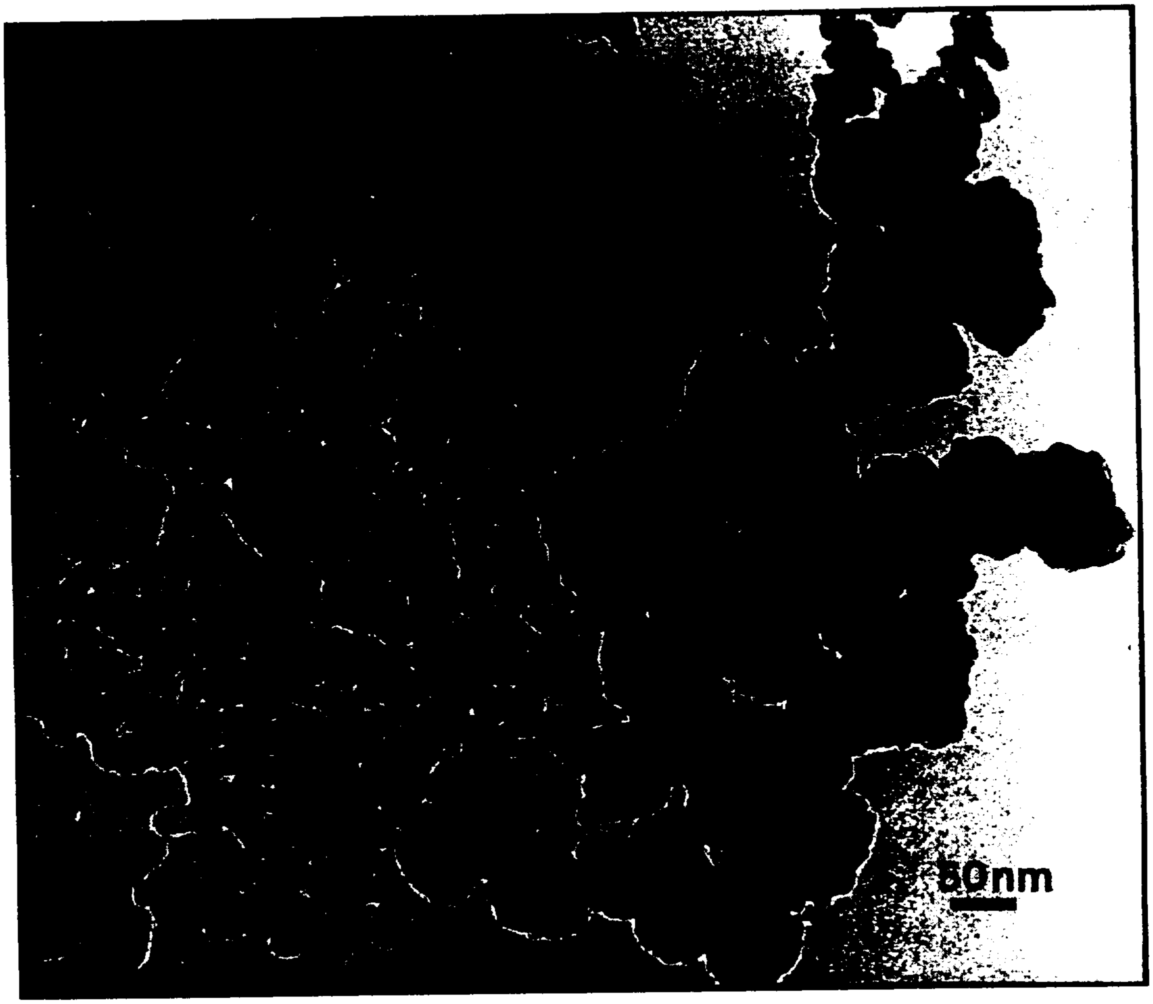

**Figure 6.4** Transmission electron micrograph showing rimmed grains and mottled grains in the original condensate. The rimmed grains are shown as tangled, fused strands and clusters between, and locally connecting, the larger mottled grains. The mottled grains occur in fluffy morphologies.

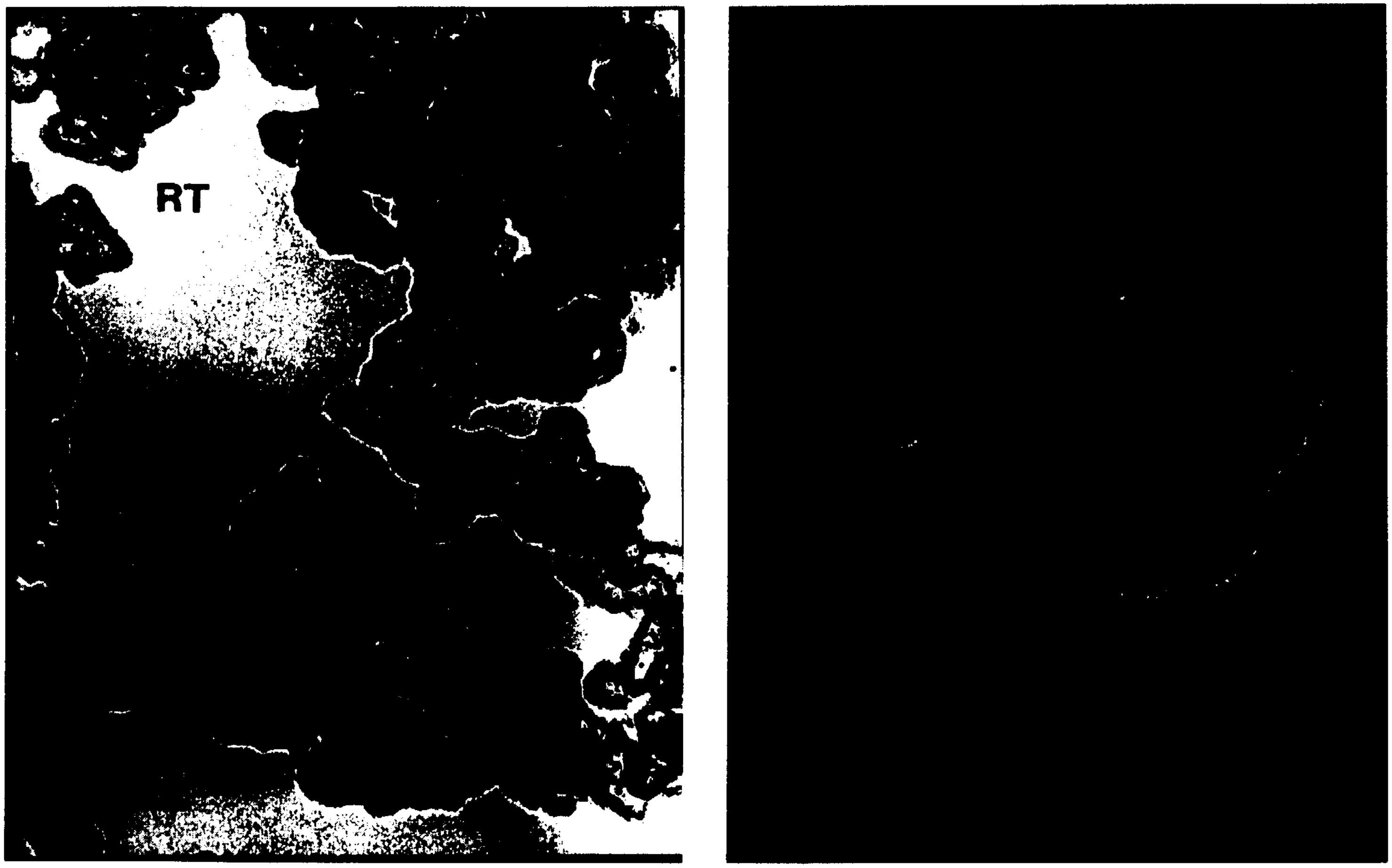

**Figure 6.5** Transmission electron micrograph showing AlSiO rimmed grains in the original condensate (RT) and the 1100 $^0$C sample. Rimmed grains in the RT sample occur mostly as strands of fused grains with a (semi)-continuous rim outlining them. Rimmed grains at 1100 $^0$C tend to occur as fused clusters wherein individual grains are only somewhat discernible.

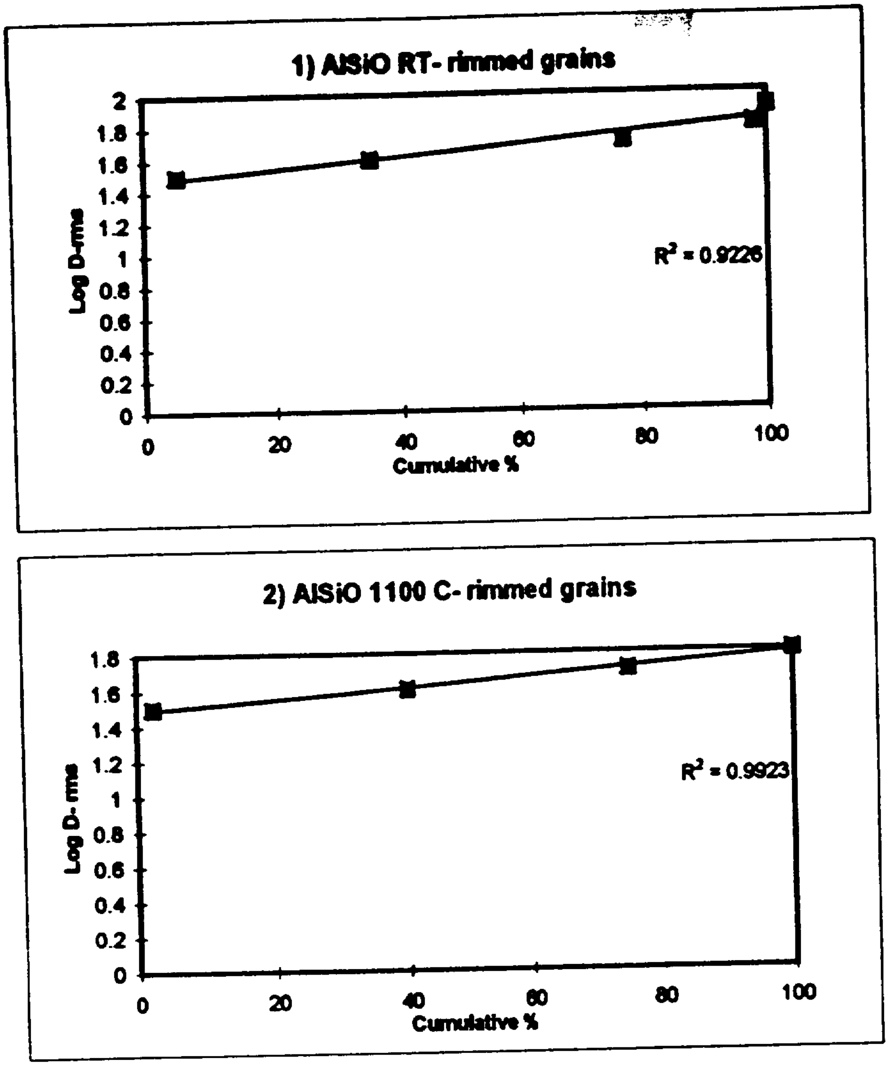

Figure 6.6 Log D (size) distributions for 66 rimmed grains in the original condensate and 40 rimmed grains in the annealed sample.

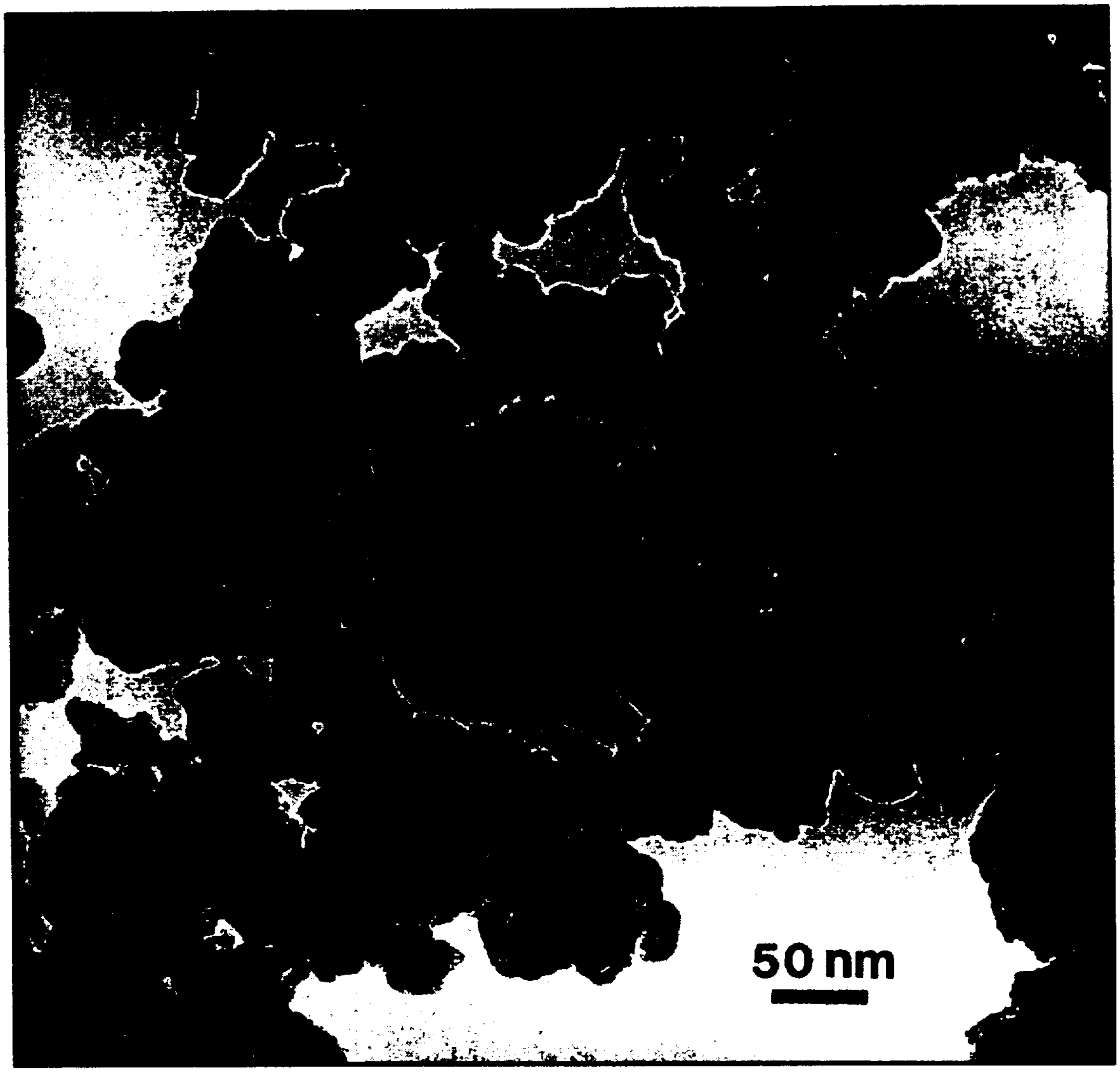

**Figure 6.7** Transmission electron micrograph showing AlSiO mottled grains in the original condensate. The clustered areas are darker in contrast compared to the lighter areas due to the amount of material. Some of the lighter areas may be single grains.

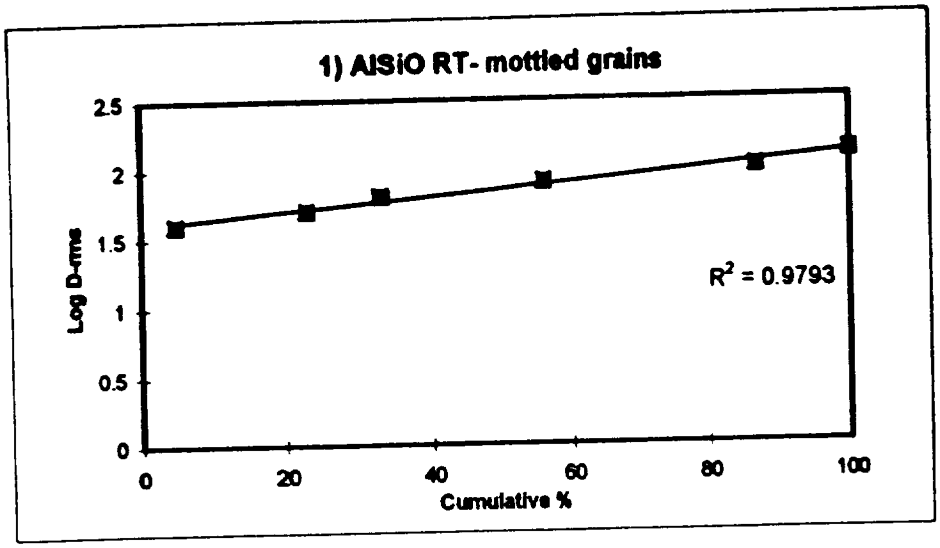

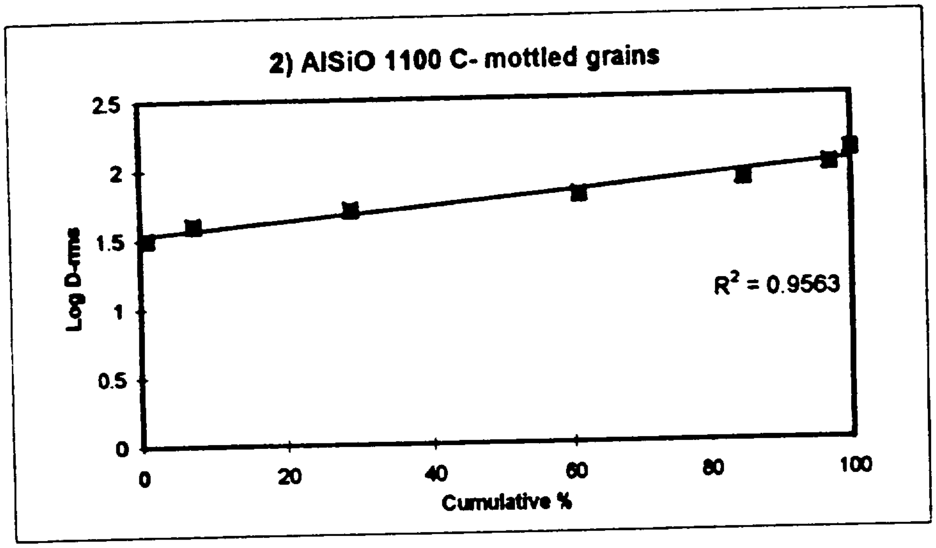

Figure 6.8 Log D (size) distributions for 39 mottled grains in the original condensate and for 80 mottled grains in the 1100 °C sample.

amorphous except for scattered electron diffraction maxima from grains with 40-60 wt.% $Al_2O_3$ (Table 6.2). The diffraction data are consistent with a silica phase (tridymite, cristobalite) and/or a aluminosilica phase, (sillimanite, mullite).

## 6.3 DISCUSSION

The fluffy texture of vapor phase condensates will isolate its individual entities that during thermal annealing they will behave as chemically closed systems (Rietmeijer, 1996b). To test this hypothesis, an AlSiO condensate was annealed at various temperatures up to $1100^0$ C, each for two hours. A relevant diffusion rate for Al in silica glass at ~ 1000 °C (Frischat, 1969) is $D = 1.3 \times 10^{-15}$ $m^2/s$. Using the diffusion equation

$$x = (2Dt)^{1/2}$$

where D = the diffusion coefficient and t = diffusion time (7200 s), a mean diffusion distance is calculated to be $x = 4.33 \times 10^{-6}$ m. Considering the size of individual entities, i.e. 30-150 nm, or $\sim 3 \times 10^{-8}$ to $1.5 \times 10^{-7}$ m in diameter, diffusion controlled reactions will be established during this time.

The grain size distributions, morphology and chemistry in the condensate and the sample annealed at $1100^0$ C are very similar. Differences between the samples include a compositional peak at 51 wt.% $Al_2O_3$ and a higher abundance of mottled grains, < 60 nm, both in the condensate. The compositional difference could be a byproduct of statistical treatment of the data where a peak at 51 wt.% $Al_2O_3$ was not obtained at an acceptable confidence level in the 1100 $^0$C sample. The greater abundance of small (< 60 nm) mottled grains in the condensate could be due either to a slight coarsening of these grains during thermal annealing, as anticipated by Ostwald ripening, or sample heterogeneity, as in the FeSiO sample [cf. Sect. 3.3].

The presence of two chemically distinct grains can be understood using the $SiO_2$ - $Al_2O_3$ equilibrium binary phase diagram (Figure 6.9) wherein compositions of the rimmed grains match those of the liquidus surface between pure $SiO_2$ and the eutectic composition at ~ 10 wt.% $Al_2O_3$. The liquidus of the phase diagram between the eutectic composition and the mullite stability field constrains the compositions of the mottled grains where peaks in the condensate and 1100 $^0$C sample match those of the putative equilibrium and spinodal solvi in this phase diagram (MacDowell and Beall, 1969). It suggests that condensation occurred at preferred $Al_2O_3$/ $SiO_2$ compositions during condensation and thermal annealing. These compositions are comparable to mottled mixed-oxide grains with variable Al/(Al +Si) found in a AlSiO condensate studied by Rietmeijer and Nuth (1990). They note that a Al/(Al +Si) value of 0.55, or ~ 51 wt.% $Al_2O_3$, is consistent with the ratios in kaolinite, meta-kaolinite, and/or halloysite and Al-Si spinel, but of course the condensates are $H_2O$ free. Their observations, and those presented here show that the stable configurations of condensed grains match those of stable mineral configurations. The preservation of compositional peaks in the annealed sample confirms that the fluffy texture of vapor phase condensates acted to isolate the entities and prevented them from reacting matching compositions of the solvus crests.

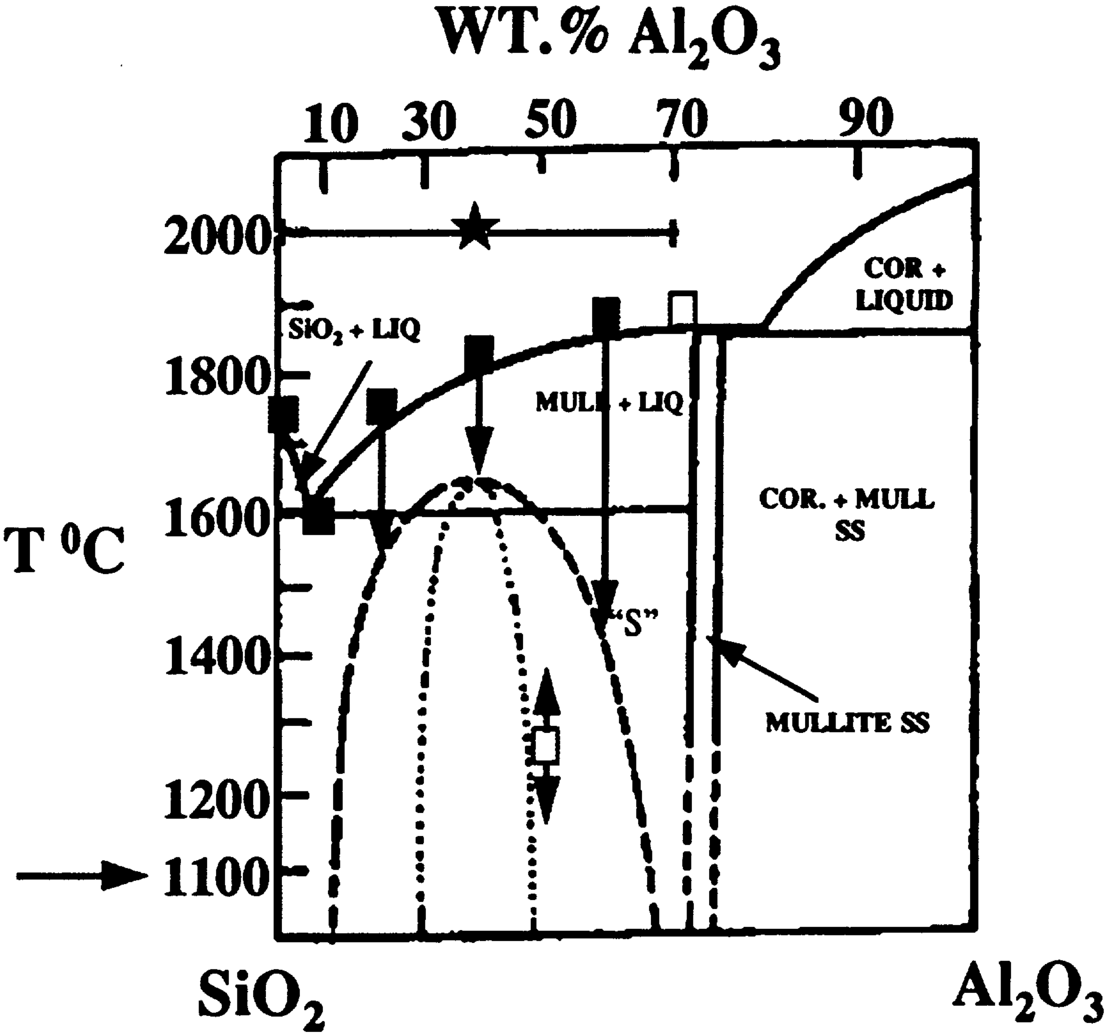

**Figure 6.9** The $SiO_2$- $Al_2O_3$ equilibrium phase diagram showing the bulk composition of the AlSiO samples (★) with the horizontal lines on either side showing the range of all compositions. The solid rectangles (■) represent compositional peaks in both the original condensate and the 1100 °C sample, while the open rectangles (□) are only found in the original condensate. Arrows stemming from rectangles link peaks with proposed solvi in this diagram. The "S" represents a sillimanite composition. The arrow pointing to 1100 °C represents the temperature of annealing. Modified after MacDowell and Beall (1969).

The mottled texture of mixed oxide grains may be the result of subsolidus phase decomposition into aluminum- and silica-rich phases. This idea is supported by Rietmeijer and Nuth (1990) who found single crystal grains of sillimanite in their condensate. Diffraction data and corresponding compositions (40-60 wt.% $Al_2O_3$) in this study support the idea that sillimanite nanocrystals and an silica-rich aluminosilica matrix formed during autoannealing. Whether the matrix was amorphous/crystalline cannot be established using the currently available data. This exsolution relationship (or texture) was preserved during thermal annealing even at 1100 °C, delineating the putative solvus, (cf. Figure 6.9).

Rietmeijer and Nuth (1990) also found smooth grains ($SiO_2$) in fused, tangled strands and irregular clusters. They proposed that the smooth grains nucleated at high supersturations and low temperatures and thus the grains possessed high surface energies. The high surface energy promoted coagulation of grains into formless strands and clusters. Here it is proposed that fused strands of rimmed grains in the unnanealed sample are due to the same effect (Figure 6.5). The coagulation of rimmed grains into dense clusters in the 1100 °C sample supports that the process was enhanced by thermal annealing (Figure 6.5). Conversely, the unchanged fluffy morphology of mottled grains after thermal annealing supports the idea that mixed-oxide clusters have a relatively low surface free energy and thus will not coagulate into large irregular areas like the $SiO_2$ grains.

## 6.4 CONCLUSIONS

1) Amorphous phase relationships during condensation of fluffy aluminosilica materials and subsequent thermal annealing follow the topology of the phase diagram and (2) coagulation of grains may be enhanced by high surface energies of pure oxide ($SiO_2$) grains.

# CHAPTER 7. A TRIGGERED LIGHTNING EXPERIMENT TO EXPLORE SOLAR NEBULA ALTERATION

- This chapter was also given as an oral presentation at the 27th Lunar and Planetary Science Conference:

J.M. Karner, P.J. Wasilewski, F.J.M. Rietmeijer, and J.A. Nuth. Preliminary electron microbeam analyses of lightning induced evaporation and gas phase mixing. *Lunar Planet. Sci. Conf. XXVII*, 647-648.

## 7.1 ABSTRACT

We took the opportunity of a triggered strike to investigate the petrological properties of alteration effects due to lightning on discs of magnetite separated by blankets of silica glass wool. The strike produced millimeter sized black spheres, several of which were removed for examination by scanning electron microscopy and transmission electron microscopy. The spheres consisted of nanometer sized domains of crystalline mullite and hercynite in Al-Si-Fe-O glass, with compositions delineated by the equilibrium phase relations in the Al-Si-Fe-(O) system. The presence of mullite and Fe-cordierite glass in the spheres indicate that temperatures of 1400 - 1700 $^{0}$C were induced by the lightning strike. These temperatures are consistent with those inferred for chondrule formation and suggest

**lightning, from a petrological perspective at least, may be a viable mechanism for chondrule formation in the early solar nebula.**

## 7.2 INTRODUCTION

The attempt to better understand lightning strikes has persisted since the late 1700s when Benjamin Franklin showed lightning to be an electrical phenomenon. We have learned since that lightning strikes are very common high energy events occurring on earth ~100 times per second and delivering $10^9$ J of energy per flash (Borucki and Chameides, 1984). With air temperatures reaching up to ~ 30,000 °C materials struck by lightning can melt or vaporize in microseconds (Essene and Fisher, 1986).

The Langmuir Laboratory for Atmospheric Research near Soccorro, New Mexico, is dedicated to the study of cloud physics, precipitation, and lightning. The location on South Baldy Mountain in the Magdelena range is ideal for experimental studies because frequent isolated summer storms are often small and stationary. We used this laboratory to conduct an experiment on lightning induced alteration of magnetite in order to experimentally duplicate the conditions that form lodestone in the natural environment. These studies also allow us to examine the possibility that lightning strikes may have been involved in chondrule formation in the solar nebula.

Terrestrial materials that have been fused or vitrified by lightning are well known throughout the world (Galliot, 1980). The resulting fulgurites are vitreous tubes and crusts formed in quartz sands, soil, and rock. These tubules are silica glass with adhering sand particles. They measure only a few centimeters in diameter but can be up to 30 m in length. Impurities such as iron, aluminum, calcium and magnesium give the glass a yellowish brown color. The presence of high temperature minerals such as cristobalite is also reported (Galliot, 1980). In a study of a fulgurite formed in a soil struck by lightning, Essene and Fisher (1986) reported metal-silicate liquid immiscibility and extremely reduced mineral phases that occurred on a micrometer to centimeter scale. The extreme reduction was probably related to the presence of carbon-rich materials in the soil and to vaporization of oxygen during the boiling process induced by the very high temperatures (Essene and Fisher, 1986). Thermodynamic calculations indicate that alteration temperatures in the materials of this fulgurite reached ~2300 $^0$C (Essene and Fisher,1986). While the pyrometamorphic changes due to a lightning strike in terrestrial soils are well documented, there are very few data on the nature of the silicate and oxide mineralogy in these events. For example, the small scale of mineralogical heterogeneity and the chemical behavior during these microsecond events remain obscure.

Recently, lightning has gained renewed attention as a possible mechanism for the formation of chondrules in the early solar nebula (Horanyi et al., 1995; Gibbard and Levy, 1994; Love et al., 1994; Wasson and Rasmussen, 1994). Chondrules are small, quenched spheres ( 0.5 - 1.5 mm in diameter) that occur in chondritic meteorites, but the exact time-scales of thermodynamic equilibrium are a fertile area for detailed petrological study. Chondrules are characterized by high temperature minerals, such as olivines and pyroxenes with characteristic textures of rapid growth, in a glassy matrix that also includes reduced phases such as iron-nickel metal. Experimental studies indicate that chondrules were heated to 1550-1980 °C, and that they were quickly cooled at rates of 100-2000 °C/hr (Hewins, 1988) to produce their characteristic textures and mineralogies. Simulation experiments to reproduce chondrule properties showed that an energy input of 1,750 - 2,100 J/g was needed to process chondrules of all compositions (Hewins and Connelly, 1996). The realization that lightning could provide efficient transient heating events for chondrule formation was first recognized by Whipple (1966) because in circulating or turbulent environments (i.e. solar nebula), dust-laden gases would provide ideal conditions for the production of lightning. Currently, there are two mechanisms for chondrule formation in the solar nebula, *viz.* gas drag heating and nebular lightning (Scott et al., 1996). Nebular lightning remains an option but the low nebula gas pressure and its high electric conductivity may limit its widespread application as an efficient physical process for chondrule formation (Love et al., 1994). We are interested to study the mineralogical and petrological properties of materials that were produced by this transient physical process.

## 7.3 EXPERIMENTAL

The experiment reported here investigates lightning strike alteration of magnetite under conditions of transient energy input *viz.* the response of magnetic materials to a lightning strike. It is the first known experiment to use selected materials and a triggered strike with the intention of examining effects on a micrometer scale. The experiment entails placing three discs of magnetite ($Fe_3O_4$), including both pure magnetite and magnetite with variable but minor amounts of unidentified (Mg,Fe,Ca)-silicates and calcite ($CaCO_3$), separated by blankets of silica glass wool (~ 1 cm thick), in a cylindrical container. The discs are placed perpendicular to the container axis and are each about 1 cm thick. A rocket linked to the container with a copper wire is fired into an overhead cloud to induce a lightning strike. The lightning flows down the wire and through the container from top to bottom thereby passing through the three discs of magnetite and both intervening blankets of glass wool. The passage of the lightning strike through the glass wool left a hole with a diameter of ~1 cm, while smaller offshoots of the strike are also seen. An orange-brown discoloration, probably hematite ($Fe_2O_3$), appears on the silica glass wool surrounding the main hole. A spray of similar discoloration occurrs on the blanket surface surrounding the hole. Several millimeter-sized black spheres and (rare) black fragments were located around the main hole where the lightning strike exited a glass wool blanket. An unintended by-product of interlayering the magnetite discs and glass wool is a first glimpse into the silicate and oxide mineralogy that formed rapidly in the transient event.

Black spheres of ~1 mm in diameter were randomly picked from the glass wool. When a slight pressure was applied, the spheres fragmented, suggesting they are hollow objects. The spheres were crushed and dispersed onto a holey carbon thin-film supported by a copper mesh grid. In addition, ultrathin (80-100 nm) sections of three spheres were prepared for analyses using a JEOL 2000FX analytical electron microscope (AEM) operating at an accelerating voltage of 200 keV. The AEM was equipped with a Tracor Northern TN-5500 energy dispersive spectrometer (EDS) for *in situ* chemical analysis of elements with atomic number >11 using a probe size ~20 nm in diameter. All phases were characterized by a combination of transmission electron microscope (TEM) imaging, selected area electron diffraction (SAED) and EDS analyses in the Electron Microbeam Analysis Facility (EMAF) at the University of New Mexico. For details of the experimental conditions at EMAF, see Rietmeijer (1996). Scanning electron microscope (SEM) imaging was done at the NASA Goddard Space Flight Center.

## 7.4 OBSERVATIONS

The compositions of the spheres are mixtures in the Al-Si-Fe-(O) system with minor Ti which is consistent with the starting materials that included magnetite, aluminosilica glass wool [42 wt.% $SiO_2$; 58 wt.% $Al_2O_3$], and single-crystal Ti-oxide impurities (~200 nm in size) associated with the glass wool. These compositions are represented in the ternary diagram $SiO_2$ - $Al_2O_3$ - $Fe_2O_3$ (wt.%) (Fig. 7.1). This phase diagram was used based on the inference that hematite was a product of the alteration. The clusters in this diagram correspond with other TEM observations. The cluster centered around $SiO_2$ = 60 wt.%, $Al_2O_3$ = 39 wt.%, and $Fe_2O_3$ = 1 wt.% represents the main sphere compositions within the mullite [$Al_6Si_3O_{15}$] stability field. The absence of diffraction maxima in SAED patterns of the spheres indicates that they are a mullite glass. The cluster around $SiO_2$ = 47 wt.%, $Al_2O_3$ = 18 wt.%, and $Fe_2O_3$= 35 wt.% is due to small domains in the spheres that match a Fe-cordierite composition with $Fe^{3+}/(Fe^{2+} + Fe^{3+}) \approx$ 0.35. This cordierite glass may contain up to ~ 7 wt.% $TiO_2$. The presence of titanium

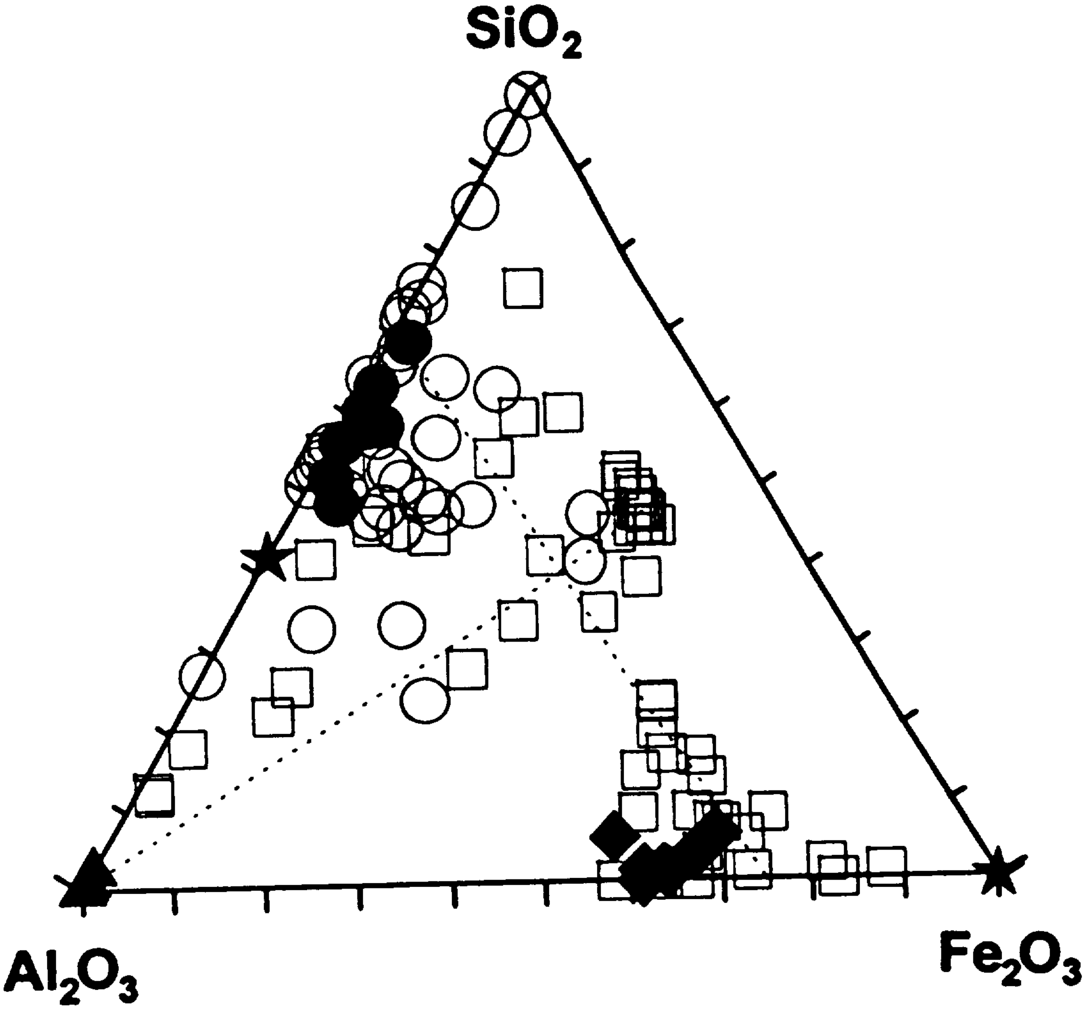

**Figure 7.1** The ternary diagram $SiO_2$ -$Al_2O_3$- $Fe_2O_3$ (wt.%) showing the compositions of the aluminosilica glass wool and magnetite discs (solid stars), Ti-free glass spheres (open circles) and glass spheres corrected for 1-10 wt.% $TiO_2$ (open squares), mullite symplectites (solid circles), hercynite inclusions [corrected for 1-7 wt.% $TiO_2$] (solid diamonds), and $Al_2O_3$ inclusions (solid triangles). The cluster of points along the dashed lines could be due to cotectic melting lines, or products of experimental error.

(- oxide) in the vapor is also supported by rare porous domains (smokes) of condensed nanometer sized $SiO_2$ - $TiO_2$ grains ($TiO_2$ = 53-81 wt.%). Another cluster occurs along the $Fe_2O_3$ - $Al_2O_3$ join of the diagram and is due to inclusions that are ~ 530 nm in length and 300-450 nm (Fig. 7.2). They were identified as single-crystal Ti-bearing hercynite [$FeAl_2O_4$] in the mullite glass spheres. These inclusions are part of symplectitic (or eutectoid) intergrowths of spinel and mullite (glass) similar to the dendritic growths on the surface of magnetite discs (Fig. 7.3). In addition, rare symplectitic intergrowths of single-crystal mullite in the glass mullite matrix are up to 300 nm in length with branches extending out from the main trunk to ~80 nm (Fig. 7.4). Lattice fringe spacings in the dendrites are ~ 0.5 nm that are consistent with the (*hkl*) (110) plane of mullite.

## 7.5 DISCUSSION

The black spheres in this experiment form from Al-Si-Fe-(O) vapors with minor Ti-O due to lightning induced melting and evaporation of magnetite discs, aluminosilica glass wool, and Ti-oxide impurities at approximately atmospheric pressure in a fully oxidizing environment. We submit that the aluminosilica glass wool decomposed into a mullite-like phase and a highly refractory $Al_2O_3$ residue. Aluminum oxide, $Fe_2O_3$ and minor $TiO_2$ reacted to form hercynite. The cordierite glass matches the ternary melt composition in the $SiO_2$ - $Al_2O_3$- $Fe_2O_3$ equilibrium phase diagram which suggests that melting temperatures induced by the lightning strike were on the order of 1400-1700 °C. (Eitel, 1965). Similar high temperatures are also supported by the refractory smokes

**Figure 7.2** Transmission electron micrograph and corresponding electron diffraction pattern of hercynite inclusions in an amorphous matrix.

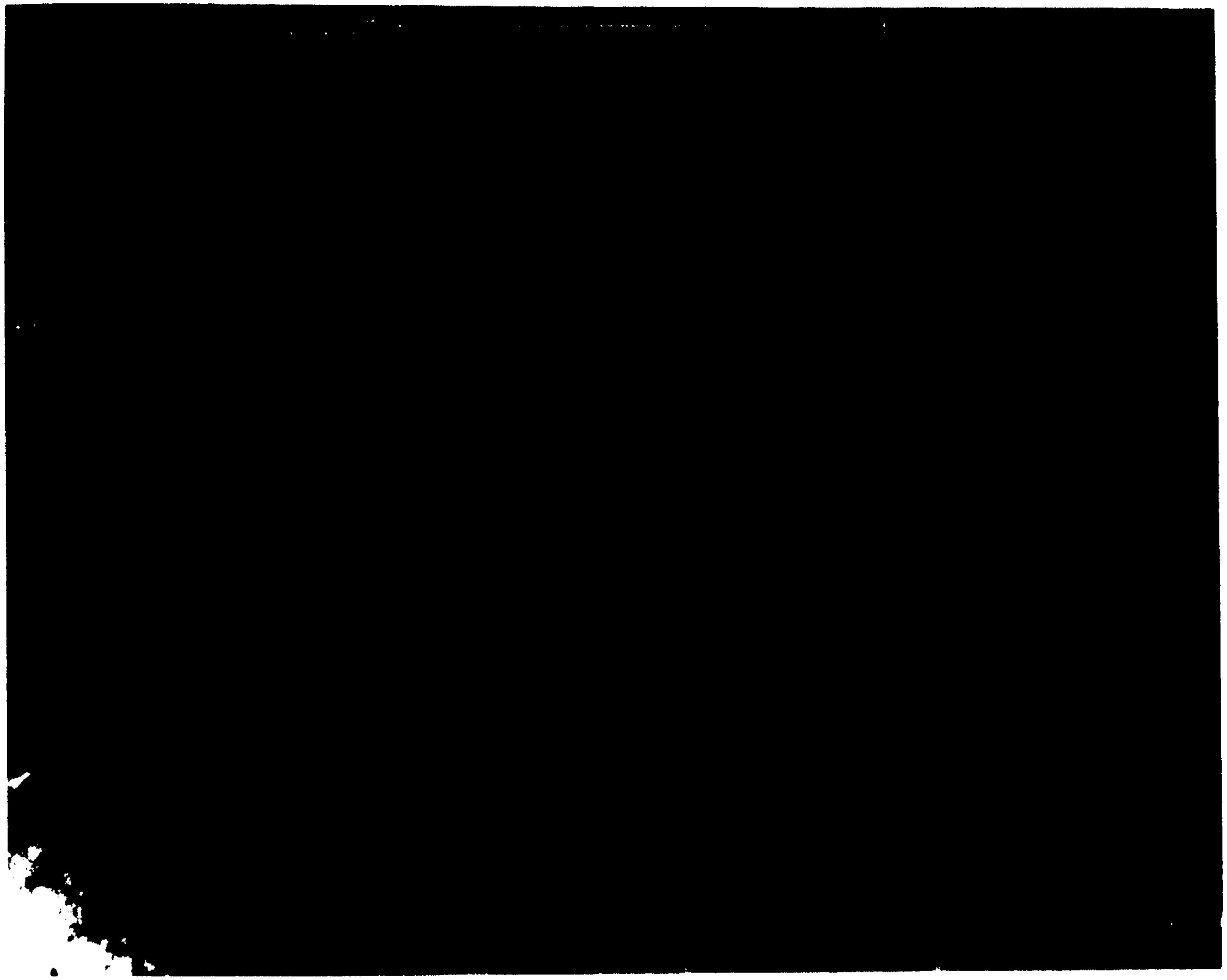

**Figure 7.3** Scanning transmission electron micrograph showing dendrites from the surface of the magnetite discs.

**Figure 7.4** Transmission electron micrograph of a single-crystal mullite symplectite in an amorphous mullite matrix with corresponding electron diffraction pattern for the crystalline phase.

associated with the spheres. The ferric iron content of Fe-cordierite and the presence of the spinel phase support oxidizing conditions during melting and quenching in the experiment. We note that symplectites of spinel in glass are common in meteorite fusion crusts wherein they are the result of rapid heating and quenching under oxidizing conditions during atmospheric entry (Blanchard and Cunningham, 1974). The mullite symplectites are textural evidence of rapid growth during quenching of the melt induced by lightning in the experiment. Similar high-temperature and highly oxidized minerals such as mullite, iron cordierite, and hercynite, formed in terrestrial pyrometamorphic rocks at appropriate chemical conditions in response to rapid (geological) heating (Cosca et al., 1989). We also note the occurrence of cordierite, along with closely related silica-alumina minerals osumilite, merrihueite, and yagiite in meteorites (Fuchs, 1969).

## 7.6 CONCLUSIONS

The results of this first experiment are encouraging and show that a triggered lightning strike induces melting and vaporization of refractory materials. It also shows that the resulting compositions of the solids mimic equilibrium conditions even though the mineral reactions in this transient, high energy event are probably dominated by kinetically controlled reactions including evaporation, mixing, and nucleation at temperatures similar to those in chondrule simulation experiments. This non-randomness is most likely related to the small scale at which mineral reactions occur for the grains that are typically less than

530 nm. These experiments show that it is possible for natural lightning strikes to cause significant alteration including textures due to high cooling rates, in refractory materials. Furthermore, one can describe the events in a systematic manner using equilibrium phase relationships. While the arguments on the physical feasibility of the proposed chondrule forming process remains unsettled, experimental lightning has shown the that the resulting solids of these processes are not random, and are probably well constrained by equilibrium phase relationships.

## 7.7 REFERENCES

Blanchard M.B., and Cunningham G.G. (1974). Artificial ablation studies: olivine. *J. Geophys. Res.* 79, 3973-3980.

Borucki W.J., and Chameides W.L. (1984) Lightning: estimates of the rates of energy dissipation and nitrogen fixation. *Rev. Geophys. Space Phys.* 22, 363-372.

Cosca M.A., Essene E.J., Geissman J.W., Simmons W.B., and Coates D.A. (1989) Pyrometamorphic rocks associated with naturally burned coal beds, Powder River Basin, Wyoming. *American Mineralogist*, 74, 85-100.

Eitel W. (1965) *Silicate Science, Vol. II, Dry silicate systems.* Academic Press Inc., New York, New York 553 pp.

Essene E.J., and Fisher, D.C. (1986) Lightning strike fusion: Extreme reduction and metal-silicate liquid immiscibility. *Science* 234, 189-193.

Fuchs L.H. (1969) Occurrence of cordierite and aluminous orthoenstatite in the Allende meteorite. *American Mineralogist* 54, 1645-1653.

Galliot M.P. (1980) "Petrified lightning" A discussion of sand fulgarites. *Rocks and Minerals*, Jan/Feb, 13-17.

Gibbard S.G., and Levy E.G., (1994) On the possibility of precipitation- induced vertical lightning in the protoplanetary nebula. In: *Chondrules and the Protoplanetary Disk*. LPI Contribution No. 844, Lunar and Planetary Institute, Houston. 50 pp.

Hewins R.H. (1988) Experimental studies of chondrules. In *Meteorites and the Early Solar System*. (eds. J.F. Kerridge and M.S Matthews), pp. 660-667. Univ. of Arizona Press, Tucson, Arizona.

Hewins R.H., and Connelly H.R.. (1996) Peak temperatures of flash-melted chondrules. In *Chondrules and the Protoplanetary Disk*. (eds. R.H. Hewins, R.H. Jones, and E.R.D. Scott), pp.197-204. Cambridge Univ. Press.

Horanyi M.G., Goertz C.K., Morfill G., and Levy E.H. (1995) Chondrule formation in lightning discharges. *Icarus* **114**, 174-185.

Love S.G., Keil K., and Scott E.R.D. (1994) Formation of chondrules by electrical discharge heating. In: *Chondrules and the Protoplanetary disk*. LPI Contribution No. 844, Lunar and Planetary Institute, Houston. 50 pp.

Rietmeijer F.J.M. (1996) CM-like interplanetary dust particles in lower stratosphere during 1989 October and 1991 June/July. *Meteoritics and Planetary Science* **31**, 278-288.

Scott R.D., Love S.G., and Krot A.N. (1996) Formation of chondrules and chondrites in the protoplanetary nebula. In *Chondrules and the Protoplanetary Disk*. (eds. R.H. Hewins, R.H. Jones, and E.R.D. Scott), pp.87-96. Cambridge Univ. Press.

Wasson J.T., and Rasmussen K.L. (1994) The fine nebula dust component: A key to chondrule formation by lightning. In: *Chondrules and the Protoplanetary Disk.* LPI Contribution No. 844, Lunar and Planetary Institute, Houston. 50 pp.

Whipple F.L. (1966) Chondrules: suggestion concerning their origin. *Science,* **153**, 54-56.

# CHAPTER 8. CONCLUSIONS

This chapter presents the conclusions about vapor phase condensation, and the products of vapor phase condensation, that are drawn from this study on silicate dust analogs. It also draws on knowledge of other theoretical and experimental studies of vapor phase condensation and dust analogs.

At the onset it must be clear that analytical microscopy is necessary to document the mineralogical and morphological properties of nanometer size grains produced by vapor phase condensation. While IR and XRD are useful, they often do not allow researchers to see the whole picture concerning dust analogs. For example, the IR data revealed semi-crystalline $SiO_2$ features in the 1100 $^0$C sample, and the XRD data noted weak intensity peaks caused by small amounts of diffracting material, -probably cristobalite. [cf. Sect. 6.2.1]. While the IR and XRD techniques identified some crystalline silica material, it took TEM imaging and electron diffraction data to show that the diffraction effects were probably from cristobalite rims on pure silica grains.

The data in this study are more comprehensive than in previous studies. This is mainly the result of the usage of ultrathin sections of the samples, which heretofore were used on a very limited basis, and not at all in the earlier (pre-1985) studies of silicate dust analogs. The ultrathin sections allow for grain size, chemical, and diffraction analysis at a level compareable to *individual* grain sizes (nanometers). Previous studies used bulk powder samples, therefore their analyses were essentially bulk analyses.

With the preceeding general conclusions out of the way, one may make some conclusions concerning the nucleation, growth and properties of condensate grains in answer to the initial question, "What are the products of vapor phase condensation, and subsequent thermal annealing?"

The size of the condensed grains in the samples of this study ranges from a few nanometers up to 400 nm in diameter. Generally, grains are less than 100 nm in size. These sizes are in good agreement with other experimental and theoretical studies [cf. Table 1.1]. The condensed grains invariably fit to log-normal size distributions that support growth by Ostwald ripening- a tendency of grains to minimize surface free energy by dissolving smaller grains to form larger ones.

The entities in silicate dust analogs produced in this study and others show a wide range of chemical compositions, and in all cases condensates with endmember compositions were readily formed. This is consistent with the idea that simple-oxide phases (Rietmeijer and Nuth, 1991) are the first to form in an evolving vapor rather than mixed binary and ternary metal oxide phases. The presence of ubiquitous endmember phases is consistent with the way the vapors are produced, mixed phases require some mixing time and turbulence before vapors condense.

Although individual grains often delineate the range between pure endmember compositions, the mixed compositions do not seem random and appear to be predictable using equilibrium phase relationships. It has become apparent that the peaks in the chemical composition histograms match the liquidus topology of the appropriate phase diagram. An example is the condensation of mixed grains in the AlSiO system [cf. Sect. 6.3]. The grains show compositional peaks near the eutectic at ~ 10 wt.% $SiO_2$ and the eutectic at ~70 wt.% $Al_2O_3$. Other compositional peaks match proposed spinodal solvi in this phase diagram [cf. Figure 6.9] This shows the grains seek out stable configurations in the $Al_2O_3$ -$SiO_2$ system during condensation and could be a combination of subsolidus relationships and formation of metastable extensions of liquidus surfaces. Condensation in the FeSiO, MgSiO, and Fe,MgSiO$_x$ systems also follow the topology of the appropriate phase diagrams but with some exceptions. For example, the FeSiO and Fe,MgSiO$_x$ samples show a compositional peak at ~27 wt.% FeO, 73 wt.% $SiO_2$. The phase diagram $Fe_3O_4$-$SiO_2$ does not predict a stable phase of this composition [cf. Figure 3.10]. Similarly, the MgSiO samples show a compositional peak at ~85 wt.% MgO that is not predicted in the phase diagram [cf. Figure 4.15]. The two aforementioned compositions are stable, configurations in the appropriate binary systems. With only the strength of these two observations, it is suggested that there may be corresponding eutectic points on the inferred liquidus surfaces in the $Fe_3O_4$- $SiO_2$ and MgO- $SiO_2$ phase diagrams.

Another conclusion is that grains of similar chemical composition may occur in several different morphologies. Silica may occur as patchy material, globules, smooth grains with rims, dense clusters and round droplet shaped grains. This is also true of mixed compositions, e.g. in the MgSiO sample round grains and irregular clusters grains both are ~ 50 wt.% MgO. While some morphological features can be attributed to autoannealing (rims on silica grains), other features may reflect properties during condensation, such as turbulence. It is proposed, for example, that patchy and clustered silica materials condensed from pockets of highly supersaturated gas, thus forming many nuclei and small grains.

The dust analogs in this study invariable contain both amorphous and crystalline material in all the samples. The proposed sequence of events is that the condensed grains are quenched amorphous solids. The onset of structural ordering in the condensed grains is thought to be caused by autoannealing. This process takes place after the condensation event and is separate from any post-condensation thermal annealing experiment. In the samples of this study autoannealing produces small domains of crystallinity in random grains that is evidenced by weak diffraction maxima of high-index planes, and high resolution imaging of lattice fringes. Key evidence for autoannealing in these samples is the clustered silica grains in the Fe,$MgSiO_x$ sample. Polycrystalline SAED patterns show that cristobalite grains within the clusters are oriented in the same direction [cf. Figure 5.2]. It is highly improbable that condensation produced crystalline grains deposited into clusters with every grain in the same orientation. Rather it appears that condensation originally produced amorphous grains deposited into clusters which subsequently, through autoannealing, were transformed into many crystalline grains in the same orientation.

The formation of metastable phases in these samples is not uncommon and is consistent with the Ostwald Step Rule. This rule predicts that the phase that represents the lowest reduction in free energy and smallest activation energy will form first from a [metastable] parent. The metastable phase may persist outside its stability field because of high activation energies that prohibit reaction to the most thermodynamically stable form [Figure 2.1]. An important thing to remember is that the high surface free energy of the nanometer size grains will play an important role in determining whether ractions will be inhibited or promoted. This is also important in regards to the shapes of nanometer size crystals. This study reports that in the $MgSiO_x$ samples that rectangular, octagonal, hexagonal and cubic grains are all identified as periclase (MgO). The octagonal and hexagonal shapes differ considerably from the macroscopic form of periclase; which is cubic. This phenomenon is also seen in very small gold particles grown in metallic thin films (two-dimensional growth) and metal particles (Fe, Mg, Al, Cr, Co, Ni, Cd, Sn, Pb, Ag, Au, Bi, Cu) condensed in argon vapors (Komodo, 1968; Kimoto and Nishida, 1967). The shapes of MgO grains in the samples of this study could be a product of two-dimensional growth (intermediate supersaturation) that creates platey grains, or a product of high surface energies of nanometer size grains that promote the growth of high index planes (Doremus, 1985).

The fluffy texture of condensates will isolate individual entities (grains) so they will behave as chemically closed systems upon thermal annealing. This is evident in the annealed samples in the AlSiO sample [Sect. 6.3] wherein textures and mineralogies are preserved in the annealed samples. Again the surface energy of the grains plays an important part as pure silica grains in the original sample are partially fused in strands, and with subsequent thermal annealing fused into dense clusters. The mixed oxide clusters experienced little coagulation, and are thought to have a lower surface energy than the pure silica grains. The FeSiO [cf. Sect. 3.3] sample shows that thermal annealing of metastable mineral phases, such as tridymite may undergo fusion below the melting temperature. This may be evidence of the Ostwald step rule in progress, whereby tridymite has to pass through a reconstructive transformation (glass-transition) before recrystallizing into a more stable phase.

There are some other implications about vapor phase condensation and silicate dust analogs and their relation to astrophysical dusts, meteorite matrix, and IDPs. The data in this study and previous studies point to the notion that vapor phase condensation is a nonequilibrium process. The production of amorphous grains and metastable assemblages is consistent with a kinetically controlled process. Furthermore, the presence of droplet shaped grains suggests a vapor-liquid-solid transition instead of vapor-solid. The dust grains are thought to condense as liquids that are quickly solidified. Therefore, condensed nanometer sized grains can be thought of as rapidly quenched (solidified) liquid droplets with high thermal energies, and high surface energies. Thus, silicate dust analogs are quite different from the stable mineral phases predicted to condense by equilibrium condensation models. It appears that these models are incorrect, and this would lead one to favor a nonequilibrium model of vapor phase condensation.

The crystalline grains in the samples of this study can be explained by post-condensation events, i.e.-autoannealing. This is an experimental artifact whereby condensed grains deposit onto a substrate. The implication of this is that condensation in interstellar and circumstellar environments will produce amorphous grains. Crystalline grains must be the products of a secondary process either in the interstellar medium or upon incorporation into a parent body such as an IDP or a meteorite. Therefore, it appears that the amorphous materials in both UOC meteorite matrix and IDPs best represent interstellar and circumstellar solids. The nanometer size pyroxene and olivine grains found in these materials have formed by the annealing of the amorphous precursors.

In a plot of the chemical composition of principle components in IDPs, the bulk compositions are mostly $(Mg,Fe)_3Si_2O_7$, which defines a serpentine dehydroxylate composition (Rietmeijer, 1996c). The bulk compositions are very similar to the compositions of grains found in the $MgSiO_x$ samples that ranged from ~30 to 70 wt.% MgO. In the $MgSiO_x$ samples olivine and pyroxene grains were found that are similar to those found in IDPs. The amorphous materials in both silicate dust analogs and IDPs are very similar and appear to represent true condensate materials. Crystalline grains in both materials represent different annealing processes after the condensation event. Thus, silicate dust analogs are a viable analog to IDPs and will help us understand the processes affecting component grains after the condensation event.

In conclusion, condensation is a nonequilibrium process that produces grains generally less than 100 nm. The grains are amorphous with some crystallinity being explained as an experimental artifact. The size, shape and phases present in condensed grains are controlled by kinetic processes and the high surface energies of nanometer size grains, but are still predictable using phase relationships in equilibrium phase diagrams. Experimental silicate dust can be used to constrain properties of condensation and post-condensation in astrophysical environments as an analog of interstellar and circumstellar dusts, including IDPs.

# REFERENCES

## (Chapters 1- 6)

Abraham F.F. (1974) *Heterogeneous nucleation theory.* Academic Press, New York.

Anders E. and Zinner E. (1993) Interstellar grains in primitive meteorites: diamond, silicon carbide, and graphite. *Meteoritics 28,* 490-514.

Baronnet A. (1984) Growth kinetics of the silicates. A review of basic concepts. *Fortschr. Miner. 62,* 187-232.

Bell J.F., Davis D.R., Hartmann W.K., and Gaffey M.J. (1988) Asteroids: the big picture, In *Asteroids II* (Binzel R.P., Gehrels T., and Matthews M.S. eds.) pp. 921-945. Univ. of Arizona Press, Tucson. Hulst eds). D. Riedel, Boston. 545p.

Blander M. and Katz J.L. (1967) Condensation of primordial dust. *Geochim. Cosmochim Acta, 31,* 1025-1034.

Bradley J.P, Brownlee D.E., and Veblen D.R. (1983) Pyroxene whiskers and platelets in interplanetary dust: evidence of vapour phase growth. *Nature 301,* 473-477.

Bradley J.P. (1988) Analysis of chondritic interplanetary dust thin sections. *Geochim. Cosmochim Acta, 52,* 889-900.

Bradley J.P., Sandford, S.A., and Walker R.M., (1988) Interplanetary dust particles. In *Meteorites and the early Solar System.* (Kerridge J.F. and Mathews M.S. eds.) Univ. of Arizona Press, Tucson.

Brearley A.J., Scott E.R.D., Keil K., Clayton R.N., Mayeda T.K., Boynton W.V., and Hill D.H.(1989) Chemical, isotopic and mineralogical evidence for the origin of matrix in ordinary chondrites. *Geochim. Cosmochim Acta, 53,* 2395-2411.

Cameron, A.G.W. (1973) In *Interstellar Dust and related topics,* (Greenberg and van de Hulst,eds).

Cliff G., and Lorimer G.W. (1975) The quantitative analysis of thin specimens. *J. Microscopy 103,* 203-207.

Day K.L. (1974) A possible identification of the 10-micron "silicate" feature. *Astrophys. J. 192,* L15-L17.

Day K.L. and Donn B. (1978a) Condensation of nonequilibrium phases of refractory silicates from the vapor. *Science 202*, 307-308.

Day K.L. and Donn B. (1978b) An experimental investigation of the condensation of silicate grains. *Astrophys. J., 222,* L45-L48.

Donn B. (1979) Some aspects of condensation in clouds. *Astrophys. Space Sci. 65,* 167 171.

Donn B., Hecht J., Khana R., Nuth J.A., Stranz D., and Anderson A.B. (1981) The formation of cosmic grains: an experimental and theoretical study. *Surface Science 106*, 576-581.

Doremus R.H. (1985) *Rates of Phase Transformations* (Curtice K. ed.) Academic Press, New York. 176p.

Eddington J.W. (1976) In *Practical Electron Microscopy in Materials Science* ( Bricknell D.B., Henshall J.L., Porter D.A., Williams D.B. eds.) N.V. Philips' Gloeilampenfabrieken, Eindhoven. 344p.

Ehlers, E.G. (1972) *The Interpretation of Geological phase diagrams.* (Gilluly J., Woodford A.O., and McCulloh T.H. eds.) W.H. Freeman Company, San Francisco. 280p.

Fegley, B. (1987) Cosmochemical trends of volatile elements in the solar system. In *Workshop on the origin of solar systems* (Nuth J.A. and Sylvester P. eds.) LPI Technical Report 88-04. p. 51-59. Lunar and Planetary Institute, Houston TX.

Fraundorf P., Brownlee D.E., and Walker R.M. (1982) Laboratory studies of interplanetary dust, In *Comets*, (Wilkening L.L. ed.) Univ. of Arizona Press, Tucson. pp. 383-409.

Fu G. and Rietmeijer F.J.M. (1994) Ferrosillite, fayalite and magnesioferrite formation by isothermal annealing of an iron-contaminated Mg-SiO smoke. (abstract) *Lunar Planet. Sci. Conf. XXV*, 493-494.

Fujimara A., Kato M., and Kumazawa M. (1983) Preffered orientation of phyllosilicate matrix of Murchison meteorite and possible mechanisms of generating the oriented texture in chondrites. *Earth Planet. Sci. Lett., 66*, 25-32.

Gilman R.C. (1969) On the composition of circumstellar grains. *Astrophys. J. 155*, L185-L187.

Grossman L. and Larimer J.W. (1974) Early chemical history of the solar system. *Rev. Geophys. Space Phys., 1,* 71-101.

Huss G.R., Keil K., and Taylor G.J. (1980) The matrices of ordinary chondrites: implications for the origin and history of chondrites. *Geochim. Cosmochim Acta, 45,* 33-51.

Kamijo F., Nakada Y., Iguchi T., Fujimoto M.K., and Takada M. (1975) Preparation of fine particles of astrophysical interest by gas evaporation techniques. *Icarus 26,* 102-110.

Karner J.M., and Rietmeijer F.J.M. (1996) A first result of isothermal annealing of an Fe-SiO smoke. (abstract) *Lunar Planet. Sci. Conf. XXVII,* 647-648.

Karner J.M., Rietmeijer F.J.M., and Janeczek J. (1996) AEM, XRD, and IR analyses of an AlSiO condensate annealed for 2 hours at room temperature up to 1100$^0$ C. (abstract) *Meteoritics and Planet. Sci. 31,* A69.

Kimoto K., and Nishida I. (1967) An electron microscope and electron diffraction study of fine smoke particles prepared by evaporation in argon gas at low pressures. *Japan. J. Appl. Phys. 6,* 1047-1059.

Komoda T. (1968) Study on the structure of evaporated gold particles by means of a high resolution electron microscope. *Japan. J. Appl. Phys. 7,* 27-30.

Kothari B.K. (1978) Constraints imposed on the cooling history of a nebula by the growth of grains and inclusions. (abstract) *Lunar and Planet. Sci. Conf. IX,* 624-626.

Kraus S. (1985) HREM studies of interfaces in $ZrO_2$/ $Al_2O_3$ ceramics. In *Proceedings, 43rd Annual Meeting of the Electron Microscopy Society of America* (Bailey, G.W., ed.) pp. 218-219. San Francisco Press, San Francisco.

Lattimer J.M., and Grossman L. (1978) Chemical condensation sequences in supernova ejecta. *Moon Planets 19,* 169-184.

Lefevre J. (1970) An experimental study of the dust of iron, carbon, silicon carbide and silica. *Astron. Astrophys. 5,* 37-44.

Lewis R.S., Anders A., and Draine B.T. (1989) Properties, detectability and origin of interstellar diamonds in meteorites. *Nature 339,* 117-121.

Lord H.C. III (1965) Molecular equilibria and condensation in a solar nebula and cool stellar atmospheres. *Icarus, 4,* 279-288.

MacDowell J.F., and Beall G.H., (1969) Immiscibility and crystallization in $Al_2O_3$ -$SiO_2$ glasses. *J. Am. Ceram. Soc. 52,* 17-25.

Mackinnon I.D.R and Kaser S.A. (1988) The clay-size fraction of CI chondrites Alais and Orqueil: an AEM study. (abstract) *Lunar Planet. Sci.Conf. XIX,* 709-710.

Mackinnon I.D.R. and Rietmeijer F.J.M. (1987) Mineralogy of chondritic interplanetary dust particles. *Rev. Geophys., 25,* 1527-1553.

Muan A., (1957). Phase equilibria at liquidus temperatures in the system iron oxide-$Al_2O_3$- $SiO_2$ in air atmosphere. *J. Amer. Ceram. Soc. 40,* 121-133.

Muan A. and Osborn E.F. (1956) Phase equilibria at liquidus temperatures in the system MgO-FeO- $Fe_2O_3$- $SiO_2$. *J. Amer. Ceram. Soc. 39,* 121-140.

Nelson R., Thiemens M., Nuth J.A., and Donn B. (1989) Oxygen isotopic fractionation in the condensation of refractory smokes. *Proc. Lunar Planet. Sci.Conf. 19th,* 559-563.

Ney E.P. (1977) Star dust. *Science 195,* 541-546.

Nuth J.A. (1981) Experimental and theoretical studies of interstellar grains. NASA Technical Memorandum 83883. Goddard Space Flight Center, Greenbelt, MD. 245p.

Nuth J.A. (1987) Are small diamonds thermodynamically stable in the interstellar medium? *Astrophys. Space Sci. 139,* 103-109.

Nuth J.A. and Donn B. (1982) Experimental studies of the vapor phase nucleation of refactory compounds. 1. The condensation of SiO. *J.Chem. Phys.77,* 2639-2646.

Nuth J.A. and Donn B. (1983) Laboratory studies of the condensation and properties of amorphous silicate smokes. *Proc. Lunar Planet. Sci.Conf. 13th,* in *J. Geophys. Res.,88,* A847- A852.

Nuth J.A. and Hecht J.H. (1990) Signatures of aging silicate dust. *Astrophys. Space Sci. 163,* 79-94.

Nuth J.A., Nelson R.N., Moore M., and Donn B. (1988) Experimental studies of circumstellar , interstellar, and interplanetary refractory grains analogs. In: *Experiments on Cosmic Dust Analogues* (Bussoletti E. ed.) pp. 191-207. Kluwer Academic Publishers, New York.

Putnis A., and McConnell J.D.C. (1980) *Principles of Mineral Behaviour* (Hallam A., ed.) Blackwell Scientific Publications, New York.

Rietmeijer F.J.M. (1992) **Mineralogy of chondritic protoplanets in the early solar system.** *Trends in Mineral. 1.* 23-41.

Rietmeijer F.J.M. (1993) Size distributions in two porous chondritic micrometeorites. *Earth and Planet. Sci. Letters 117,* 609-617.

Rietmeijer F.J.M. (1996a) An analytical electron microscope study of hydrous alteration in a smoke of modal forsterite composition. (abstract) *Lunar and Planet. Sci. Conf, XXVII,* 1069-1070.

Rietmeijer F.J.M., (1996b) Principle components constrain dynamic pyrometamorphism in a partially melted interplanetary dust particle. (abstract) *Lunar and Planet. Sci. Conf. XXVI,* 1071-1072.

Rietmeijer F.J.M., (1996c) A test of isochemical behavior of principle components in chondritic porous IDPs. (abstract) *Meteoritics and Planet. Sci. 31,* A114.

Rietmeijer F.J.M., and Nuth J.A. (1990) Analytical electron microscope analyses of refractory circumstellar, interstellar and interplanetary dust analogs. (abstract) *Lunar Planet. Sci. Conf. XXI,* 1017-1018.

Rietmeijer F.J.M., and Nuth J.A. (1991) Tridymite and maghemite formation in an Fe-SiO smoke. *Proc. Lunar Planet. Sci. Conf. 21st,* 591-599.

Rietmeijer F.J.M., Nuth J.A. and Mackinnon I.D.R. (1986) Analytical electron microscopy of Mg-SiO smokes: A comparison with infrared and XRD studies. *Icarus 66,* 211-222.

Salpeter E.E. (1974) Nucleation and growth of dust grains. *Astrophys. J.* 193, 579-584.

Stephens J.R. and Kothari B.K. (1978) Laboratory analogues to cosmic dust. *Moon Planets 19,* 139-152.

Williams D.B. (1984) Quantitative x-ray microanalysis. In *Practical Electron Microscopy in Materials Science* pp. 55-89. Electron Optics Publishing Group, New Jersey.

Wood J.A. (1963) On the origin of chondrules and chondrites. *Icarus 2,* 152-180.

Zolensky M. and McSween H.Y. (1988) Introduction: Aqueous Alteration. In: *Meteorites and the early Solar System.* (Kerridge J.F. and Mathews M.S. eds.) Univ.of Arizona Press, Tucson.

Zook H.A., and McKay M.S. (1986) On the asteroidal component of cosmic dust (abstract). *Lunar Planet. Sci. Conf. 17,* 977-978.